



# ILLUMINATING THE DARK

with cosmic explosions and their afterglows

Dissertation submitted for the degree of

## PHILOSOPHIÆ DOCTOR

to the PhD School of The Faculty of Science, University of Copenhagen

on March 22 2018, by

**Jonatan Selsing**

Supervisor: *Lise Bech Christensen*

Committee:

*Prof. Carole Mundell,*

*University of Bath, United Kingdom*

*Prof. Stephen J. Smartt,*

*Queen's University Belfast, Northern Ireland, United Kingdom*

*Assoc. Prof. Steen H. Hansen,*

*University of Copenhagen, Denmark*



# ILLUMINATING THE DARK

with cosmic explosions and their afterglows

*If anyone can refute me – show me I am making a mistake or looking at things from the wrong perspective – I will gladly change. It is the truth I am after, and the truth never harmed anyone.*

— Marcus Aurelius, *Meditations*



## ABSTRACT

---

The large majority of our Universe is dark, its vast expanse only sparsely permeated by a thin web of matter. Inside this web, gravity has worked to form islands of light made up of immense collections of stars. These conglomerations of matter, what we have come to know as galaxies, carry with them the story of the life they have experienced in the form of their chemical compositions. At any time, this composition is set by the seed gas from which they were formed, but also the inevitable enrichment carried by the stellar appetite for turning light elements heavier. The cataclysmic explosions that either mark the end of stellar lives or are the results of mergers of stellar remnants, scatter enriched material throughout galaxies in which they live, providing the sustenance of a new generation of stars, richer and more complex in their compositions. In order for us to understand our place as humans in this universe, we need to investigate the cosmic history carried by the elements from which we are formed. This thesis investigates the most powerful explosions in the universe, gamma-ray bursts, how these can be used to probe the dark universe intersected by their light, and what consequence these events have for the universe that harbors them. I here present a homogeneously selected sample of gamma-ray burst (GRB) afterglows that are the results of more than eight years of sustained effort. This dataset is a unique resource that can be used to harvest the potential of GRB afterglows in illuminating the universe. These spectra contain rich information about the gas, dust, metals, molecules surrounding the GRB explosions, spanning a wide range of redshifts, thus providing unique insights in the star formation and chemical history of the universe. This treasure trove allowed me to discover especially significant events and in particular, I was able to single out GRB 111117A as the most distant short GRB ever discovered. The study of this single event allowed to me to constrain the intrinsic redshift distribution of short GRBs and the conditions of the progenitor system of short GRBs. I also present the observations of an electromagnetic counterpart to a simultaneous gravitational wave signal and short GRB, which is caused by the merger of two neutron stars. These data hold the secret to understanding the physical mechanisms behind this enigmatic phenomenon that has now come to be named a kilonova. Lastly, in these spectroscopic data of the kilonova, the spectral signatures of light *r*-process elements are identified, providing the first compelling evidence for the site of at least the light *r*-process elements.

## **ACKNOWLEDGMENTS**

---

First and foremost, my deepest gratitude and appreciation goes to my wonderful wife, Malene. You (are my) rock. Thank you for supporting me and our life together. Without you, my life would be empty. During the course of my PhD, you have given me the greatest gift, our daughter Marie. You both continuously remind me that you are the most important content of my life. And Marie, coming home to your smiling face brings me more meaning than any amount of GRB spectra can ever do.

Thank you, Lise. As my PhD supervisor you have given me the chance to find my own feet in this wondrous world of science. You have always been welcoming and appreciative of my new projects while correctly pushing me to finish what I start. Your door have always been open for me and this has given be a sense of safety that have allowed me build the confidence required to pursue my ideas.

There are a lot of people, especially at DARK, that deserve my deepest appreciations. Darach, our work on AT 2017gfo has been extremely rewarding, and I feel that we are making some really great progress in a very interesting field. Johan, thanks for trusting me with your GRB sample and it has been great working with you. Jens, our work on lensed supernovae have been a source of great fun and phenomenal physical phenomena. Daniele, I consider you my mentor in science and I hope to continue relying on your deep understanding of physics. Peter, thanks for being the most awesome office mate, although you could do with a bit more foosball training. Thank you to all of my fellow postdoc and PhD students that have shared this road with me, through the years. All of you have made the daily life a breeze and I consider you all to be my good fiends and colleagues. Thanks you to all the people in the XSGRB and stargate collaboration. You may not realize it, but you have all been a large part of my PhD life and I appreciate the collaboration. Thank you Enrico and Jason for hosting me in Santa Cruz. Thanks Aldo for your patience with me. Thank you Philip and Chris for being awesome. Thanks to all the graduate students at Santa Cruz - you really have a welcoming place. Thank you, Pat. Our work on SN Refsdal was really fun.

Thanks to my family. My parents, my Bedste and Morfar, my brothers and sister, Rune, Lea, Emil and Malte. Thanks Stefan. Thank you, my TSC friends – you are all awesome.

## MOTIVATION AND THESIS STRUCTURE

---

Understanding the evolution of the universe from the Big Bang to our present day presents itself with a problem of almost boundless complexity. By focusing on tiny pieces of this evolution, we can make incremental advances, which over time allows the formation of a coherent picture of understanding. Gamma-Ray Bursts (GRBs) are powerful tools in this endeavor because, due to their extreme brightness, they are visible almost all the way to the edge of the observable universe. In pencil-beams of light, they illuminate the path carved out between their explosions and us. We can therefore use them to explore the intervening universe. In addition to their use as cosmological probes, as I have helped to show, it turns out that the short GRBs themselves are an essential component to explain the abundances of the heaviest elements we observe here on Earth.

This thesis is based on parts of the work I have carried out over the last years. It is not a complete account of the work I have done, but a selected story that presents a single narrative. It is based on papers that I have either led or contributed significantly to. For an overview of the publications I have contributed to, see Sect. 5.2.6. Because the common theme for the work presented here is the study of GRBs, I begin the thesis with an introduction to our understanding of GRBs - both long and short duration GRBs. This is in Chapter 1. I outline the historical development of this understanding and describe the current physical picture for the inner workings of this energetic phenomenon.

In Chapter 2, I present an effort that has been carried out over the last 8 years to gather a homogeneous collection of both long and short GRB afterglows, viewed with X-shooter, one of the best spectrographs in the world. I characterize the sample in terms of how complete it is with respect to the underlying parent population of GRB afterglows and measure key quantities. I format and release the data behind the sample, allowing the astronomical community to harvest the rich potential of these GRB afterglow spectra. A series of forthcoming publications based on this sample will investigate subjects ranging from the interaction of the GRBs with their surroundings to the transparency of the universe to ionizing radiation as a function of redshift.

In Chapter 3, I present the most distant bona-fide short GRB ever found, GRB 111117A. I characterize the host properties and due to the redshift, I can put constraints on the redshift

distribution of short GRBs. This has profound consequences for the projected number of short GRBs in the universe throughout cosmic history and through this, the chemical evolution history of the universe. Additionally, due to the relatively short time between the explosion of this short GRB and the formation of the universe, I can put constraints on the initial separation between the two neutron stars that merged and generated the GRB. This has important implications for the formation models of these types of systems.

In Chapter 4, I present the discovery of the kilonova, AT 2017gfo, which is the first electromagnetic counterpart to a gravitational wave signal. This discovery was named the Science breakthrough of 2017. I additionally present circumstantial evidence that the counterpart was powered by the decay of freshly synthesized *r*-process elements. The *r*-process elements make up the heaviest elements found in nature and include well known elements such as gold and platinum. This discovery shows that *r*-process elements are likely formed in the mergers of neutron stars.

In Chapter 5 I present the discovery of the spectral signature of light *r*-process elements in the spectra of AT 2017gfo. With the identification of spectral features from Sr II, I show that the merger of two neutron stars forms at least the light *r*-process elements. This direct evidence contradicts previous claims of element detections and supports the idea of a blue kilonova component, primarily formed of light *r*-process elements.

I conclude the thesis by summing up the advances in our understanding of the universe I have contributed with and outline what is the likely directions of continued research.

# CONTENTS

---

<b>Abstract</b>	<b>iii</b>
<b>Acknowledgments</b>	<b>iv</b>
<b>Motivation and Thesis Structure</b>	<b>v</b>
<b>Contents</b>	<b>vii</b>
<b>1 Introduction</b>	<b>1</b>
1.1 Gamma-Ray Bursts . . . . .	1
1.2 Long Gamma-Ray Bursts . . . . .	5
1.2.1 Associated transients . . . . .	6
1.2.2 Environments . . . . .	8
1.2.3 Progenitors . . . . .	9
1.2.4 Long GRB model . . . . .	11
1.3 Short Gamma-Ray Bursts . . . . .	13
1.3.1 Environments . . . . .	14
1.3.2 Associated transients . . . . .	15
1.3.3 Gravitational waves . . . . .	16
1.3.4 GW170817/GRB170817A/AT2017GFO . . . . .	17
1.3.5 Short GRB/kilonova progenitor systems . . . . .	18
<b>2 A complete sample of GRB afterglows</b>	<b>22</b>
2.1 Introduction . . . . .	23
2.2 Sample selection criteria and observations . . . . .	25
2.2.1 Sample selection criteria . . . . .	25
2.2.2 Follow-up procedure . . . . .	27
2.2.3 Rapid response mode (RRM) observations . . . . .	27
2.2.4 Observations . . . . .	28

<b>2.3</b>	<b>Data processing</b>	<b>35</b>
2.3.1	Post-processing	36
2.3.2	Correction for offsets in the wavelength calibration	37
2.3.3	Spectral resolution	39
2.3.4	Spectral extraction	40
2.3.5	Telluric correction	41
2.3.6	Continuum estimate	42
2.3.7	Science data products	44
<b>2.4</b>	<b>Results</b>	<b>45</b>
2.4.1	Follow-up timing and afterglow brightness	45
2.4.2	Sample completeness	45
2.4.3	On the redshift distribution of GRBs	49
2.4.4	Sample darkness	51
2.4.5	Hydrogen column densities	55
<b>2.5</b>	<b>Discussion and conclusions</b>	<b>56</b>
<b>3</b>	<b>The highest measured redshift of a short GRB and the physical implications</b>	<b>99</b>
3.1	Introduction	100
3.2	Observations and results	103
3.2.1	Spectroscopic observations and analysis	103
3.2.2	Imaging observations and SED analysis	106
3.2.3	X-ray temporal and spectral analysis	109
3.3	Reinterpretation of the rest-frame properties	109
3.3.1	Classification	109
3.3.2	Rest-frame $N_{\text{H},\text{X}}$	111
3.3.3	Host galaxy	114
3.4	Implications for the redshift distribution of sGRBs	115
3.5	Constraints on progenitor separation	116
3.6	Conclusions	118
<b>4</b>	<b>Observations of a neutron star merger</b>	<b>121</b>
4.1	Main	122
4.2	Methods	130
4.2.1	Optical/NIR imaging	130
4.2.2	FORS2 spectroscopic observations	131
4.2.3	X-shooter spectroscopic observations	132
4.2.4	Foreground dust extinction	133

4.2.5	Spectrum analysis and interpretation . . . . .	133
4.2.6	Description of the spectral evolution . . . . .	134
4.2.7	Host emission analysis . . . . .	135
4.2.8	Off-beam jet scenario . . . . .	135
<b>5</b>	<b>Finding the origin of r-process elements in the universe</b>	<b>142</b>
5.1	Main . . . . .	143
5.2	Methods . . . . .	152
5.2.1	Spectral synthesis . . . . .	152
5.2.2	Spectral modelling . . . . .	156
5.2.3	P Cygni modelling . . . . .	160
5.2.4	Expansion velocity evolution . . . . .	161
5.2.5	TARDIS modelling . . . . .	161
5.2.6	Exclusion of the Cs I and Te I identification . . . . .	162
	<b>Conclusions and Outlook</b>	<b>164</b>
	<b>List of Publications</b>	<b>167</b>
	<b>Resumé på dansk</b>	<b>169</b>
	<b>Bibliography</b>	<b>170</b>



# 1

## INTRODUCTION

The overarching theme of this thesis is the study of explosive transients. This includes both the consequences of the events themselves for the evolution of the universe and use of these bright events as probes of the universe. The primary focus is on gamma-ray bursts (GRBs) and the associated signals that accompany these bright events – the afterglows of the GRBs that arise as the ejected material interacts with the surrounding gas (Chapter 2), the distribution of these events throughout cosmological time (Chapter 3) and the electromagnetic transients that are formed by the progenitor system during the creating of the GRB (Chapter 4 and 5). I will start with a general introduction to GRBs and their associated transients.

### 1.1 Gamma-Ray Bursts

In 1963, in an effort to slow the nuclear arms race, the Partial Test Ban Treaty was signed between the United States, the United Kingdom, and the Soviet Union, with a large number of countries joining later. This treaty was meant to prohibit testing of nuclear weapons in the atmosphere, in space, and under water as a means to prevent the proliferation of nuclear arms throughout the globe. To ensure treaty compliance, a number of satellites were sent in orbit by the United States and the Soviet Union with on-board detection instruments, sensitive in X-rays and  $\gamma$ -rays. These satellites, called the Vela satellites, were designed to detect any nuclear detonation on Earth or the Moon, through the brief X-ray and  $\gamma$ -ray signature accompanying such a detonation. However, not long after the launch, the Vela satellites started picking up bursts of  $\gamma$ -rays, not consistent with known  $\gamma$ -ray temporal signature and with an apparent isotropic celestial distribution. The apparent isotropic celestial distribution (See Figure 1.1) of the events detected by the Vela satellites meant that these phenomena were likely of cosmic origin and not related to any known structure local to Earth, and thus a new transient astronomical entity was born ([Klebesadel et al. 1973](#)). These events had not been found before due to the inability of  $\gamma$ -rays to penetrate the Earth's atmosphere, leaving them only detectable from space.

With the launch of the Compton Gamma Ray Observatory (CGRO) in 1991 with the on-board Burst and Transient Source Experiment (BATSE), the rate of detected GRBs increased significantly. An increased number of sources coupled with an additional improvement of the localization accuracy of GRBs meant that, before long deviations from isotropy in the celestial distribution of GRBs were constrained to be very small. Constrained to show no directional preference, the cosmological origin of GRBs became the favored model, replacing the previously popular Galactic origin (Meegan et al. 1992). However, the large error boxes of the GRBs detected with BATSE meant that it was not possible to localize the optical counterparts of the detected GRBs and thus studies were limited to the high-energy regime. The temporal properties of the BATSE observed  $\gamma$ -ray signals provided strong evidence for two distinct classes of GRBs. The duration is measured by  $T_{90}$ , which is the time in which 90 per cent of the source photon counts are collected and is therefore also a function of the sensitivity and energy band used. An apparent bimodal distribution of the recorded burst durations (Kouveliotou et al. 1993) was observed, with a division around 2 seconds. When investigating the spectral properties of the two temporal groups, further evidence for the division of GRBs in two classes was found in the different spectral hardness of the two classes, with the shorter bursts having harder spectra. These two physically distinct phenomena were named, based on their relative durations, short GRBs and long GRBs.

With the launch of the BeppoSAX satellite (Boella et al. 1997), a significant advancement in the understanding of GRBs was achieved with the discovery of the X-ray counterpart of the long GRB 970228 (Costa et al. 1997). The X-ray localization, with a much smaller error on the position of the burst, additionally led to the discovery of the first optical counterpart (van Paradijs et al. 1997) of the same GRB, found in imaging data obtained by the William Herschel Telescope (WHT). The counterpart, detected in any part of the electromagnetic spectrum, of a GRB is referred to as the GRB afterglow. With the discovery of the optical counterparts it was possible to localise bursts to sub-arcsecond precision and at the position of GRB 970508 a galaxy was found, located at cosmological distances (Metzger et al. 1997). The unequivocal association of a GRB with a galaxy at cosmological distances coupled with the measured fluxes, clearly constrained the energy scale of these events to be enormous and the time-scale of variation found in the first radio-counterpart (Frail et al. 1997), constrained the ejecta to be moving close to the speed of light. The afterglows of GRBs are bright, pencil-beams of light that pierce through the universe. Anything between the GRB and us leaves its prints in the afterglow light, allowing us to study not just the GRBs themselves, but also the intervening universe (van Paradijs et al. 2000). These sight-lines can be seen as samplings of the universe, allowing us to draw inferences about the intervening universe, without relying on persistent sources of radiation, freeing us from some of the biases of sensitivity (Meszaros & Rees 1996; Ricker & Team 2004) traditionally affecting luminosity selected samples. Due to the immense brightness of GRBs, they can be seen to the highest redshifts (Tanvir et al.

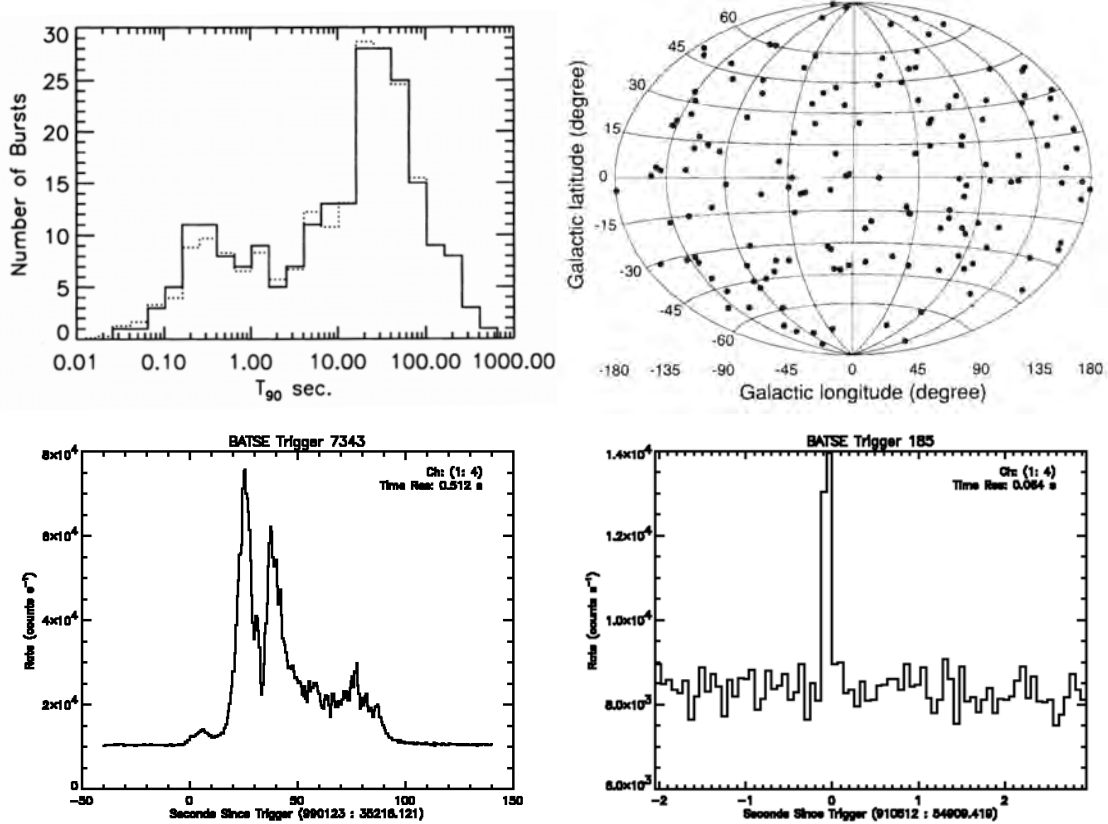


**Figure 1.1:** High-energy properties of the GRBs detected by BATSE. The upper left corner shows the distribution of burst duration,  $T_{90}$ , for the 222 GRBs in the first BATSE catalog as presented in Kouveliotou et al. (1993). The bimodal distribution of burst durations is evident, with the minimum between the two distributions at 2 seconds. The upper right corner shows the isotropic celestial distribution of the 158 bursts presented by Meegan et al. (1992). To illustrate the typical light-curves for the two different classes of GRBs, the lower left corner contains the long GRB 990123 ( $T_{90} = 63.30 \pm 0.26$  s; GCN #224), while the lower right corner contains the short GRB 990511 ( $T_{90} = 0.132 \pm 0.077$  s; BATSE duration table). The typical difference in light-curve structure between long and short GRB is illustrated in the lower two panels

2012a; Cucchiara et al. 2013; Tanvir et al. 2017a), making it a unique tool to investigate the early universe (Lamb & Reichart 2000).

In 2004, the field of GRB was revolutionized when the *Swift* Gamma-Ray Burst Mission (Gehrels et al. 2004) was launched into space. Later renamed the Neil Gehrels *Swift* Observatory, in honour of the late PI, Neil Gehrels, it is most commonly known as *Swift*. *Swift* is currently the powerhouse of GRB localizations<sup>1</sup> and together with the *Fermi* space telescope (Atwood et al. 2009), they provide the majority of GRB detections. A number of other GRB observatories

<sup>1</sup>For an overview of the registered GRBs and their detection instrument, services like the one maintained by Jochen Greiner and by Daniel Perley provide valuable information, such as detection of optical afterglow, redshift, burst duration, etc.

(*Konus-Wind*; Aptekar et al. 1995, *INTEGRAL*; Winkler et al. 2003, *MAXI*; Matsuoka et al. 2009, and *AGILE*; Tavani et al. 2009) deliver GRB detections on a regular basis, where however the localizational accuracy often hampers the follow-up success. *Swift* made it possible to harvest much of the potential of GRBs as probes of the intergalactic medium (IGM). Built with rapid follow-up in mind, *Swift* has three instruments on board that makes it very effective at finding and following up GRBs. Always observing is the Burst Alert Telescope (BAT; Barthelmy et al. 2005). It covers one sixth of the entire sky in a single pointing in the 15–350 keV band, although the sensitivity is highest in center of the detector and falls off towards the edges. The detector is continuously being read out, and a complex triggering algorithm searches the data for new sources in real time. When a new source is detected, BAT can localize it to within 4 arcminutes, and the telescope can immediate turn (slew) to face the detected direction. Here the two other instruments can begin their job. While BAT is continuously integrating to build a light-curve for the new source, the X-Ray Telescope (XRT; Burrows et al. 2005), and the UltraViolet and Optical Telescope (UVOT; Roming et al. 2005) can begin observations. XRT has a field-of-view (FOV) of 23.6 arcminutes in the 0.2–10 keV energy range and is able to localize a new X-ray source to  $< 5$  arcsec precision within 10 seconds. With an X-ray position of this accuracy, it is possible to locate an afterglow of sufficient brightness in ground-based follow-up. UVOT is designed to be able to capture the presence of an optical afterglow, however it only detects afterglows in  $\approx 30\%$  of cases. This is due to its limited collecting area; and in some cases, the lack of detection is due to obscuration by dust in the GRB host galaxy or absorption by neutral hydrogen for high-redshift events. A robotic system is set up to automatically filter through the BAT triggers and distribute a notice with the position and intensity to the ground based observers called the Gamma-Ray Burst Coordinates Network (GCN) (Barthelmy 2000). The rapid availability of afterglow positions, coupled with prompt availability of 8-meter class telescopes, means that, currently the astronomical community is in a very good position to study GRBs and use them as probes of the universe.

The high-energy properties of GRBs are well studied, due to the large number of events recorded so far. BATSE alone triggered on 2704 GRBs (BATSE catalog overview; Preece et al. 1999) and *Swift* has to date (21.03.2018) triggered on 1342 bursts (*Swift* GRB catalog; Lien et al. 2016). Filtering the *Swift* GRB catalog by  $T_{90} > 2$  s, there are 1022 long GRB and 109 short GRBs. This highlights another difference between the two types of GRB. Long GRBs are detected much more frequently than their long counterparts. The relative detection ratios of the two events depend sensitively on the instrument. I will in the following two sections describe the characteristics of the two classes and cursory review the current understanding of the progenitor systems that are believed to give rise to events.

## 1.2 Long Gamma-Ray Bursts

The temporal evolution of GRBs are separated in two phases. The prompt phase and the *afterglow* phase. The prompt phase refers to the part of the light-curve that is detected by trigger instrument, usually covering the highest energies available (typically  $> 10$  keV). The prompt phase of long GRB is characterized by an intense  $\gamma$ -ray flux, which together with a measured redshift and assumed isotropic emission would suggest a luminosity of  $\lesssim 10^{54}$  erg s $^{-1}$  for the brightest bursts, rivaling that of all the stars in the entire observable universe together (Kumar & Zhang 2015).

The duration of the prompt phase in long bursts extends from 1 s up to  $\sim 1000$  s (Lien et al. 2016). There are some suggestions of ultra-long GRBs constituting a subclass of long GRBs (Levan et al. 2013; Virgili et al. 2013) with durations of the order  $10^4 - 10^5$  s. The light-curve often consists of multiple pulses, with significant substructure and a variability time-scale down to milliseconds, as shown in the lower left panel in Fig. 1.1. In a single pulse, there is a temporal delay between the arrival of the photons of different energy, with the higher energy photons arriving first (Norris et al. 1996; Norris & Bonnell 2006). This temporal delay is called the *spectral lag* is an additional diagnostics used to separate long and short GRBs as short GRBs exhibit negligible lags. The time-scale of the shortest variations constrains the spatial extent of the emission engine to be well below the stellar scale, and with the energies inferred under the assumption of isotropic emission implies that the emitting material would be optically thick to itself due to pair-production (the co-called compactness problem; Cavallo & Rees 1978).

As indicated by the time-scale of the radio scintillation in GRB 970508 (Frail et al. 1997), and the inferred superluminal expansion velocity of the ejecta of GRB 030329 (Taylor et al. 2004), the emission process of both the prompt and the afterglow phase are generated by material moving close to the speed of light. Initially the material is moving ultrarelativistically, with Lorentz factors  $\Gamma \approx 100 - 1000$  (Soderberg & Ramirez-Ruiz 2003). It later slows down to only mildly relativistic flows (Piran 2004). With the detection of the jet break in GRB 990123 (Kulkarni et al. 1999a,b; Sari et al. 1999), the material was additionally constrained to be launched in a jet-like structure. The combination of relativistic motion, which reduces the luminosity compared to the non-relativistic case, coupled with a jet opening angle of typically  $< 10^\circ$  (Goldstein et al. 2015), means that the actual luminosities of the long GRBs are more likely  $\lesssim 10^{51}$  erg s $^{-1}$ . This energy release is still enormous, but it is on the scale of the kinetic energy of SNe (Piran 2004) and thus not unprecedented. At the inferred luminosities, the energy density is not high enough for pair-production, leaving the emitting material optically thin to the emergent radiation, providing a natural solution to the compactness problem. The prototypical engine for launching astrophysical jets requires strong poloidal magnetic fields and a consequence of the strong magnetic fields is that the radiation of the afterglow is expected to exhibit a significant, variable degree of linear polarization (Ghisellini & Lazzati 1999; Rossi et al. 2004). The measurement of a variable, high

degree of linear polarization in the afterglow of both GRB 120308A ([Mundell et al. 2013](#)) and GRB 160625B ([Troja et al. 2017a](#)), suggested that the launching mechanism is driven by large-scale ordered magnetic fields generated by the central engine. However, with the measurements of a large degree of circular polarization in the afterglow of GRB 121024A ([Wiersema et al. 2014](#)), it seems like the emission mechanism of the afterglow radiation is not entirely driven by shocks ([Nava et al. 2016](#)).

The spectrum of the high-energy prompt emission is detected from X-ray energies, increasing in flux up to  $\sim 300$  keV ([Preece et al. 1999](#)), where after it drops off, sometimes detected extending all the way up to GeV energies ([Ackermann et al. 2014](#)). The high-energy spectrum is well described by two power-laws joined together at the peak energy and falling off at both sides ([Band et al. 1993](#)), with the peak flux energy distribution covering two orders of magnitude in energy (2 keV – 1 MeV), suggesting significant variation in the emission engine across the GRB population. The spectrum is non-thermal, which together with the relativistic motion of the ejecta potentially suggests that synchrotron radiation ([Rees & Meszaros 1992](#); [Katz 1994](#); [Lloyd & Petrosian 2000](#); [Piran 2004](#); [Xu et al. 2018](#)) generated by internal shocks in the ejecta material could play a role in the spectral formation. However, the presence of relativistically moving electrons suggests that inverse Compton scattering could potentially alter either an intrinsically thermal ([Pe'er 2008](#); [Pe'er et al. 2012](#)) or synchrotron radiation spectrum ([Sari & Esin 2001](#)), making the radiation generation mechanism less certain.

### 1.2.1 Associated transients

Not long after the discovery of the first GRB afterglow, a strong clue to the likely stellar origin of long GRBs came from the detection of a supernova (SN), SN 1998bw, spatially and temporally coincident with GRB 980425 ([Galama et al. 1998](#)). GRB 980425 is, still to this date, the closest GRB ever detected at a distance of only 37 Mpc ( $z = 0.008$ ) and thus it is still an excellent test bed of the environmental properties of the regions hosting long GRBs ([Krühler et al. 2017](#)). SN 1998bw was a broad-lined type Ic SN ([Woosley et al. 1999](#)), a rare subtype of SN that exhibit signatures from neither hydrogen nor helium in their spectra with highly velocity broadened spectral features. The absence of hydrogen and helium in the spectra suggests progenitor stars that are heavily stripped and the broad spectral features can be interpreted as due to large ejecta velocities. Because GRB 980425 was sub-luminous by 4 orders of magnitude compared to typical, cosmological GRBs, it was unclear how representative the connection between GRB 980425 and SN 1998bw was for the general population of GRBs. The definitive evidence for a stellar link to long GRBs came five years later with detection of another close-by ( $z = 0.1685$ ) GRB, GRB 030329, and the associated SN, SN2003dh ([Hjorth et al. 2003](#); [Stanek et al. 2003](#)). Fig. 1.2 shows transition from the featureless power-law shaped spectrum generated by synchrotron radiation of the early

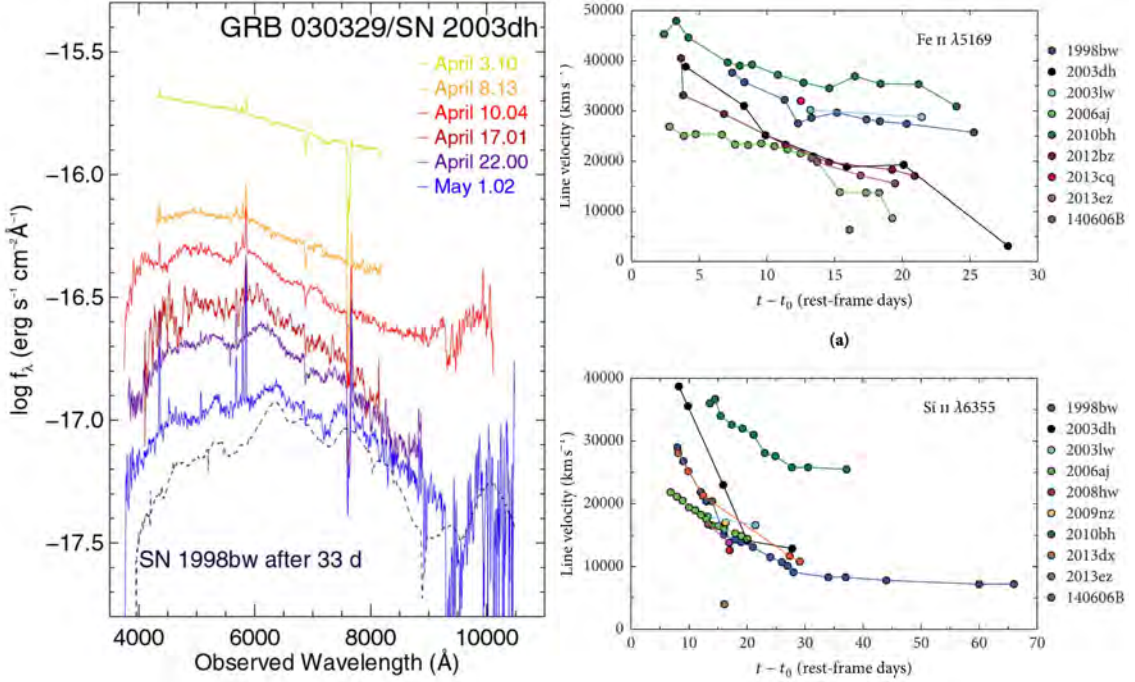


**Figure 1.2:** The left panel shows the spectral evolution of GRB 030329/SN 2003dh in colored lines. It is reproduced here from Hjorth et al. (2003). The first spectra are shown at the top are almost featureless, save for host emission lines and telluric absorption. The subsequent evolution introduces broad undulations across the spectra coverage. The spectra obtained last are similar to SN 1998bw, shown in the black-dashed line. The transition from a pure afterglow power-law to a SN spectrum establishes the stellar origin of long GRBs. The right panel shows the photospheric expansion velocity evolution for a number of GRB-SN measured. It is adapted here from Cano et al. (2017b). The initial expansion velocity is a significant fraction of the speed of light, illustrating the high velocities of GRB-SN.

afterglow to a SN spectrum with broad undulations. In term of energy budget, GRB 030329 was as a completely regular cosmological GRB and thus there is no ambiguity in the generalization of this event. SN2003dh was spectroscopically confirmed to be very similar to SN 1998bw and the similarity between the spectroscopic characteristics suggests a class of SN that are intimately related to the GRB phenomena.

Since the detection of the first GRB-SN, a number of similarly associated events have been found, GRB 031203/SN 2003lw (Malesani et al. 2004), GRB 060218/SN 2006aj (Pian et al. 2006; Modjaz et al. 2006), GRB 091127/SN 2009nz (Cobb et al. 2010), GRB 100316D/SN 2010bh (Bufano et al. 2012), GRB 101219B/SN 2010ma (Sparre et al. 2011a), GRB 120422A/SN 2012bz (Schulze et al. 2014a), GRB 130427A/SN 2013cq (Xu et al. 2013a), GRB 130702A/SN 2013dx (D’Elia 2015), GRB 130215A/SN 2013ez (Cano et al. 2014), GRB 161219B/SN 2016jca (Cano et al. 2017a; Ashall et al. 2017), and GRB 171205A/SN 2017iuk (Izzo et al. in prep), establishing a connection between GRBs and SNe beyond any reasonable doubt. The right panel of Fig. 1.2 shows the measured

expansion velocities of some of these GRB-SN, showcasing the large expansion velocities of the SNe associated with GRBs. Another case is that of GRB 111209A/SN 2011kl, however the extreme duration of that bursts indicates a potentially different physical driver (Greiner et al. 2015). Common for all the GRB-SN is that they are all at low redshift as we do still not have the sensitivity to detect these types of SNe at larger distances. There are examples (Fynbo et al. 2006; Gal-Yam et al. 2006; Della Valle et al. 2006) of apparently long GRBs which show no SN to deep limits, however lots of controversy has gone into their classification (Gehrels et al. 2006), and there is no consensus whether these are in fact extreme cases of short GRBs (where no SN would be expected). The converse is, however concretely true - that the detection of a SN Ic-BL does not imply a GRB (Soderberg et al. 2010; Modjaz et al. 2015), although some tentative evidence exists that in some cases, radio-loudness similar to the GRB-SN is associated to some of these SNe without a GRB (Corsi et al. 2016).

### 1.2.2 Environments

We only discover the position of a GRB once it explodes. No GRB progenitors have been observed in pre-explosion imaging and therefore a large part of our understanding regarding these phenomena rests on our ability to piece together circumstantial evidence. One essential avenue in investigating GRBs is the environments in which they are formed. As we have seen in the previous section, GRBs are of stellar origin and associated with stripped envelope core-collapse SNe. Because the progenitors of stripped envelope core-collapse SNe are very massive stars, the lifetime of GRB progenitors are expected to be short and its position coincident with a star forming region. Due to the short turnover between formation and explosion, the conditions of the gas local to the burst can to a first order be considered the same as the parent star (Modjaz 2011). Therefore important constraints on the conditions required for the GRB engine to function can be learned from investigating the systematics of the environments local to the GRB.

Not long after their discovery, it was found that GRBs at low redshift ( $z \lesssim 1$ ) are not hosted in typical field galaxies, but instead they seem to prefer faint hosts dominated by blue light (Fruchter et al. 1999; Le Floc'h et al. 2003; Christensen et al. 2004). Coupled with a preference for hosts with low stellar masses and high specific star-formation rates (Castro Cerón et al. 2006; Savaglio et al. 2009), means that GRBs were potentially not the un-biased tracers of star-formation they had been thought to be (Kistler et al. 2009; Robertson & Ellis 2012; Tanvir et al. 2012a). With the accurate localization of the GRB positions, it became possible to pinpoint the exact location of long GRBs within their host galaxies. Long GRBs are almost exclusively associated with the brightest parts of their host galaxy (Bloom et al. 2002; Fruchter et al. 2006; Svensson et al. 2010; Lyman et al. 2017), where the star-formation is also most intense. Due to their origin from massive stars, star-formation is expected to be the main driver of these events, however, at least at low

redshift, GRBs additionally seems to prefer environments where the metallicity is low (Prochaska et al. 2004; Gorosabel et al. 2005; Stanek et al. 2007; Kewley et al. 2007; Graham & Fruchter 2013, 2017).

The apparent preference of GRBs to be hosted in small, irregular galaxies, has in part turned out to be an effect of the chemical evolution of the universe and partly a selection effect. With more detailed studies, based on deeper searches, hosts that are heavier in terms of stellar mass and with redder colors have been found (Krühler et al. 2011a; Rossi et al. 2012) as well as hosts with closer to solar metallicities (Elliott et al. 2013a; Schady et al. 2015). This type of selection highlights the need for *complete* samples of GRBs in order to address the population properties. Complete means unbiased with respect to the underlying, parent GRB population. Complete samples are constructed based on a set of selection criteria that are assumed to be unrelated to the GRB engine itself, but more reflect telescope sensitivity or burst observability. These cuts significantly increase the completeness (the fraction of bursts fulfilling the cuts, observed as part of the sample) at the cost of significantly reduced number statistics. There has been a number of attempts at constructing complete samples (Jakobsson et al. 2006; Greiner et al. 2011; Salvaterra et al. 2012; Hjorth et al. 2012; Vergani et al. 2015; Perley et al. 2016a; Selsing et al. 2018a), and these systematically contain a higher fraction of redder, heavier and more dust-obscured hosts.

The complete samples paint a picture of GRBs hosts that are indeed less massive in term of stellar mass than field galaxies (Perley et al. 2016b), fainter (Schulze et al. 2015), and shows a preference for low-metallicity environments (Krühler et al. 2015a). However, the preference is not nearly as strong as suggested earlier and does not seem sharp. Additionally, due to chemical evolution of the universe, these preferences becomes less prominent at higher redshift, where the metallicity evolution of the universe more easily lets more massive galaxies host GRBs (Kocevski et al. 2009). I show the results of Perley et al. (2016b) in Fig. 1.3, where low observed brightness, low stellar mass, and metal aversion of long GRBs in terms of their hosts is visible.

### 1.2.3 Progenitors

Directly finding the progenitor stars of SNe is notoriously hard as it requires pre-explosion observations and has still only been accomplished in a few cases (For II-P Dyk et al. 2003; Maund et al. 2004; Smartt et al. 2004; Smartt 2009, Ib Cao et al. 2013, and Ic Van Dyk et al. 2018). Still this has not been accomplished for either SN Ic-BL or GRB-SN. However, parts of the physical nature of the stellar progenitors can still be inferred from associated transients, namely the absence of hydrogen and helium in their spectra along with very high ejection velocities (Woosley et al. 1999).

Wolf-Rayet stars are a late evolution stage of some massive stars. In Wolf-Rayet stars the outer envelope of hydrogen and helium has been stripped, due to immense radiation pressure from

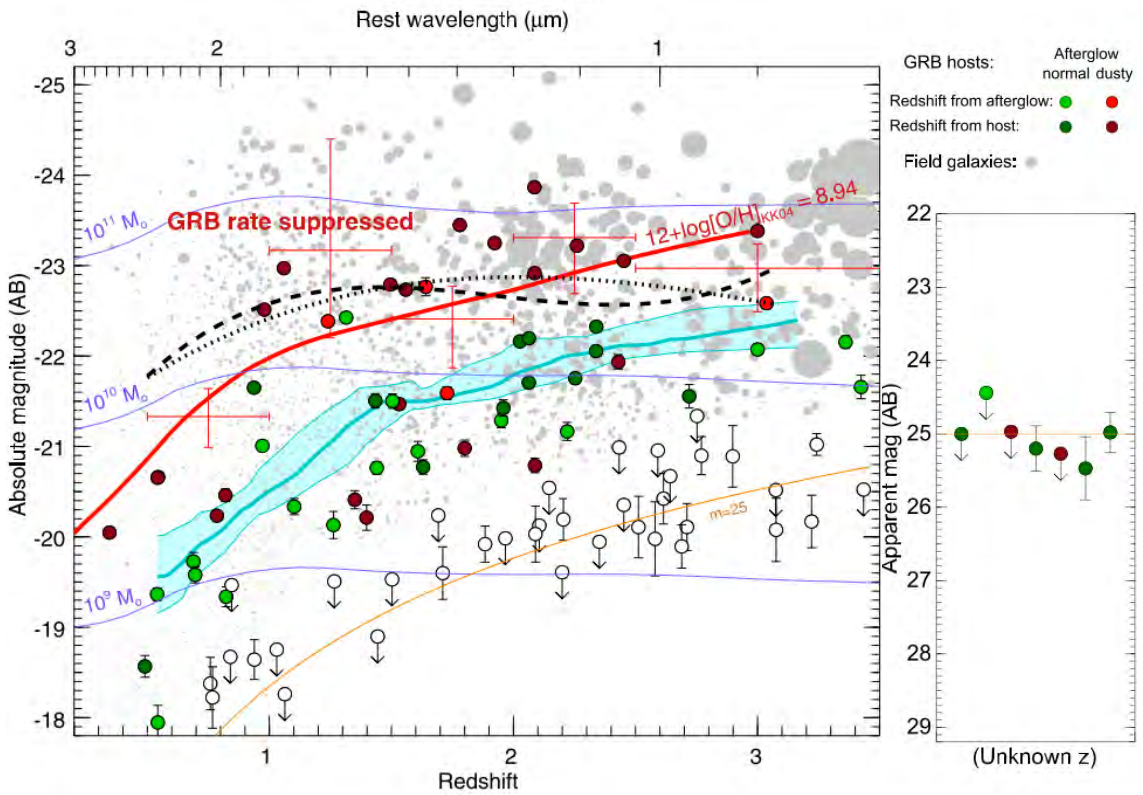


**Figure 1.3:** Long GRB host galaxies of the Swift GRB Host Galaxy Legacy Survey (SHOALS, [Perley et al. 2016a](#)) compared to the general population of galaxies, adapted from [Perley et al. \(2016b\)](#). In green and red are the GRB hosts, where red dots represents a dust-obscured host. The grey shading shows a similarly complete selection of field galaxies, where the sizes of the dots reflect the star formation rates. If GRBs are unbiased tracers of star formation, the hosts should follow the dotted and dashed, black lines which represent the field population from MODS/GOODS-N and CANDELS/UDS. The red, solid line indicates the average mass of field galaxies with a metallicity lower than a suggested threshold.

the underlying, hot core. Line-opacity from metals in the envelope delivers the push required to remove the outer layers ([Lucy & Solomon 1970](#); [Castor et al. 1975](#)) and the content of metal in the envelope delivering the opacity is in turn set by the metal richness of the gas that forms the star ([Vink & de Koter 2005](#); [Vink et al. 2011](#)) and the degree to which the inner, heavier burn products are moved to the surface. In some cases, GRB positions are found close to regions of Wolf-Rayet stars ([Hammer et al. 2006](#); [Kröhler et al. 2017](#)).

The launching of a jet is in all models tied closely together with rotation of the parent star ([Yoon & Langer 2005](#); [Woosley & Heger 2006](#); [Yoon et al. 2006](#)). Increased stellar rotation will increase the degree of chemical mixing in the star, which will lead to an increase in the content of metals in the outer layers leading to an increase in the mass loss of the stellar wind. As the angular momentum of the star tends to pile up at the edges of the star ([Spruit 2002](#)), from where

the mass is lost, the spin-history of a given star will depend on the metallicity the gas. For a given metallicity, increasing the rotational speed will increase the mass loss, and for a given initial rotation, increasing the metallicity will slow the star down. For this reason, the progenitor stars of GRBs, if they are in a single system, are expected to be formed in low-metallicity environments, where the highest degree of rotation can be retained during the stellar lifetime.

The requirement for low metallicity can be loosened if the star is formed in a binary system (Smartt et al. 2002; Fryer & Heger 2005) and the large majority of massive stars are formed in binary systems (Sana et al. 2008, 2009). In binary systems, a star can be stripped of the outer layers through either Roche lobe overflow or common envelope evolution. Additionally, the torques introduced by the binary can help keep spinning the core sufficiently fast (De Mink et al. 2013). These qualities make binary systems tractable as a likely ingredient in a successful GRB, however no progenitor system has been found.

#### 1.2.4 Long GRB model

No single model has yet to effectively capture the complexity of the observed phenomena. It is especially the difficulty of producing both a relativistic jet that can pierce through the star and interact with the circumstellar material on a relatively short timescale, coupled with a very energetic supernova, powered by radioactive decay of several solar masses of  $^{56}\text{Ni}$ . However, parts of the observed characteristics have found attractive explanations and several models exist that attempt to paint a coherent physical picture of the origin of long GRBs. Common to all models of long GRBs is that they must initially be based on stars, due to association with SNe.

At the end of the life of a rapidly spinning, envelope stripped, massive star, likely binary member, the iron core undergoes gravitational collapse (Janka et al. 2007; Janka 2012; Müller 2017). The collapse is initiated because the electron degeneracy pressure of the core is no longer sufficient to withstand the gravitational pull of the core. During the collapse, iron nuclei are photodisintegrated from the thermal gamma-ray photons which along with electron capture not only speeds up the collapse, but also turns the material more neutron rich. When the material reaches nuclear densities ( $2.3 \times 10^{17} \text{ kg m}^{-3}$ ) the material experiences a new type of support from the color confinement of the strong nuclear force as well as degeneracy pressure from neutrons. The models vary in the endpoint in the evolution of the collapse, where either a black hole or a neutron star is formed.

In the canonical model for the GRB phenomena based on a single progenitor, called the ‘collapsar’ model (Woosley 1993; MacFadyen & Woosley 1999a; MacFadyen et al. 2001; Woosley & Heger 2006), two possible outcomes are envisioned with the same endpoint - a black hole. In a type I collapsar, the collapse is not stalled by the strong forces and the core forms a black hole directly. Material outside the black hole has sufficient angular momentum to form an accretion disc around

the black hole and, once an accretion disc has been formed, the ingredients are there for a jet. Through either neutrino annihilation (Popham et al. 1999; Di Matteo et al. 2002; Levinson & Globus 2013; Nagataki 2018) or the MHD-based Blandford-Znajek mechanism (Blandford & Znajek 1977; Gammie et al. 2003; Tchekhovskoy et al. 2008; Komissarov & Barkov 2009; Nagataki 2009; Maeder & Meynet 2012), relativistic jets are launched along the polar directions. The accompanying SN is launched as a disk-wind and is therefore inherently different from traditional SNe. Alternatively, in the type II collapsar, the collapse is halted when the densities reach nuclear and the SN is launched by the traditional bounce of the core (Colgate & White 1966; Bethe & Wilson 1985; Bethe 1990). Some of the ejected material remains bound and fall-back to the newly formed neutron star causes it to collapse to a black hole, where again the accretion disk can form. In the type II collapsar, the accretion disk is formed after the SN has been launched and the jet then has to go through the expanding SN, which causes problems for the stability of the jet (McKinney & Blandford 2009; McKinney et al. 2012; Bromberg et al. 2014). In the collapsar model, the energy of the GRB comes from the conversion of gravitational energy by black-hole accretion (Blandford & Znajek 1977).

An alternative model is called the ‘magnetar’ engine (Usov 1992; Duncan & Thompson 1992; Wheeler et al. 2000; Uzdensky & MacFadyen 2006; Metzger et al. 2011). In the magnetar engine, a black hole does not form, but instead the energy is extracted from the spin-down of a newly formed rapidly-spinning, magnetized neutron star through magnetic braking. In the magnetar picture, an accretion disk is typically not formed and the mechanism invoked to launch the jet is instead magnetic dipole radiation (Poynting flux) from the surface of the newly formed neutron star (Thompson et al. 2004; Metzger et al. 2007). In the magnetar picture, the SN is formed through the traditional channel, but the energetics are affected by the jet (Bucciantini et al. 2006).

The lifetime of the jet is set by the amount of material available to continuously feed the accretion disk with new material and irregularities in the density of the disk causes variation in the ejection energetics. These irregularities cause “shells” in the ejecta, traveling with different velocities (Fenimore et al. 1996; Sari et al. 1999; Pe’er et al. 2017). These shells run into each other which causes shocks - these shocks produce the emission that are visible in the prompt emission signal (Nakar & Piran 2003; Piran 2004), described in the previous sections. Long GRBs are formed from massive stars and a significant amount of material can continuously feed the accretion disk where epochs of fall-backs give the complex light-curves of the prompt signal. Once the jet encounters the circumstellar material, new shocks are formed (Piran 1999, 2004). A forward traveling shockwave continuously shocks material further from the burst. A reverse shock is generated (Mészáros & Rees 1993; Sari et al. 1999), as the jet encounters the surrounding material, which then travels backwards through the ejecta. The combination of the forward traveling shock and the reverse shock is what generates the X-ray through radio afterglow (Piran 2004).

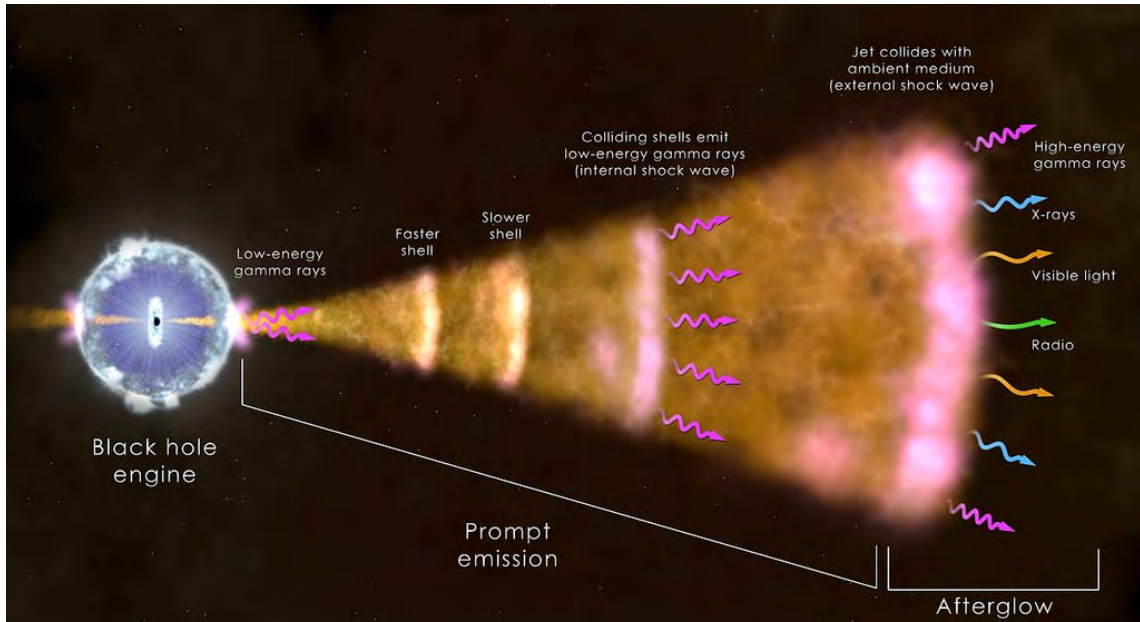


**Figure 1.4:** Schematic of long GRB emission mechanism for the collapsar model. The jet is launched inside the progenitor star as described in the text. Shells in the jet of different velocities run into each other, due to their varying speed, and these shocks generate the prompt emission. Once the jet runs into the circumstellar material, additional shocks generate the afterglow in the X-ray though radio. The schematic is adapted here from [a Nasa press release regarding the 1000th burst detected by \*Swift\*](#).

### 1.3 Short Gamma-Ray Bursts

The division between long and short GRBs is often blurry, as the observables used to separate the two classes exhibit a significant degree of overlap ([Lien et al. 2014, 2016](#)). Traditionally, the duration, the hardness of the spectrum and the presence of a spectral lag are used to divide the two classes. The two duration populations both have a wide distribution and the measured characteristics of the distributions depends on the observing telescope as the different observing bands probe a different structure ([Bromberg et al. 2013](#)). The same is true for the hardness distributions ([Dong & Qin 2005](#)), where short GRBs tends to have harder spectra, meaning a higher fraction of the radiation is emitted in the high-energy bands. As some long GRBs do not show any significant spectral lag ([Bernardini et al. 2015](#)), it is also not a unique characteristic of either type of burst. Therefore demarcation between the two burst types is preferentially done on the basis of multiple, simultaneous high-energy diagnostics ([Zhang et al. 2009; Kann et al. 2011; Bromberg et al. 2012, 2013](#)).

The total energies of short GRBs are typically lower, compared to long GRBs ([Berger 2014; D'Avanzo 2015](#)). Both the prompt gamma-rays, the X-ray afterglow and the optical afterglow are significantly fainter than the long GRB equivalents. Due to the short duration and lower fluxes,

they are much more difficult to localize, however, the key reason why short GRB afterglows were not discovered until *Swift* is that the triggering algorithm of BeppoSAX was not sensitive to short GRBs. For this reason and due to the scarcity of short GRBs compared to long ones meant that the first afterglow of a short GRB was only found after the launch of *Swift*, the one of GRB 050509B (Gehrels et al. 2005; Castro-Tirado et al. 2005; Hjorth et al. 2005b; Bloom et al. 2006), 8 years after the first afterglow of a long GRB was detected. And still, only a limited number of radio afterglows have been found (Berger et al. 2005; Soderberg et al. 2006). Because short GRBs are much less studied, they are more poorly understood, however many of the fundamental mechanisms are usually found to operate of similar basis (Ghirlanda et al. 2009; Pe’er 2015). Namely, the prompt signal is still the jet velocity stratification interaction and the afterglow is generated by the interaction of the ejected material from the jet with the circumburst material (Pe’er 2015; Meng et al. 2018). Because the time-scale of the prompt phase is short and exhibit very rapid variation, the physical scale of the progenitor is found to small, well below the stellar scale (Berger 2007; Barnacka & Loeb 2014).

### 1.3.1 Environments

Another clue to the different nature of short and long GRBs comes from the very different environments they are found in. Where long GRBs are always found associated with star-formation, short GRBs seem much more independent from any local environments (Berger 2010; Fong et al. 2013; Berger 2014). The hosts of GRBs are found to be much less intensively forming stars and, in a significant amount of cases, be completely missing (Berger 2010). The hosts are not just star-forming galaxies, but early-type galaxies as well (Fong et al. 2013) and, in general, they seem much more representative of field galaxies, as shown in Fig. 1.5. This indicates that short GRBs are likely more tied to stellar mass than star formation (Berger 2014). This potentially implies that no special conditions are required to generate short GRBs. Only stellar mass and time. Also in terms of metallicity, contrary to what is observed for long GRBs, short GRBs do not seem to prefer low-metallicity environments (Berger 2009, 2011a).

When the positions of short GRBs are investigated within their hosts they are often found to exhibit a significant degree of offset from their host centers, which means they are more often located further from where the star-formation took place (Fong et al. 2010; Fong & Berger 2013). This means that they are either formed in the outskirts of their hosts or that they travel around their host. In some cases, hosts cannot be found, even in very deep searches. These “hostless” short GRBs suggest that either the hosts are extremely faint or that the progenitor system have been ejected from whatever host they were originally embedded in.

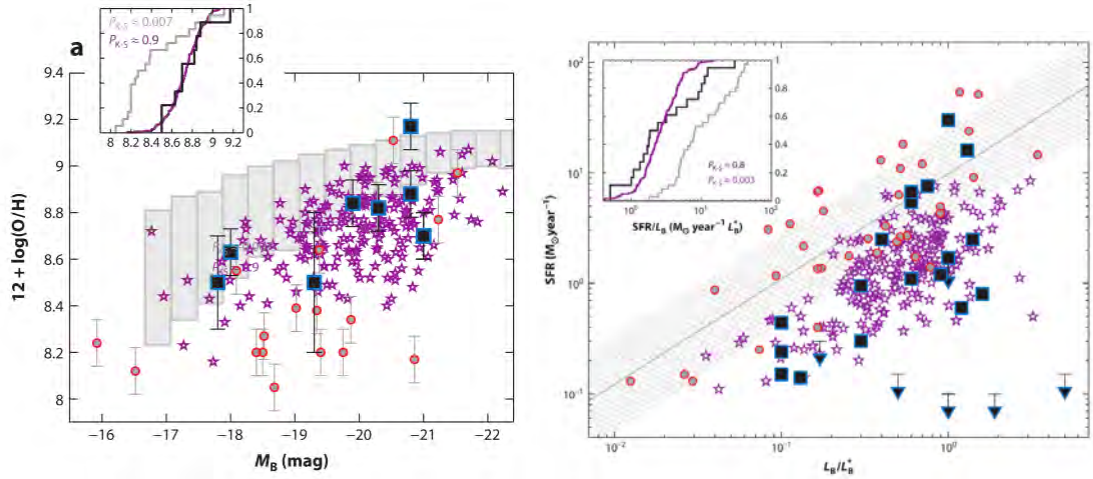


**Figure 1.5:** Short GRB environments, adapted from Berger (2014). On the left panel is shown the metallicity distribution as a function of host absolute  $B$ -band magnitude. The blue squares are the short GRB hosts galaxies, the red points are long GRB host galaxies, the purple stars are field galaxies and the grey shaded area are SDSS galaxies. Here it is shown that the hosts of short GRB follow the general evolution of field galaxies, in contrast to what is found for long GRBs. The right panel shows the host star formation rate as a function of B-band luminosity, normalized to the mean B-band luminosity at a given redshift. The symbols means the same as in the left panel. Here it is shown that the star formation rate is significantly lower in galaxies hosting short GRBs compared to those hosting long GRBs. However, the short hosts are representative of the general field population.

### 1.3.2 Associated transients

Since the discovery of short GRBs, potential associated transients have been predicted (Paczynski 1986; Eichler et al. 1989; Narayan et al. 1992). Due to the very short time-scales seen in short GRBs, the progenitor systems were known to be compact (Barnacka & Loeb 2014) and the merger of two neutron stars or the merger of a black hole and a neutron star were seen as likely candidates. The hypothesized associated transient to such a merger has been explored in detail, prior to them being detected (Li & Paczynski 1998; Rosswog 2005; Kulkarni 2005; Nakar 2007; Metzger et al. 2010; Metzger & Berger 2012b; Goriely et al. 2011; Piran et al. 2013; Barnes & Kasen 2013; Bauswein et al. 2013). Dubbed kilonova or macronova (Kulkarni 2005; Perego et al. 2014) based on the expected strength of the signal compared to classical nova, they were expected to be detectable only in the closest observed short GRBs.

The first kilonova detected appeared as an excess in the smooth light-curve decay in the GRB 130603B (Tanvir et al. 2013a; Berger et al. 2013a). Where kilonova-less afterglows decay as  $t^{-\alpha}$  in segments of power-laws, GRB 130603B exhibited a near-infrared excess after  $\sim 9$  days (Tanvir et al. 2013a). I show the light-curve of GRB 130603B in Fig. 1.6. Other potential signals with similar characteristics have been reported in other short GRB afterglow light curves (Yang

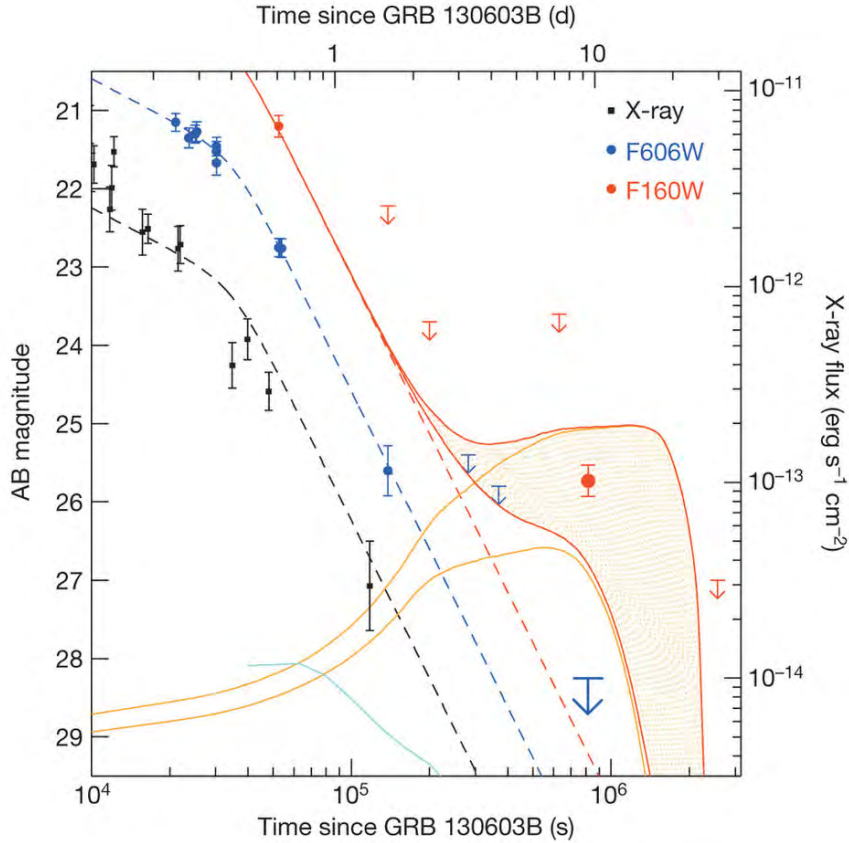


**Figure 1.6:** The kilonova in GRB 130603B from [Tanvir et al. \(2013a\)](#). The points represent the measurements, taken in X-rays by *Swift/XRT* and in F606W, F160W filters of HST. Overlaid in the dashed line are power-law segments of expected, pure GRB afterglow decays. The detection in F160W at  $\sim 9$  days is in clear conflict with the expected power-law decay. The yellow shaded area shows the models of expected kilonova contribution to the afterglow light from the models by [Barnes & Kasen \(2013\)](#); [Tanaka & Hotokezaka \(2013\)](#); [Grossman et al. \(2014\)](#).

et al. 2015a; Jin et al. 2015). Due to their faintness, compared to supernovae, kilonovae are expected to be rarely detected and only seen in local short GRBs (Fong et al. 2016a; Metzger 2017). However another promising avenue for detection of kilonovae has opened.

### 1.3.3 Gravitational waves

The existence of gravitational waves has been known since the discovery of the orbital decay of the Hulse-Taylor (Hulse & Taylor 1974) binary neutron star system (Esposito & Harrison 1975). With the direct detection of gravitational waves from multiple mergers of black holes (Abbott et al. 2016b,a, 2017b,a,f), a new and powerful tool has become available to humanity that is potentially extremely efficient at finding the sources that give rise to kilonovae (Metzger & Berger 2012a). Gravitational waves are gravity-equivalents of electromagnetic waves and are similarly so generated by perturbations of the gravitational field (Postnov & Yungelson 2014). Gravitational

waves, when they pass through the universe, compress and stretch space-time orthogonal to the direction of propagation. The sources expected to give rise to the loudest gravitational waves are exactly the inspirals of compact objects - either in the form of black holes or neutron stars (Shakura & Sunyaev 1973). Black holes, being heavier than their neutron star counterparts, will give out the most energy and therefore be detectable to the highest distances (Abadie et al. 2012; Abbott et al. 2016c). However, the mergers of black holes are not expected to be associated to any electromagnetic counterpart. Indeed, searches for electromagnetic counterparts toward the black hole merger of GW 150914 did not find any convincing electromagnetic signatures (Abbott et al. 2016d). The merger of two neutron stars or the merger of a neutron star and a black hole, on the other hand, are expected to be associated with a detectable electromagnetic counterpart.

### 1.3.4 GW170817/GRB170817A/AT2017GFO

On the 17th of August 2017 at 12:41:04 UTC, LIGO/Virgo triggered on a new gravitational wave-event (Abbott et al. 2017b). The duration of the signal meant that the mass range of the objects involved was potentially in the range of neutron stars (Abbott et al. 2017e). Delayed by only 1.7 seconds from the gravitational wave signal, the GBM instrument onboard the Fermi space telescope triggered on a new short GRB (Goldstein et al. 2017) also visible in *INTEGRAL* data (Savchenko et al. 2017a). The simultaneous detection of signal in both gravitational waves and electromagnetic waves meant that a new era in astronomy had begun (Abbott et al. 2017d). A multimessenger era where multiple avenues of sensing could be used to investigate the universe.

With the localization skymaps from the LIGO/Virgo collaboration, the optical counterpart was found independently by 6 different teams (Coulter et al. 2017; Soares-Santos et al. 2017; Valenti et al. 2017; Lipunov et al. 2017; Tanvir et al. 2017b; Arcavi et al. 2017). Located in the outskirts of NGC 4993 at a distance of  $\approx 120$  lightyears (Hjorth et al. 2017; Im et al. 2017; Cantiello et al. 2018), this was one of the most closeby GRBs ever observed, only contested by GRB 980425/SN1998bw. Once the optical localization was available, follow-up across the entire electromagnetic spectrum could be carried out (Andreoni et al. 2017; Cowperthwaite et al. 2017; Díaz et al. 2017; Drout et al. 2017; Evans et al. 2017; Hu et al. 2017; Kasliwal et al. 2017; Pian et al. 2017; Pozanenko et al. 2017; Smartt et al. 2017; Troja et al. 2017c; Chornock et al. 2017; Nicholl et al. 2017; Shappee et al. 2017; Levan et al. 2017; Verrecchia et al. 2017; Covino et al. 2017). What was observed was a blue optical counterpart that quickly faded in the blue, becoming redder and redder as the fading continued. I show the spectral evolution of the kilonova in the first 4 spectroscopic epochs, as seen by the cross-dispersed echelle spectrograph, X-shooter in Fig. 1.7. The simultaneous detection of gravitational waves and electromagnetic radiation means that at least some short GRBs are likely caused by the merger of two neutron stars. The late-time observations of GW 170817/GRB 170817A are still ongoing, and the evolution since discovery allows details of the jet structure of GRBs to be

investigated in more detail (Lyman et al. 2018; Margutti et al. 2018; D’Avanzo et al. 2018).

### 1.3.5 Short GRB/kilonova progenitor systems

The physical process behind a short GRB and the associated kilonova can be understood as follows. Firstly, a binary neutron star systems needs to be formed. This can be accomplished through a range of processes (Tauris et al. 2017). One channel is an initial formation as a stellar binary system of two massive stars (Voss & Tauris 2003; Belczynski et al. 2016; de Mink & Mandel 2016). During the life-time of the system, both constituent binary members go off as core-collapse supernovae, leaving two orbiting neutron stars (Belczynski et al. 2006, 2017). The interaction between the two members and the potential common envelope evolution means that the two neutron stars are formed initially very close to each other. The respective SN explosions will tend to elongate the orbits, however they circularize in time (Postnov & Yungelson 2014). Due to the proximity of the two neutron stars at progenitor formation, this channel can operate on very short timescales (< 1000 years, Belczynski et al. 2006). Alternatively, two (or more) free neutron stars can form a bound system. This can happen, if they by chance pass close enough by each other for a sufficient gravitational energy loss to tie the orbits of the two neutron stars together (Samsing et al. 2014; Rodriguez et al. 2016). Because they are formed further from each other, the decay time of the systems formed this way is longer, possibly lasting more than a Hubble time. The environments for these two channels are different (Belczynski et al. 2006; O’Shaughnessy et al. 2008; Ivanova et al. 2008) and the timescales from formation to coalescence differ. By observing short GRBs at the highest possible redshift, constraints can be derived on the initial separation of the systems - this is what I have done in Selsing et al. (2018b), presented in Chapter 3.

Once the two neutron stars are formed, they will radiate gravitational energy, due to their orbit (Postnov & Yungelson 2014). The gravitational waves will carry away angular momentum and, as a consequence, the orbital distance will shrink. Because the energy loss due to gravitational radiation depends on separation between the two neutron star, the orbital collapse will speed up as the two compact object approach each other (Postnov & Yungelson 2014). As the orbit shrinks, the orbital period decreases while the velocity of the two neutron stars increases. This runaway gravitational decay of the orbit continues until either the neutron stars rotate faster than their break-up speed or their surfaces touch (Fernández & Metzger 2016; Metzger 2017). The shock of the encounter between the two neutron stars likely launches ejecta in the polar direction at the interface (Oechslin et al. 2006; Sekiguchi et al. 2016), while in the orbital plane, the part of the neutron stars moving faster than the escape velocity is dynamically lost, or flung out (Ruffert, M.; Janka, H.-T.; Schaefer 1996; Rosswog et al. 1998; Metzger et al. 2010; Metzger 2017). The amount of material lost in both process is unknown, however it is potentially a fraction of a solar mass in both cases (Siegel & Metzger 2017; Kasen et al. 2017). The velocity of the material in the orbital

plane is expected to be close to the escape velocity of the system, and therefore close to the speed of light (Kyutoku et al. 2015; Foucart et al. 2017). Similar to the failed SN model, used to explain the SN Ic-BL accompanying long GRBs, a disk wind is expected to form at the accretion disk of a neutron star merger (Perego et al. 2014; Kasen et al. 2015; Tanaka 2016; Fernández & Metzger 2016). The relative contributions from the different types of ejecta are still an open question.

At the core of the system, a central compact object is formed. This can either be in the form of super-heavy neutron star (Grossman et al. 2014; Kastaun et al. 2017), or the collapse can continue directly to a black hole (Shibata & Taniguchi 2006; Siegel et al. 2013). In the case where a super-heavy neutron star is formed, the object is sustained by rotational support. As the rotation decays, also the super-heavy neutron star collapses to a black hole, but the presence of super-heavy neutron star, even though short, is expected to significantly alter the composition of the ejected material, due to the increased neutrino flux (Wu et al. 2017). Due to the immense rotation of the merging neutron stars, the merging material has a large amount of angular momentum, and therefore, regardless of the nature of the central object, an accretion disk is likely formed (Fernández & Metzger 2016; Siegel & Metzger 2017). Once an accretion disk has been formed, a jet can be launched through similar process as the ones described for long GRB (see Section 1.2).

### **Chemical enrichment from short GRBs**

One of the reasons why the merger of two neutron stars has been the focus of so much interest is the composition of the ejecta (Lattimer et al. 1977; Li & Paczyński 1998; Metzger et al. 2010; Metzger 2017). Where the SNe associated with long GRBs are dominated by the ash products of stellar fusion, the kilonova is dominated by the ejecta from neutron stars. This ejecta are expected to be extremely neutron heavy (Metzger et al. 2010; Metzger 2017), and be associated with a very intense flux of free neutrons. Exactly these conditions make the merger of two neutron stars the prime place for the *r*-process (Goriely et al. 2011).

The chemical enrichment history of the heaviest elements in the universe has for a long time been an open question (Burbidge et al. 1957a), because the sources of an effective *r*-process had still not been found (Qian 2000; Argast et al. 2004; Wanajo 2013; Wallner et al. 2015), however the abundance patterns of stars in the ultra-metal poor galaxy, Reticulum II, seems to suggest that whatever process is responsible for the *r*-process enrichment is extremely rare (Ji et al. 2016). In chapter 5, I show the spectroscopic evidence for the formation of the light *r*-process element in the merger of two neutron stars.

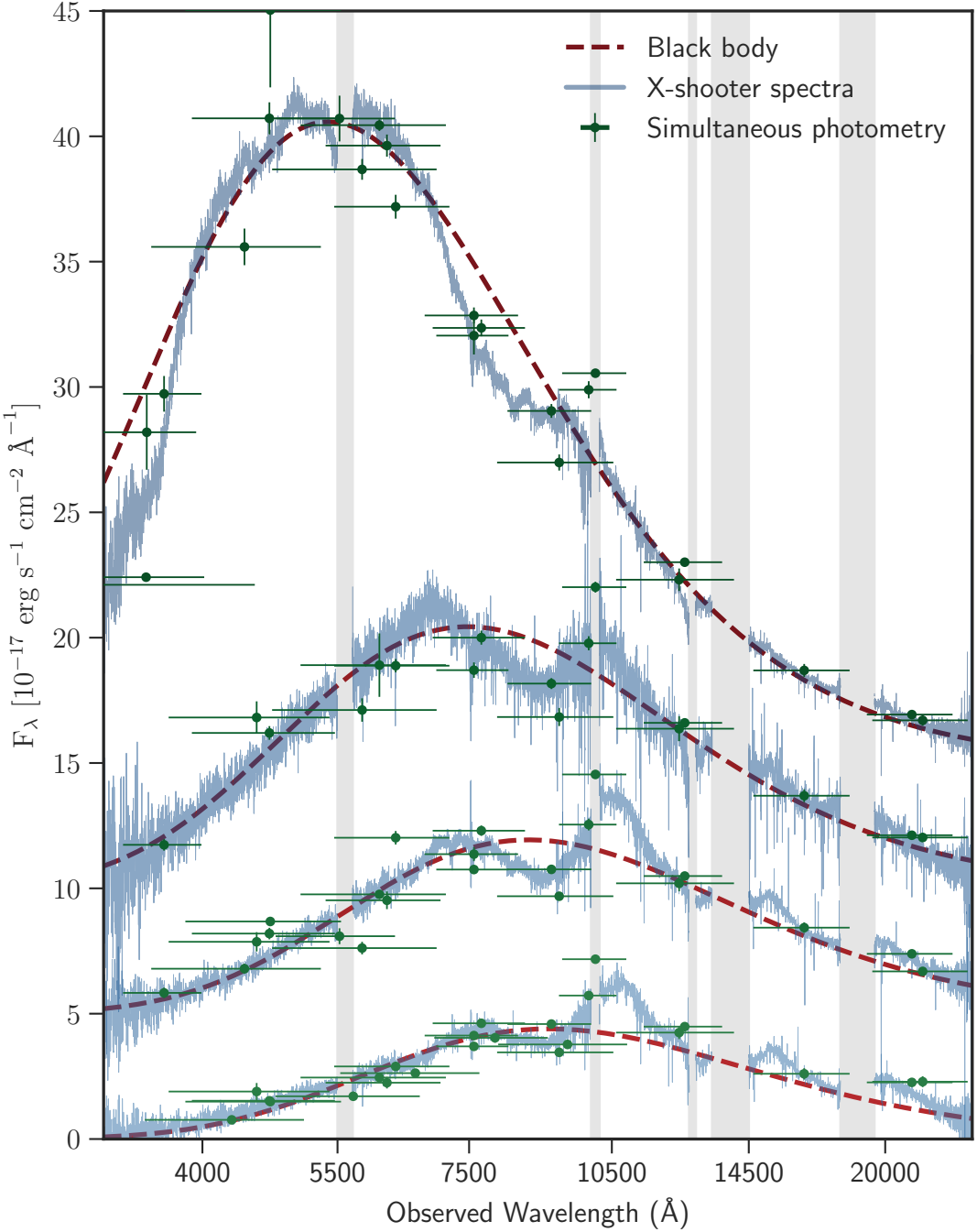


**Figure 1.7:** Spectral evolution of the kilonova AT 2017gfo, as seen by VLT/X-shooter. I here show the first 4 epochs of X-shooter data, taken 1.5, 2.5, 3.5, and 4.5 after the neutron star merger. The spectra are shown in the blueish colors. The consecutive spectra are artificially offset for clarity. Simultaneous photometry, taken from Villar et al. (2017), shows the accuracy of the flux calibrations – the spectra have not been scaled. The red, Planckian spectral shape visible in the first epoch quickly cools, where the spectrum rapidly transitions into being dominated by wide spectral features located at 0.7, 1.1, 1.6, and 2.1  $\mu\text{m}$ .

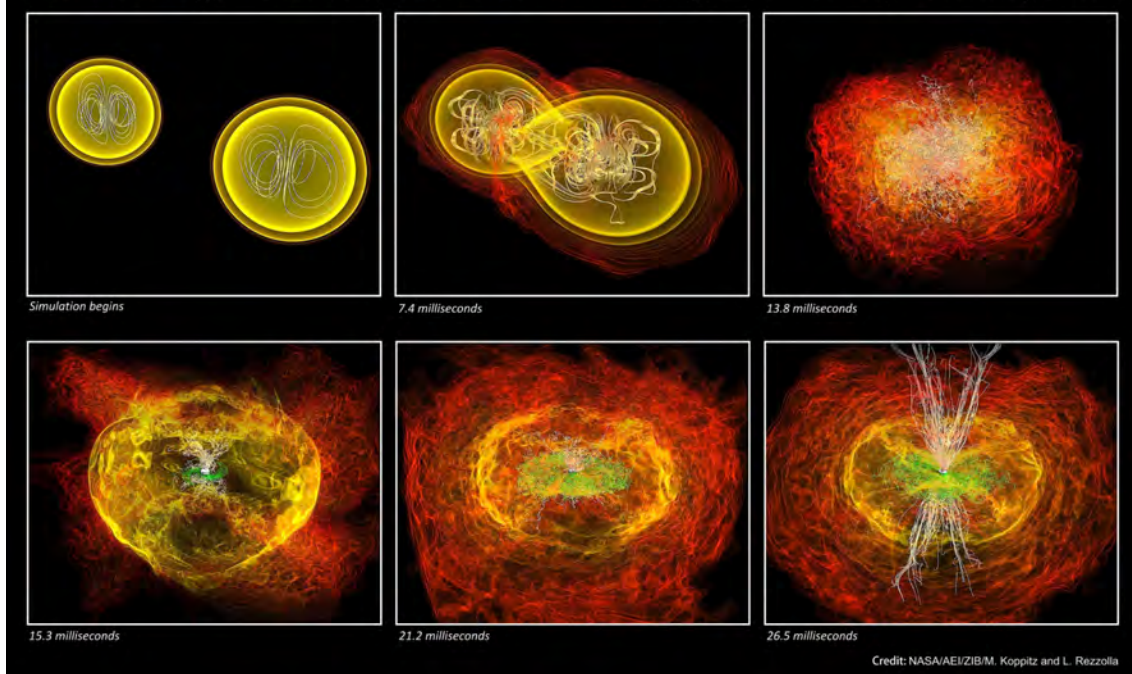


**Figure 1.8:** Simulation showing the temporal evolution of the merger of two neutron stars from Rezzolla et al. (2011). The upper left panel shows the first snapshot and the lower right panel shows the last snapshot. In the first snapshot, the two neutron stars are orbiting each other. In the second frame, the inner sides have begun to merge, as the gravitational pull from the center of mass becomes higher than the one from each of their centers. In panels 3 - 5, an inner black hole is formed and material is ejected in red. In green is shown the accretion disk. The magnetic fields generated by the accretions disk and potentially responsible for the launching of the jet is shown as white lines.

# 2

## A COMPLETE SAMPLE OF GRB AFTERGLOWS

This chapter contains the following article:

### **“The X-shooter GRB afterglow legacy sample (XS-GRB)”\***

Submitted for publication in *Astronomy and Astrophysics*, 2018.

Authors:

J. Selsing, D. Malesani, P. Goldoni, J. P. U. Fynbo, T. Krühler, L. A. Antonelli, M. Arabsalmani, J. Bolmer, Z. Cano, L. Christensen, S. Covino, P. D’Avanzo, V. D’Elia, A. De Cia, A. de Ugarte Postigo, H. Flores, M. Friis, A. Gomboc, J. Greiner, P. Groot, F. Hammer, O.E. Hartoog, K. E. Heintz, J. Hjorth, P. Jakobsson, J. Japelj, D. A. Kann, L. Kaper, C. Ledoux, G. Leloudas, A.J. Levan, E. Maiorano, A. Melandri, B. Milvang-Jensen, E. Palazzi, J. T. Palmerio, D. A. Perley, E. Pian, S. Piranomonte, G. Pugliese, R. Sánchez-Ramírez, S. Savaglio, P. Schady, S. Schulze, J. Sollerman, M. Sparre, G. Tagliaferri, N. R. Tanvir, C. C. Thöne, S.D. Vergani, P. Vreeswijk, D. Watson, K. Wiersema, R. Wijers, D. Xu, & T. Zafar

---

\*Based on observations collected at the European Southern Observatory, Paranal, Chile, Program IDs: 084.A-0260, 084.D-0265, 085.A-0009, 086.A-0073, 087.A-0055, 088.A-0051, 089.A-0067, 090.A-0088, 091.A-0877, 0091.C-0934, 092.A-0124, 092.D-0056, 093.A-0069, 094.A-0134, 095.A-0045, 095.B-0811, 096.A-0079, 097.A-0036, and 098.A-0055.

In this work we present spectra of all  $\gamma$ -ray burst (GRB) afterglows that have been promptly observed with the X-shooter spectrograph until 31/03/2017. In total, we obtained spectroscopic observations of 103 individual GRBs observed within 48 hours of the GRB trigger. Redshifts have been measured for 97 per cent of these, covering a redshift range from 0.059 to 7.84. Based on a set of observational selection criteria that minimize biases with regards to intrinsic properties of the GRBs, the follow-up effort has been focused on producing a homogeneous sample of 93 afterglow spectra for GRBs discovered by the *Swift* satellite. We here provide a public release of all the reduced spectra, including continuum estimates and telluric absorption corrections. For completeness, we also provide reductions for the 18 late-time observations of the underlying host galaxies. We provide an assessment of the degree of completeness with respect to the parent GRB population, in terms of the X-ray properties of the bursts in the sample and find that the sample presented here is representative of the full *Swift* sample. We constrain the fraction of dark bursts to be < 28 per cent and we confirm previous results that higher optical darkness is correlated with increased X-ray absorption. For the 42 bursts for which it is possible, we provide a measurement of the neutral hydrogen column density, increasing the total number of published HI column density measurements by  $\sim 33$  per cent. This dataset provides a unique resource to study the ISM across cosmic time, from the local progenitor surroundings to the intervening universe.

## 2.1 Introduction

Gamma-ray bursts (GRBs) are bright glimpses of electromagnetic radiation that pierce through the universe, all the way from the edges of the observable universe. They provide constraints on a very wide range of topics in astrophysics. Examples range from small-scale phenomena relating to magnetars, properties of highly relativistic jets, hyper/supernova explosions, the interstellar medium, dust extinction curves, starburst galaxies, chemical and molecular abundances, escape of ionizing radiation, the ionization state of the intergalactic medium, intervening absorption systems to standard candles in cosmology (e.g., [Wijers et al. 1998](#); [Savaglio 2006](#); [Ghirlanda 2007](#); [Molinari et al. 2007](#); [Amati et al. 2008](#); [Vergani et al. 2009](#); [Prochaska et al. 2009](#); [Hjorth & Bloom 2011](#); [Rowlinson et al. 2017](#); [Christensen et al. 2017](#)).

The *Neil Gehrels Swift Observatory* (*Swift*) satellite ([Gehrels et al. 2004, 2009](#)), which was launched in 2004, has made it possible to harvest much of the great potential in using GRBs as probes of the intergalactic medium, which was already hinted at by results from earlier missions (e.g., [van Paradijs et al. 2000](#); [Ricker & Team 2004](#)). With the three on-board instruments, the Burst Alert Telescope (BAT; [Barthelmy et al. 2005](#)), the X-Ray Telescope (XRT; [Burrows et al. 2005](#)), and the UltraViolet and Optical Telescope (UVOT; [Roming et al. 2005](#)), *Swift* is an ideal observatory for GRB hunting. A crucial aspect of the success of the *Swift* mission has been the extensive ground-based follow-up observations of the afterglows and of the host galaxies

of the GRBs, involving a large community of researchers. This fruitful collaboration has been facilitated by the open data access policy of the *Swift* mission. The close collaboration between detection facilities and electromagnetic follow-up campaigns continue to be immensely rewarding, as recently highlighted by the simultaneous detection of gravitational waves and light from the neutron star merger in the shape of GW170817/GRB170817A/AT2017gfo (Abbott et al. 2017b,d).

In the beginning of the *Swift* era most of the follow-up afterglow spectroscopy was secured using low-resolution spectrographs (typically  $R = \lambda/\Delta\lambda < 1000$ , e.g., Fynbo et al. 2009). Spectroscopy is powerful as it allows us to secure information even for very faint targets (Krühler et al. 2012a). This allows the measurement of a number of important parameters such as redshifts, spectral slopes, and extinction. For a handful of very bright afterglows high-resolution (typically  $R > 20000$ ) spectra have been secured, and for these events much more information about conditions inside the host galaxies were extracted (e.g., Fiore et al. 2005; Thöne et al. 2007; Prochaska et al. 2007; Vreeswijk et al. 2007; D’Elia et al. 2009; Castro-Tirado et al. 2010).

The X-shooter spectrograph (Vernet et al. 2011) was the first of the second generation instruments at the ESO Very Large Telescope (VLT). It was designed very much with transient follow-up in mind as the fading luminosities of such sources makes it urgent to secure as extensive wavelength coverage as possible in the shortest possible time. At the same time, the resolution was designed to be in the range 4000–9000 in order to be able to get a large useful spectral range between the many sky-background emission lines in the red and near-IR spectral ranges. The near-IR spectral coverage allows for spectroscopic observations of the highest redshift GRBs.

In this paper, we present the results of a dedicated effort over the years 2009 – 2017 to use the X-shooter spectrograph to secure spectroscopic observations of afterglows and host galaxies of GRBs detected by *Swift*. We here make all the data resulting from the survey publicly available in reduced form (see Sect 2.3.7).

The paper is organized in the following way: In Sect. 2.2 we describe the sample including the sample selection criteria and the observational strategy. In Sect. 2.2.4, we describe the observations and the instrumental setups, and in Sect. 2.3 we detail the methodological strategies adopted in the data reduction process and auxiliary material. In Sect. 2.4 we describe the results of the survey, i.e. the efficiency of the follow-up effort and the characteristics of the observed bursts. We also assess the completeness of the realized sample. Finally, we offer our conclusions in Sect. 2.5. We use the  $\Lambda$ CDM cosmology parameters provided by the Planck Collaboration et al. (2016) in which the universe is flat with  $H_0 = 67.7 \text{ km s}^{-1} \text{ Mpc}^{-1}$  and  $\Omega_m = 0.307$ .

## 2.2 Sample selection criteria and observations

### 2.2.1 Sample selection criteria

Being of transient nature, it is difficult to impose strong sample selection criteria on GRBs without hampering the follow-up effort. Many natural follow-up restrictions exist already, being it weather conditions, pointing restrictions of the telescope or unconstrained burst localizations as reported by the alerting facility. To maximize the return of the follow-up campaign, we have chosen a few selection criteria that facilitate an unbiased selection of bursts, while at the same time allowing for a high follow-up success rate. The importance of defining unbiased selection criteria has been highlighted previously ([Jakobsson et al. 2006](#); [Salvaterra et al. 2012](#); [Hjorth et al. 2012](#); [Vergani et al. 2015](#); [Perley et al. 2016a](#)), when trying to address the intrinsic underlying distribution functions such as the redshift distribution, host metallicity distribution, or afterglow brightness distribution. When investigating a specific distribution function, a high degree of *completeness* is desired (e.g., [Perley et al. 2016b](#)).

In defining the selection criteria, we simultaneously aim to minimize any biases against intrinsic astrophysical conditions while at the same time maximizing the likelihood of successful observations, hence allowing us to obtain a higher degree of completeness. By restricting the selection criteria to conditions local to the Milky Way and therefore independent of intrinsic GRB properties, the aim is that the collected sample represents the underlying distribution of GRBs in a fair way. The selection criteria used here are based on previous, similar studies ([Jakobsson et al. 2006](#); [Fynbo et al. 2009](#); [Hjorth et al. 2012](#)). We characterize the sample completeness in Sect. 2.4.2.

The selection criteria that define a GRB as part of our initial *statistical* sample are:

1. GRB trigger by BAT onboard the *Swift* satellite
2. XRT started observing within 10 minutes after the GRB; an XRT position must be distributed within 12 hr.
3. The target must be visible from Cerro Paranal for at least 60 minutes, 30 degrees above the horizon, with the Sun below  $-12$  degrees<sup>2</sup>.
4. Galactic  $A_V \leq 0.5$  mag according to the maps of [Schlegel et al. \(1998\)](#).
5. No bright, nearby stars within  $1.8 + 0.4 \times \exp[(20 - R)/2.05]$  arcsec, where  $R$  is the USNO magnitude of the star)

Our ability to observe GRB afterglows is strongly dependent on the timing and the precision of the target positions delivered by the triggering facilities. By selecting only bursts that have

---

<sup>2</sup>Note that in the P84 proposal the criteria have been stated differently, the visibility constraint being replaced by a declination + Sun angle constraint. The criteria listed above are, however, those defining the sample.

been triggered on board the *Swift* space telescope (Gehrels et al. 2004), based on the BAT, we start out with a sample where burst characteristics are delivered immediately, allowing for an informed follow-up strategy. However, the BAT sensitivity varies across its field of view, so selection is not entirely homogeneous. Despite the complexity of the triggering mechanism on board *Swift* (Band 2006; Coward et al. 2013), attempts at inferring properties of the underlying GRB population based on the detection thresholds and triggering algorithms have been made (Lien et al. 2014; Graff et al. 2016). Restricting the follow-up effort to bursts detected by *Swift*, we therefore ensure that the limitations of the parent sample are well studied.

Because the localization accuracy of BAT is 1 – 4 arcminutes (Barthelmy et al. 2005), an afterglow identification based on BAT alone would be harder, and host association impossible. We therefore additionally require an X-ray position from XRT to be distributed to the GCN network (Barthelmy 2000) within 12 hours and to account for observing constraints on *Swift* that XRT began observations within 10 minutes. The additional timing requirement of the XRT follow-up means that all bursts in our sample have detected X-ray afterglows. Because the XRT completeness is very high for promptly-repointed GRBs (Burrows et al. 2007), this cut should not alter the parent sample significantly.

To ensure a minimum of observability, we require that the GRB is visible from the telescope site at Cerro Paranal, Chile, for at least 1 hour after the trigger with the sun below  $-12$  degrees. This secures time for the spectroscopic observations to be completed. Since the GRB population is isotropically distributed on the sky as seen from Earth, and because the GRB properties do not depend on position on the sky (Meegan et al. 1992; Briggs et al. 1996; Ukwatta & Wózniak 2016), this cut does not influence our ability to fairly sample the underlying GRB population. The same arguments apply to the requirement that there are no nearby foreground bright stars. We additionally require that the Galactic extinction is below  $A_V \lesssim 0.5$  mag, based on the extinction maps by Schlegel et al. (1998)<sup>3</sup>. Choosing low-extinction sightlines also reduces the problem of field crowding and the contamination from Galactic outbursts posing as GRB impostors. These additional cuts should not influence the optical properties of the bursts themselves, only our ability to successfully secure the observations that allow us to investigate the spectroscopic properties of GRBs.

Bursts that fulfill these selection criteria are what we define as our initial *statistical* sample. To reach a higher degree of sample completeness, we impose additional cuts that increase our ability to infer population properties. These are presented in Sect. 2.4.2. Using this sample we will be able to address population properties of *Swift*-detected bursts. We further discuss the effect of these selection criteria and their implication for the completeness of the sample in Sect. 2.4.2.

---

<sup>3</sup>We use the updated values of Schlafly & Finkbeiner (2011) to correct for foreground extinction, but the sample criterion is based on the old Schlegel et al. (1998) values for consistency with the first semesters of our program.

### 2.2.2 Follow-up procedure

Our collaboration has set up a procedure to promptly react to alerts from *Swift* and other satellites (such as *Fermi*). We process automatically GCN notices in order to flag those events belonging to our statistical sample. Two people are permanently on alert to manually supervise each event, for example to recognize events of special interest beyond their inclusion in the sample. Members of our collaboration have access to numerous facilities spread throughout the world, among which the William Herschel Telescope (WHT), Nordic Optical Telescope (NOT), the Gran Telescopio Canarias (GTC), the Telescopio Nazionale Galileo (TNG), the Gamma-Ray Burst Optical Near-infrared Detector (GROND [Greiner et al. 2008](#)), and the Xinlong observatory. Thanks to this network, we can often conduct searches for optical/NIR afterglows ahead of the time of the X-shooter spectroscopy, thus helping to plan the spectroscopic observations. If this is not possible, we use the built-in acquisition camera of X-shooter to search for counterparts, and adapt the observing strategy on the fly. In many cases we could interact directly with the staff at the telescope to aid the observation. Raw data are usually available within minutes in the [ESO archive](#) and are promptly reduced by members of our collaboration, often using archival calibration data which are readily available. This allows us in most cases to report the preliminary results (redshift, identification of the most prominent emission and absorption feature, etc.) within a few hours after the beginning of the observations and plan additional X-shooter observations if deemed necessary.

### 2.2.3 Rapid response mode (RRM) observations

Under rare circumstances, the use of the ESO rapid response mode (RRM; [Vreeswijk et al. 2010](#)) has been possible. The RRM is a system to automatically override ongoing observations at the telescope. This allows the shortest possible delay between the GRB trigger and the initiation of observations, where spectroscopic integration of the rapidly fading, optical transient can commence within minutes of the burst. One limitation is that no instrument change is allowed in RRM, which lowers the number of successful triggers (X-shooter shares the telescope with two other instruments). In case of a promptly visible GRB, a robotic trigger is sent to the telescope if at the time of the GCN notice the GRB fulfills the following criteria:

1. The GRB triggered *Swift* onboard.
2. The X-ray position must be available less than 1 hr after the GRB.
3. The elevation of the source in the sky is  $> 22^\circ$  (both at trigger time and 15 min after).
4. The Sun elevation from Paranal is  $< -12^\circ$  (both at trigger time and 15 min after).
5. Galactic  $A_V \leq 1.0$  mag according to the maps of [Schlegel et al. \(1998\)](#).

- The *Swift*-circulated tags: KNOWN\_SOURCE, COSMIC\_RAY, DEF\_NOT\_GRB are set to false (PROB\_NOT\_GRB can be true)<sup>4</sup>.

The criteria to trigger RRM are looser than those that define the statistical sample. This is both because of the expected larger brightness of GRB counterparts soon after the explosion, and because of the rarity of RRM triggers.

The use of RRM is unique as it allows to sample a long logarithmic time span in the GRB lifetime, and it exploits the extreme brightness of early afterglows. A pivotal example is the study of temporal variability of GRB afterglow absorption systems due to effect of the GRB itself on the surrounding medium (e.g., see [Dessauges-Zavadsky et al. 2006](#); [Vreeswijk et al. 2007](#); [D'Elia et al. 2009](#); [Vreeswijk et al. 2013](#)).

There are nine GRBs that have been observed with X-shooter in RRM mode. One of the RRM triggers is outside the statistical sample, and two of the RRM triggers are on short GRBs. Our fastest response (between the *Swift* GRB trigger time and the beginning of spectroscopic integration) was for GRB 160410A, for which the delay was only 8.4 minutes.

In many cases, unfortunately, we could not use RRM even for promptly visible events, e.g. because of the unavailability of X-shooter. Potentially, the proximity of the telescope (Cerro Paranal, Chile) to the South Atlantic Anomaly (SAA) affects the rate of RRM triggers ([Greiner et al. 2011](#)). BAT switches off when the satellite goes through the SSA and that means we have fewer events immediately observable, compared to the rest of the *Swift* orbit.

#### 2.2.4 Observations

The observations obtained for this sample have been secured with the cross-dispersed echelle spectrograph, X-shooter ([Vernet et al. 2011](#)), mounted on one of two Unit Telescopes at ESO/VLT, UT2 (Kueyen) and UT3 (Melipal) during the duration of this follow-up campaign. The observations have been taken during a period of eight years corresponding to the ESO observing periods P84 through P98 under the following programme IDs: 084.A-0260, 085.A-0009, 086.A-0073, 087.A-0055, 088.A-0051, 089.A-0067, 090.A-0088, 092.A-0124, 093.A-0069, 094.A-0134, 095.A-0045, 096.A-0079, 097.A-0036, and 098.A-0055 (PI: Fynbo) and 0091.C-0934 (PI: Kaper). These proposals were initiated on Guaranteed Time. We have included a few additional bursts, from the programmes 084.D-0265 (PI: Benetti), 091.A-0877 (PI: Schady), 092.D-0056 (PI: Rau), 092.D-0633 (PI: Greiner), and 095.B-0811 (PI: Levan). The total collection of spectra represents *all* GRB afterglows that have been followed up by X-shooter up to 31/03/2017, which marks the end of the XS-GRB legacy follow-up program.

The first GRB followed up was GRB 090313 ([de Ugarte Postigo et al. 2010](#)), observed on the 15th of March, 2009, during the commissioning of X-shooter on the second Unit Telescope (UT2)

---

<sup>4</sup>These tags are distributed as part of the GCN notices. Explanations for all tags are [available online](#).

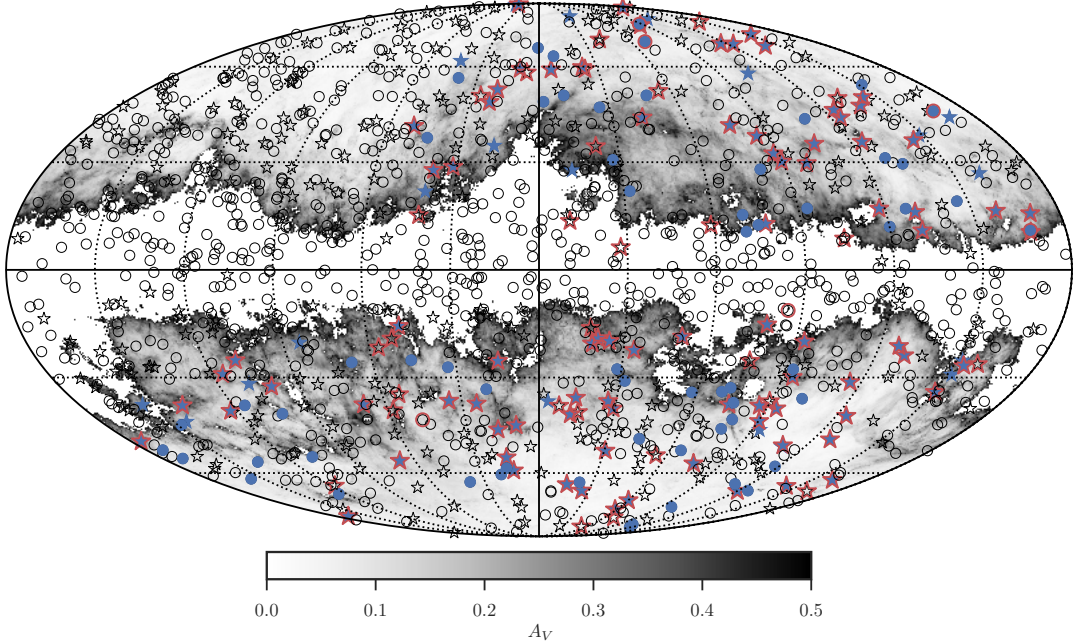


**Figure 2.1:** Mollweide projection in Galactic coordinates of the full sky showing the positions on the sky of the bursts presented in this work. The equator is the Galactic plane. The empty stars/circles are the positions of all the 1266 *Swift* bursts detected until 31/03/2017. Stars indicate bursts with measured redshifts and circles indicate those without. Blue stars indicate the position of the 104 bursts fulfilling the sample criteria specified in Sect. 2.2.1 that have a measured redshift. Red outlines are added to the 84 GRBs that enter our statistical sample with both X-shooter spectroscopy and a measured redshift. Red outlines of empty stars represent bursts which have been observed with X-shooter and has a measured redshift, but is not a part of our statistical sample. The blue dots show the positions of the 61 GRBs of our statistical sample that lack redshift measurements. A red outline is added around the six bursts in our statistical sample which were observed with X-shooter, but did not yield a redshift measurement. Two empty circles with red outlines indicate bursts outside the statistical sample that were followed up with X-shooter, but without a redshift measurement. The different samples are compared in Sect. 2.4. The background shows the dust maps presented in Schlegel et al. (1998). Please note that we removed the background where the sample criterion is violated ( $A_V > 0.5$  mag) and replaced it with a white background. The grey scale bar below indicates the value of  $A_V$  on the plot. The dotted lines indicate intervals of  $30^\circ$  in longitude and latitude.

of the VLT . The bursts observed during the commissioning or the science verification process (GRB 090313, GRB 090530, GRB 090809, GRB 090926A) are not a part of the sample we use to investigate the statistical properties of GRB afterglows, due to the different criteria for their selection. The first burst observed after science verification and the mounting of X-shooter on UT2, was GRB 091018, which is the first burst entering our statistically homogeneous sample. For all bursts that fulfill our sample selection criteria, described in Sect. 2.2.1, spectroscopic follow-up

have been attempted with X-shooter. Various conditions can affect our ability to follow up a given burst, and a discussion of these conditions and their consequences for the sample is included in Sect. 2.4.2.

X-shooter covers the spectral wavelength region from 300 nm to 2480 nm in a single exposure, by splitting the light into three separate spectroscopic arms through the use of two dichroics. The ultraviolet blue (UVB) arm covers 300 - 550 nm, the visual (VIS) arm covers 550 - 1020 nm, and the near-infrared (NIR) arm covers 1020 - 2480 nm. For some of the observations, we have applied a  $K$ -band blocking filter, cutting the coverage of the NIR arm at 2100 nm. The  $K$ -band blocking filter is only used after 2012, where it was installed. This is done to reduce the amount of scattered background light from the thermal infrared. For the majority of observations, a nodding observing scheme has been employed, with a nodding throw of 5". Each nodding observation has typically been carried out in a standard ABBA pattern. For some cases, conditions during the follow-up (either technical or weather), have necessitated alterations to this scheme as described in App. 2.5. For RRM triggers, a slightly different observing strategy was employed. Starting as rapidly as possible, a simple stare mode sequence was started, with 5 spectroscopic integrations with increasing exposure times.

For the majority of the bursts, we have observed with a slit width of 1''.0, 0''.9, and 0''.9 for the UVB, VIS, and NIR-arm respectively. This sets a lower limit on the delivered resolving power of the spectra based on the tabulated values of the delivered resolutions, which is 4350, 7450, and 5300 for the UVB, VIS and NIR-arm respectively<sup>5</sup>. For accurate measurements involving line profiles, knowledge of the precise instrumental resolution is required. The spectral resolution becomes better than the nominal one, when the delivered seeing is smaller than the projected width of the slit on the sky. We discuss how we determine the effective instrumental resolution in Sect. 2.3.3.

Due to a mechanical failure, the atmospheric dispersion corrector (ADC) was disabled from 1st of August 2012 until the end of this program. Only GRB 100728B was affected by the failing ADC prior to disablement, resulting in a lower-than-nominal throughput. To avoid chromatic slit losses due to atmospheric dispersion, nearly all subsequent observations have been carried out at parallactic angle. A consequence of this is that for all observations following 1st of August 2012, the centroid of the trace of the source changes position across the spatial direction of the slit as a function of wavelength. This effect has been modeled in the extraction procedure, as described in Sect. 2.3.4.

---

<sup>5</sup>See [this URL](#) for the nominal spectral resolutions.

**Table 2.1:** The full sample of afterglows and hosts observed in the program. We here list the burst names and details of the spectroscopic observations. The exposure times and slit widths are given in the order UVB/VIS/NIR. The column  $\Delta t$  shows the time after trigger when the spectroscopic observation was started.  $\text{Mag}_{\text{acq}}$  gives the approximate magnitude (typically in the  $R$ -band) of the afterglow or the host in the acquisition image.

GRB	Obs Date	Exptime	Slit width	Airmass	Seeing	$\Delta t$	$\text{Mag}_{\text{acq}}$	Redshift	Notes
		(ks)	(arcsec)		(arcsec)	(hr)			
GRB090313 <sup>a</sup>	2009-03-15	6.9/6.9/6.9	1.0/0.9/0.9	1.2–1.4	1.5	45	21.6	3.374	2.5
GRB090530 <sup>a</sup>	2009-05-30	4.8/4.8/4.8	1.0/1.2/1.2	1.6–2.2	1.7	20.6	22	1.266	2.5
GRB090809 <sup>a</sup>	2009-08-10	7.2/7.2/7.2	1.0/0.9/0.9	1.2–1.1	1.1	10.2	21	2.737	2.5
GRB090926A <sup>a</sup>	2009-09-27	7.2/7.2/7.2	1.0/0.9/0.9	1.4–1.5	0.7	22	17.9	2.106	2.5
GRB091018	2009-10-18	2.4/2.4/2.4	1.0/0.9/0.9	2.1–1.8	1.0	3.5	19.1	0.971	2.5
GRB091127	2009-12-02	6.0/6.0/6.0	1.0/0.9/0.9	1.1–1.2	1.0	101	21.2	0.490	2.5
GRB100205A	2010-02-08	10.8/10.8/10.8	1.0/0.9/0.9	1.9–1.8	0.9	71	>24	–	2.5
GRB100219A	2010-02-20	4.8/4.8/4.8	1.0/0.9/0.9	1.3–1.1	0.8	12.5	23	4.667	2.5
GRB100316B	2010-03-16	2.4/2.4/2.4	1.0/0.9/0.9	2.0–2.4	0.6	0.7	18.2	1.180	2.5
GRB100316D-1 <sup>b</sup>	2010-03-17	3.6/3.6/3.6	1.0/0.9/0.9	1.2–1.3	0.8	10	21.5	0.059	2.5
GRB100316D-2	2010-03-19	2.4/2.4/2.4	1.0/0.9/0.9	1.1–1.2	0.9	58	20.2	0.059	2.5
GRB100316D-3	2010-03-20	2.6/2.6/3.2	1.0/0.9/0.9	1.1–1.2	1.1	79	19.9	0.059	2.5
GRB100316D-4	2010-03-21	2.6/2.6/3.2	1.0/0.9/0.9	1.1–1.2	1.5	101	19.9	0.059	2.5
GRB100418A-1	2010-04-19	4.8/4.8/4.8	1.0/0.9/0.9	1.6–1.3	0.7	8.4	18.1	0.624	2.5
GRB100418A-2	2010-04-20	4.8/4.8/4.8	1.0/0.9/0.9	1.2–1.3	0.6	34	19.2	0.624	2.5
GRB100418A-3	2010-04-21	4.8/4.8/4.8	1.0/0.9/0.9	1.2–1.4	0.7	58	>24	0.624	2.5
GRB100424A <sup>c</sup>	2013-03-11	4.8/4.8/4.8	1.0/0.9/0.9	1.1–1.2	0.9	25239	>24	2.465	2.5
GRB100425A	2010-04-25	2.4/2.4/2.4	1.0/0.9/0.9	1.5–1.3	0.7	4	20.6	1.755	2.5
GRB100615A <sup>c</sup>	2013-03-05	4.8/4.8/4.8	1.0/0.9/0.9	1.0–1.1	0.9	23859	>24	1.398	2.5
GRB100621A	2010-06-21	2.4/2.4/2.4	1.0/0.9/0.9	1.3–1.4	1.0	7.1	22	0.542	2.5
GRB100625A <sup>cf</sup>	2010-07-07	4.8/4.8/4.8	1.0/0.9/0.9	1.1–1.0	0.8	278.7	>24	0.452	2.5
GRB100724A <sup>ad</sup>	2010-07-24	4.2/4.2/4.2	1.0/0.9/0.9	1.5–2.3	0.7	0.2	19.52	1.288	2.5
GRB100728B <sup>e</sup>	2010-07-29	7.2/7.2/7.2	1.0/0.9/0.9	1.5–1.1	0.6	22	23	2.106	2.5
GRB100814A-1 <sup>d</sup>	2010-08-14	0.9/0.9/0.9	1.0/0.9/0.9	1.9–1.7	0.5	0.9	19	1.439	2.5
GRB100814A-2	2010-08-14	4.8/4.8/4.8	1.0/0.9/0.9	1.5–1.2	0.7	2.1	19	1.439	2.5
GRB100814A-3	2010-08-18	4.8/4.8/4.8	1.0/0.9/0.9	1.2–1.0	0.6	98	20	1.439	2.5
GRB100816A <sup>f</sup>	2010-08-17	4.8/4.8/4.8	1.0/0.9/0.9	1.8–1.6	0.8	28.4	21.6	0.805	2.5
GRB100901A	2010-09-04	2.4/2.4/2.4	1.0/0.9/0.9	1.5–1.5	1.9	66	>24	1.408	2.5
GRB101219A	2010-12-19	7.2/7.2/7.2	1.0/0.9/0.9	1.1–1.7	1.8	3.7	>24	0.718	2.5

**Table 2.1:** The full sample of afterglows or hosts observed in the program (continued).

GRB	Obs Date	Exptime	Slit width	Airmass	Seeing	$\Delta t$	Mag <sub>acq</sub>	Redshift	Notes
		(ks)	(arcsec)		(arcsec)	(hr)			
GRB101219B-1 <sup>a</sup>	2010-12-20	4.8/4.8/4.8	1.0/0.9/0.9	1.6–2.6	1.4	11.6	20	0.552	2.5
GRB101219B-2 <sup>a</sup>	2011-01-05	7.2/7.2/7.2	1.0/0.9/0.9	1.2–2.0	1.0	394	22.7	0.552	2.5
GRB101219B-3 <sup>a</sup>	2011-01-25	7.2/7.2/7.2	1.0/0.9/0.9	1.4–2.1	0.7	886	>24	0.552	2.5
GRB110128A	2011-01-28	7.2/7.2/7.2	1.0/0.9/0.9	2.0–1.6	0.6	5.5	22.5	2.339	2.5
GRB110407A	2011-04-08	9.6/9.6/9.6	1.0/0.9/0.9	1.4–1.3	2.1	12.4	23	–	2.5
GRB110709B <sup>c</sup>	2013-03-19	7.2/7.2/7.2	1.0/0.9/0.9	1.6–1.1	0.9	14835	>24	2.109	2.5
GRB110715A <sup>a</sup>	2011-07-16	0.6/0.6/0.6	1.0/0.9/0.9	1.1–1.1	1.6	12.3	18.5	0.823	2.5
GRB110721A <sup>a</sup>	2011-07-22	2.4/2.4/2.4	1.0/0.9/0.9	1.2–1.4	2.3	28.7	>24	0.382	2.5
GRB110808A	2011-08-08	2.4/2.4/2.4	1.0/0.9/0.9	1.2–1.1	1.0	3.0	21.2	1.349	2.5
GRB110818A	2011-08-19	4.8/4.8/4.8	1.0/0.9/0.9	1.3–1.3	0.9	6.2	22.3	3.36	2.5
GRB111005A <sup>ac</sup>	2013-04-01	1.2/1.2/1.2	1.0/0.9/0.9	1.3–1.3	0.7	13052	>24	0.013	2.5
GRB111008A-1	2011-10-09	8.8/8.8/8.4	1.0/0.9/0.9	1.1–1.0	1.3	8.5	21	4.990	2.5
GRB111008A-2	2011-10-10	8.0/8.0/7.2	1.0/0.9/0.9	1.3–1.0	0.9	20.1	22	4.990	2.5
GRB111107A	2011-11-07	4.8/4.8/4.8	1.0/0.9/0.9	1.8–1.5	0.8	5.3	21.5	2.893	2.5
GRB111117A <sup>f</sup>	2011-11-19	4.8/4.8/4.8	1.0/0.9/0.9	1.5–1.4	0.7	38	>24	2.211	2.5
GRB111123A-1	2011-11-24	6.2/6.6/6.6	1.0/0.9/0.9	1.6–1.1	0.8	12.2	>24	3.152	2.5
GRB111123A-2 <sup>c</sup>	2013-03-07	2.4/2.4/2.4	1.0/0.9/0.9	1.0–1.0	0.5	11266	>24	3.152	2.5
GRB111129A	2011-11-30	3.6/3.6/3.6	1.0/0.9/0.9	1.6–2.1	1.9	8.7	>24	1.080	2.5
GRB111209A-1	2011-12-10	4.8/4.8/4.8	1.0/0.9/0.9	1.1–1.2	0.8	17.7	20.1	0.677	2.5
GRB111209A-2	2011-12-29	9.6/9.6/9.6	1.0/0.9/0.9	1.2–2.0	1.0	497	23	0.677	2.5
GRB111211A <sup>a</sup>	2011-12-13	2.4/2.4/2.4	1.0/0.9/0.9	1.4–1.6	0.6	31	19.5	0.478	2.5
GRB111228A	2011-12-29	2.4/2.4/2.4	1.0/0.9/0.9	1.4–1.4	0.7	15.9	20.1	0.716	2.5
GRB120118B <sup>c</sup>	2013-02-13	3.6/3.6/3.6	1.0/0.9/0.9	1.1–1.0	0.7	9393	>24	2.943	2.5
GRB120119A-1	2012-01-19	2.4/2.4/2.4	1.0/0.9/0.9	1.1–1.1	0.6	1.4	17	1.728	2.5
GRB120119A-2	2012-01-19	1.2/1.2/1.2	1.0/0.9/0.9	1.8–1.9	0.5	4.5	20	1.728	2.5
GRB120119A-3 <sup>c</sup>	2013-02-26	4.8/4.8/4.8	1.0/0.9/0.6JH	1.0–1.1	1.8	9694	>24	1.728	2.5
GRB120211A-1 <sup>c</sup>	2013-02-17	4.8/4.8/4.8	1.0/0.9/0.9	1.1–1.4	1.3	8919	>24	2.346	2.5
GRB120211A-2 <sup>c</sup>	2013-03-20	3.6/3.6/3.6	1.0/0.9/0.9	1.1–1.2	1.2	9660	>24	2.346	2.5
GRB120224A	2012-02-25	2.4/2.4/2.4	1.0/0.9/0.9	1.7–2.1	1.3	19.8	22.3	1.10	2.5
GRB120311A <sup>a</sup>	2012-03-11	2.4/2.4/2.4	1.0/0.9/0.9	1.6–1.4	0.7	3.7	21.6	0.350	2.5
GRB120327A-1 <sup>a</sup>	2012-03-27	2.4/2.4/2.4	1.0/0.9/0.9	1.6–1.4	0.6	2.1	18.8	2.815	2.5
GRB120327A-2 <sup>a</sup>	2012-03-28	4.2/4.2/4.2	1.0/0.9/0.9	1.0–1.1	0.6	29	22.5	2.815	2.5

**Table 2.1:** The full sample of afterglows or hosts observed in the program (continued).

GRB	Obs Date	Exptime	Slit width	Airmass	Seeing	$\Delta t$	Mag <sub>acq</sub>	Redshift	Notes
		(ks)	(arcsec)		(arcsec)	(hr)			
GRB120404A	2012-04-05	9.6/9.6/9.6	1.0/0.9/0.9JH	1.7–1.3	1.3	15.7	21.3	2.876	2.5
GRB120422A	2012-04-22	4.8/4.8/4.8	1.0/0.9/0.9	1.3–1.3	0.7	16.5	22	0.283	2.5
GRB120712A	2012-07-13	4.8/4.8/4.8	1.0/0.9/0.9	1.5–2.5	1.5	10.4	21.5	4.175	2.5
GRB120714B	2012-07-15	4.8/4.8/4.8	1.0/0.9/0.9JH	1.5–1.2	1.2	7.8	22.1	0.398	2.5
GRB120716A <sup>a</sup>	2012-07-19	3.6/3.6/3.6	1.0/0.9/0.9JH	1.8–2.6	1.1	62	20.9	2.486	2.5
GRB120722A <sup>b</sup>	2012-07-22	4.8/4.8/4.8	1.0/0.9/0.9	1.3–1.3	1.2	10.3	23.6	0.959	2.5
GRB120805A <sup>b</sup>	2012-08-14	3.6/3.6/3.6	1.0/0.9/0.9JH	1.3–1.7	0.9	218	>24	3.9	2.5
GRB120815A <sup>a</sup>	2012-08-15	2.4/2.4/2.4	1.0/0.9/0.9	1.3–1.4	0.7	1.69	18.9	2.358	2.5
GRB120909A <sup>d</sup>	2012-09-09	1.2/1.2/1.2	1.0/0.9/0.9	1.6–1.6	1.6	1.7	21	3.929	2.5
GRB120923A	2012-09-23	9.6/9.6/9.6	1.0/0.9/0.9JH	1.2–1.4	1.0	18.5	>24	7.84	2.5
GRB121024A	2012-10-24	2.4/2.4/2.4	1.0/0.9/0.9	1.2–1.1	0.6	1.8	20	2.300	2.5
GRB121027A	2012-10-30	8.4/8.4/8.4	1.0/0.9/0.9	1.3–1.3	1.3	69.4	21.15	1.773	2.5
GRB121201A	2012-12-02	4.8/4.8/4.8	1.0/0.9/0.9JH	1.1–1.1	1.1	12.9	23	3.385	2.5
GRB121229A	2012-12-29	4.8/4.8/4.8	1.0/0.9/0.9JH	1.4–1.2	1.5	2	21.5	2.707	2.5
GRB130131B <sup>c</sup>	2013-03-09	7.2/7.2/7.2	1.0/0.9/0.9JH	1.3–1.6	1.1	874	>24	2.539	2.5
GRB130408A <sup>a</sup>	2013-04-08	1.2/1.2/1.2	1.0/0.9/0.9	1.0–1.0	0.9	1.9	20	3.758	2.5
GRB130418A	2013-04-18	1.2/1.2/1.2	1.0/0.9/0.9	1.4–1.3	1.2	4.6	18.5	1.222	2.5
GRB130427A	2013-04-28	1.2/1.2/1.2	1.0/0.9/0.9JH	1.8–1.8	0.8	16.5	19	0.340	2.5
GRB130427B	2013-04-28	1.2/1.2/1.2	1.0/0.9/0.9JH	1.2–1.0	1.0	20.3	22.7	2.780	2.5
GRB130603B <sup>f</sup>	2013-06-04	2.4/2.4/2.4	1.0/0.9/0.9	1.4–1.4	1.1	8.2	21.5	0.356	2.5
GRB130606A	2013-06-07	4.2/4.2/4.2	1.0/0.9/0.9JH	1.7–1.9	0.9	7.1	19	5.91	2.5
GRB130612A	2013-06-12	1.2/1.2/1.2	1.0/0.9/0.9	1.3–1.3	1.5	1.1	21.5	2.006	2.5
GRB130615A	2013-06-15	1.2/1.2/1.2	1.0/0.9/0.9	2.1–2.2	1.0	0.8	21	2.9	2.5
GRB130701A	2013-07-01	1.2/1.2/1.2	1.0/0.9/0.9JH	2.0–2.0	1.4	5.5	19.9	1.155	2.5
GRB130925A	2013-09-25	5.88/6.0/6.9	1.0/0.9/0.9JH	1.0–1.0	0.6	3.5	>24	0.347	2.5
GRB131011A <sup>a</sup>	2013-10-13	4.5/4.5/4.5	1.0/0.9/0.9	1.1–1.1	0.8	34.2	>24	1.874	2.5
GRB131030A	2013-10-31	3.6/3.6/3.6	1.0/0.9/0.9	1.1–1.1	1.1	3.4	18.0	1.296	2.5
GRB131103A	2013-11-05	2.4/2.4/2.4	1.0/0.9/0.9JH	1.1–1.1	1.0	5.8	20.48	0.599	2.5
GRB131105A	2013-11-05	4.8/4.8/4.8	1.0/0.9/0.9	1.3–1.4	0.8	1.3	22.4	1.686	2.5
GRB131117A	2013-11-17	4.8/4.8/4.8	1.0/0.9/0.9JH	1.3–1.2	1.7	1.1	20	4.042	2.5
GRB131231A <sup>a</sup>	2014-01-01	2.4/2.4/2.4	1.0/0.9/0.9JH	1.4–1.3	0.9	20.2	18.5	0.642	2.5
GRB140114A <sup>c</sup>	2014-03-28	5.4/5.4/5.4	1.0/0.9/0.9JH	1.7–1.7	1.2	1746	>24	3.0	2.5

**Table 2.1:** The full sample of afterglows or hosts observed in the program (continued).

GRB	Obs Date	Exptime	Slit width	Airmass	Seeing	$\Delta t$	Mag <sub>acq</sub>	Redshift	Notes
		(ks)	(arcsec)		(arcsec)	(hr)			
GRB140213A <sup>a</sup>	2014-02-14	1.2/1.2/1.2	1.0/0.9/0.9JH	1.5–1.5	0.7	5.8	19.5	1.208	2.5
GRB140301A	2014-03-02	7.2/7.2/7.2	1.0/0.9/0.9JH	1.1–1.1	0.9	9	23.1	1.416	2.5
GRB140311A <sup>a</sup>	2014-03-13	7.6/6.3/8.4	1.0/0.9/0.9JH	1.2–1.2	0.6	32.5	>24	4.954	2.5
GRB140430A <sup>a</sup>	2014-04-30	1.2/1.2/1.2	1.0/0.9/0.9	2.0–1.8	1.6	2.5	19	1.601	2.5
GRB140506A-1	2014-05-07	4.8/4.8/4.8	1.0/0.9/0.9	1.3–1.4	0.7	8.8	20.9	0.889	2.5
GRB140506A-2	2014-05-08	4.8/4.8/4.8	1.0/0.9/0.9	1.2–1.3	0.7	32.9		0.889	2.5
GRB140515A	2014-05-16	4.8/4.8/4.8	1.0/0.9/0.9	1.3–1.3	1.4	15.5	>24	6.327	2.5
GRB140614A	2014-06-14	2.4/2.4/2.4	1.0/0.9/0.9	1.8–1.8	0.7	3.8	21.5	4.233	2.5
GRB140622A <sup>f</sup>	2014-06-22	1.2/1.2/1.2	1.0/0.9/0.9	1.4–1.3	1.0	0.8	>24	0.959	2.5
GRB141028A <sup>a</sup>	2014-10-29	2.4/2.4/2.4	1.0/0.9/0.9	1.5–1.4	1.0	15.4	20	2.332	2.5
GRB141031A <sup>ac</sup>	2015-01-29	2.4/2.4/2.4	1.0/0.9/0.9	1.2–1.3	0.8	10912	>24	–	2.5
GRB141109A-1	2014-11-09	2.4/2.4/2.4	1.0/0.9/0.9JH	1.5–1.7	0.8	1.9	19.2	2.993	2.5
GRB141109A-2	2014-11-10	4.3/4.3/4.5	1.0/0.9/0.9JH	1.7–2.0	0.8	25.4		2.993	2.5
GRB150206A <sup>a</sup>	2015-02-07	2.4/2.4/2.4	1.0/0.9/0.9	2.1–1.9	0.8	10	21.9	2.087	2.5
GRB150301B	2015-03-02	3.6/3.6/3.6	1.0/0.9/0.9JH	1.2–1.2	1.1	5.1	21.0	1.517	2.5
GRB150403A	2015-04-04	2.4/2.4/2.4	1.0/0.9/0.9	1.6–1.7	0.7	10.8	19.1	2.057	2.5
GRB150423A <sup>df</sup>	2015-04-23	4.8/4.8/4.8	1.0/0.9/0.9	2.7–2.4	1.4	0.4	>24	1.394	2.5
GRB150428A	2015-04-28	2.4/2.4/2.4	1.0/0.9/0.9JH	1.6–1.5	0.8	3.7	>24	–	2.5
GRB150514A <sup>a</sup>	2015-05-15	2.4/2.4/2.4	1.0/0.9/0.9	2.3–2.1	0.9	28.4	19.5	0.807	2.5
GRB150518A <sup>a</sup>	2015-05-20	2.4/2.4/2.4	1.0/0.9/0.9JH	1.3–1.3	1.7	30.7	>24	0.256	2.5
GRB150616A <sup>ac</sup>	2015-09-12	2.4/2.4/2.4	1.0/0.9/0.9JH	1.2–1.1	1.2	2092	>24	1.188	2.5
GRB150727A	2015-07-28	3.6/3.6/3.6	1.0/0.9/0.9JH	1.2–1.2	1.4	5.0	20.5	0.313	2.5
GRB150821A <sup>d</sup>	2015-08-21	2.4/2.4/2.4	1.0/0.9/0.9	2.0–1.8	1.3	0.2	16	0.755	2.5
GRB150910A	2015-09-11	1.8/1.8/1.8	1.0/0.9/0.9JH	1.9–1.9	1.3	20.1	21.2	1.359	2.5
GRB150915A	2015-09-16	4.8/4.8/4.8	1.0/0.9/0.9JH	1.1–1.1	1.6	3.3	23	1.968	2.5
GRB151021A <sup>d</sup>	2015-10-21	4.2/4.2/4.2	1.0/0.9/0.9	1.0–1.1	1.4	0.75	18.2	2.330	2.5
GRB151027B	2015-10-28	2.4/2.4/2.4	1.0/0.9/0.9JH	1.5–1.7	1.2	5	20.5	4.063	2.5
GRB151029A	2015-10-29	1.2/1.2/1.2	1.0/0.9/0.9JH	1.9–1.7	1.1	1	20	1.423	2.5
GRB151031A <sup>d</sup>	2015-10-31	4.2/4.2/4.2	1.0/0.9/0.9	1.1–1.1	1.1	0.3	20.4	1.167	2.5
GRB160117B	2016-01-18	4.8/4.8/4.8	1.0/0.9/0.9JH	1.1–1.2	1.1	13.5	20.8	0.870	2.5
GRB160203A <sup>d</sup>	2016-02-03	6.6/6.6/6.6	1.0/0.9/0.9	1.0–1.8	1.0	0.3	18	3.518	2.5
GRB160228A <sup>c</sup>	2016-03-12	4.8/4.8/4.8	1.0/0.9/0.9JH	1.7–1.7	1.0	296	>24	1.640	2.5

**Table 2.1:** The full sample of afterglows or hosts observed in the program (continued).

GRB	Obs Date	Exptime	Slit width	Airmass	Seeing	$\Delta t$	Mag <sub>acq</sub>	Redshift	Notes
		(ks)	(arcsec)		(arcsec)	(hr)			
GRB160303A <sup>f</sup>	2016-03-04	4.8/4.8/4.8	1.0/0.9/0.9JH	1.6–1.5	0.8	19.1	>24	–	2.5
GRB160314A	2016-03-15	4.8/4.8/4.8	1.0/0.9/0.9JH	1.3–1.3	0.8	13.0	21.7	0.726	2.5
GRB160410A <sup>df</sup>	2016-04-10	1.8/1.8/1.8	1.0/0.9/0.9	2.5–2.3	0.5	0.15	20.3	1.717	2.5
GRB160425A	2016-04-26	4.8/4.8/4.8	1.0/0.9/0.9JH	1.3–1.3	0.5	7.2	21.1	0.555	2.5
GRB160625B <sup>a</sup>	2016-06-27	2.4/2.4/2.4	1.0/0.9/0.9JH	1.3–1.3	0.7	30	19.1	1.406	2.5
GRB160804A-1 <sup>a</sup>	2016-08-04	2.4/2.4/2.4	1.0/0.9/0.9JH	1.4–1.3	0.6	22.4	21.2	0.736	2.5
GRB160804A-2 <sup>ac</sup>	2016-08-27	3.6/3.6/3.6	1.0/0.9/0.9JH	1.9–1.8	0.6	574	>24	0.736	2.5
GRB161001A	2016-10-01	2.4/2.4/2.4	1.0/0.9/0.9JH	1.2–1.3	0.5	6.1	>24	0.891	2.5
GRB161007A <sup>c</sup>	2016-10-14	2.4/2.4/2.4	1.0/0.9/0.9JH	1.6–1.6	0.7	323	>24	–	2.5
GRB161014A	2016-10-15	4.8/4.8/4.8	1.0/0.9/0.9JH	1.1–1.2	0.5	11.6	21.4	2.823	2.5
GRB161023A <sup>a</sup>	2016-10-24	1.2/1.2/1.2	1.0/0.9/0.9JH	1.2–1.2	0.9	3	17.5	2.710	2.5
GRB161117A	2016-11-17	2.4/2.4/2.4	1.0/0.9/0.9	1.8–1.6	2.6	0.73	19	1.549	2.5
GRB161219B	2016-12-21	2.4/2.4/2.4	1.0/0.9/0.9JH	1.1–1.1	0.9	35.7	19.5	0.146	2.5
GRB170113A	2017-01-14	4.8/4.8/4.8	1.0/0.9/0.9JH	1.5–1.4	0.9	15.23	21.7	1.968	2.5
GRB170202A	2017-02-03	2.4/2.4/2.4	1.0/0.9/0.9JH	1.3–1.2	0.7	9.7	20.8	3.645	2.5

<sup>a</sup> Not part of the statistical sample. <sup>b</sup> Spectrum dominated by light from the host galaxy. <sup>c</sup> Spectrum of the host galaxy taken long after the burst. <sup>d</sup> RRM observation. <sup>e</sup> ADC malfunction during observation. <sup>f</sup> Short burst.

We provide an overview of all the observations in Table 2.1 and plot the positions of all the bursts on the celestial sphere in Galactic coordinates in Fig. 2.1. Away from the central zone of avoidance, due to high Galactic extinction cutoff (marked in white), the GRB positions have an isotropic distribution, except in the upper left quadrant which cannot be observed from Paranal due to the declination constraints of the telescope.

Thirty percent of the spectra presented here, primarily host observations, have already been published in Krühler et al. (2015a). Single bursts have additionally been published, based on unusual properties in their afterglows. We present individual notes on all the X-shooter spectra and their previous use in App. 2.5. We include independent reductions of them here for completeness.

## 2.3 Data processing

In this section we describe how the final data products are produced and subsequently post-processed. All post-processing scripts developed for this dataset are made publicly available at [https://github.com/jselsing/XSGRB\\_reduction\\_scripts](https://github.com/jselsing/XSGRB_reduction_scripts).

Before any reductions are initiated, the raw object images are run through the cosmic-ray removal algorithm (van Dokkum 2001) implementation, *Astro-SCRAPPY*<sup>6</sup>, where a wide clipping radius was used around detected cosmic ray hits to ensure that edge residuals are robustly rejected.

The basis for the reductions is the VLT/X-shooter pipeline, version 2 . 7 . 1 or newer (Goldoni et al. 2006; Modigliani et al. 2010). The pipeline is managed with the Reflex interface (Freudling et al. 2013) and is used for subtraction of bias level, flat-fielding, tracing of the echelle orders, wavelength calibrations with the use of arc-line lamps, flux calibration using spectrophotometric standards (Vernet et al. 2009; Hamuy et al. 1994), mirror flexure compensation(see Sect. 2.3.2), sky-subtraction and lastly the rectification and merging of the orders. Errors and bad pixel maps are propagated throughout the extraction. For the initial sky-subtraction, the background has been estimated by a running median in regions adjacent to the object trace clear of contaminating sources. Due to the broken ADC, for some objects there is curvature in the object trace along the dispersion axis of the slit(see Sect. 2.3.4). This means that for these bursts, the initial sky-estimate was made from a limited number of pixels in the spatial direction. The subtraction of the sky background on the un-rectified image ensures that the bulk of the sky background is not redistributed by the rectification process.

X-shooter is an echelle spectrograph, and therefore the individual echelle orders are curved across image space. The individual orders therefore need to be rectified. In order to transform the image space (pixels) into a physical (wavelength-slit) space, the image pixels are resampled onto a physical grid, while propagating the pixel uncertainties derived by the pipeline. This rectification process correlates neighboring pixels and in order to minimize the degree of correlation, we need to choose a physical sampling that matches the pixel sampling. We rectified the image onto an equidistant grid with a dispersion sampling of 0.02 nm/pixel and a 0''.16 per pixel spatial sampling for the UVB and VIS arm and 0.06 nm/pixel with a 0''.21 per pixel in the NIR arm. Because the tabulated resolution is a lower limit to the delivered resolution, we choose a sampling of 0.02 nm/pixel to ensure that the lowest wavelength part of neither of the arms have a sampling lower than the Nyquist sampling rate of 2 pixels per resolution FWHM.

### 2.3.1 Post-processing

For a typical observation, each of the exposures in the nodding sequence have been reduced as a single observation and then subsequently combined to form a single image. We employ this strategy so that we can reject outliers in the stack and weight by an averaged measure of the inverse variance of the background. When weighting images, where the noise in each pixel is dominated by Poisson noise, it is important to estimate the background variance in a large enough region, so that any correlation between the signal and the weights are removed. To this end, the

---

<sup>6</sup><https://github.com/astropy/astroscrappy>

weight map is generated by a running median window over the variance map produced by the pipeline, where the trace has been masked and the width of the window is chosen to be wide enough for the median variance to be calculated on the basis of several hundred pixels. This weighting scheme automatically also optimally combines images of different exposure times or images where the background is varying, which is often the case when a burst has been observed close to twilight.

An additional sky-subtraction procedure is run on all rectified 2D spectra. This is done to remove residual sky, still present. At each pixel in the dispersion direction, the spatial dimension is fit with a low-order polynomial, after all sources are masked out. This low order polynomial is then convolved with a few pixel wide Gaussian filter in the dispersion direction and subtracted from the entire 2D image.

In the NIR arm, where the background is very bright and there are a high number of bright sky-lines, an alternative approach to sky subtraction has been employed. When there are no contaminating sources in the slit, the sky has been put back on the images and the images are combined in pairs of two before extraction, subtracting the two from each other while keeping the WCS static. Due to the nodding offsets used between observations, this conserves the source flux while removing the sky at the expense of a decrease in signal-to-noise by a factor of  $\sqrt{2}$ . This amounts to the regular nodding reduction, only we can reject outliers and weight by the averaged inverse variance map.

Reducing the images as single observations for all exposures, we additionally get a spectrum of the sky which we can use to recalibrate the wavelength solution in the post-processing steps.

### 2.3.2 Correction for offsets in the wavelength calibration

Since X-shooter is installed at the VLT Cassegrain focus, it is prone to flexures. The flexures modify the projection of the slit on the detector with respect to the one obtained in daytime calibration. This requires a modification of the wavelength solution in order to correctly process the night-time data. Part of this correction is performed by the pipeline using the frames taken during the X-shooter Active Flexure Compensation procedure<sup>7</sup>. The remaining offset is corrected by cross-correlating the observed sky spectrum with a synthetic sky spectrum (Noll et al. 2012; Jones et al. 2013) after the continuum, estimated as the mode of all flux values, has been subtracted. To get the correct seeing point-spread-function (PSF) with which to convolve the synthetic sky, an initial refinement of the wavelength solution has been obtained by cross-correlating the observed sky with an unconvolved synthetic sky. This preliminary wavelength calibration is applied to the observed sky. The synthetic spectrum is then convolved with an increasing seeing PSF and the width that minimizes  $\chi^2$  with the updated observed sky is chosen to be the effective sky-PSF.

---

<sup>7</sup>X-shooter User Manual available at [ESO website](#).

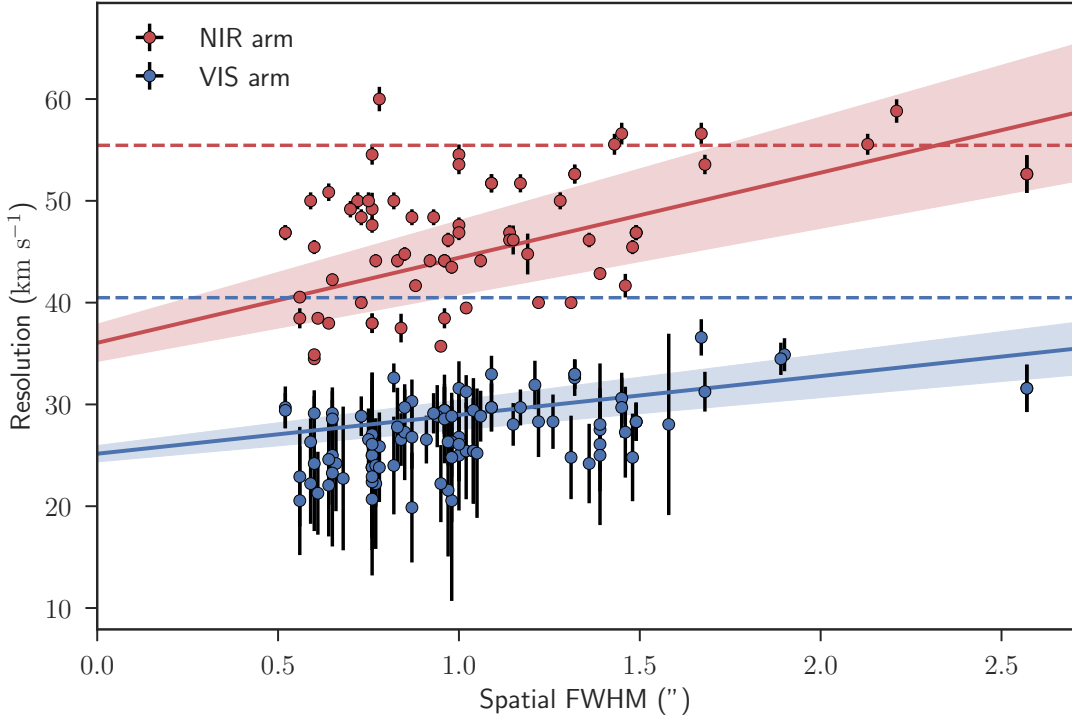


**Figure 2.2:** Blue data points show the FWHM (km/s) of Gaussian fits to unresolved telluric absorption lines in the VIS spectra, as a function of the airmass corrected DIMM seeing. The red data points show a subsample of measurements obtained for NIR spectra. The colored lines show the corresponding linear fits to the data points. The colored bounds contain 68 per cent of the best-fit probability mass. The red and blue dashed lines indicate the nominal resolution for the slit-widths used for the telluric standard observations. As can be seen, the effective resolution is in many cases superior to the nominal one.

Using the synthetic sky with the matched resolution, a final wavelength calibration can then be calculated by cross-correlating the observed sky with the correctly broadened sky spectrum as a function of a velocity offset. Both a multiplicative and an additive offset to the wavelength calibration has been tested, but in terms of  $\chi^2$ , the model with only a multiplicative offset is preferred. The resulting offsets, which were smaller than 0.01 nm in the UVB and VIS data and smaller than 0.05 nm in the NIR spectra, but changing over short periods of time were applied to the corresponding spectra<sup>8</sup>. Using the convolved synthetic sky, the pixels containing the brightest sky lines have been flagged as such in the bad pixel map.

### 2.3.3 Spectral resolution

The afterglow spectra described in this paper are obtained in Target-of-Opportunity mode. In most cases, there is little possibility to tweak slit widths to the seeing at the time of observations (i.e. to optimize spectral resolution and signal-to-noise), and almost all our data are therefore taken with a fixed set of slit widths and binning, described above. In a fair number of cases, the seeing full width at half maximum (FWHM) is considerably smaller than the slit width, and the delivered spectral resolution will then be determined by the seeing rather than by the slit width, as afterglows are point sources (this is evidently not the case for extended sources, e.g. for host galaxies). The delivered resolution for slit-width dominated spectra post-reduction and extraction can easily be determined from the bright sky emission lines. For afterglow spectra with very high signal-to-noise, the delivered spectral resolution can at times be determined from the science data themselves. However, in the presence of multiple velocity components in absorption, other forms of line broadening, and a lack of lines at some redshifts, this is difficult to do at lower signal-to-noise ratios (the majority of spectra in our sample). A broad starting value for the expected resolution will help fitting of these spectra, and can be important in upper limit determination, and for this reason we construct a crude relation between the seeing and the delivered resolution at our slit width, binning, and reduction pipeline settings.

To this end we use observations of telluric standard stars that are taken with identical instrument settings as our afterglow spectra, usually just after the science data, as part of the ESO X-shooter calibration plan. These spectra have been reduced together with the afterglow spectra, using identical pipeline settings with the same version of the pipeline. To get the resolution for each observation, we select a series of atmospheric transitions that are resolved multiples which should be intrinsically unresolved, and are in areas with well defined continuum flux. We then fit the lines with Voigt-profiles and calculate a corresponding FWHM, which we can then convert to a delivered resolution using the wavelength of the chosen transitions. To get the resolution as a function of ambient conditions, for each observations we also calculate the airmass-corrected [DIMM](#) seeing, which is measured at 500 nm.

The resulting distribution of spectral FWHM (km/s) as a function of spatial FWHM at 500 nm is fairly well described in the VIS arm by a linear relation  $a + b * x$ , with  $x$  the spatial FWHM in arcseconds,  $a = 25.2 \pm 0.8$  km/s,  $b = 3.8 \pm 0.7$  (see Fig. 2.2). For the NIR arm the corresponding relation is  $a = 36.0 \pm 1.8$  km/s,  $b = 8.4 \pm 1.8$ . We use these linear relations as a way to estimate the spectral resolution for medium to low signal-to-noise afterglow spectra. To extend this to the UVB arm, we calculate the ratio between the VIS and the NIR arm resolutions and find that the resulting distribution is consistent with a simple scaling of the VIS arm relation by the ratio of resolutions of the NIR and VIS arm for unresolved, slit filling, sources as given on the [ESO](#)

---

<sup>8</sup>The wavelength shifts have been extensively studied by ESO staff in [this document](#).

[instrument website](#). The UVB arm contains no suitable absorption lines to use, and we therefore use a scaled value. This simple analysis gives a sufficiently accurate estimate for the analysis of the low signal-to-noise science spectra. In all cases the determined resolution is written to the header with the "RESOLUTION" keyword.

#### 2.3.4 Spectral extraction

To extract the afterglow spectrum from the rectified 2D-image, several techniques have been employed based on the brightness of the afterglow and the complexity of the objects entering the slit. Due to the malfunctioning ADC (see Sect. 2.2.4), the spectral trace changes position across the slit in the spatial direction as a function of wavelength. For a large fraction of the observed bursts, using a single aperture for the spectral extraction is inadequate due to the large amount of background that would then enter the slit. To optimally select the extraction regions we therefore need to model the trace position.

To get the shape and the position of the spectral PSF as a function of location on the image, we need to chose a model which can represent how the light falls on the slit. We know from Trujillo et al. (2001) that a Moffat function (Moffat 1969) with an index of  $\beta = 4.765$  adequately describes an imaging PSF due to atmospheric turbulence, but because of aberrations in the optical dispersion elements and the rectification process, the PSF we are trying to model is different from this profile. To allow for flexibility in the model, we have chosen the Voigt function as a model for the spectral PSF and we describe how this is evaluated in App. 2.5. Since the host galaxy could also give a contribution to the image profile, this choice allows for the required freedom if additional flux is in the wings of the profile.

To guide the estimated position of the trace on the slit as a function of wavelength, we have used the analytic prescription for the trace position described in Filippenko (1982), where the header keywords of the observations have been queried for the ambient conditions which controls the degree to which the trace changes position in the spatial direction. This analytic approach is only valid for a plane-parallel atmosphere, but because the final position is refined in the fit, it is adequate for our purposes.

Based on the signal-to-noise of the afterglow continuum, the 2D-image has been binned in the spectral direction to a number of elements that allows for an accurate tracing of the PSF, typically 200 bins for moderate signal-to-noise. For each of the bins, using the analytically guided guess position, the spectral PSF has been fit using the unweighted chi-squared minimization algorithm implemented in `scipy.optimize.curve_fit` (Jones et al. 2001). Since we know that the trace varies slowly as a function of wavelength, we have then fitted a low-order polynomial to the fit parameters as a function of wavelength, which allows us to evaluate the spectral PSF at all wavelengths and in this way accurately model the entire spectral PSF.

Equipped with a model for how the light is distributed across the entire dispersion direction, we can employ the optimal extraction algorithm (Horne 1986), which weights the extraction aperture by the spectral profile, or alternatively sum all pixels within 1 FWHM of the modeled profile. Where possible, we have used the optimal extraction. In cases where the trace is very weak, even in the binned images, an aperture has been selected manually which covers all emission lines, if present, and when nothing is immediately visible, the entire nodding window. The error- and bad pixel maps are in all cases propagated throughout the extraction.

In cases where multiple traces are visible in the slit, additional components for the profile are used in the optimal extraction. The additional components do not share the PSF parameters and in cases where the additional component is an extended object, the fits have been inspected to ensure that the additional component does not skew the fit towards a different PSF. The additional components are not used for the weights in the extractions.

The spectra are corrected for Galactic extinction using the  $E(B - V)$  value from the dust maps of Schlegel et al. (1998) with the update in Schlafly & Finkbeiner (2011)<sup>9</sup>, and the extinction curve by Cardelli et al. (1989) with a total to selective extinction  $R_V = 3.1$ . The wavelengths of the extracted 1D-spectra are wavelength recalibrated (described in Sect. 2.3.2), moved to vacuum, and corrected for barycentric motion. Pixels with pixel-to-pixel variation larger than  $50\sigma$  are additionally added to the bad pixel map.

### 2.3.5 Telluric correction

For all Earth-based telescopes, the light first has to pass through Earth’s atmosphere, where the atmospheric content and conditions make an imprint on the received spectrum. These telluric features can be corrected for in a multitude of ways. We employ a prioritized list of methods here, depending on the availability of the chosen methods. Since the observations are often taken at odd times under varying conditions, this prioritized list ensures that we are always doing the best possible correction.

The highest priority method is using the GRB afterglow continuum itself, where the atmospheric conditions have directly been imprinted on the spectrum. The telluric features can directly be fit with an atmospheric model (Molecfit; Smette et al. 2015; Kausch et al. 2015)<sup>10</sup>, which can then be used to correct for the absorption. The accuracy of the correction depends on the signal-to-noise per pixel of the target spectrum, where we have chosen the requirement that the afterglow continuum spectrum has a median signal-to-noise higher than a value of 10.

If the afterglow is not sufficiently bright, telluric standard stars observed close in time to the GRB can be used as a proxy for the atmospheric condition during the GRB observation. Here we

---

<sup>9</sup>Queried from <http://irsa.ipac.caltech.edu/applications/DUST/index.html> using astroquery (Ginsburg et al. 2016).

<sup>10</sup><http://www.eso.org/sci/software/pipelines/skytools/molecfit>

employ the telluric correction method that has been developed in [Selsing et al. \(2015\)](#), where a library of synthetic templates is fit to the observed telluric standard.

In the last case, where the object is neither bright enough, or there for some reason a telluric standard have not been observed, we rely on a synthetic sky model ([Noll et al. 2012](#); [Jones et al. 2013](#)) for which we generate a synthetic transmission spectrum, where the ambient parameters for the observations have been used.

### 2.3.6 Continuum estimate

We additionally provide an estimate of the continuum for all the spectra presented here. For this, we have developed an algorithmic approach that attempts to automatically estimate the continuum placement along with the error on the continuum estimate through an iterative procedure. The method is entirely data-driven and does not rely on any physical assumptions. The method is applied on each arm separately for each spectrum, to allow the widest possible wavelength range of the spectral shape to guide the normalization.

To estimate the continuum, a number of points (typically on the order of 100) are inserted at random positions along the wavelength direction, and the flux-density of each point is determined by the median value of the spectrum in a small region ( $\sim 1 \text{ \AA}$ ) surrounding each point. The points are fitted with a low order polynomial (we use `numpy.polynomial.chebyshev`) and iteratively, the point furthest away is removed until the polynomial fit differed from the points by less than  $\sim 5$  per cent. This filtering is used because the intrinsic afterglow continuum of GRBs can be modeled by power laws ([Piran 2005](#)), and removing points that differ significantly from a smooth continuum shape will guide the continuum estimate to a shape more reasonable for GRB afterglows. The reason for the non-physical model for the normalization is that it has the flexibility to capture instrumental variations of the continuum level that are not easily contained in a more physically motivated model. Additionally, points spaced closer than 1 per cent of the total spectral coverage are pruned. The remaining filtered and pruned points are then spline interpolated using `scipy.interpolate.splrep.splev`, which serves as a first estimate of the continuum placement. To prevent the spline from diverging at the edges, the spline-based continuum is tapered with a low order polynomial. An attempt to identify absorption and emission regions is then carried out, where they are marked as such if the difference between the estimated continuum and the observed spectrum is larger than 3 - 5 times the associated error spectrum. All regions marked as affected are then masked.

Using the masked spectrum, the entire process is then repeated 500 times where the final continuum estimate is the mean of the continuum realizations and the associated error estimate is the standard deviation. This error reflects the stability of the algorithm across the spectrum. An example of the performance is shown in Fig. 2.3. In the Ly $\alpha$  forest, where there is very little flux at

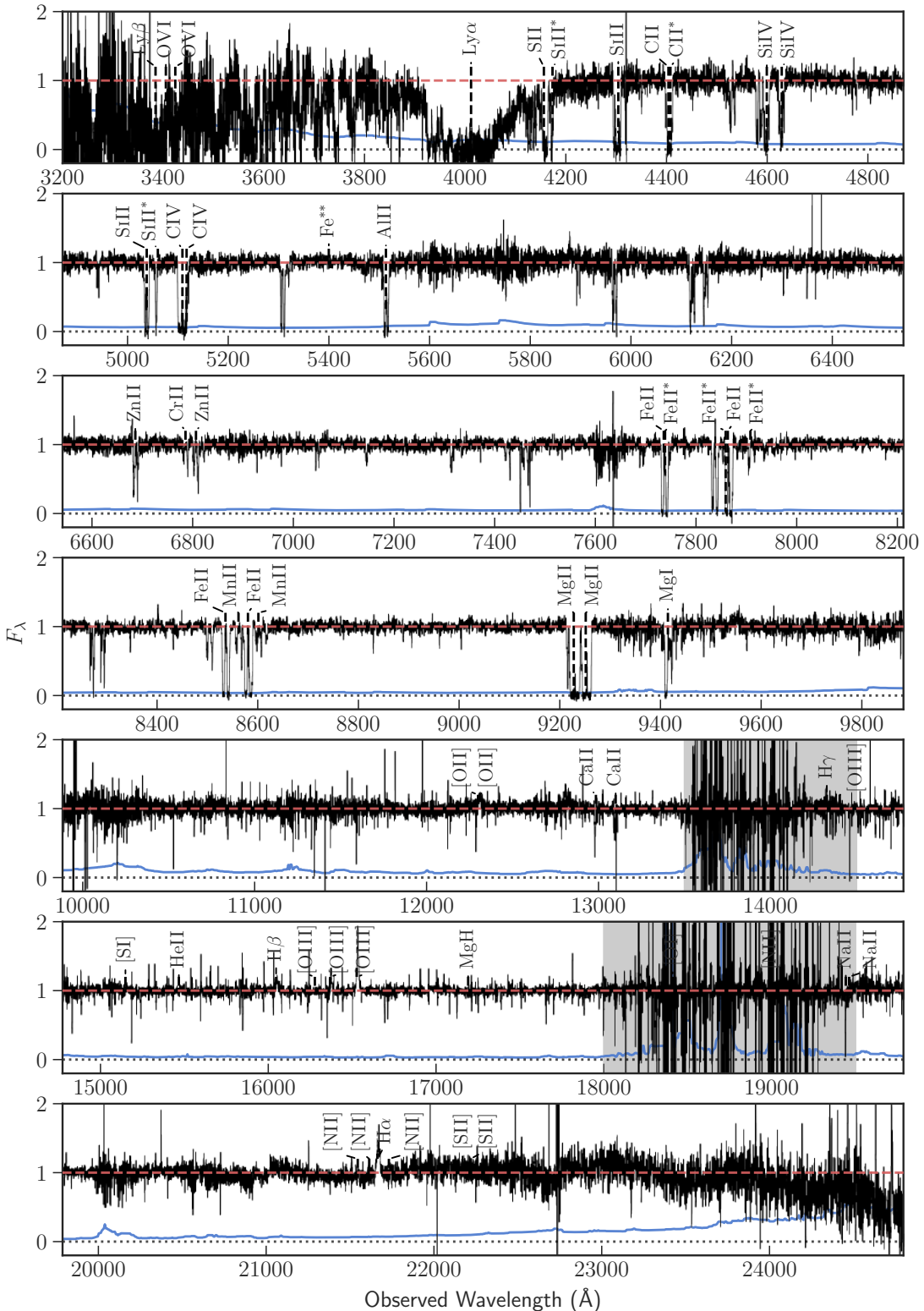


**Figure 2.3:** Telluric corrected, normalized spectrum of GRB 121024A at  $z = 2.300$  that illustrates the typical data quality. The continuum estimate is shown in dashed red and the error spectrum in solid blue. The acquisition magnitude is  $R = 20$ , meaning it is in the brighter end of the sample presented here, but not the brightest. The spectrum is rich in absorption and emission lines, including absorption from molecular H<sub>2</sub>. The absorption trough visible at  $\sim 4000$  is due to Ly $\alpha$  in the host. We have marked the most prominent lines seen in GRB afterglows from Christensen et al. (2011). The regions of most severe telluric absorption are highlighted by grey-shading the background. Additionally, three intervening systems are seen in this sightline. This spectrum has been analyzed in detail in Friis et al. (2015).

the continuum level, the performance of the normalization algorithm depends on the continuum coverage redwards of the Ly $\alpha$  line. In some cases, very little continuum is contained in a single arm and a manual continuum estimate is provided, similar to what is done in López et al. (2016). In these cases the continuum error is set to 10 per cent. The code for the continuum estimate is released along with the paper at <https://github.com/jselsing/XSGRB-sample-paper>.

### 2.3.7 Science data products

All the spectra are made available as a single [ZIP file](#), through <http://grbspec.iaa.es> (?), and additionally through the ESO archive in the form of [phase 3 material](#). This release includes both prompt afterglow observations as well as late time observations of the associated hosts, and represents *all* afterglow spectra of GRBs carried out by the X-shooter spectrograph since the commissioning of the instrument, 14/03/2009, and until the end of the last period of the program 098.A-0055, 31/03/2017 and thus constitutes eight years of GRB afterglow observations with X-shooter. An overview of all the spectra and their observational setups is given in Table 2.1. For each burst, each individual observation is provided in a separate reduction, and in cases where observations have been repeated for an increased signal-to-noise or to follow the temporal evolution, a combined spectrum is also provided. No attempt has been made to join the spectroscopic arms, so for each observation, three spectra are provided in separate files.

All spectra are released in the ESO Science Data Product (SDP) format (Micol et al. 2016), and formatted as binary FITS files. The naming convention is based on the GRB name and the observation number, and follow the scheme GRBxxxxxx\_OBxarm.fits. For example, the visual arm of the third observation of GRB 151021A, observed in RRM mode (see Sect. 2.2.3), is named GRB151021A\_OB3VIS.fits.

Each file contains 7 columns with the following contents and descriptions:

- WAVE - Observed wavelength in vacuum, corrected for barycentric motion and drifts in the wavelength solution ( $\text{\AA}$ ).
- FLUX - Observed flux density ( $\text{ergs}^{-1}\text{cm}^{-2}\text{\AA}^{-1}$ ).
- ERR - Associated flux density error ( $\text{ergs}^{-1}\text{cm}^{-2}\text{\AA}^{-1}$ ).
- QUAL - Bad pixel map, where a value different from zero indicates a bad pixel.
- CONTINUUM - Continuum estimate based on Sect. 2.3.6 ( $\text{ergs}^{-1}\text{cm}^{-2}\text{\AA}^{-1}$ ).
- CONTINUUM\_ERR - Relative error on the continuum estimate.
- TELL\_CORR - Inverse transmission spectrum. Multiply FLUX and ERR column with this column to correct for telluric absorption.

## 2.4 Results

In this section, we describe the efficiency of the follow-up effort and the characteristics of the observed bursts. We also assess the degree to which the obtained sample is representative for the full *Swift* sample. An important note is that here we provide a release for *all* GRBs after 14/03/2009, that have been observed with X-shooter, while only a subset of these constitutes our *statistical sample*. The statistical sample is based on the selection criteria described in Sect. 2.2.1. Some bursts not fulfilling the sample criteria have been followed up due to interesting characteristics, e.g., curious properties of their light curves, their brightness, etc. These bursts are not discussed as part of the investigation of the statistical properties of the GRB population. A prime example of a spectacular burst outside the statistical sample is the bright *INTEGRAL* burst GRB 161023A (de Ugarte Postigo et al., in prep), that contains at least 15 intervening absorption systems (See 2.5).

### 2.4.1 Follow-up timing and afterglow brightness

Redshift determination of bursts for which the host is too faint for a spectroscopic redshift measurement relies on the detection of absorption lines imprinted on the GRB afterglow continuum. Because the optical afterglow rapidly fades (typically as  $\sim t^{-1}$ ) a rapid follow-up is essential. In Fig. 2.4 we plot the delay from the BAT trigger to the start of the spectroscopic observation. The shortest delays are observed in RRM-mode. The fastest follow-up between BAT trigger and start of spectroscopic observations for any observation is for the short,  $z = 1.717$ , GRB 160410A for which spectroscopic integration was initiated only 8.4 minutes after the BAT trigger. To illustrate the importance of the follow-up delay for the redshift completeness, we plot the redshift completeness as a function of delay time in Fig. 2.4 for all the bursts we have followed up, including the ones outside the statistical sample. As can be seen from the figure, the fraction of GRBs with a redshift determination decreases with follow-up delay. The redshift completeness for bursts that we have followed up is 94 per cent. This degree of completeness in the followed bursts, illustrates the efficiency of VLT/X-shooter in redshift determination. Not shown in the figure are an additional 12 bursts that have redshift determinations based on late-time host observations with delay times longer than  $\sim 10$  days.

### 2.4.2 Sample completeness

Of all the BAT-triggered bursts, a total of 165 bursts fulfill the sample criteria specified in Sect. 2.2.1, since the commissioning of VLT/X-shooter. This sample constitutes the *statistical sample* from which we will derive statistical properties of the GRB population. The redshift completeness of the full statistical sample is 61 per cent. We return to the question of redshift completeness in

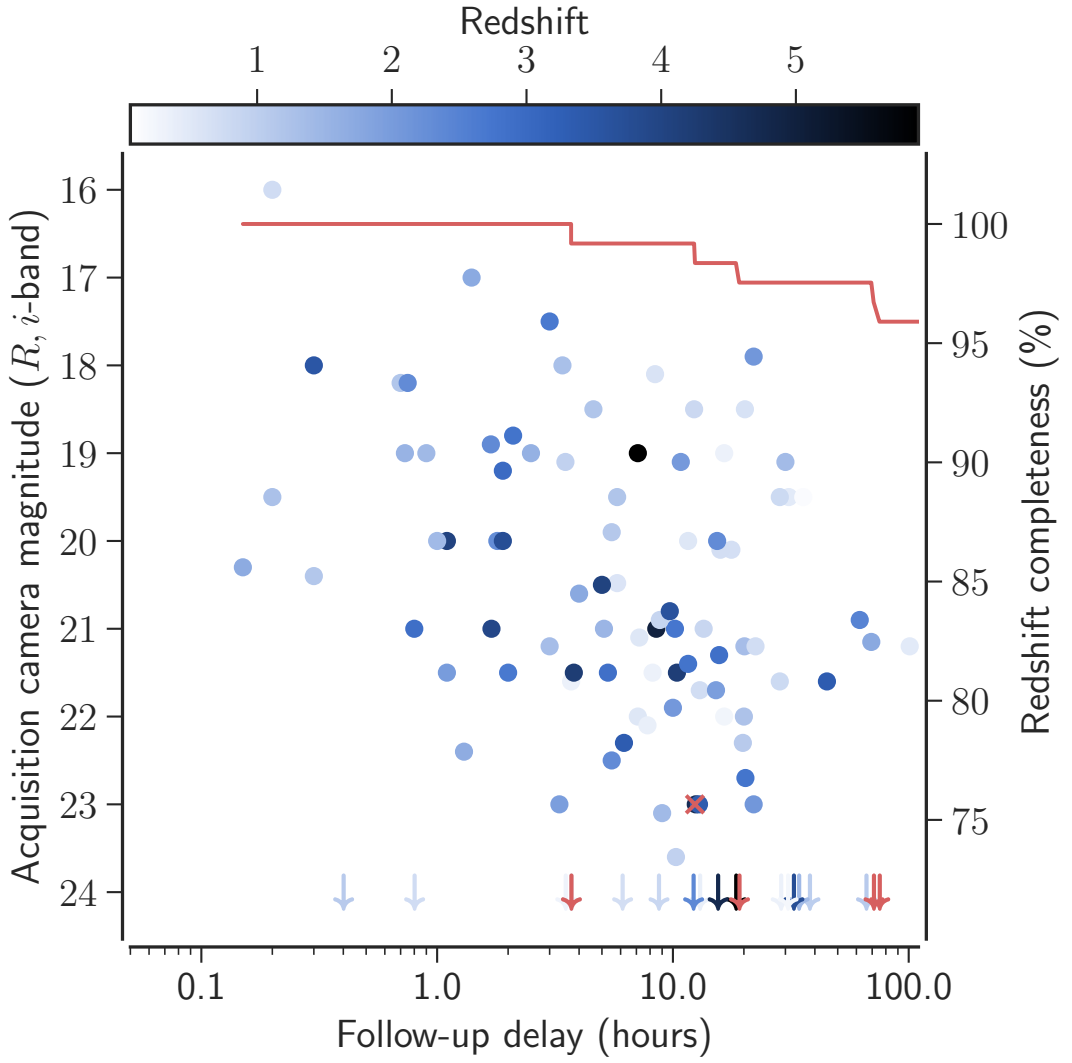


**Figure 2.4:** Afterglow magnitude at the start of observation and redshift completeness as a function of follow-up delay for all the afterglows that have been followed up. The points have been colored based on the redshift of the corresponding burst. Red symbols indicate GRBs without a measured redshift and arrows indicate bursts for which the afterglow was not detected in the acquisition image. In red is shown the redshift completeness as a function of follow-up delay.

Sect. 2.4.3. From this sample, 93 GRBs have been spectroscopically followed up with X-shooter. In order to assess whether the subset of bursts followed up are representative of the underlying GRB parent population, we compare intrinsic properties of GRBs in our sample to GRBs in the full sample followed up by *Swift*. We show the comparison between the BAT (15 – 150 keV) fluence, the XRT flux (0.3 – 10 keV) at 11 hours, and the intrinsic X-ray derived equivalent hydrogen column density at the redshift of the GRB, in excess of the Galactic X-ray absorption column,  $N_{\text{HI},\text{X}}$ , in Fig. 2.5. For the latter, we can only use values of  $N_{\text{HI},\text{X}}$  derived for bursts with a

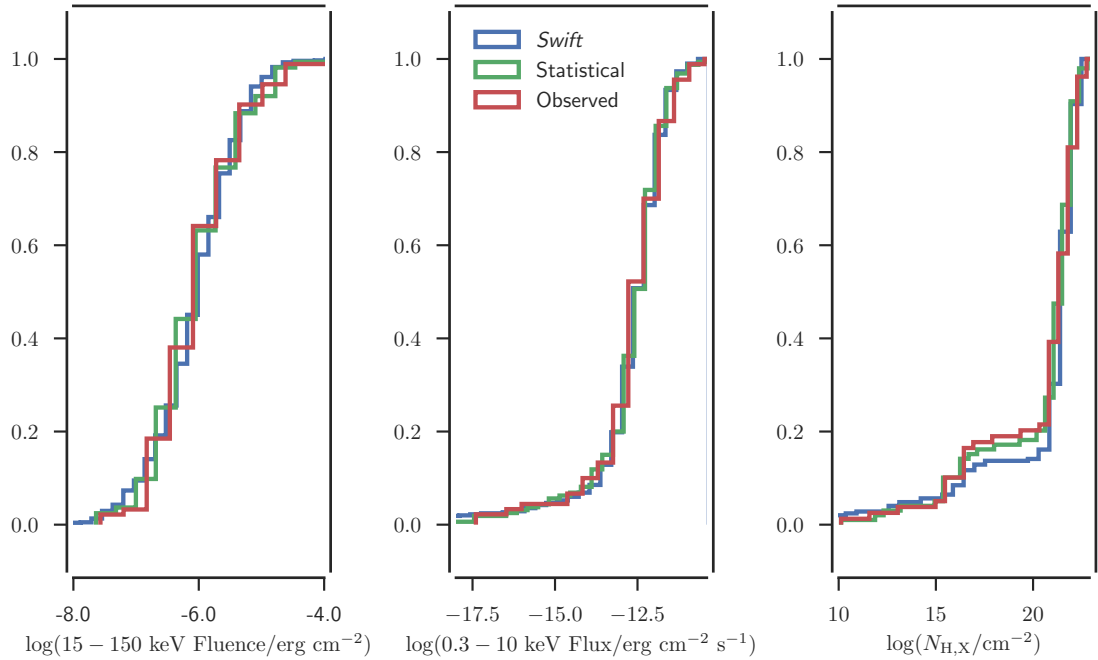


**Figure 2.5:** Comparison between the burst properties of all bursts observed with *Swift* (blue), the statistical sample that fulfill the criteria specified in Sect. 2.2.1 (green), and the subset that has been observed as part of the statistical sample (red). The left plot shows the fluence in the 15–150 keV band as observed by BAT. The middle panel shows the 0.3–10 keV flux, 11 hours after the bursts as measured by XRT. In the right most panel, we show  $N_{\text{HI},X}$  based on the XRT spectrum (Evans et al. 2009).

measured redshift, excluding  $\sim 75$  per cent of the full *Swift* sample. We return to the last point in Sect. 2.4.4.

Using the observational characteristics of the 1266 bursts observed until 31/03/2017 by *Swift*, and the derived  $N_{\text{HI},X}$  (Evans et al. 2009), we can quantify the degree to which our sample is biased relative to the overall *Swift* sample. The values are queried from the online *Swift* database<sup>11,12</sup>. Three samples are of interest in order to assess the completeness of the follow-up campaign (Fig. 2.5); the full *Swift* sample consisting of all the bursts observed by *Swift* (blue), all the bursts that fulfill the selection criteria imposed in Sect. 2.2.1 (green), and the bursts actually followed up with X-shooter (red).

For each of the samples, we calculate the median, 16th, and 84th percentiles of each of the distributions, which can be used as point estimates for the population distribution. These are provided in Table 2.2. It can be seen from the values that the three samples have very similar distributions in terms of the point estimates chosen. This suggests that our selection criteria are unbiased compared to the *Swift*-sample and that additionally, the follow-up effort conserves the

<sup>11</sup>[http://swift.gsfc.nasa.gov/archive/grb\\_table/](http://swift.gsfc.nasa.gov/archive/grb_table/)

<sup>12</sup>[http://www.swift.ac.uk/xrt\\_live\\_cat/](http://www.swift.ac.uk/xrt_live_cat/)

**Table 2.2:** Population properties (median and 16th and 84th percentiles as the error intervals) for the *Swift sample* and the subset of bursts fulfilling the sample criteria. The population characteristics of the three samples are very similar, which shows that our selection criteria effectively conserve the statistical properties of the underlying population, at least for these parameters. Notice that not all bursts have measurements of the quantities we compare.

	Full <i>Swift</i> sample	Statistical sample	Followed up bursts
$N_{BAT}$	981	163	92
$\log(15 - 150 \text{ keV fluence})$	$-5.9^{+0.7}_{-0.6}$	$-5.9^{+0.7}_{-0.6}$	$-5.9^{+0.7}_{-0.7}$
$N_{XRT}$	902	160	90
$\log(0.3 - 10 \text{ keV flux})$	$-12.3^{+0.7}_{-0.8}$	$-12.4^{+0.7}_{-0.8}$	$-12.4^{+0.9}_{-0.7}$
$N_{\text{HI},x}$	248	99	79
$\log(N_{\text{HI},x})$	$21.7^{+0.6}_{-0.9}$	$21.5^{+0.7}_{-3.4}$	$21.6^{+0.7}_{-4.5}$

distributions of the intrinsic GRB properties (except perhaps for  $N_{\text{HI},x}$ , see Sect. 2.4.4).

Additionally, using a 2-sided Kolmogorov-Smirnov test (KS-test), we can assess the degree to which the null hypothesis, that the two distributions are drawn from the same parent distribution, can be rejected. We show a graphic representation of the test statistics in Fig. 2.6. A high  $p$ -value indicates little evidence against the null hypothesis. The distribution of  $N_{\text{HI},x}$  exhibits the highest degree of dissimilarity, but the two distribution are still consistent with being drawn from the same underlying distribution.

We therefore conclude that the statistics of the sample presented here, conserves the intrinsic properties of the GRBs in the full *Swift* sample - at least in terms of BAT fluence and X-ray flux at 11 hours.

### Properties of rejected triggers

Out of the 165 bursts meeting our initial selection criteria for the statistical sample, 36 (22 per cent) were not observed due to reasons unrelated to the GRB or afterglow properties. The reasons include unavailability of the telescope due to technical maintenance (e.g., mirror re-coating), a visiting observer rejecting the ToO trigger, or bad weather. Because this cut is unrelated to the GRB properties, it will not change the statistical properties of the full sample. Removing these bursts from the statistical sample, dramatically improves the redshift completeness from 61 per cent to 88 per cent. The remaining burst not followed up already had a redshift from other instruments or were very faint and without a host association, thus observations were unlikely to yield a redshift measurement. In the remainder of the text, we consider the 129 bursts our statistical sample.

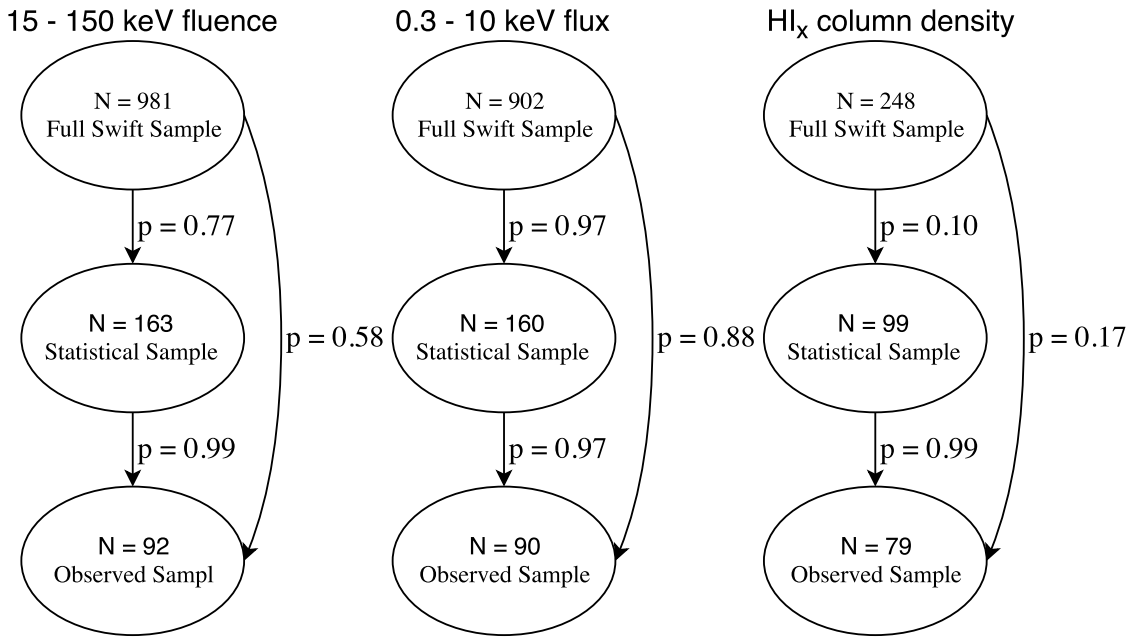


**Figure 2.6:** Relational graph showing the respective  $p$ -values. They all represent the degree that the different samples are drawn from the same underlying distribution. The arrows represent the comparison direction with each of the  $p$ -values they are listed next to. Only in the HI column density distribution is there mild evidence against the null hypothesis, but the discrepancy is mainly driven by a relatively larger fractional contribution from low-column hosts in the statistical sample.

#### 2.4.3 On the redshift distribution of GRBs

One of the objectives of our follow-up campaign is to measure the redshift distribution for a well-defined, observationally unbiased and statistically useful sample of GRBs. The imposed selection criteria (see Sect. 2.2.1) ensure that the GRBs entering our homogeneous sample, fairly represent the underlying population. The redshift distribution of such a sample holds valuable information about the occurrence of GRBs through cosmic time (Jakobsson et al. 2012a; Perley et al. 2016a).

**Table 2.3:** Comparison between the redshift distributions of previous complete samples. The SHOALS redshift characteristics are taken from [Perley et al. \(2016a\)](#), the BAT6 redshifts are from [Salvaterra et al. \(2012\)](#) with the update from [Pescalli et al. \(2016\)](#), TOUGH is from [Hjorth et al. \(2012\)](#) with the update from [Schulze et al. \(2015\)](#), and Fynbo09 are from [Fynbo et al. \(2009\)](#). The errors shown on the median redshift contain 68 per cent of the probability mass.

Sample	N <sub>bursts</sub>	$z_{\text{completeness}}$	$z_{\text{mean}}$	$z_{\text{med}}$
XS-GRB	129	88 %	1.89	$1.52^{+1.83}_{-0.91}$
SHOALS	119	99 %	2.18	$2.06^{+1.27}_{-1.20}$
BAT6	58	97 %	1.90	$1.71^{+1.31}_{-1.04}$
TOUGH	69	87 %	2.20	$2.11^{+1.42}_{-1.36}$
Fynbo09	146	49 %	2.2	$2.1^{+1.28}_{-1.23}$

In Fig. 2.7 we show the redshift distribution of all the observed GRBs. In the top panel we show a histogram for the full sample and the statistical sample and in the main panel, we show the redshifts of the individual bursts as a function of GRB energy in the observed 15 – 150 keV band. To calculate the energy,  $E_{\text{BAT}}$ , we follow a similar procedure as [Lien et al. \(2016\)](#) and define  $E_{\text{BAT}} = F_{\gamma} 4\pi d_L^2 (1+z)^{-1}$ , where  $F_{\gamma}$  is the observed BAT fluence in the 15–150 keV band and  $d_L$  is the luminosity distance to the burst at the given redshift. Note that this measure of luminosity does not include any  $k$ -correction. As an indication of the effect of the *Swift* sensitivity limit on the redshift distribution, also in the figure, we have shown the so called  $\sim 1$  s flux BAT sensitivity limit ( $\sim 3 \times 10^{-8}$  erg s $^{-1}$  cm $^{-2}$ ; [Baumgartner et al. 2013](#); [Lien et al. 2016](#)). Due to the complex triggering mechanism of *Swift*, this sensitivity limit should be interpreted with some caution as the effective limit depends on the light curve of the prompt emission signal. Due to the dilution of light with distance, the *Swift* GRB luminosity detection limit is almost an order of magnitude brighter at  $z = 2$  than at  $z = 1$ . At  $z \geq 4$  we are only able to observe GRBs that are  $\sim$  hundred times brighter than the faintest bursts at  $z = 1$  and below. The effect of GRB redshift on the *Swift* triggering criteria have previously been studied in detail ([Littlejohns et al. 2013](#)).

We compare the point estimates for the redshift distributions of previous complete samples of GRBs in Tab. 2.3. We see that when we compare to other complete samples, the XS-GRB presented here has the lowest average redshift. However, the other samples also exhibit a large spread in the redshift distributions. A 2-sided KS test reveals that the XS-GRB sample is consistent with being drawn from the same parent sample with the following  $p$ -values: SHOALS ( $p$ -value = 0.13), BAT6 ( $p$ -value = 0.95), Fynbo09 ( $p$ -value = 0.08) and TOUGH ( $p$ -value = 0.09). As a small note, the redshift distribution of BAT6 are not expected to be identical to the other complete samples due to the additional cut on the GRB peak flux in the BAT band.

Because the redshift completeness of our statistical sample is 88 per cent, making an inference of the *true* redshift distribution of GRBs based on this sample is impossible. For instance, only the brightest GRBs are seen above redshift  $z \gtrsim 1$  as shown in Fig. 2.7. As described in detail in Hjorth et al. (2012) and Perley et al. (2016b), bursts for which the redshift is measured from the afterglow are systematically found in host galaxies with a lower luminosity than bursts for which the redshift is measured from the host galaxy. Only a few GRBs hosted in galaxies, with stellar masses more than  $10^{10} M_{\odot}$  have the redshift measured based on the afterglow continuum. This is likely related to the presence of higher contents of dust in more massive galaxies, leading to a larger fraction of extinguished afterglows.

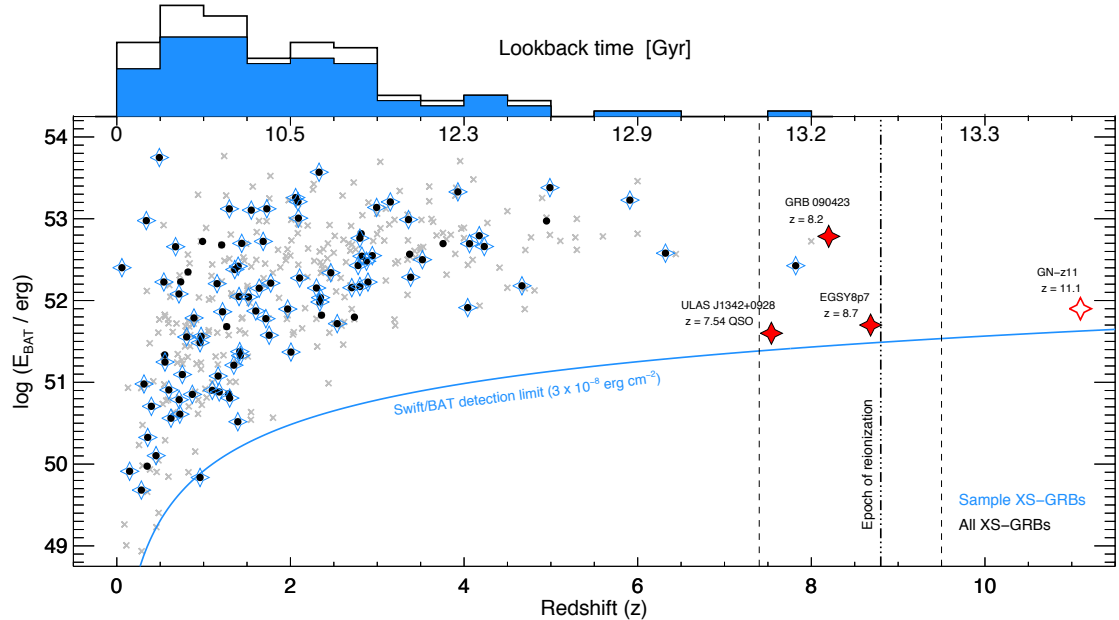


**Figure 2.7:** Redshift distribution as a function of intrinsic BAT  $\gamma$ -ray energy,  $E_{\text{BAT}}$ . Bursts that are a part of the statistical sample are marked by blue stars whereas black dots show all GRBs observed with X-shooter. All *Swift* GRBs with measured redshifts are shown in gray. For comparison, we overplot with red stars the GRB (Tanvir et al. 2009; Salvaterra et al. 2009), quasar (Bañados et al. 2017), and galaxies (Zitrin et al. 2015; Oesch et al. 2016) with the highest spectroscopically confirmed redshifts, the latter three shown at arbitrary  $E_{\text{BAT}}$ . The blue solid line represents the so-called 1 s BAT sensitivity limit described in the text. The estimated epoch of reionization is shown by the black dot-dashed line, with the uncertainty shown as the black dashed lines, from the most recent measurement by Planck Collaboration et al. (2016). On the top of the plot is shown the marginalization of the redshift. Again the blue histogram represents the bursts than enter our sample and the white histogram the full GRB population.

#### 2.4.4 Sample darkness

A fraction of all GRBs exhibit no detectable or very faint optical afterglows (Groot et al. 1998; Djorgovski et al. 2001; Fynbo et al. 2001). The degree of optical extinction relative to the X-ray

brightness has been parametrized in terms of their optical darkness, using the measurement of, or limit on, the optical to X-ray spectral index  $\beta_{OX}$  (Jakobsson et al. 2004; Rol et al. 2005; van der Horst et al. 2009). The X-ray properties of such bursts have previously been investigated (De Pasquale et al. 2003; Fynbo et al. 2009; Melandri et al. 2012) and there are some indications that dark bursts have somewhat higher X-ray luminosity and  $N_{H,X}$  compared to the optically bright bursts (Campana et al. 2012; Watson & Jakobsson 2012). The X-ray column density has been shown to be roughly correlated with the gas column density, which, for a given metallicity, also correlates with the dust extinction (Watson et al. 2013; Covino et al. 2013), though the range in metallicity introduces a large additional scatter in the correlation between the extinction and the  $N_{H,X}$ . This indicates along with investigations of host galaxy properties (Greiner et al. 2011; Krühler et al. 2011b; Hjorth et al. 2012; Perley et al. 2016b), that the extinction of the optical afterglows is primarily driven by the presence of dust in the host galaxies and not solely by unfortunate placement of the synchrotron spectral break frequencies. Hjorth et al. (2012) find that systems with no optical afterglow have higher  $N_{H,X}$ , irrespective of the nature of the host – which however also turn out to be redder. Additionally, the ISM absorption lines in dark sight-lines are found to be stronger compared to optically brighter bursts (Christensen et al. 2011), which is consistent with the dark bursts being found in more metal-rich and dustier galaxies.

For all bursts with follow-up within 100 hours we calculate the "darkness"-parameter,  $\beta_{OX}$  (Jakobsson et al. 2004). This requires the simultaneous measurement of the X-ray flux density and the optical flux density which is in practice possible, but in reality extremely rarely available. As a proxy, we use the measured acquisition camera magnitude reported in Table 2.1 to get the optical flux density at the beginning of the spectroscopic integration. Because we know the delay between the follow-up and the *Swift* trigger, we can use the measured XRT lightcurve (Evans et al. 2007, 2009)<sup>13</sup> to infer the corresponding X-ray flux density at the time of the optical observation. This is done by either linearly interpolating between temporally neighboring XRT measurements or by extrapolating the last few X-ray data points to the time of the spectroscopic observation. When the afterglow is not detected in the acquisition camera, an upper limit of  $> 24$  mags is used, which propagates into an upper limit on  $\beta_{OX}$ .

In Fig. 2.8 we compare the  $\beta_{OX}$  -  $N_{H,X}$  distribution with the one presented in Fynbo et al. (2009). We take the  $N_{H,I,X}$  values from the XRT spectral fits (Evans et al. 2009). The values from Fynbo et al. (2009) have been treated as detections, meaning that we artificially bias the distribution towards higher  $\beta_{OX}$ -values. The two distributions exhibit a large degree of overlap. We confirm the result by Fynbo et al. (2009), that dark bursts,  $\beta_{OX} < 0.5$ , have higher  $\log(N_{HI}/\text{cm}^{-2})$ . Specifically, for bursts with measured redshift either from the afterglow or the host galaxy, we find the following: For bursts with  $\beta_{OX} \geq 0.5$  we find  $\log(N_{HI}/\text{cm}^{-2}) = 21.4^{+0.7}_{-1.0}$ , whereas

---

<sup>13</sup>[http://www.swift.ac.uk/xrt\\_curves/trigger\\_numer/flux.qdp](http://www.swift.ac.uk/xrt_curves/trigger_numer/flux.qdp)

for  $\beta_{OX} < 0.5$  we find  $\log(N_{\text{HI}}/\text{cm}^{-2}) 21.8^{+0.5}_{-0.9}$  where 68 per cent of the probability mass is contained within the error intervals. A 2-sided KS test fails to reject the null hypothesis that they are drawn from the same distribution with  $p = 0.11$ , meaning that there is no strong evidence for a discrepancy. A Kendall's  $\tau$  test, however, suggest a statistically significant, low degree of negative correlation ( $\Gamma = -0.21$  at a  $p$ -value = 0.01).

Using the table maintained by J. Greiner<sup>14</sup>, we can see how the presence of an optical afterglow affects the follow-up statistics. 50.5 per cent of all *Swift*-triggered bursts in this list do not have a detected optical afterglow. This number also includes bursts where no optical observations were available, so the real number is likely to be lower. For the bursts that enter our statistical sample, the percentage of bursts without a detected optical afterglow is 28 per cent, close to the upper limit on the fraction of dark bursts found in a complete sample with a very high degree of redshift completeness (Melandri et al. 2012). Of the bursts for which follow-up has actually been attempted, this number is 23 per cent, suggesting a slight bias against bursts without a detected optical afterglow in the spectroscopic sample.

However, the fraction of dark bursts for which we have measured redshifts is lower than the ones with a detected optical afterglow. For the afterglows we have observed as part of the statistical sample that do not have a detected optical afterglow, the redshift completeness is 53 per cent. For comparison, for the afterglows in the statistical sample we have observed with an optical afterglow detected, the redshift completeness is 92 per cent. This also shows that the lack of redshift completeness in the sample presented here is in part due to the increased difficulty of measuring a redshift for bursts without an afterglow. To measure a redshift, we either need a detected afterglow to obtain a spectrum or to locate the host galaxy and determine the redshift from there. It is more difficult to correctly associate a galaxy with a burst when there is no detected optical afterglow and hence a correct redshift measurement is more difficult to make, see Jakobsson et al. (2005); Levesque et al. (2010) and Perley et al. (2017).

Regardless the fraction of dark bursts being lower in the observed sample, compared to the statistical sample, the X-ray properties do not differ significantly, as shown in Sect. 2.4.2. This is despite spectroscopic follow-up only being carried out in cases where either a detectable optical afterglow or a clear counterpart are seen, which naively should be biased against dark bursts occurring in more obscured galaxies, which is shown to exhibit different galactic properties (Perley et al. 2009; Krühler et al. 2011b; Rossi et al. 2012; Perley et al. 2013, 2015). That the decreased fraction of dark bursts in observed sample does not alter the observed prompt X-ray brightness distribution, potentially reflects the independence of the X-ray brightness on the density of the circumburst medium (Freedman & Waxman 2001; Berger et al. 2003; Nysewander et al. 2009), if the measured  $N_{\text{H},\text{X}}$  is primarily driven by the gas column in the neighborhood of the burst. Because

---

<sup>14</sup><http://www.mpe.mpg.de/jcg/grbgen.html>

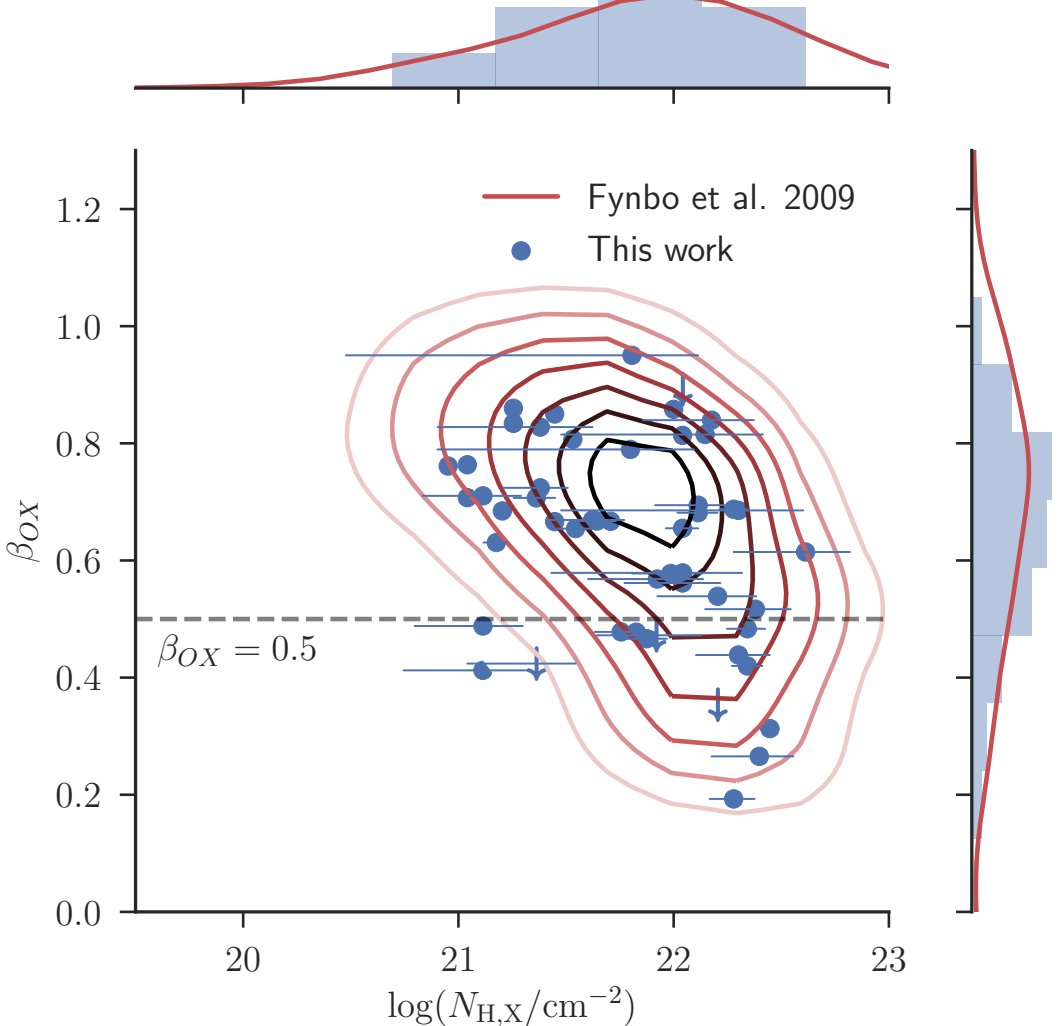


**Figure 2.8:**  $\beta_{OX}$  against X-ray derived hydrogen column density. In red is shown the sample presented in Fynbo et al. (2009) where the lines indicate the kernel density estimate of the distribution. For the kernel density estimate, the limits have been replaced with values. We note that contrary to what is presented in Fynbo et al. (2009), we exclude all bursts for which we do not have a redshift. Darker colors represent a higher density of points. In blue are the points for the bursts presented here along with the marginal histograms. Limits on  $\beta_{OX}$  are shown by downwards facing arrows. The corresponding marginal distributions are shown along the edges of the plot. A Kendall's  $\tau$  test, indicates a statistically significant, low degree of negative correlation ( $\Gamma = -0.21$  at a  $p$ -value = 0.01)

we only use values for  $N_{H,X}$  in the comparison for which the GRB has a measured redshift, this measure is likely biased toward optically brighter bursts (e.g. Watson & Jakobsson 2012).

#### 2.4.5 Hydrogen column densities

The locations of long GRBs are associated with intensely star-forming regions (Hogg & Fruchter 1999; Bloom et al. 2002; Fruchter et al. 2006; Lyman et al. 2017). Because a significant fraction of the hydrogen along the line of sight in these regions has not been ionized, the optical depth at the wavelength of Ly $\alpha$  is very high, saturating not only the line center, but also the damping wings. This causes a strong absorption system from the Ly $\alpha$ -transition to appear in the afterglow continuum. For bursts with  $z \gtrsim 1.7$ , the position of Ly $\alpha$  moves into the spectroscopic coverage of X-shooter, meaning that we are able to detect this absorption trough due to Ly $\alpha$ . The exceptionally good UV response of X-shooter, allows us to robustly measure H<sub>I</sub>-columns - also at these relatively low redshifts.

Due to the stochastic nature of the Ly $\alpha$ -forest, the blue wing of the Lyman- $\alpha$  absorption line is randomly superposed with Lyman- $\alpha$  forest systems, along with strong absorption from Mn II and Si III, making it notoriously difficult to model. Additionally, the red wing has ISM signatures imprinted on it, especially strong absorption due to Si II, S II and N V, which can exhibit significant velocity structure. Along with instrumental effects, the generative model for the data that we would use in a likelihood-based analysis would be very complicated. We have therefore decided not to make formal  $\chi^2$  fitting of the hydrogen column densities, but instead use a more subjective visual measurement to the absorption profile. Using an analytic approximation to the absorption profile from Tepper García (2006), we overplot a synthetic absorption line with a specified column density on our observed, normalised spectrum. By tuning the value of the hydrogen column density until the synthetic absorption line matches the spectrum, we can thereby infer the actual column density of the GRB sight line in a manual way. Similarly, the uncertainty on the hydrogen column can be estimated by adjusting the error, until the confidence bounds contain the continuum variation. We show the results of this procedure for all bursts where possible in Fig. 2.10 and the inferred hydrogen column densities in Table ??.

12 of the  $N_{\text{HI}}$  measurements for these spectra have previously been presented in Cucchiara et al. (2015) (See Table ??). We provide new measurements here for completeness. In the compilation of  $N_{\text{HI}}$  measurements towards GRBs in Tanvir et al. (submitted) there are 93 published  $N_{\text{HI}}$  values, excluding the measurements provided here. We here provide 30 new neutral hydrogen column density measurements – an increase of the number of optically derived hydrogen column densities of  $\sim 33$  per cent. We show the two distributions in Fig. 2.9. We compare the median, the 16th, and 84th percentiles of the two distributions. The sample presented has a Thöne =  $21.8^{+0.3}_{-0.8}$  and the rest of the literature values has  $\log(N_{\text{HI}}/\text{cm}^{-2}) = 21.5^{+0.4}_{-1.5}$ . We see that the two distributions have a large degree of overlap due to the large width of the distributions, but we find a slightly higher median value for the new sample presented here. A 2-sided KS test gives a  $p$ -value of  $p = 0.006$ , meaning relatively strong evidence against the null hypothesis that the two samples are

drawn from the same underlying distribution. Because the bursts that have measurements of the hydrogen column density are selected solely based on our ability to infer a column, it is difficult to make any strong conclusions about the population statistics in terms of gas content.

In Fig. 2.9, we also show the column density distribution for the 12081 quasar absorbers with  $\log(N_{\text{HI}}/\text{cm}^{-2}) > 20$  from Noterdaeme et al. (2012). The fact that GRBs are systematically located behind the highest  $\log(N_{\text{HI}}/\text{cm}^{-2})$ , previously noted (e.g., Prochaska et al. 2007; Fynbo et al. 2009), is very clear in this figure. The reason for this is that quasar sample sight-lines through galaxies that are cross-section selected, whereas GRB sight-lines probe the dense, star-forming regions in their hosts.

## 2.5 Discussion and conclusions

In this paper we have presented the results of a dedicated effort over the years 2009 – 2017 to use the X-shooter spectrograph on the ESO-VLT to secure spectroscopic observations of afterglows and host galaxies of GRBs detected by *Swift*. This work was initiated by the consortium that built X-shooter and included this project as a key part of the GTO program, but over the years the project continued in open time.

The sample presented here includes spectroscopic observations of 93 systems fulfilling our sample criteria, including 18 spectra that are late-time observations of the underlying host galaxies. All spectra have been made publicly available in the reduced form used in this paper.

Our sample serves the purpose to further characterize the environments of GRBs that was also much advanced by the previous surveys based primarily on lower-resolution spectroscopy. GRB afterglow sight-lines are unique in the sense that only after observing more than 12000 damped Lyman- $\alpha$  absorbers (DLAs) towards about  $10^5$  quasars, a handful systems with  $\log(N_{\text{HI}}/\text{cm}^{-2}) > 22$  have been identified (e.g., five in Noterdaeme et al. 2012). Long GRB afterglow spectra, by contrast, reveal such systems routinely (Jakobsson et al. 2006; Fynbo et al. 2009; Cucchiara et al. 2015, and this work). With afterglow spectroscopy (throughout the electromagnetic spectrum from X-rays to the sub-mm) we are able to characterize the properties of star-forming galaxies over cosmic history in terms of redshifts, metallicities, molecular contents, ISM temperatures, UV-flux densities, extinction curves, etc. A number of independent papers have been published or submitted for publication focusing on many of these specific issues of our sample such as extinction curves (Japelj et al. 2015, Zafar et al. submitted, see also Fynbo et al. 2014a; Heintz et al. 2017), emission lines from the underlying host galaxies (Krühler et al. 2015a), the frequency of intervening Mg II absorbers (Christensen et al. 2017), Arabsalmani et al. (2018) on the metallicity-scaling relations, and escape of ionizing radiation (Tanvir et al., submitted). A number of additional companion papers are also planned, investigating the detailed properties of the sample presented here, including equivalent width distributions (de Ugarte Postigo et al., in preparation), metallicities

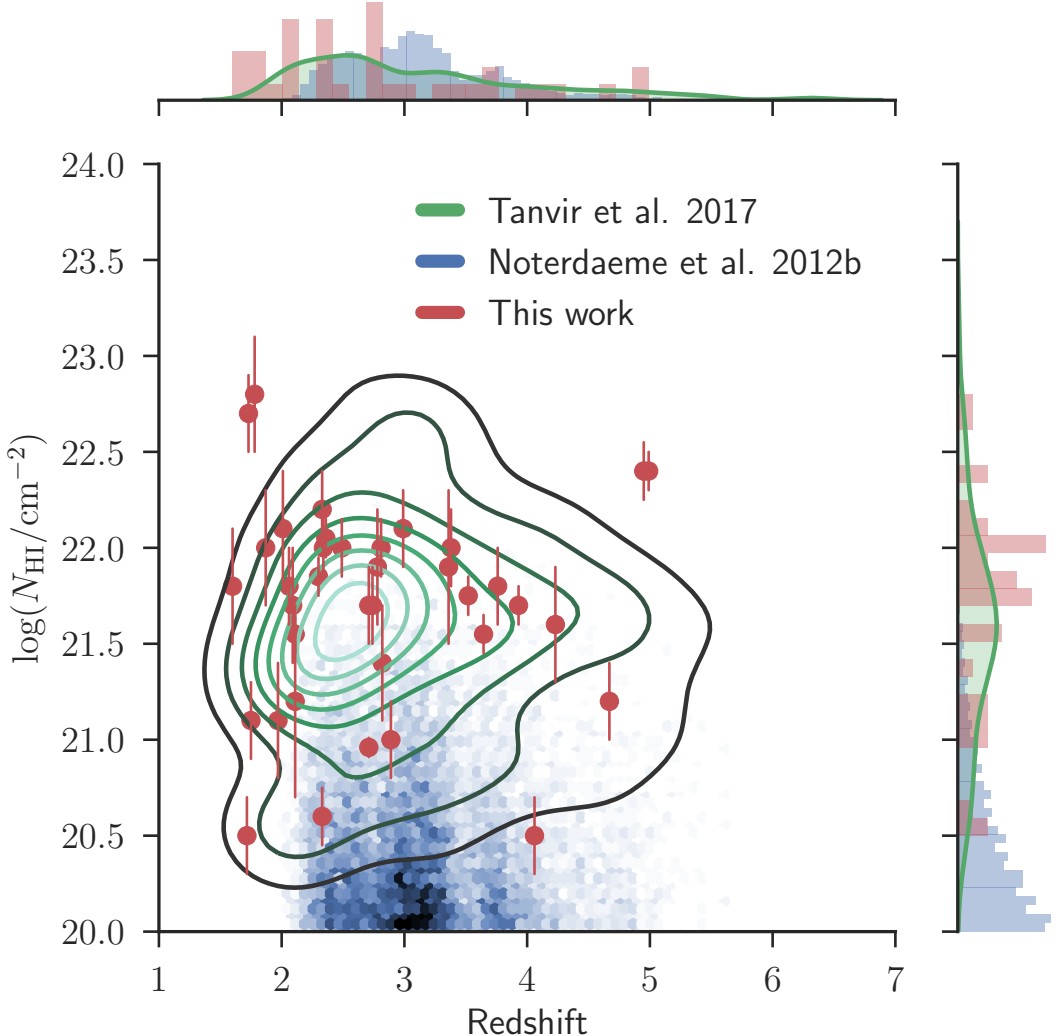


**Figure 2.9:** Distributions of hydrogen column densities for absorbers found in quasar absorption lines, from [Noterdaeme et al. \(2012\)](#) in blue. Overplotted in green is the kernel density estimate of absorbers in GRB sightlines. Values are taken from the compilation in [Tanvir et al. \(submitted\)](#), along with the new values presented in this sample. We also show in the red the values derived in [this work](#). The marginal distributions for the three samples are also shown along the left side and on the top, where the different environments probed are clearly visible in the hydrogen column densities, as previously also noted in [Fynbo et al. \(2009\)](#).

and kinematics (Thöne et al., in preparation), high ionization lines (Heintz et al., in submitted), molecular lines (Bolmer et al., in preparation), fine-structure lines (Vreeswijk et al., in preparation), and composite GRB afterglow spectrum (Selsing et al., in preparation).

The potential of using GRB sightlines as probes is far from fully harvested. The sample of sightlines probed by our spectra are not representative for all GRB sightlines as we have shown

and consistent with earlier findings from samples based on low-resolution spectroscopy (e.g., Fynbo et al. 2009) and from studies of complete samples of GRB host galaxies (Hjorth et al. 2012; Covino et al. 2013; Perley et al. 2016a). Krühler et al. (2013a) argue, that very rich sightlines like that probed by the remarkable GRB 080607 (Prochaska et al. 2009; Sheffer et al. 2009; Perley et al. 2011) are probably significantly more frequent than in the sightlines sampled by our spectra. However, with current instrumentation, these sightlines are out of reach except under very fortunate circumstances as in the case of GRB 080607 when the afterglow could be observed only a few minutes after the burst with a 10-m class telescope. Observations of such sightlines with X-shooter-like spectrographs on the next generation of 20–40-m telescopes is likely to be very rewarding, given that a suitable GRB detector will be available.

## Acknowledgements

Much of the work done here would not have been done without Neil Gehrels, who has now passed away. We owe him a large debt for his invaluable work with the *Swift* satellite. We also want to remember Javier Gorosabel, who was taken from us too early. JPUF, BMJ and DX acknowledge support from the ERC-StG grant EGGS-278202. The Dark Cosmology Centre was funded by the Danish National Research Foundation. This work was supported by a VILLUM FONDEN Investigator grant to JH (project number 16599). TK acknowledges support by the European Commission under the Marie Curie Intra-European Fellowship Programme in FP7. LK and JJ acknowledges support from NOVA and NWO-FAPESP grant for advanced instrumentation in astronomy. KEH and PJ acknowledge support by a Project Grant (162948–051) from The Icelandic Research Fund. AG acknowledges the financial support from the Slovenian Research Agency (research core funding No. P1-0031 and project grant No. J1-8136). CT acknowledges support from a Spanish National Research Grant of Excellence under project AYA 2014-58381-P and funding associated to a RamÃ±n y Cajal fellowship under grant number RyC-2012-09984. AdUP acknowledges support from a RamÃ±an y Cajal fellowship, a BBVA Foundation Grant for Researchers and Cultural Creators, and the Spanish Ministry of Economy and Competitiveness through project AYA2014-58381-P. ZC acknowledges support from the Spanish research project AYA 2014-58381-P and support from Juan de la Cierva IncorporaciÃ³n fellowships IJCI-2014-21669. DAK acknowledges support from the Spanish research project AYA 2014-58381-P and support from Juan de la Cierva IncorporaciÃ³n fellowships IJCI-2015- 26153. RSR acknowledges AdUP’s BBVA Foundation Grant for Researchers and Cultural Creators and support from ASI (Italian Space Agency) through the Contract n. 2015-046-R.0 and from European Union Horizon 2020 Programme under the AHEAD project (grant agreement n. 654215). GL is supported by a research grant (19054) from VILLUM FONDEN. SDV acknowledges the support of the French National Research Agency (ANR) under contract ANR-16-CE31-0003 BEaPro DM acknowledges support

from the Instrument Center for Danish Astrophysics (IDA). This work made use of data supplied by the UK *Swift* Science Data Centre at the University of Leicester. Finally, it is with pleasure that we acknowledge expert support from the ESO staff at the Paranal and La Silla observatories in obtaining these target of opportunity data.

<sup>a</sup> Has Ly $\alpha$  emission in the trough. <sup>b</sup> Short burst. <sup>c</sup> Previously published in Cucchiara et al. (2015).

GRB	Hydrogen Column $\log(N_{\text{HI}}/\text{cm}^{-2})$
GRB 090809A <sup>c</sup>	21.7 ± 0.2
GRB 090926A	21.55 ± 0.10
GRB 100219A <sup>c</sup>	21.2 ± 0.2
GRB 100425A <sup>c</sup>	21.0 ± 0.2
GRB 100728B	21.2 ± 0.5
GRB 110128A	21.90 ± 0.15
GRB 110818A	21.9 ± 0.4
GRB 111008A <sup>c</sup>	22.40 ± 0.10
GRB 111107A <sup>c</sup>	21.0 ± 0.2
GRB 120119A	22.6 ± 0.2
GRB 120327A <sup>c</sup>	22.00 ± 0.05
GRB 120404A	20.7 ± 0.3
GRB 120712A	19.95 ± 0.15
GRB 120716A <sup>c</sup>	21.80 ± 0.15
GRB 120815A <sup>c</sup>	22.10 ± 0.10
GRB 120909A <sup>c</sup>	21.75 ± 0.10
GRB 121024A <sup>c</sup>	21.85 ± 0.10
GRB 121027A	22.8 ± 0.3
GRB 121201A <sup>ac</sup>	22.0 ± 0.3
GRB 121229A	21.8 ± 0.2
GRB 130408A <sup>c</sup>	21.80 ± 0.10
GRB 130427B	21.9 ± 0.3
GRB 130606A	19.91 ± 0.05
GRB 130612A	22.1 ± 0.2
GRB 131011A	22.0 ± 0.3
GRB 131117A	20.0 ± 0.3
GRB 140311A	22.40 ± 0.15
GRB 140430A	21.8 ± 0.3
GRB 140515A	19.0 ± 0.5
GRB 140614A	21.6 ± 0.3
GRB 141028A	20.60 ± 0.15
GRB 141109A	22.10 ± 0.10
GRB 150206A	21.7 ± 0.4
GRB 150403A	21.8 ± 0.2
GRB 150915A <sup>a</sup>	21.2 ± 0.3
GRB 151021A <sup>a</sup>	22.3 ± 0.2
GRB 151027B	20.5 ± 0.2
GRB 160203A	21.75 ± 0.10
GRB 160410A <sup>b</sup>	21.2 ± 0.2
GRB 161014A	21.4 ± 0.3
GRB 161023A	20.96 ± 0.05
GRB 170202A <sup>a</sup>	21.55 ± 0.10

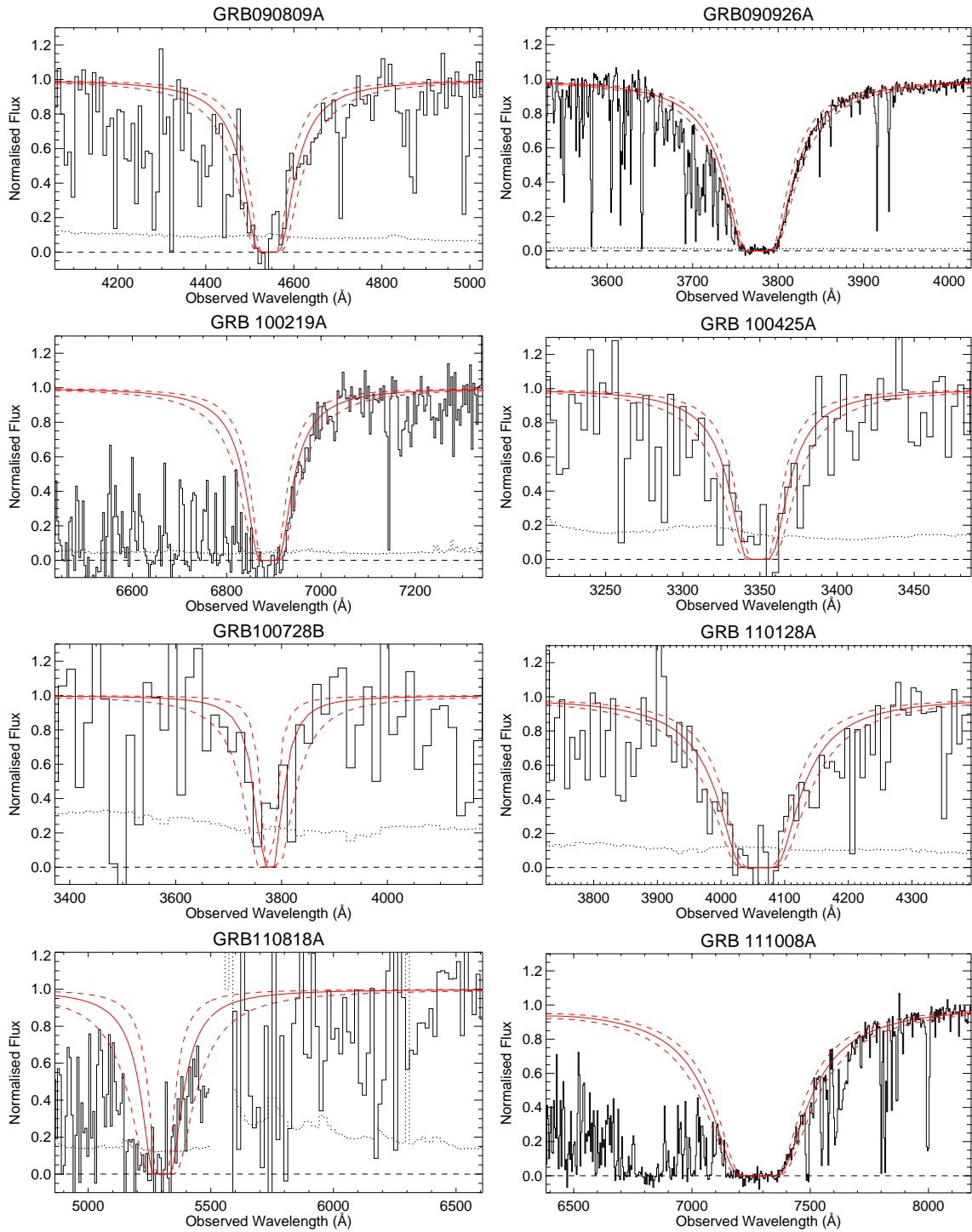


**Figure 2.10:** Measurements of the hydrogen column densities for all bursts with a clear Lyman alpha absorption system. In solid black is shown the spectrum with black dotted giving the corresponding  $1-\sigma$  error. The black dashed line shows zero flux density. The solid red line is the absorption of column density equal to the value presented in Tab. ?? with the  $1-\sigma$  interval shown with dashed lines.<sup>61</sup>

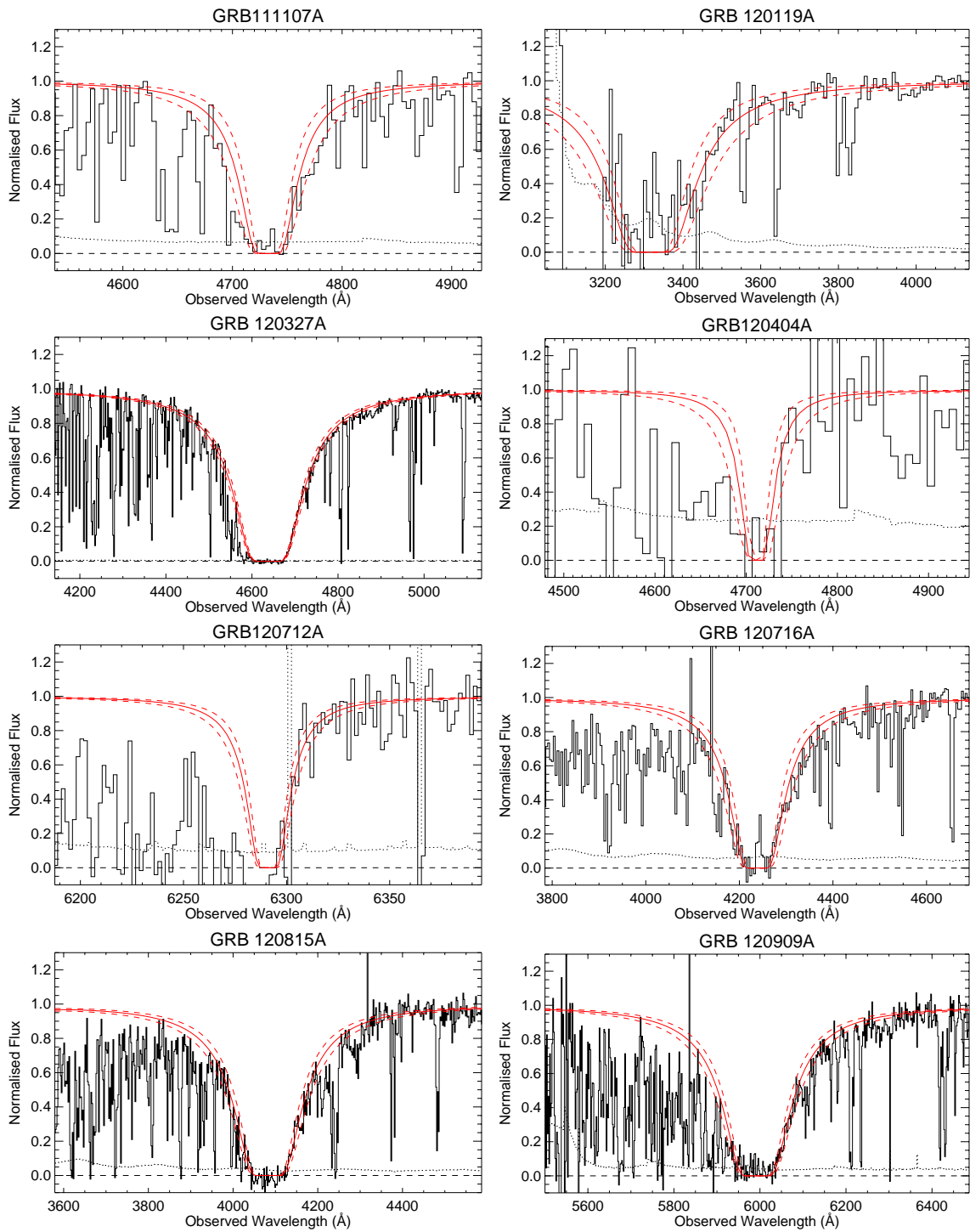


Fig. 2.10. continued.

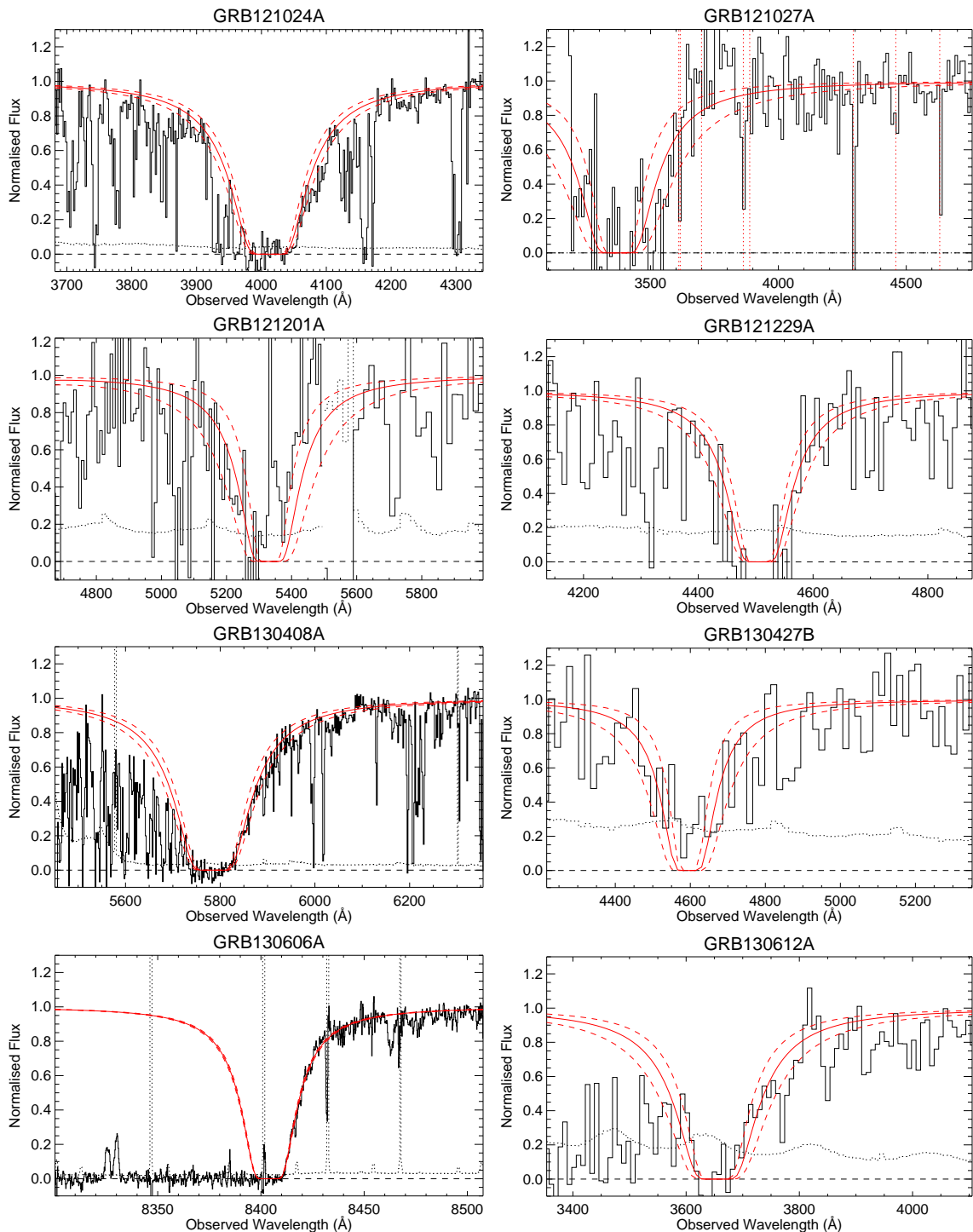


Fig. 2.10. continued.

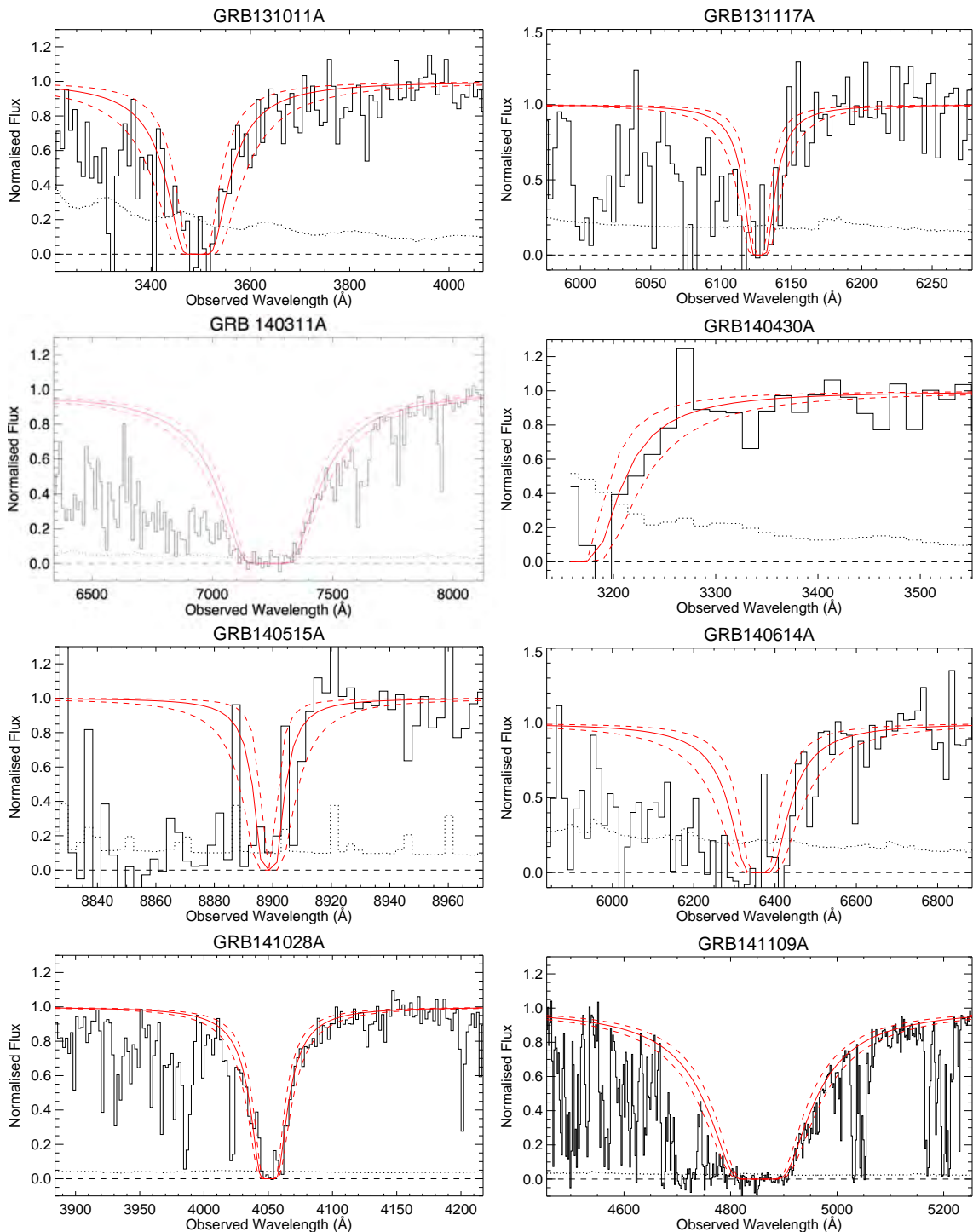


Fig. 2.10. continued.

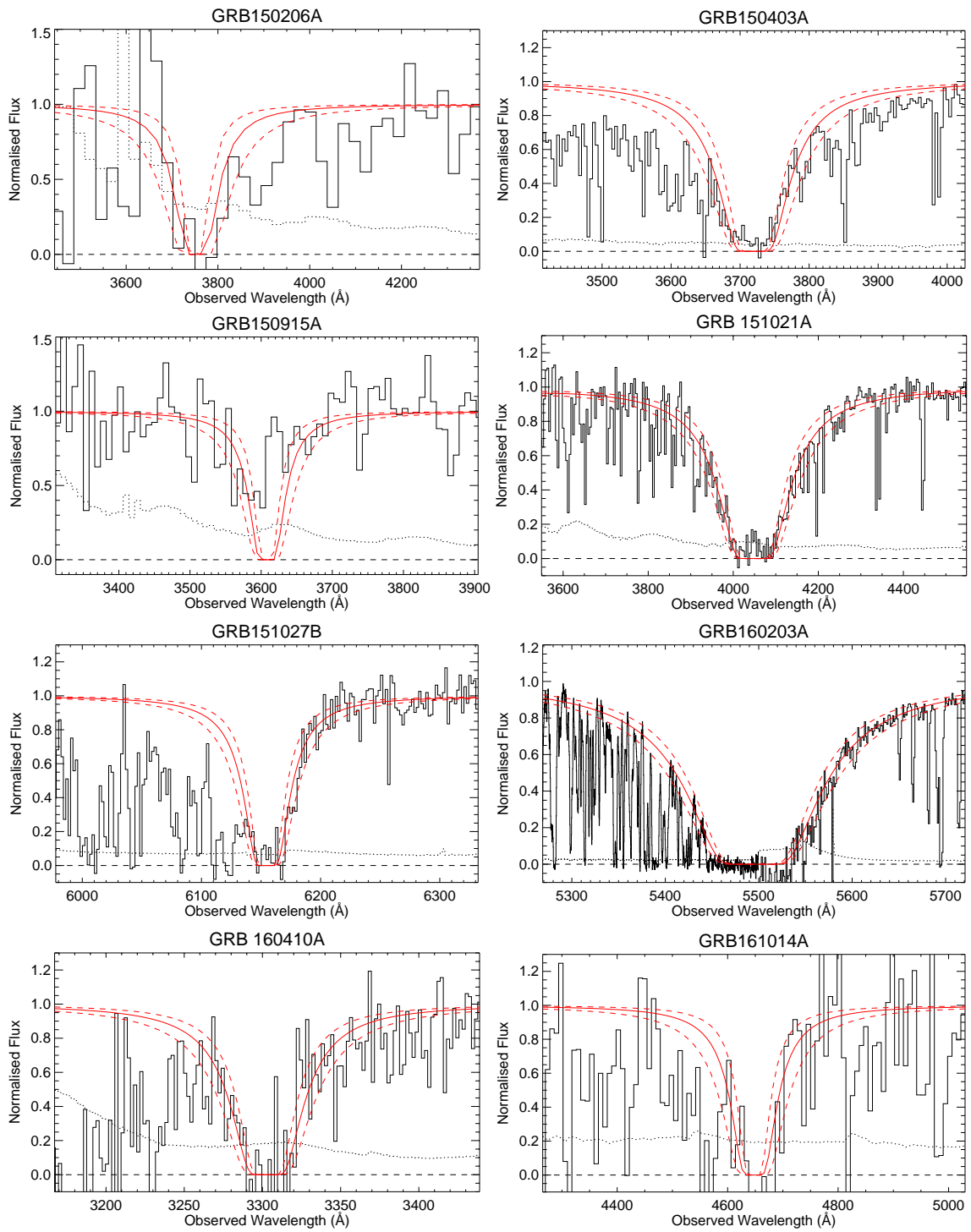


Fig. 2.10. continued.

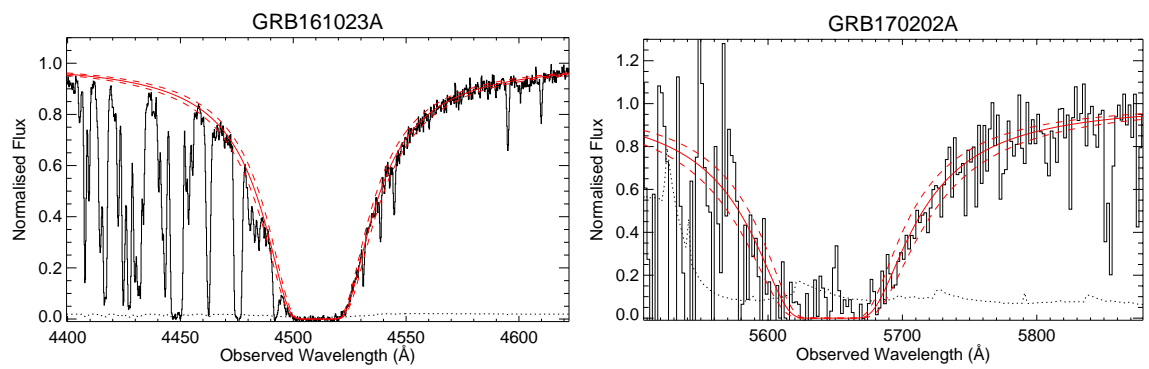


Fig. 2.10. continued.

## Appendix

### The complex error function and the Voigt profile

When modeling the spectral PSF, we need to evaluate the Voigt-profile. The Voigt profile, which is the convolution of the Gaussian and Lorentzian profiles, can, centered at zero, be written as ([Pagnini & Mainardi 2010](#))

$$\begin{aligned}
V(\lambda, \sigma, \gamma) &= G(\lambda, \sigma) \otimes L(\lambda, \gamma) \\
&= \int_{-\infty}^{\infty} G(\xi, \sigma) L(\lambda - \xi, \gamma) d\xi \\
&= \int_{-\infty}^{\infty} \frac{1}{\sqrt{2\pi}\sigma} e^{-\left(\frac{\xi}{\sqrt{2}\sigma}\right)^2} \frac{1}{\gamma\pi} \frac{\gamma^2}{(\lambda - \xi)^2 + \gamma^2} d\xi \\
&= \frac{\gamma}{\sqrt{2}\sigma} \frac{1}{\pi^{3/2}} \int_{-\infty}^{\infty} \frac{e^{-\left(\frac{\xi}{\sqrt{2}\sigma}\right)^2}}{(\lambda - \xi)^2 + \gamma^2} d\xi.
\end{aligned} \tag{2.1}$$

We can by making the following substitution,  $\xi = \sqrt{2}\sigma$  and  $d\xi = \sqrt{2}\sigma dt$ , write it as

$$\begin{aligned}
V(\lambda, \sigma, \gamma) &= \frac{\sqrt{2}\sigma}{\sqrt{\pi}} \frac{\frac{\gamma}{\sqrt{2}\sigma}}{\pi} \int_{-\infty}^{\infty} \frac{e^{-t^2}}{(\lambda - \sqrt{2}\sigma t)^2 + \gamma^2} dt \\
&= \frac{1}{\sqrt{2\pi}\sigma} \frac{\frac{\gamma}{\sqrt{2}\sigma}}{\pi} \int_{-\infty}^{\infty} \frac{e^{-t^2}}{\left(\frac{\lambda}{\sqrt{2}\sigma} - t\right)^2 + \left(\frac{\gamma}{\sqrt{2}\sigma}\right)^2} dt.
\end{aligned} \tag{2.2}$$

This form of the convolution is closely related to the complex probability function ([Letchworth & Benner 2007; Abrarov & Quine 2015a](#)),

$$W(z) = \frac{i}{\pi} \int_{-\infty}^{\infty} \frac{e^{-t^2}}{z - t} dt \tag{2.3}$$

for any complex argument,  $z = x + iy$ . The complex probability function can be expressed as a sum of a real and an imaginary part ([Benner et al. 1995; Abrarov & Quine 2015b](#)),

$$\begin{aligned}
W(x, y) &= K(x, y) + iL(x, y) \\
&= \frac{y}{\pi} \int_{-\infty}^{\infty} \frac{e^{-t^2}}{(x - t)^2 + y^2} dt + \frac{i}{\pi} \int_{-\infty}^{\infty} \frac{(x - t)e^{-t^2}}{(x - t)^2 + y^2} dt,
\end{aligned} \tag{2.4}$$

where the real part,  $\text{Re}[W(x, y)] = \sqrt{2\pi}\sigma V(\lambda, \sigma, \gamma)$  if  $x = \frac{\lambda}{\sqrt{2}\sigma}$  and  $y = \frac{\gamma}{\sqrt{2}\sigma}$ , which can be obtained by using the complex argument,  $z = \frac{\lambda+iy}{\sqrt{2}\sigma}$ , in the complex probability function. If  $\text{Im}[z] \geq 0$ , which is always guaranteed for the width of a spectral profile, the complex probability function equals the complex error function. The complex error function has numerous, fast,

numerical approximations where in this work we use the `scipy.special.wofz` ([Jones et al. 2001](#)) implementation.

## Notes on Individual objects

### GRB 090313 (z = 3.373)

The first GRB ever observed with X-shooter, during the commissioning of the instrument, these data formed the basis of GCN 9015 ([de Ugarte Postigo et al. 2009a](#)) and are published in [de Ugarte Postigo et al. \(2010\)](#). Due to the lingering brightness of GRB 090313, 6.9 ks spectroscopic integration starting 45 hours after the BAT trigger reveals a wealth of absorption features superposed on the afterglow continuum at a common redshift of  $z = 3.373$ . Two intervening systems at  $z = 1.959$  and  $z = 1.800$  are identified based on strong Mg II-absorption. Because this burst is observed before the instrument is science-verified, it does not enter into the statistical sample.

### GRB 090530 (z = 1.266)

Observed during paranalization of the instrument, these data forms the basis of GCN 15571 ([Goldoni et al. 2013](#)), but are not published elsewhere. Observations began 20.6 hours after the BAT trigger and 4.8 ks spectroscopic integration in all three arms reveals the absorption signature for a host at  $z = 1.266$  from the detection of Mg II, Mg I, Si II, Fe II, Al III. Because this burst was observed before the instrument was science-verified, it does not enter into the statistical sample.

### GRB 090809 (z = 2.737)

Observed during the first science verification period and was reported in GCN 9761 ([Malesani et al. 2009a](#)) and is additionally used as the basis for the master thesis by Ása Skúladóttir (2010). 7.2 ks integration starting 10.2 hours after the GRB trigger yields a clear afterglow continuum in all arms. The simultaneous detection of absorption lines identified as Ly $\alpha$ , Si II, O I, Si I\*, Si IV, C IV, Fe II, Al II, Al III and Mg II at  $z = 2.737$  sets it as the redshift of the GRB. Because this burst is observed before the instrument was science-verified, it does not enter into the statistical sample.

### GRB 090926A (z = 2.106)

Obtained during the second science verification period, this dataset forms the basis of GCN 9942 ([Malesani et al. 2009b](#)) and is additionally published in [D'Elia et al. \(2010\)](#). Spectroscopic integration started 22 hours after the BAT trigger and from the acquisition camera the optical afterglow is measured to R = 17.9 mag at the beginning of the observations which causes a strong continuum to be seen in all arms. An absorption trough due to Ly $\alpha$  is clearly visible along with

numerous metal resonance lines C IV, Si II, Si II\* Fe II, Mg II, all at  $z = 2.106$ . Because this burst was observed before the instrument was science-verified, it does not enter into the statistical sample.

### **GRB 091018 (z = 0.971)**

The first burst observed during normal operation after science verification was completed and the first burst that enters the statistical sample. These data are the basis for GCN 10042 ([de Ugarte Postigo et al. 2009b](#)) and is published in [Wiersema et al. \(2012a\)](#). With a bright afterglow and a rapid follow-up, this spectrum is of pristine quality. The afterglow continuum is bright throughout all spectroscopic arms which allows the ready detection of Al II, Al III, Fe II, Mn II, Mg II, Mg I, and Ca II - all located at  $z = 0.971$ , setting it as the redshift of the GRB.

### **GRB 091127 (z = 0.490)**

Obtained 4 days after the burst trigger, these data forms the basis for GCN 10233 ([Thöne et al. 2009](#)) and are published in [Vergani et al. \(2011a\)](#). Due to the late follow-up and a nearby moon, the signal-to-noise of the afterglow continuum is low, especially in the UVB arm. This is why no clear absorption lines are detected against the afterglow continuum, although see [Vergani et al. \(2011a\)](#) which report a tentative detection of Mg II. Emission lines from the underlying host are clearly visible with lines from [O II], H $\beta$ , [O III], and H $\alpha$  all at  $z = 0.490$ . This bursts is additionally associated with SN2009nz ([Cobb et al. 2010; Berger et al. 2011; Olivares E. et al. 2015](#)).

### **GRB 100205A (z = na)**

Observed 3 days after the *Swift* trigger. No afterglow or host detected is in 10.8 ks. The GRB is likely located at high redshift (GCN GCN10399; [Perley et al. 2010](#)). The spectrum has not otherwise been published previously.

### **GRB 100219A (z = 4.667)**

These data presented here have also formed the basis of GCN 10441 ([Groot et al. 2010](#)) and are published in [Thöne et al. \(2013\)](#). Observations started 12.5 hours after the *Swift* trigger and has a total exposure time of 4.8 ks. Absorption features, including those of Ly $\alpha$  and from a multitude of ions are detected against the afterglow continuum at  $z = 4.667$ . Additionally, absorption from an intervening system is found at  $z = 2.181$ .

### **GRB 100316B (z = 1.180)**

The data presented here also formed the basis of GCN 10495 ([Vergani et al. 2010a](#)). The spectrum has not otherwise been published. Observations started 44 minutes after the *Swift* trigger and have a total exposure time of 2.4 ks. Absorption features from Fe II, Al II, Al III, Mg II and Mg I are well detected against the afterglow continuum at  $z = 1.180$ . Additionally, strong absorption lines from Fe II and Mg II from an intervening system are found at  $z = 1.063$ .

### **GRB 100316D (z = 0.059)**

The data presented here also formed the basis of GCN 10512 ([Vergani et al. 2010b](#)), GCN 10513 ([Vergani et al. 2010c](#)), GCN 10543 ([Bufano et al. 2010](#)) and are published in [Bufano et al. \(2012\)](#) and [Starling et al. \(2011\)](#). This GRB is very close by and has an associated SN, SN2010bh, and has therefore undergone intense follow-up ([Olivares E. et al. 2012](#); [Cano et al. 2011](#); [Izzo et al. 2017](#)). The spectra presented here consists of a subset of the entire VLT/X-shooter campaign, covering the four first observing days while the afterglow still contributes significantly to the total emission. The first observations started 10 hours after the burst, before the SN was discovered, and targeted the star-forming 'A'-region ([Starling et al. 2011](#)), not the GRB. A very rich spectrum containing a multitude of emission lines puts the host at  $z = 0.059$ . For three consecutive nights, 58, 79 and 101 hours after the *Swift* trigger, the afterglow was observed as it transitioned into the spectrum of a high-velocity Ic-BL SN. The observations taken 79 and 101 hours after the burst are taken under programme 084.D-0265(A) (PI: Benetti), but with an identical setup to the first two observations.

### **GRB 100418A (z=0.624)**

The data presented here also formed the basis of GCN 10620 ([Antonelli et al. 2010](#)) and GCN 10631 ([Malesani & Palazzi 2010](#)) and are published in [de Ugarte Postigo et al. \(2011a\)](#). The burst has been followed up in three epochs of observations, 0.4, 1.4, and 2.4 days after the burst, each lasting 4.8 ks. The unambiguous redshift of the host,  $z = 0.624$ , is found from the simultaneous detection of emission features belonging to nebular lines, including H I, [O II], [O III], [Ne III], N II, [S II], [S III], and He I as well as absorption features due to the presence of Zn II, Cr II, Fe II, Mn II, Mg II, Mg I, Ti II, and Ca II, all at a consistent redshift. Temporal evolution of the fine structure lines belonging to Fe II\* is found between the epochs.

### **GRB 100424A (z=2.465)**

The data presented here also formed the basis of GCN 14291 ([Malesani et al. 2013b](#)). The spectrum has not otherwise been published. Observations were carried out long after the burst afterglow

had faded. Emission lines from the host are detected at  $z = 2.465$ .

### **GRB 100425A (z=1.1755)**

The spectra presented here also formed the basis of GCN 10684 ([Goldoni et al. 2010](#)) and are used in Skuladottir (2010), but not published elsewhere. Observations started 4 hours after the *Swift* trigger, totaling 2.4 ks. Absorption features from Mg II and Fe II in the afterglow continuum are detected at  $z = 1.1755$ .

### **GRB 100615A (z=1.398)**

The data presented here also formed the basis of GCN 14264 ([Kröhler et al. 2013b](#)), but are not published elsewhere. Host observation of a dark burst ([D'Elia & Stratta 2011](#)) taken long after the afterglow had faded. Emission lines from the host belonging to [O II], [Ne III], [O III] and H $\alpha$  are detected at a common redshift of  $z = 1.398$ .

### **GRB 100621A (z=0.542)**

The data presented here also formed the basis of GCN 10876 ([Milvang-Jensen et al. 2010](#)), but are not published elsewhere. Beginning 7.1 hours after the GRB, 2.4 ks observations reveal emission lines from [O II], H $\beta$  and [O III] at a common redshift of  $z = 0.542$  and a very weak afterglow continuum.

### **GRB 100625A (z=0.452)**

The data presented here is of the candidate host galaxy, taken long after the burst had faded and have not previously been published. 4.8 ks of exposure reveals a weak continuum present in all arms, but an absence of emission lines. This could indicate that the host primarily contains an older stellar population. The redshift,  $z = 0.452$ , is taken from [Fong et al. \(2013\)](#).

### **GRB 100724A (z = 1.288)**

The data presented here also formed the basis of GCN 10971 ([Thöne et al. 2010](#)). The spectrum has not otherwise been published previously. The observations were carried out in RRM starting 11 min after the GRB trigger. See section [2.2.3](#), for a description of the RRM scheme. Absorption lines from several ionic species are detected in the afterglow continuum at a common redshift of  $z = 1.288$ .

### **GRB 100728B (z=2.106)**

The data presented here also formed the basis of GCN 11317 ([Flores et al. 2010](#)). The spectrum has not otherwise been published previously. Starting 22 hours after the burst trigger, 7.2 ks of observations reveals a faint afterglow continuum with Ly $\alpha$ - and Mg II-absorption at  $z = 2.106$ . Due to a malfunctioning ADC, the sensitivity of X-shooter is depressed with respect to normal operations, resulting in a lower throughout. Additionally, the position of the trace on the slit moves due to atmospheric differential refraction. The presence of the DLA is confirmed in the 2D image and despite the observational challenges that affects this spectrum, we measure  $\log(N_{\text{HI}}/\text{cm}^{-2}) = 21.2 \pm 0.15$ .

### **GRB 100814A (z=1.439)**

The spectra presented here has not been published previously. The observations consist of three visits, the first beginning only 0.9 hours after the *Swift* trigger, the other two visits were 2.13 and 98.40 hours after the trigger, respectively. A bright afterglow continuum is present in all visits, allowing identification of absorption features belonging to a wide range of ions at  $z = 1.439$ . A complex velocity structure in the absorption features belonging to Mg II, shows several components, separated by as much as 500 km/s, pointing to a likely merger scenario in the host or starburst driven outflows.

### **GRB 100816A (z=0.805)**

The data presented here also formed the basis of GCN 11123 ([Tanvir et al. 2010](#)). The spectrum has not otherwise been published previously. This short GRB was observed 28.4 hours after the GRB trigger. 4 x 1200 s of exposure reveals two distinct sets of emission lines, spatially offset  $\lesssim 1''$ , very close in redshift space,  $z = 0.8034$  and  $z = 0.8049$ , indicating either an interacting host or some complex velocity structure of the host. Faint underlying continua are present under both sets of emission lines.

### **GRB 100901A (z=1.408)**

The data presented here have been published in [Hartoog et al. \(2013a\)](#). Because of the unusual lingering brightness of this GRB, 2.4 ks of observations taken 65.98 hours after the GRB trigger still reveals an afterglow continuum visible across the entire spectral coverage of X-shooter. Absorption lines from a wide range of ions sets the redshift at  $z = 1.408$ , with intervening absorption systems at  $z = 1.3147$  and  $z = 1.3179$ .

### **GRB 101219A (z=0.718)**

These data have not been published before. Starting 3.7 hours after the GRB trigger, 7.2 ks of exposure time reveal a very faint continuum in the visual and near-infrared, only visible when heavily binning the images. No redshift estimate is available from these observations. Late-time Gemini-North observations reveal emission lines from the host at  $z = 0.718$  ([Chornock & Berger 2011](#)).

### **GRB 101219B (z=0.552)**

The data presented here also formed the basis of GCN 11579 ([de Ugarte Postigo et al. 2011b](#)) and are published in [Sparre et al. \(2011a\)](#). The first observation, taken 11.6 hours after the burst trigger and lasting 4.8 ks, reveals absorption from Mg II and Mg I in the host located at  $z = 0.552$  on a featureless continuum visible across the entire coverage of X-shooter. Subsequent observations taken 16 and 37 days after the trigger shows the fading spectral signature of a SN, SN2010ma.

### **GRB 110128A (z=2.339)**

These observations form the basis of GCN 11607 ([Sparre et al. 2011b](#)), but have not been published before. Spectroscopic integration started 6.55 hours after the *Swift* trigger and lasted for a total of 7.2 ks. The afterglow continuum is detected across the entire spectral coverage at moderate signal-to-noise. Absorption lines in the continuum are detected from Ly $\alpha$ , O I, C II, Si IV, C IV, Si II and Fe II, all at a common redshift of  $z = 2.339$ . From the broad Ly $\alpha$  trough, a hydrogen column density  $\log(N_{\text{HI}}/\text{cm}^{-2}) = 22.6 \pm 0.2$  is derived. An intervening system at  $z = 2.20$  is tentatively identified from an absorption feature, likely due to C IV.

### **GRB 110407A (z=na)**

These observations have not been published before. Starting 12.36 hours after the BAT trigger, 4.8 ks spectroscopic integration yields a very faint trace down to  $\sim 430$  nm, only visible after binning heavily. This could indicate a redshift,  $z \sim 2.5$ , but no emission lines or absorption lines are immediately visible to support this.

### **GRB 110709B (z=2.109)**

This is a late-time observation ( $> 1$  year) and has previously been used in [Perley et al. \(2016a\)](#). In this reduction of the 7.2 ks spectroscopic integration, the tentative detection of [O III] reported in [Perley et al. \(2016a\)](#) is confirmed along with low-significance detection of H $\alpha$  at the end of the spectral coverage, both at a consistent redshift,  $z = 2.109$ , securing it as the redshift of the GRB host.

### **GRB 110715A (z=0.823)**

These observations, starting 12.3 hours after the trigger, have been published in [Sánchez-Ramírez et al. \(2017\)](#) and additionally formed the basis of GCN 12164 ([Piranomonte et al. 2011](#)). Only a single exposure of 600 s was obtained, before strong winds interrupted the observations. A red continuum is detected across all arms and a multitude of absorption lines are superposed on the afterglow continuum. We identify lines belonging to Al II, Al III, Zn II, Cr II, Fe II, Mg II, Mg I, Ca II, and Ca III, all at  $z = 0.823$ , marking it as the redshift of the GRB.

### **GRB 110721A (z=0.382)**

This is a Fermi burst with a LAT detection and thus outside the statistical sample, but nonetheless followed up due to the extremely high peak energy ([Axelsson et al. 2012](#)). Starting 28.7 hours after the burst trigger, 2.4 ks spectroscopic observation reveals after heavy binning, a wide, faint trace down to  $\sim 580$  nm, offset by 2.5" relative to the centering of the slit. No good redshift measurement can be inferred from this. We have adopted the redshift from GCN 12193 ([Berger 2011b](#)).

### **GRB 110808A (z=1.348)**

This spectrum has already formed the basis of GCN 12258 ([de Ugarte Postigo et al. 2011c](#)), but is not published otherwise. Starting 3 hours after the *Swift* trigger, a rich spectrum is obtained in 2.4 ks spectroscopic integration. The GRB afterglow continuum is visible across all three spectroscopic arms of VLT/X-shooter with emission lines identified as [O II], [O III], H $\alpha$  all at  $z = 1.348$ . At the same redshift, we identify absorption lines superposed on the afterglow continuum from Mg II and Fe II.

### **GRB 110818A (z=3.36)**

Starting 6.15 hours after the BAT trigger, spectroscopic integration for 4.8 ks reveals a moderate signal-to-noise GRB afterglow continuum, down to  $\sim 500$  nm. The simultaneous detection of absorption features identified as Ly $\alpha$ , Si II, C IV, Al II, Ca H, Ca K, and Mg II, and emission from the [O III]-doublet, securely sets  $z = 3.36$  as the redshift of the GRB. These data form the basis of GCN 12284 ([D'Avanzo et al. 2011a](#)), but is not published elsewhere.

### **GRB 111005A (z=0.013)**

The data presented here have previously been published in [Michałowski et al. \(2016\)](#). 2.4 ks spectroscopic integration of the host galaxy, obtained long after the burst had faded, contains bright emission lines filling the entire slit on top of a broad, underlying stellar continuum. We

identify emission lines from [O II], H $\delta$ , H $\gamma$ , H $\beta$ , [O III], N II, H $\beta$ , [S II], Ar III, and [S III], all at  $z = 0.013$ . Significant velocity structure of the lines across the spatial direction of the slit indicates a large degree of coherent motion relative to the line-of-sight.

### GRB 111008A (z=4.989)

These data formed the basis of GCN 12431 ([Wiersema et al. 2011](#)) and are additionally published in [Sparre et al. \(2014\)](#). Observations of this GRB afterglow were initiated 7.71 hours after the BAT trigger and had a duration of 8.4 ks. A second observational epoch started 20.1 hours after the GRB trigger and lasted for 6.6 ks. The GRB afterglow continuum is well detected down to  $\sim 760$  nm, with several strong absorption features imprinted, all at a common  $z = 4.990$ . Ly $\alpha$  is clearly detected and we additionally detect lines identified as Si II, Fe II, C IV, Mg II, Si II\*, S II\*, O I\*. An intervening DLA system is additionally detected at  $z = 4.61$  as seen from Ly $\alpha$  and Mg II absorption.

### GRB 111107A (z=2.893)

GCN 12542 ([D'Avanzo et al. 2011b](#)) is based on this spectrum, but it is not published elsewhere. Spectroscopic integration started 5.26 hours after the *Swift* trigger and consists of  $4 \times 1200$  s integration in the UVB and VIS and  $16 \times 300$  s in NIR, the observations ending in twilight. The GRB afterglow continuum is well detected across the arms with absorption lines from Ly $\alpha$ , C IV, Fe II, and Mg II, all at a consistent redshift of  $z = 2.893$ . Additionally an intervening Mg II system is detected at  $z = 1.998$ . From the Ly $\alpha$  absorption trough, we additionally infer  $\log(N_{\text{HI}}/\text{cm}^{-2}) = 21.0 \pm 0.2$ .

### GRB 111117A (z=2.211)

These data have previously been used to form some of the basis of [Selsing et al. \(2018b\)](#). Starting 37.3 hours after the BAT trigger, 4.8 ks of spectroscopic integration yields faint emission lines identified at [O II], H $\beta$ , [O III] and H $\alpha$ , all at a common  $z = 2.211$ , marking it as the redshift of the GRB host. No afterglow continuum is detected. This is the highest redshift short GRB detected to date.

### GRB 111123A (z=3.151)

These data formed the basis of GCN 14273 ([Xu et al. 2013b](#)), but are not published elsewhere. Observed twice, the first time shortly after the GRB and the second long after the burst had faded, securely sets the redshift of the host at  $z = 3.151$  based on the detection of emission lines identified as [O II] and [O III].

### **GRB 111129A (z=1.080)**

Starting 8.26 hours after the GRB trigger and lasting 3.6 ks, these observations have previously been published in Krühler et al. (2015a). A very faint continuum is visible after severe binning and a redshift is suggested in Krühler et al. (2015a), based on the detection of [O II]. At this redshift, H $\beta$  and [O II] are located in the gap between the VIS and NIR arm and H $\alpha$  is located in the middle of the *JH*-bandgap and is therefore not detected.

### **GRB 111209A (z=0.677)**

These spectra have previously been used in Levan et al. (2013); Greiner et al. (2015); Krühler et al. (2015a); Kann et al. (2017) and additionally formed the basis for GCN 12648 (Vreeswijk et al. 2011). The first epoch of spectroscopic observations was initiated 17.7 hours after the BAT trigger and lasted for 4.8 ks. A very bright afterglow continuum is detected across the entire spectral coverage of X-shooter, with several absorption features imprinted. The absorption features are identified as Fe II, Mg II, Mg I, Ca H, and Ca K - all at a common redshift of  $z = 0.677$ . The second epoch, taken 20 days later, still contains a faint continuum detected across all arms. The detection of nebular emission lines identified as [O II], [O III] and H $\alpha$  at the same redshift, securely marks it at the redshift of this ultra-long GRB with accompanying GRB-SN.

### **GRB 111211A (z=0.478)**

These data formed the basis for GCN 12677 (Vergani et al. 2011b) and are also published in Krühler et al. (2015a). Observations began 31 hours after the AGILE trigger and consisted of  $4 \times 600$  s. A bright GRB afterglow continuum is detected across the entire spectral coverage of X-shooter with absorption and emission features visible. We identify absorption features due to Fe II, Mg II, and Ca II and emission lines from [O III] and H $\alpha$ , all at a common  $z = 0.478$ , which we suggest is the redshift of the GRB. Additionally detected in the GRB afterglow continuum are broad undulation, suggesting an accompanying SN.

### **GRB 111228A (z=0.716)**

These data formed the basis of GCN 12770 (Schulze et al. 2011) and are also published in Krühler et al. (2015a). Observations began 15.9 hours after the BAT trigger and consist of  $4 \times 600$  s. The GRB afterglow continuum is clearly detected in all the spectroscopic arms and superposed on the continuum are absorption features identified as due to Fe II, Mn II, Mg II, Mg I, Ca H, and Ca K, all at  $z = 0.716$ . Supporting this redshift measurement as the redshift of the GRB is the detection of nebular emission from [O III].

### **GRB 120118B (z = 2.943)**

The data presented here also formed the basis of GCN 14225 ([Malesani et al. 2013a](#)), but are not published otherwise. This late-time observation of the host of GRB 120118B consists of 3.6 ks exposures and contains emission lines belonging to [O II] and [O III] at  $z = 2.943$ , suggested to be redshift of the host.

### **GRB 120119A (z = 1.728)**

The data presented here have been examined by [Japelj et al. \(2015\)](#) and Zafar et al. (submitted), who both find a significant amount of extinction,  $A_V \approx 1$  mag, also supported by previous measurements ([Morgan et al. 2014](#)). Three epochs of observations have been obtained, the first two immediately after the burst, and the last one long after the afterglow had faded. Starting 1.4 hours after the *Swift* trigger, the first epoch contains bright afterglow continuum. Rich in absorption features belonging to a multitude of ions at  $z = 1.728$  is estimated for the host with intervening systems at  $z = 1.476$ ,  $z = 1.214$ ,  $z = 0.662$  and  $z = 0.632$ . The second epoch, obtained 4.5 hours after the burst contains the fading afterglow. A third epoch is obtained  $> 1$  year after the GRB in which emission lines from H $\beta$  and H $\alpha$  are found at the redshift of the host, confirming the association of the absorption line system and the host. We also detect C I in absorption which indicates the presence of cold gas.

### **GRB 120211A (z = 2.346)**

The data presented here have been published in [Krühler et al. \(2015a\)](#). Two observations of the host of GRB 120211A has been obtained, starting 2013.02.17,  $> 1$  year after the burst has faded. A redshift for this object has been reported by [Krühler et al. \(2015a\)](#) and the features seen by those authors are reproduced in these reductions, confirming  $z = 2.346$ .

### **GRB 120224A (z = 1.10)**

The data presented here have formed the basis of GCN 12991 ([Wiersema et al. 2012b](#)), and have also been published in [Krühler et al. \(2015a\)](#). Starting 19.8 hours after the GRB trigger, a total exposure time of 2.4 ks reveals a faint continuum, starting at  $\sim 700$  nm and extending all the way through 2500 nm. In the 2D-spectrum we detect a  $\sim 2\sigma$  emission line which, if interpreted as H $\alpha$ , gives  $z = 1.10$ , supporting the photometric redshift ( $0.9 < z_{\text{phot}} < 1.3$ ) derived by [Krühler et al. \(2015a\)](#).

### **GRB 120311 (z = 0.350)**

The data presented here have formed the basis of GCN 12991 ([Wiersema et al. 2012b](#)), but are not published otherwise. Starting just before twilight, 3.65 hours after the burst, a faint afterglow continuum is detected at all wavelengths. Due to the faintness of the afterglow, no absorption features are discernible superposed on the continuum. Displaced from the afterglow continuum by  $1''.4$ , emission lines belonging to H $\beta$ , [O III] and H $\alpha$  are detected at  $z = 0.350$ . The line belonging to H $\alpha$  shows some extended emission toward the afterglow continuum. The angular distance between the two sources correspond to a projected distance in the host plane of 6 kpc, posing a potential problem for the host redshift, unless the GRB occurred in a merging system. The extended emission in H $\alpha$ , supports this interpretation. This burst is not a part of the statistical sample.

### **GRB 120327A (z = 2.813)**

The data presented here also formed the basis of GCN 13134 ([Krühler et al. 2012b](#)) and are published in [D'Elia et al. \(2014\)](#). The observation consists of two visits, 2.13 hrs and 29.98 hrs after the burst, with an afterglow continuum visible in all arms for both visits. We detect absorption features from Ly-limit, Ly $\alpha$ , C II/C II\*, Si II/Si II\*, Al I, Fe II and Mg II at a consistent redshift,  $z = 2.813$ .

### **GRB 120404A (z = 2.876)**

The data presented here have formed the basis of GCN 13227 ([D'Elia et al. 2012a](#)), but are not published otherwise. 9.6 ks integration, starting 15.7 hours after the *Swift*-trigger reveals a low-intensity afterglow continuum on which absorption from Ly $\alpha$  is detected in two distinct regions at redshifts  $z = 2.876$  and  $z = 2.55$ . These absorption systems are confirmed by ionic absorption features at both of these redshifts.

### **GRB 120422A (z = 0.283)**

The data presented here also formed the basis of GCN 13257 ([Schulze et al. 2012](#)) and are published in [Schulze et al. \(2014a\)](#). Being a GRB-SN, this burst has been followed up multiple times. The data presented here only contain the first epoch in which the afterglow is still visible and before the rise of SN2012bz. Starting 16.5 hours after the burst, 4.8 ks integration time captures both the host and the burst in emission. A blue afterglow continuum is detected at all wavelengths covered by X-shooter, on which Mg II absorption at  $z = 0.283$  is found. Offset by  $1''.75$ , the host is clearly detected at a consistent redshift with a rich emission line spectrum, the lines extending towards to burst.

### **GRB 120712A (z = 4.175)**

The data presented here also formed the basis of GCN 13460 ([Xu et al. 2012](#)), but are not published elsewhere. 4.8 ks integration time, starting 10.5 hours after the BAT trigger, shows a bright afterglow continuum starting at  $\sim 472$  nm, signifying the onset of the Lyman alpha forest, for a GRB located at  $z = 4.175$ . Absorption features from Ly $\alpha$ , Fe II, Mg II and Si II are readily detected at a consistent redshift.

### **GRB 120714B (z = 0.398)**

The data presented here also formed the basis of GCN 13477 ([Fynbo et al. 2012a](#)) and are discussed in Klose et al. (submitted), but are not published anywhere. Observations of this burst started 7.8 hours after the GRB trigger, lasting 4.8 ks. A continuum is visible across the entire spectral coverage of X-shooter, with both emission lines from [O II], H $\beta$ , [O III] and H $\alpha$ , as well as absorption from Mg II detected at  $z = 0.398$ , securely setting it as the redshift of the GRB.

### **GRB 120716A (z = 2.486)**

The data presented here also formed the basis of GCN 13494 ([D'Elia et al. 2012b](#)), but are not published elsewhere. Despite observations starting 62 hours after the *Swift* trigger and lasting 3.6 ks, a bright afterglow is clearly seen, along with a plethora of absorption features. Absorption of Ly $\alpha$ -photons in the host leaves a broad trough, beyond which the Lyman alpha forest is visible bluewards, all the way down to the Lyman limit. Metal absorption lines from C II, Si II, O I, Fe II, C IV, Si IV, including fine structure transitions identified as C II\*, Si II\*, Fe II\* and metastable Ni II lines are all detected at  $z = 2.486$

### **GRB 120722A (z = 0.959)**

The data presented here also formed the basis of GCN 13507 ([D'Elia et al. 2012c](#)), but are not published elsewhere. In 4.8 ks integration time, starting 10 hours after the burst trigger, the simultaneous detection of absorption features belonging to Mg II and Fe II superposed on a blue continuum, and emission lines from [O II], H $\gamma$ , H $\beta$ , [O III] and H $\alpha$ , all at  $z = 0.959$ , confidently sets it as the redshift of the GRB.

### **GRB 120805A (z = 3.9)**

A separate reduction of this burst has been published in [Krühler et al. \(2015a\)](#), but is not used otherwise. Starting 9 days after the burst trigger, this is a host observation and does not contain any afterglow continuum. In 3.6 ks integration time, we detect a faint continuum visible from 450 nm and all the way through 2100 nm, in contrast to what is found previously. The continuum

from 450 - 600 nm is detected at very low significance. If the drop at 450 nm is the Lyman limit, this fits with Lyman alpha at  $\sim 600$  nm, giving  $z \sim 3.9$ . The absence of nebular lines is due to [O II] falling in a telluric absorption band and the rest of the strong nebular lines being shifted out of the wavelength coverage.

### **GRB 120815A (z = 2.358)**

Not a part of the statistical sample, this burst also formed the basis of GCN 13649 ([Malesani et al. 2012](#)) and is published in [Krühler et al. \(2013a\)](#). Observations started 1.69 hours after the BAT trigger and consist of 2.4 ks integration. A bright afterglow continuum is detected across the entire spectral coverage of X-shooter, with a multitude of absorption lines superposed. Absorption features from the host at  $z = 2.358$  include a DLA as well as metal absorption lines from N V, S II, Si II, O I, C IV, Si IV, Fe II, Al II, Al III, Mn II, Mg II, and Mg I. Also fine structure lines from Ni II and Fe II are excited in the local environment of the GRB. Additionally, this spectrum is one of the rare cases in which we detect lines from molecular hydrogen, H<sub>2</sub>. From the Ly $\alpha$ -line we measure  $\log(N_{\text{HI}}/\text{cm}^{-2})=22.1 \pm 0.10$ . Intervening systems are found at  $z = 1.539$ ,  $z = 1.693$ , and  $z = 2.00$ .

### **GRB 120909A (z = 3.929)**

The data presented here have formed the basis of GCN 13730 ([Hartoog et al. 2012](#)), but are not published otherwise. Follow-up, started only 1.7 hours after the BAT trigger. This 1.2 ks observation captures a very bright afterglow continuum, starting at 450 nm, signifying the onset of the Lyman limit for a system at  $z = 3.929$ . Absorption from high-column density hydrogen leaves very prominent absorption features in the form of Ly $\alpha$ , Ly $\beta$ , and Ly $\gamma$ , visible in the Lyman alpha forest. Metal absorption lines arising from Fe II, Ni II, Si II, S II, Al II, Al III, C II, O I, C IV, and Zn II are all detected along with the corresponding fine structure lines (Fe II\*, Si II\*, O I\*, O I\*\*\*, C II\*), securely anchoring the redshift of the host.

### **GRB 120923A (z = 7.84)**

This spectrum has previously been published in [Tanvir et al. \(2017a\)](#). Starting 18.5 hours after the BAT trigger, the final spectrum is based on  $2 \times 4 \times 1200$  s spectroscopic integration for a total of 160 minutes. Nothing is immediately visible in the 2D-spectra, however after severe binning in the dispersion direction, a faint trace shows up in the NIR arm, suggesting a very high redshift. We here adopt the redshift ( $z = 7.84$ ) suggested by [Tanvir et al. \(2017a\)](#).

### **GRB 121024A (z = 2.300)**

The data presented here also formed the basis of GCN 13890 ([Tanvir et al. 2012b](#)) and are published in [Friis et al. \(2015\)](#). Starting 1.8 hours after the *Swift* trigger, a bright afterglow continuum is visible across all arms. A broad absorption feature from Lyman alpha, along with narrow lines from C IV, Si II, Si IV, Fe II, S II, and Al II, as well as fine structure lines associated with Si II\* are all detected at  $z = 2.300$ , securely setting it as the redshift of the GRB.

### **GRB 121027A (z = 1.773)**

The data presented here have formed the basis of GCN 13930 ([Krühler et al. 2012c](#)), but are not published otherwise. Starting 69.6 hours after the GRB trigger, we detect the afterglow continuum at high significance in all arms with 8.4 ks integration, testifying to the brightness of this burst. The concurrent identification of emission lines from [O III] and absorption from C IV, Al II, Al III, Mg I, Mg II, and Fe II, tightly constrains the redshift of the burst to be  $z = 1.773$ .

### **GRB 121201A (z = 3.385)**

These data formed the basis for GCN 14035 ([Sanchez-Ramirez et al. 2012](#)) and are additionally published in [Krühler et al. \(2015a\)](#). These observations started 12.9 hours after the *Swift* trigger and consist of 4.8 ks spectroscopic integration under good atmospheric conditions. The GRB afterglow continuum is well detected at all arms. A broad absorption trough due to Ly $\alpha$  is visible at  $z = 3.385$ , which along with the detection of absorption features identified as Si IV, C IV, Al II, and Al III, marks it as the redshift of the GRB. In the middle of the Ly $\alpha$  trough, we additionally detect Ly $\alpha$  emission. By modelling the Ly $\alpha$  absorption, we infer  $\log(N_{\text{HI}}/\text{cm}^{-2}) = 22.0 \pm 0.3$ .

### **GRB 121229A (z = 2.707)**

These data formed the basis for GCN 14120 ([Fynbo et al. 2012b](#)), but are not published elsewhere. Taken under poor seeing conditions, a total of 4.8 ks spectroscopic integration starting 2 hours after the *Swift* trigger yields a low signal-to-noise GRB afterglow continuum in all arms. Binning the spectrum reveals broad absorption troughs, which we identify as Ly $\beta$  and Ly $\alpha$  at  $z = 2.707$ . Additionally, an intervening system at  $z = 1.658$  is detected from absorption features of Mg II. From the absorption trough due to Ly $\alpha$ , we infer  $\log(N_{\text{HI}}/\text{cm}^{-2}) = 21.7 \pm 0.2$ . Due to strong contamination in the slit, the background is slightly over subtracted, causing the background to be negative in the center of the Ly $\alpha$  trough.

### **GRB 130131B (z = 2.539)**

These data formed the basis for GCN 14286 ([Fynbo et al. 2013](#)) and are additionally published in [Krühler et al. \(2015a\)](#). This is a late-time observation, taken long after the GRB afterglow had faded. In 7.2 ks spectroscopic integration, emission lines identified as [O II] and [O III] are detected at a common  $z = 2.539$ , which we suggest is the redshift of the GRB.

### **GRB 130408A (z = 3.758)**

The data presented here also formed the basis of GCN 14365 ([Hjorth et al. 2013](#)). The spectrum has not otherwise been published previously. The observations consists of two 600 s spectra taken 1.9 hours after the burst. We detect absorption features from a wide range of ions. We also detect intervening absorption at  $z = 1.255$  and  $z = 3.248$ .

### **GRB 130418A (z = 1.222)**

GCN 14390 ([Krühler et al. 2013c](#)) is based on this spectrum, but it is not published elsewhere. Starting only 4.57 hours after the *Swift* trigger, 1.2 ks observations contain a bright GRB afterglow continuum, visible across the entire spectral coverage of X-shooter. Superposed on the afterglow continuum are absorption features which we identify as C IV, Fe II, and Mg II, caused by an absorber at  $z = 1.217$ , and additional absorption from C IV at  $z = 1.222$ . The two systems are offset by  $\sim 1500 \text{ km s}^{-1}$  and the proximity of the two absorption systems in velocity space, suggests a possible association of the two systems with peculiar velocity affecting the measured redshift. We adopt  $z = 1.222$  as the redshift of the GRB. Note, that this value is slightly different from the one reported in GCN 14390.

### **GRB 130427A (z = 0.340)**

This spectrum is also published in [Xu et al. \(2013a\)](#) and [Krühler et al. \(2015a\)](#) and additionally has formed the basis for GCN 14491 ([Flores et al. 2013a](#)). Starting 16.5 hours after the BAT trigger, these observations lasting  $2 \times 600$  s contain a very bright GRB afterglow continuum across the total spectral coverage of X-shooter. In absorption we identify features from the following metal resonance lines: Fe II, Mn II, Mg II, Mg I, Ti II and additional line absorption from Ca II and Na ID. Simultaneously, we find emission lines from H $\alpha$ , H $\beta$ , [O III], [O II]- all at common redshift of  $z = 0.340$ , which is the redshift of the GRB. This is one of the most energetic GRBs observed, and its proximity along with the associated broad-lined Type Ic SN, 2013cq has caused it to be one of the more well-studied GRBs ([Maselli et al. 2014](#); [Perley et al. 2014](#); [Ackermann et al. 2014](#)).

### **GRB 130427B (z = 2.780)**

This spectrum formed the basis of GCN 14493 ([Flores et al. 2013b](#)), but are not published otherwise. A short, 2x600 s spectroscopic integration obtained before twilight, 20.6 hours after the BAT trigger, captures a faint afterglow continuum visible across the entire spectral coverage at low signal-to-noise. Due to the low signal-to-noise, the metal lines are weak, but the broad absorption trough due to Ly $\alpha$  is detected. From the Ly $\alpha$  line we measure the redshift to be  $z = 2.780$  and provide a measure of the neutral hydrogen column density,  $\log(N_{\text{HI}}/\text{cm}^{-2}) = 21.9 \pm 0.3$ . The redshift is confirmed by the presence of Fe II absorption at a consistent redshift.

### **GRB 130603B (z = 0.356)**

This burst is the first short GRB observed with a potential associated kilonova ([Tanvir et al. 2013a](#); [Berger et al. 2013a](#)). GCN 14757 ([Xu et al. 2013c](#)) was based on this spectrum and it is additionally published in [de Ugarte Postigo et al. \(2014a\)](#). Starting 8.2 hours after the *Swift* trigger, a total of 2.4 ks spectroscopic integration was obtained. Spectral continuum is clearly detected across all arms from both host and afterglow and superposed are both absorption (Ca H & K and Mg II) and emission lines ([O II], H $\beta$ , [O III], H $\alpha$ , and [S II]), all at a consistent redshift of  $z = 0.356$ , which is the redshift of the GRB.

### **GRB 130606A (z = 5.913)**

The data presented here also formed the basis of GCN 14816 ([Xu et al. 2013d](#)) and are published in [Hartoog et al. \(2015\)](#). The observations consist of three  $2 \times 600$  s visits starting 7.1 hours after the burst at fairly high airmass. We detect absorption features from a wide range of ions at  $z = 5.913$  as well as intervening absorption at  $z = 2.3103, 2.5207, 3.4515, 4.4660, 4.5309, 4.5427, 4.6497$  and  $4.7244$ .

### **GRB 130612A (z = 2.006)**

The spectral features of this spectrum have previously been reported in GCN 14882 ([Tanvir et al. 2013c](#)), but are not published elsewhere. Starting only 1.1 hours after the *Swift* trigger,  $2 \times 600$  s spectroscopic integration captures a moderate signal-to-noise afterglow continuum across the total spectral coverage of X-shooter. At a consistent redshift of  $z = 2.006$ , absorption from the metal resonance lines Fe II, Mn II, Mg II, Mg I are identified. Additionally, Ly $\alpha$  is visible as a broad absorption trough, from which we can infer  $\log(N_{\text{HI}}/\text{cm}^{-2}) = 22.2 \pm 0.2$ , which is in the upper end of the hydrogen column density distribution. The blue part of the GRB continuum exhibits a downturn in the continuum level which could indicate the presence of a significant amount of dust along the line-of-sight.

### **GRB 130615A (z = 2.9)**

This spectrum has not previously been published. Starting only 45 minutes after the BAT trigger,  $2 \times 600$  s spectroscopic integration carried on into the beginning twilight. Observed at very high airmass with a quickly varying background, a faint afterglow trace is visible across all arms of X-shooter, down to 480 nm, which if interpreted as the break due to Ly $\alpha$  suggests  $z = 2.9$ . This supports the approximate redshift suggested in GCN 14898 ([Elliott et al. 2013b](#)).

### **GRB 130701A (z = 1.155)**

These data formed the basis for GCN 14956 ([Xu et al. 2013e](#)) and are additionally published in [Krühler et al. \(2015a\)](#). Starting 5.5 hours after the GRB trigger,  $2 \times 600$  s reveals a bright continuum visible across the entire spectral coverage of X-shooter. Superposed are absorption features which we identify as due to Fe II, Mg II, Mg I, and Ca II - all at a consistent redshift of  $z = 1.155$ , which we take to be the redshift of the GRB.

### **GRB 130925A (z = 0.347)**

This spectrum has already been used in GCN 15250 ([Sudilovsky et al. 2013](#)) and is additionally published in [Schady et al. \(2015\)](#) and [Krühler et al. \(2015a\)](#). Observations of this burst began with X-shooter 3.5 hours after the *Swift* trigger. 6 ks spectroscopic integration captures a heavily dust obscured afterglow ( $A_V = 5.9 \pm 0.7$ ; [Greiner et al. 2014](#)), with the spectrum primarily dominated by host emission lines. All the nebular lines ([O II], H $\gamma$ , H $\beta$ , [O II], H $\alpha$ , N II, [S II]) are well detected at  $z = 0.347$ , as well as those from Pa $\delta$ , Pa $\gamma$ , and Pa $\beta$ . We take this as the redshift of the GRB. This spectrum is taken under ESO programme ID: 091.A-0877(A) (PI: Schady).

### **GRB 131011A (z = 1.874)**

These data formed the basis for GCN 15330 ([Rau et al. 2013](#)), but are not published elsewhere. Starting  $\sim 1.5$  days after the Fermi-GBM trigger, 4.5 ks spectroscopic integration captures a modest signal-to-noise GRB afterglow continuum all the way down to  $\sim 320$  nm. Imprinted on the continuum are absorption features, which we identify as due to Ly $\alpha$ , Fe II, Mg II, Mg I at the same redshift, which we measure to be  $z = 1.874$ . From the broad absorption trough due to Ly $\alpha$ , we infer  $\log(N_{\text{HI}}/\text{cm}^{-2}) = 22.0 \pm 0.3$ . This spectrum is taken under ESO programme ID: 092.D-0056(A) (PI: Rau).

### **GRB 131030A (z = 1.296)**

These data has not been published before. Starting 3.4 hours after the *Swift* trigger,  $6 \times 600$  s exposure were taken under good conditions, containing a bright GRB afterglow continuum across

the entire spectral coverage of X-shooter. A myriad of absorption features are superposed on the afterglow continuum which we identify as being caused by Si IV, Si II, C IV, Al II, Al III, Zn II, Cr II, Ni II, Fe II, Ni II\*, and Fe II\* at  $z = 1.296$ . A very strong Mg II-absorber is also detected, intervening the line-of-sight at  $z = 1.164$  with lines from Si II, C IV, Al III, Al III, Fe II, Mn II, and many more.

### **GRB 131103A (z = 0.599)**

This spectrum has already been used to form the basis for GCN 15451 ([Xu et al. 2013g](#)) and is additionally published in [Krühler et al. \(2015a\)](#). Starting 5.8 hours after the BAT trigger,  $4 \times 600$  s exposure captures a modest signal-to-noise continuum across all arms. Imprinted on the continuum are absorption features identified as due to Fe II and Mg II as well as emission lines from [O II], H $\delta$ , H $\gamma$ , H $\beta$ , [O III], H $\alpha$ , and [N II]. All the lines are measured at a consistent redshift of  $z = 0.599$ , which we take as the redshift of the GRB.

### **GRB 131105A (z = 1.686)**

This spectrum has already been used in GCN 15450 ([Xu et al. 2013f](#)) and is additionally published in [Krühler et al. \(2015a\)](#). Starting only 1.3 hours after the *Swift* trigger, a total of 4.8 ks spectroscopic integration contains a low signal-to-noise GRB afterglow continuum across the entire spectral coverage of X-shooter. There are deviations from the continuum at both emission and absorption. We identify lines from H $\beta$ , [O III], and H $\alpha$  in emission and Fe II, and Mg II in absorption. All lines are at a consistent  $z = 1.686$ , which is probably the redshift of the GRB. Absorption lines at shorter wavelengths are also detected, but at low significance due to an apparent downturn in the continuum caused by the presence of dust local to the burst.

### **GRB 131117A (z = 4.042)**

This spectrum has previously been used in GCN 15494 ([Hartoog et al. 2013b](#)), but is not published in a refereed paper. Starting only 68 minutes after the BAT trigger, 4.8 ks spectroscopic integration secures afterglow continuum for this burst, which is measured to be at  $z = 4.042$ . A moderate signal-to-noise GRB afterglow continuum is detected down to  $\sim 610$  nm, signifying the onset of the Ly $\alpha$  forest, with part of the forest also visible. Metal absorption lines from Si II and Si IV are detected at a consistent redshift.

### **GRB 131231A (z = 0.642)**

This spectrum has previously been published in [Krühler et al. \(2015a\)](#) and additionally forms the basis for GCN 15645 ([Xu et al. 2014a](#)). This spectrum, observed the following year (20.2 hours

after the *Swift* trigger), consists of  $4 \times 600$  s exposures. A high signal-to-noise GRB afterglow continuum is detected all the way through the X-shooter arms. We identify absorption features imprinted in the continuum as caused by Fe II, Mg II, and Ca H & K at a consistent  $z = 0.642$ . By subtracting off the bright afterglow continuum, we readily detect emission lines arising from [O II], H $\gamma$ , H $\beta$ , [O III], and H $\alpha$  in the GRB host galaxy. This GRB is the subject of a forthcoming work Kann et al. (in prep).

### **GRB 140114A (z = 3.0)**

This spectrum has previously been published in Krühler et al. (2015a). This is a late time observation, taken long after the GRB had faded. Despite a long integration time of 5.4 ks, no clear features stand out to clearly secure a redshift measurement. By heavily binning the spectrum, a faint trace is visible down to 485 nm, which if interpreted at the onset of Ly $\alpha$  signifies  $z \sim 3$ . We adopt the redshift inferred in Krühler et al. (2015a).

### **GRB 140213A (z = 1.208)**

The data presented here also formed the basis of GCN 15831 (Schulze et al. 2014b) and are additionally published in Krühler et al. (2015a). Starting 5.8 after the *Swift* trigger alert,  $2 \times 600$  s spectroscopic integration contains a high signal-to-noise GRB afterglow continuum across the entirety of X-shooter. Imprinted on the afterglow continuum are absorption features, which we identify as metal resonance lines from C IV, Al II, Al III, Fe II, Mg II, and Mg I. These lines are likely formed by metals in the GRB host, which we measure to be at  $z = 1.208$ .

### **GRB 140301A (z = 1.416)**

These data formed the basis for GCN 15900 (Krühler et al. 2014a) and are additionally published in Krühler et al. (2015a). Spectroscopic follow-up began 9 hours after the BAT trigger and lasted for  $12 \times 600$  s. A low signal-to-noise, spatially extended continuum is visible across the entire spectral coverage of X-shooter. The GRB afterglow continuum is visible at moderate signal-to-noise on top of the underlying host continuum. The host exhibits usual nebular emission from [O II], H $\beta$ , [O III], H $\alpha$ , N II, and [S II] which puts it at  $z = 1.416$ . Supporting this as the redshift of the GRB are absorption features from the Mg II-doublet in the GRB afterglow continuum.

### **GRB 140311A (z = 4.954)**

This spectrum has not been published previously. Starting 32.5 hours after the GRB trigger onboard *Swift*, this observation lasted  $14 \times 600$  s for a total of 8.4 ks. Some loss occurred during the observations, which reduced integration time in the UVB and VIS arm slightly. The GRB

afterglow continuum is clearly visible in the VIS and NIR arm of X-shooter. The continuum is very rich in absorption features, with at least the following lines identified: Ly $\gamma$ , Ly $\beta$ , Ly $\alpha$ , Si II, Si IV, C IV, Al II, Al III, Fe II, Mg II, and Mg I. All of these lines are at  $z = 4.954$ , which we take as the redshift of the GRB. This spectrum is taken under ESO programme ID: 092.D-0633(E) (PI: Greiner).

### **GRB 140430A (z = 1.601)**

A separate reduction of this burst has been published in Krühler et al. (2015a), and additionally the spectrum has also been used in GCN 16194 (Krühler et al. 2014b). Observations for this burst began in twilight, 2.5 hours after the BAT trigger and lasted for  $2 \times 600$  s. The spectrum contains a moderate signal-to-noise GRB afterglow continuum all the way through the spectroscopic arms of X-shooter. We identify absorption features in the afterglow continuum from Si II, C IV, Al II, Fe II, and Mg II, and emission lines from [O II] and [O III] - all at  $z = 1.601$  which is likely the redshift of the GRB.

### **GRB 140506A (z = 0.889)**

The data presented here has formed the basis of GCN 16217 (Fynbo et al. 2014b) and is published in Fynbo et al. (2014a), Krühler et al. (2015a), and Heintz et al. (2017). The observations consists of  $4 \times 600$  s at 8.8 and 33 hours after the burst. We detect absorption features from a wide range of ions, together with molecular absorption from CH+, all at  $z = 0.889$ . The optical/near-infrared afterglow reveals an unusual steep extinction curve which is found to be caused by dust very close to the burst.

### **GRB 140515A (z = 6.327)**

This spectrum has previously been used in Melandri et al. (2015). Starting 15.5 hours after the *Swift* trigger,  $8 \times 600$  s spectroscopic integration captures this very high redshift GRB afterglow. The Gunn-Peterson trough is visible against the GRB afterglow continuum, starting at 890 nm, which along with absorption lines from the Mg II doublet securely sets the redshift of this GRB at  $z = 6.327$ . From the red wing of the Ly $\alpha$ -profile we measure  $\log(N_{\text{HI}}/\text{cm}^{-2}) = 19.0 \pm 0.5$ , which is very low compared to the measured distribution of  $N_{\text{HI}}$ .

### **GRB 140614A (z = 4.233)**

This spectrum forms the basis for GCN 16401 (Krühler et al. 2014c), but is not published elsewhere.  $4 \times 600$  s spectroscopic integration, starting 3.8 hours after the BAT trigger catches this GRB afterglow, which turns out to be at very high redshift. The continuum is detected at moderate

signal-to-noise in both the VIS and NIR arms of X-shooter, heavily affected by absorption features. We identify the the lines belonging to Ly $\alpha$ , Si II, C II, C II\*, Al II, Al III, Fe II, and Mg II at a consistent redshift of  $z = 4.233$ . From the shape of the Ly $\alpha$  absorption trough we measure  $\log(N_{\text{HI}}/\text{cm}^{-2}) = 21.3 \pm 0.3$ .

### **GRB 140622A (z = 0.959)**

The characteristics of this short ( $T90 = 0.13 \pm 0.04$  s; [Lien et al. 2016](#)) GRB spectrum has been published in GCN 16437 ([Hartoog et al. 2014](#)), but does not appear in the refereed literature. Spectroscopic observations began with X-shooter only 34 minutes after the BAT trigger and lasted for  $2 \times 600$  s. In the spectrum, we detect continuum across all three arms of X-shooter. In the UVB arm, the continuum is only visible after heavily binning the spectrum in the dispersion direction. It is unclear how much of the continuum is from the host galaxy and how much is from the potential GRB afterglow. Superposed on the continuum, emission lines from [O II], H $\beta$ , [O III], H $\alpha$  are all detected at  $z = 0.959$ . We use this as the likely redshift of the GRB.

### **GRB 141028A (z = 2.332)**

This spectrum has already been used in GCN 16983 ([Xu et al. 2014b](#)), but is not published elsewhere. Starting 15.4 hours after the *Swift* trigger and lasting for a total of 2.4 ks, these observations captures a bright GRB afterglow. Very rich in absorption, the continuum is detected across the entire spectral coverage of X-shooter, except the blue half of the UVB arm, where the Ly $\alpha$ -forest absorbs the continuum. The redshift of the host of the GRB is measured based in the detection of features from Ly $\alpha$ , Si II, C IV, C II, Fe II, and Mg II- all at a consistent  $z = 2.332$ . From the Ly $\alpha$  trough we infer  $\log(N_{\text{HI}}/\text{cm}^{-2}) = 20.6 \pm 0.15$ . Two intervening system at  $z = 1.823$  and  $z = 2.09$  are also found in the spectrum based on the detection of C IV.

### **GRB 141031A (z = na)**

This spectrum is an attempt at a late-time host redshift measurement for GRB 141031A. The spectrum is taken long after the burst has faded and consists of  $4 \times 600$  s spectroscopic integration. In the 2D spectrum are two sources, which are both offset from the targeted host position and are thus likely foreground objects. The spectrum does not contain anything that can be used to measure a redshift from.

### **GRB 141109A (z = 2.993)**

The gross content of the spectrum has been issued in GCN 17040 ([Xu et al. 2014c](#)), but it is not used otherwise. Starting only 1.9 hours after the BAT trigger, these  $4 \times 600$  s spectra contain

a high signal-to-noise GRB afterglow. The afterglow continuum is readily detected all the way down to 370 nm, although the bluest part is affected by the Ly $\alpha$ -forest. A broad absorption trough from neutral hydrogen is clearly visible, with additional, narrower absorption features identified as due to Si II, Si II\*, C II, C II\*, Si IV, C IV, Fe II, Fe II\*, O I\*, and N II\*. These are all detected at a consistent  $z = 2.993$ , which due to the detection of the locally excited fine-structure lines securely sets this as the redshift of the GRB. Additionally, two Mg II absorption systems are detected at  $z = 1.67$  and  $z = 2.5$ . From the broad Ly $\alpha$ -absorption, we measure a neutral hydrogen column density of  $\log(N_{\text{HI}}/\text{cm}^{-2}) = 22.1 \pm 0.1$ .

### **GRB 150206A (z = 2.087)**

This spectrum has previously been used to form the basis for GCN 17420 (Kröhler et al. 2015b), but it is not published in the refereed literature. Due to the short visibility of this burst, it does not enter into the statistical sample. Beginning in twilight,  $4 \times 600$  s integration time contains a weak/moderate signal-to-noise GRB afterglow continuum throughout the X-shooter spectral coverage, down to  $\sim 375$  nm. In the continuum are absorption features, which we identify as due to metal lines from Zn II, Fe II, and Mg II. Additionally, Ly $\alpha$ -absorption is seen at the end of the trace. The spectral position of the lines means that this GRB is at  $z = 2.087$ . From the Ly $\alpha$  trough, we infer  $\log(N_{\text{HI}}/\text{cm}^{-2}) = 21.7 \pm 0.4$ . The afterglow continuum appears depressed in the blue end of the spectrum, suggesting dust extinction in the host.

### **GRB 150301B (z = 1.517)**

This spectrum has already been used in GCN 17523 (de Ugarte Postigo et al. 2015a), but it is not used elsewhere. Starting 5.1 hours after the BAT trigger, this spectrum is based on  $6 \times 600$  s spectroscopic integration. The GRB afterglow continuum is well detected across the entire spectral coverage of X-shooter at moderate signal-to-noise. Imprinted on the continuum are absorption features which we identify as being caused by Si II, C IV, Al II, Fe II, Mg II, and Mg I-all at a similar redshift of  $z = 1.517$ , which is likely the redshift of the GRB.

### **GRB 150403A (z = 2.057)**

This spectrum has previously been used to form the basis for GCN 17672 (Pugliese et al. 2015).  $4 \times 600$  s spectroscopic integration, starting 10 hours after the GRB trigger, captures a bright GRB afterglow. A broad absorption trough centered at  $\sim 370$  nm due to Ly $\alpha$  signals the redshift of the GRB, which is refined to  $z = 2.057$  based on the additional detection of metal absorption lines. We readily identify features associated with S II, Si IV, O I, Si II, Si II\*, C II, C II\*, C IV, Al II, Fe II, Fe II\*, Mn I, Mg II, and Mg I in the host of the GRB. An intervening C IV absorber is additionally

detected at  $z = 1.76$ . From the absorption trough due to Ly $\alpha$ , we infer the amount of neutral hydrogen in the host along the line of sight to be  $\log(N_{\text{HI}}/\text{cm}^{-2}) = 21.8 \pm 0.2$ .

### GRB 150423A (z = 1.394)

The gross content of these observations have previously been presented in GCN 17755 ([Malesani et al. 2015a](#)), but is not published as part of any refereed paper. This bona-fide short GRB (T90 = is  $0.22 \pm 0.03$  s; [Lien et al. 2016](#)) was observed in RRM mode and spectroscopic integration started after only 22 minutes. A series of stare mode observations, increasing in exposure time, and ending with a nodding sequence, totaling  $\sim 5000$  s, are combined to form this spectrum. A faint, almost featureless continuum is detected at low signal-to-noise all the way to the bluest part of the spectrum. An absorption doublet is detected in the VIS arm against the GRB afterglow continuum, which we identify as Mg II at  $z = 1.394$ .

### GRB 150428A (z = na)

This spectrum is empty, but is included here for completeness. It is not published anywhere.  $4 \times 600$  s spectroscopic observation, starting 3.7 hours after the trigger does not reveal anything conclusive. The host association is additionally ambiguous for this, likely extincted (GCN 17767; [Knust et al. 2015](#)), GRB.

### GRB 150514A (z = 0.807)

This spectrum has already been used in GCN 17822 ([de Ugarte Postigo et al. 2015b](#)). Spectroscopic observations began 28.4 hours post trigger and consist of a  $4 \times 600$  s nodding sequence. The GRB afterglow continuum is detected at moderate signal-to-noise across the entire spectral coverage of X-shooter. Narrow absorption features are imprinted in the continuum where we identify features from multiple Fe II transitions as well as the Mg II-doublet and the Mg I $\lambda 2852.96$  resonance line. These lines are all found at a position matching  $z = 0.807$ , suggesting it is the redshift of the GRB.

### GRB 150518A (z = 0.256)

This gross content of this data has previously been issued in GCN 17832 ([Xu et al. 2015a](#)), but is not published. Starting  $> 1$  day after the GRB trigger,  $4 \times 600$  s spectroscopic integration securely allows us to measure the redshift of the host. A continuum is detected all the way through the spectral coverage with multiple emission lines superposed. It is not clear to what degree the GRB afterglow contributes to the continuum. We identify the emission lines as [O II], H $\beta$ , [O III], H $\alpha$ , [N II], H $\alpha$ , and [S II] - all at  $z = 0.256$ . Due to the spatial proximity of this burst, it is a candidate

for SN follow-up and indeed there are indications of re-brightening at the burst position (GCN 17903; [Pozanenko et al. 2015](#)).

### **GRB 150616A (z = 1.188)**

These host observations are taken long after the burst had faded and have not been published before. They are included here for completeness. This bursts is excluded from the sample because an observing constraint delayed the *Swift* slew, causing the XRT observations to begin 16 minutes post trigger. No continuum is detected, but emission lines from [O II], [O III], and H $\alpha$  are all detected at  $z = 1.188$ , setting it as the redshift of the GRB host.

### **GRB 150727A (z = 0.313)**

The overall content of these observations have previously been reported in GCN 18080 ([Tanvir et al. 2015a](#)), but is not published. Starting 5 hours after the *Swift* GRB trigger, these observations consist of a combined  $2 \times 1200$  s and  $2 \times 600$  s integration. A blue continuum is detected across the entire spectral coverage of X-shooter, suggesting a significant contribution from the GRB afterglow. Superposed on the continuum are emission lines which we identify as H $\beta$ , [O III], and H $\alpha$  with a measured redshift of  $z = 0.313$ . Supporting this redshift is the tentative detection of the Mg II absorption doublet in the afterglow continuum. The relative strength of the lines suggest that the line-forming region is dust obscured, contrary to the story told by the blue afterglow continuum.

### **GRB 150821A (z = 0.755)**

The gross content of this spectacular spectrum has already been issued in GCN 18187 ([D'Elia et al. 2015a](#)), but the spectrum has not been published. Starting just 12.4 minutes after the onboard trigger of *Swift*, a total of  $4 \times 600$  s spectroscopic integration was obtained. The observations began just before dawn and the last two exposures are heavily affected by the brightening sky. A bright, high signal-to-noise GRB afterglow continuum is detected all across the the spectral window and imprinted on this are a myriad of absorption features. We identify individual lines from transitions in Al III, Cr II, Zn II, Ni II\*, Fe II, Fe II\*, Sc II, Mn II, Mg II, Mg I, Ti II, and Ca II - all at a consistent redshift of  $z = 0.755$ . The detection of fine-structure lines, excited local to the burst, clearly marks this as the redshift of the GRB.

### **GRB 150910A (z = 1.359)**

This spectrum has not previously been published. Starting  $\sim 20$  hours after the BAT trigger, these observations were stopped after  $2 \times 600$ s, when it became apparent that only a modest

signal-to-noise was obtainable, and the redshift had already been published in GCN 18273 ([Zheng et al. 2015](#)) and GCN 18274 ([de Ugarte Postigo et al. 2015c](#)). The continuum is detected at low signal-to-noise all across X-shooter and Mg II is detected at the suggested redshift, which we take as the redshift of the GRB.

### **GRB 150915A (z = 1.968)**

The gross content of these spectra have already been issued in GCN 18318 ([D'Elia et al. 2015b](#)). Observations began 3.3 hours after the *Swift* trigger and lasted for  $4 \times 1200$  s. A moderate signal-to-noise afterglow continuum is detected across the entire spectral coverage of X-shooter, where the bluest part is affected by Ly $\alpha$ -forest absorption. Imprinted on the afterglow continuum are a wealth of both emission and absorption features, all caused in a system for which we measure a redshift of  $z = 1.968$ . We identify in emission [O II], H $\beta$ , [O III], and H $\alpha$  and absorption due to Ly $\alpha$ , C IV, Al II, Si II, Fe II, and Mg II. We additionally identify fine-structure absorption lines from Si II\* and Fe II\*, at a similar redshift, which unequivocally sets the suggested redshift as the redshift of the GRB. The Ly $\alpha$ -line is affected by an atmospheric transmission drop and Ly $\alpha$  emission in the trough, making the measurement of the neutral hydrogen column density difficult. We measure  $\log(N_{\text{HI}}/\text{cm}^{-2}) 21.2 \pm 0.3$ .

### **GRB 151021A (z = 2.330)**

The data presented here also formed the basis of GCN 18426 ([Pugliese et al. 2016](#)) and are not published elsewhere. The observation was carried out in RRM starting 44 minutes after the GRB trigger. We detect absorption features from a wide range of ions at  $z = 2.330$  as well as intervening absorption at  $z = 1.49$ .

### **GRB 151027B (z = 4.063)**

The content of these spectra has previously been issued in GCN 18506 ([Xu et al. 2015b](#)), but is not published. Beginning 5 hours after the BAT trigger, 4 spectroscopic integrations obtained in a nodding sequence, each lasting for 600s, securely allows us to measure a redshift for this GRB. Beginning at  $\sim 470$  nm, the Ly $\alpha$ -forest is clearly detected at high signal-to-noise leading up to the broad Ly $\alpha$  absorption trough and the onset of a bright GRB afterglow continuum. Imprinted in the afterglow continuum are a range of absorption lines which we identify as due to Si II, Si II\*, O I, C II, C II\*, C IV, Al II, Al II, Fe II, and Fe II\*. These lines are all detected at  $z = 4.063$  and the presence of fine-structure lines at a consistent redshift securely sets this as the redshift of the GRB. GRB 151027B was the 1000th GRB detected by *Swift*. The afterglow of this burst is the subject of a forthcoming publication ([Greiner et al. 2018](#)).

### **GRB 151029A (z = 1.423)**

The gross content of these observations have previously been described in GCN 18524 ([Tanvir et al. 2015b](#)). Starting only 1 hour after the BAT trigger,  $2 \times 600$  s observations, extending into the morning twilight, were obtained of this GRB. The brightening sky affects the signal-to-noise of these spectra - especially in the blue end. The GRB afterglow is well detected over the entire spectral coverage of X-shooter, with spectral features from Fe II and Mg II imprinted by an absorber at  $z = 1.423$ . The absorber is likely the host of the GRB and we therefore consider  $z = 1.423$  the redshift of the GRB.

### **GRB 151031A (z = 1.167)**

The spectral features in this spectrum has previously been reported in GCN 18540 ([Malesani et al. 2015b](#)). Observed in RRM mode, these observations were initiated only 19 minutes after the BAT trigger. As per the standard RRM scheme, a series of stare observation, increasing in exposure time and ending with a regular  $4 \times 600$  s nodding sequence, were acquired for this burst. A moderate signal-to-noise continuum is detected all the way through the X-shooter spectral coverage. In the GRB afterglow continuum, we identify absorption features as Fe II, Mg II, Mg I, and Ca II at a consistent redshift of  $z = 1.167$ . Supporting this as the redshift of the GRB host galaxy are the simultaneous detection of nebular emission lines from [O II], H $\beta$ , and [O III].

### **GRB 160117B (z = 0.870)**

A preliminary analysis of these spectra have previously been presented in GCN 18886 ([de Ugarte Postigo et al. 2016a](#)). Starting 13.5 hours after the *Swift* trigger, these spectra are formed on the basis of  $4 \times 1200$  s spectroscopic integration. The GRB afterglow is clearly detected at high signal-to-noise across the entire spectral coverage of X-shooter. Superposed on the continuum are absorption and emission features, which are identified as Fe II, Mg II, Mg I in absorption, and [O II], H $\beta$ , and [O III]. The spectral positions of these lines all correspond to a redshift of  $z = 0.870$ , which most likely is the redshift of the GRB.

### **GRB 160203A (z = 3.518)**

The data presented here also formed the basis of GCN 18982 ([Pugliese et al. 2016](#)) and are not published elsewhere. The observation was carried out in RRM starting 18 minutes after the GRB trigger. We detect absorption features from a wide range of ions at  $z = 3.518$  as well as intervening absorption at  $z = 2.203$ . From the very high signal-to-noise spectrum we are able to measure  $\log(N_{\text{HI}}/\text{cm}^{-2}) = 21.75 \pm 0.10$ , based on the shape of the Ly $\alpha$  profile. This burst is the subject of a forthcoming publication (Pugliese et al. in prep.).

### **GRB 160228A (z = 1.640)**

The gross content of these spectra have previously been presented in GCN 19186 ([Krühler et al. 2016a](#)). Taken long after the burst had faded, the target is the likely host galaxy. In  $4 \times 1200$  s spectroscopic integration we detected emission lines from the host. We find [O III] and H $\alpha$  at a consistent  $z = 1.640$ . We therefore suggest that this is the redshift of the GRB.

### **GRB 160303A (z = na)**

This is potentially a short burst with extended emission (GCN 19148; [Ukwatta et al. 2016](#)). The content of the spectra have previously been reported in GCN 19154 ([de Ugarte Postigo et al. 2016b](#)). Observations began 19.1 hours after the BAT trigger and consist of  $4 \times 1200$  s spectroscopic integration. A very faint continuum is detected in the UVB and VIS arm after binning in the dispersion direction, but no clear redshift can be inferred from the continuum shape. No emission lines are readily apparent, suggesting little or no star formation in the host.

### **GRB 160314A (z = 0.726)**

The gross content of these spectra have previously been issued in GCN 19192 ([D'Elia et al. 2016](#)). Spectroscopic integration began 13 hours post GRB trigger and lasted for  $4 \times 1200$  s. In the data we see a moderate signal-to-noise continuum across the entire spectral coverage of X-shooter. Clearly visible on top of the continuum are emission lines from [O II], H $\delta$ , H $\gamma$ , H $\beta$ , [O III], H $\alpha$ , [N II], and [S II] at a consistent redshift of  $z = 0.726$ . It is unclear how much of the continuum is due to the host and how much is from the GRB afterglow. At the same redshift, we see the tentative detection of Fe II-absorption, supporting the redshift measurement and suggesting a significant afterglow contribution to the continuum.

### **GRB 160410A (z = 1.717)**

This short GRB with extended emission (GCN 19276; [Sakamoto et al. 2016](#)) was observed in RRM mode, with observations starting after only 7.7 minutes. The gross content has already been presented in GCN 19274 ([Selsing et al. 2016a](#)). These observations have the shortest delay between trigger time and start of observation. Spectroscopic integration began after 8.4 minutes and lasted for  $3 \times 600$  s. The last image in the nodding sequence was aborted because the object was setting and the telescope reached the hardware limit. A blue, moderate signal-to-noise continuum is detected across the entire spectral coverage of X-shooter with multiple absorption features imprinted on it. At  $z = 1.717$  we detected the broad absorption trough due to Ly $\alpha$  and we additionally find Al II and Fe II at a consistent redshift, setting it as the redshift of the GRB. Additionally, two intervening C IV absorption systems are detected at  $z = 1.444$  and

$z = 1.581$ . From the Ly $\alpha$  absorption trough, we measure a neutral hydrogen column density of  $\log(N_{\text{HI}}/\text{cm}^{-2}) = 21.2 \pm 0.2$ . This is the only short GRB for which we have a measurement of  $N_{\text{HI}}$  and is the subject of an forthcoming paper (Selsing et al. in prep).

### GRB 160425A (z = 0.555)

These spectra were already used to form the basis for GCN 19350 ([Tanvir et al. 2016a](#)), but are not published anywhere else. Spectroscopic integration started after 7.2 hours and lasted for  $4 \times 1200$  s. A low signal-to-noise continuum is detected across the spectral coverage of X-shooter, but no clear absorption lines are discernible. It is therefore unclear how much of the continuum is due to the host and how much is due to the GRB. Superposed on the continuum are two sets of emission lines, offset spatially, but at very similar redshifts. We identify lines from [O II], H $\beta$ , [O III], H $\alpha$ , [N II], and [S II] in both systems – all at  $z = 0.555$ . As per GCN 19350 ([Tanvir et al. 2016a](#)), the GRB probably occurred in an interacting pair of galaxies.

### GRB 160625B (z = 1.406)

GRB 160625B is the first GRB for which a significant linear polarization was measured ([Troja et al. 2017b](#)). Because this burst was detected by *Fermi*, it is therefore not a part of the statistical sample. The gross content of these spectra has previously been presented in GCN 19600 ([Xu et al. 2016a](#)). Starting 30 hours after the trigger, these spectra are obtained in  $4 \times 600$  s. The GRB afterglow continuum is detected at high signal-to-noise throughout the spectral coverage of X-shooter. Imprinted on the afterglow continuum are a multitude of absorption features, from which we identify the responsible elements as Si II, O I, Si IV, C IV, Al II, Al III, Fe II, Zn II, Mg II, and Mg I at a consistent redshift of  $z = 1.406$ . An additional intervening Mg II absorber is detected at  $z = 1.319$ .

### GRB 160804A (z = 0.736)

The data presented here also formed the basis of GCN 19773 ([Xu et al. 2016b](#)), and are published in [Heintz et al. \(2018\)](#). Observations started 22.37 hours after the BAT trigger and lasted for 2.4ks. The afterglow continuum is detected across the entire spectral coverage of X-shooter and absorption lines from Mg I, Mg II, Fe II and Al II are found at  $z = 0.736$ . At the same redshift, emission lines from [O II], [O III], H $\alpha$ , H $\beta$ , H $\gamma$ , [N II], [S II], and [S III] are found. A second epoch, lasting 3.6ks, is obtained after the afterglow had faded, confirming the emission line detections. The host galaxy is found to have a roughly solar metallicity and is among the most luminous GRB hosts at  $z < 1$ .

## **GRB 161001A (z = 0.891)**

The content and scope of these spectra has previously been issued in GCN 19971 (Krühler et al. 2016b).  $4 \times 600$  s spectroscopic integration was obtained of this potentially short GRB (GCN 19974; Markwardt et al. 2016), starting 6.1 hr after the GRB trigger. Close to the XRT error circle (Osborne et al. 2016) there is a bright, point-like source, also visible in archival images. Our spectrum reveals that this is an M-type star, based on the presence of TiO bands, and is thus unrelated to the GRB. Two more objects lie within or in the near proximity of the X-ray error circle, as visible in our images from the acquisition camera. One is blended with the above mentioned star, and is serendipitously covered by the X-shooter slit, revealing emission lines from [O II], H $\beta$ , and H $\alpha$  at a consistent redshift of  $z = 0.891$ . The second source, first noted by Chen et al. (2016), is extended and lies just outside the XRT error circle. Based on GROND imaging, Chen et al. (2016) report moderate variability, and suggest this object as an afterglow candidate. Following our original imaging, we thus secured further late-time photometry with the X-shooter acquisition camera, starting on 2016 Oct 5.26 UT (4.22 days after the GRB), securing  $3 \times 120$  s in each of the  $g$  and  $r$  filters. No variability is apparent in either bands. In offline analysis of the GROND data (T. Krühler, priv. comm.), the evidence for fading is less significant than originally reported. The situation is thus left ambiguous, but due to the consistency of the  $z = 0.891$  object with the XRT localization, we consider this as the most likely redshift of GRB 161001A.

## **GRB 161007A (z = na)**

These data have not been published elsewhere. Observations for GRB 161007A started 323 hr after the burst trigger and were centered on the potential host galaxy (see GCN 20014 (de Ugarte Postigo et al. 2016c) and GCN 20020 (Heintz et al. 2016)).  $4 \times 600$  s of observations were obtained revealing a faint continuum rising abruptly above the noise at  $\sim 685$  nm and extending up to 2100 nm. A very low significance continuum is detected at shorter wavelengths, down to  $\sim 600$  nm. No significant emission features could be identified. Two possibilities can explain the observed continuum break, but neither are fully satisfactory. The first option is the Lyman alpha cutoff at  $z \sim 4.6$ ; at this redshift, the usually detected strong nebular lines would be shifted out of the covered wavelength range. The host would be however exceptionally bright, with an absolute magnitude at  $\approx 150$  nm  $M = -23.8$  AB, that is about 2.8 mag brighter than  $M^*$  at that redshift (e.g. Bouwens et al. 2015). The inferred X-ray hydrogen-equivalent column density would also be a record-high  $4 \times 10^{23}$  cm $^{-2}$  (see e.g. Campana et al. 2012). Alternatively, the continuum discontinuity could be the 400 nm break at  $z = 0.71$ ; such feature is however prominent only in early-type galaxies, which are unlikely hosts of long-duration GRBs (but see Rossi et al. 2014). Given the lack of optical variability, it cannot be excluded that the object within the XRT error circle is a chance association, as the probability of a random alignment is small but non negligible

(of the order of 1%). In conclusion, we cannot provide a secure redshift for GRB 161007A.

### **GRB 161014A (z = 2.823)**

The data presented here also formed the basis of GCN 20061 ([Selsing et al. 2016b](#)), but are not published elsewhere. Starting 11.6 hours after the GRB trigger, 4.8 ks of integration time captures the afterglow continuum across all three spectroscopic arms. A broad absorption trough due to Lyman alpha is visible, along with metal absorption features from Mg II, Si II, C II, C IV, Al II, Al III, and Fe II, all at  $z = 2.823$ . Similar to GRB 140506 ([Fynbo et al. 2014a; Heintz et al. 2018](#)), a break in the continuum shape is tentatively detected bluewards of 600 nm, possible signifying some anomalous form of extinction.

### **GRB 161023A (z = 2.710)**

The gross content of these spectra have previously been reported in GCN 20104 ([Tanvir et al. 2016b](#)). This extremely bright *INTEGRAL* burst is not a part of the statistical sample. Starting 3 hours after the trigger, the spectra are based on  $2 \times 600$  s. The GRB afterglow continuum is detected with the highest signal-to-noise of all the spectra presented here. A myriad of absorption features are visible against the continuum, many of which would not be visible against lower signal-to-noise spectra. We identify at least 15 intervening absorbers between  $z = 1.243$  and  $z = 2.710$ . In the host system we clearly see absorption from Ly $\beta$ , Ly $\alpha$ , S II, Si II, O I, Si IV, C IV, Al II, Al III, Fe II, Mg II, and Mg I. Several fine-structure transitions are additionally seen, clearly associating the  $z = 2.710$  system with the GRB. From the Ly $\alpha$ -line we infer  $\log(N_{\text{HI}}/\text{cm}^{-2}) = 20.96 \pm 0.05$ . This spectrum will be further analyzed in de Ugarte Postigo et al. (in prep).

### **GRB 161117A (z = 1.549)**

The majority of the spectral features of these spectra have previously been reported in GCN 20180 ([Malesani et al. 2016](#)). Starting only  $\sim 40$  minutes after the BAT trigger, these observations consist of  $4 \times 600$  s, taken under relatively poor observing conditions. The GRB afterglow continuum is detected throughout most of the X-shooter spectral coverage at low-to-moderate signal-to-noise, however the continuum level drops below the noise in the bluest part of the UVB arm at  $\sim 380$  nm. Imprinted in the continuum are absorption features, which we identify as due to Fe II, Mg II, and Mg I in an absorption system at  $z = 1.549$ . We consider this the likely redshift of the GRB.

### **GRB 161219B (z = 0.148)**

The core signatures in these spectra have already been issued in GCN 20321 ([Tanvir et al. 2016c](#)), and are additionally used in both [Ashall et al. \(2017\)](#) and [Cano et al. \(2017a\)](#). This GRB is very

close-by and is associated with the SN Ic-BL SN2016jca (GCN 20342; [de Ugarte Postigo et al. 2016d](#)). The observations consist of  $4 \times 600$  s spectroscopic integration, starting 1.5 days after the GRB trigger. The GRB afterglow continuum is detected at high signal-to-noise across the entire spectral coverage of X-shooter. Superposed on the continuum are absorption features, which we identify as being formed by the Mg II, Mg I, and the Ca H & K-lines at  $z = 0.148$ . Underneath the glaring afterglow continuum we additionally detect nebular emission from [O II], H $\beta$ , [O III], H $\alpha$ , and [S II] at a consistent redshift, which is the likely redshift of the GRB.

### **GRB 170113A (z=1.968)**

These gross content of these data have previously been issued in GCN 20458 ([Xu et al. 2017](#)). Starting 15.2 hours after the BAT trigger, these observations consist of  $4 \times 1200$  s spectroscopic integration. The GRB afterglow continuum is detected at moderate signal-to-noise across across the entire spectral coverage of X-shooter. In the bluest end of the spectral coverage, the background noise increases, thus lowering the continuum below detection. Superposed on the afterglow continuum are both absorption lines and emission lines. In absorption we identify lines from Si II, Fe II, and Mg II, and in emission we detect [O II], H $\beta$ , and [O III]. All the lines are detected at a consistent redshift of  $z = 1.968$ , which we take as the redshift of the GRB.

### **GRB 170202A (z=3.645)**

GRB 170202A is the last GRB afterglow observed in this work. It concludes the follow-up effort that has lasted for 8 years. The majority of the spectral features in this spectrum have previously been reported in GCN 20589 ([Palmerio et al. 2017](#)). Spectroscopy began 9.7 hours after the BAT trigger, and lasted for  $4 \times 600$  s. The GRB afterglow is well detected at moderate-to-high signal-to-noise throughout the spectral coverage of X-shooter, down to 430 nm. The lowest wavelength continuum from 430 nm to 560 nm is absorbed by the Ly $\alpha$  forest, with the broad Ly $\alpha$  absorption trough centered at 565 nm. In the continuum, we additionally identify metal absorption features from Si II, C IV, Si IV, Fe II, and Mg II, with the additional detection of Si II\* fine-structure lines. With an additional detection of [O III] and all lines detected at  $z = 3.645$ , this unequivocally marks this as the redshift of the GRB. There is an additional C IV absorber at  $z = 3.077$ . From the Ly $\alpha$  absorption we measure  $\log(N_{\text{HI}}/\text{cm}^{-2}) = 21.55 \pm 0.10$ .

# 3

## THE HIGHEST MEASURED REDSHIFT OF A SHORT GRB AND THE PHYSICAL IMPLICATIONS

This chapter contains the following article:

**“The host galaxy of the short GRB 111117A at  $z = 2.211$ :  
Impact on the short GRB redshift distribution and progenitor channels”\***

Accepted for publication in *Astronomy and Astrophysics*, 2018.

Authors:

J. Selsing, T. Krühler, D. Malesani, P. D’Avanzo, S. Schulze, S. D. Vergani, J. Palmerio, J. Japelj, B. Milvang-Jensen, D. Watson, P. Jakobsson, J. Bolmer, Z. Cano, S. Covino, V. D’Elia, A. de Ugarte Postigo, J. P. U. Fynbo, A. Gomboc, K. E. Heintz, L. Kaper, A. J. Levan, S. Piranomonte, G. Pugliese, R. Sánchez-Ramírez, M. Sparre, N. R. Tanvir, C. C. Thöne, & K. Wiersema

---

\*Based on observations collected at ESO/VLT under programme 088.A-0051 and 091.D-0904, at TNG under programme A24TAC\_38, at Gemini North under programme GN-2011B-Q-10 and GTC under programme GTC43-11B.

It is notoriously difficult to localize short  $\gamma$ -ray bursts (sGRBs) and their hosts to measure their redshifts. These measurements, however, are critical for constraining the nature of sGRB progenitors, their redshift distribution, and the  $r$ -process element enrichment history of the universe. Here we present spectroscopy of the host galaxy of GRB 111117A and measure its redshift to be  $z = 2.211$ . This makes GRB 111117A the most distant high-confidence short duration GRB detected to date. Our spectroscopic redshift supersedes a lower, previously estimated photometric redshift value for this burst.

We use the spectroscopic redshift, as well as new imaging data to constrain the nature of the host galaxy and the physical parameters of the GRB. The rest-frame X-ray derived hydrogen column density, for example, is the highest compared to a complete sample of sGRBs and seems to follow the evolution with redshift as traced by the hosts of long GRBs. From the detection of Ly $\alpha$  emission in the spectrum, we are able to constrain the escape fraction of Ly $\alpha$  in the host.

The host lies in the brighter end of the expected sGRB host brightness distribution at  $z = 2.211$ , and is actively forming stars. Using the observed sGRB host luminosity distribution, we find that between 43% and 71% of all *Swift*-detected sGRBs have hosts that are too faint at  $z \sim 2$  to allow for a secure redshift determination. This implies that the measured sGRB redshift distribution could be incomplete at high redshift. The high  $z$  of GRB 111117A is evidence against a lognormal delay-time model for sGRBs through the predicted redshift distribution of sGRBs, which is very sensitive to high- $z$  sGRBs.

From the age of the universe at the time of GRB explosion, an initial neutron star (NS) separation of  $a_0 < 3.1 R_\odot$  is required in the case where the progenitor system is a circular pair of inspiralling NSs. This constraint excludes some of the longest sGRB formation channels for this burst.

### 3.1 Introduction

There is mounting evidence that short-duration  $\gamma$ -ray bursts (sGRBs) come from the merger of a neutron star (NS) either with another NS or with a black hole, due to their apparent association with kilonovae (Barnes & Kasen 2013; Tanvir et al. 2013b; Berger et al. 2013b; Yang et al. 2015b; Jin et al. 2016; Rosswog et al. 2017). This association has recently been confirmed by the simultaneous and co-spatial detection of gravitational waves (GWs) from a binary neutron star merger and a sGRB (Abbott et al. 2017c; Goldstein et al. 2017; Savchenko et al. 2017b); however, to what degree the sGRB associated with GW170817 is a cosmological sGRB remains an open question (Lyman et al. 2018; Margutti et al. 2018). The absence of associated supernovae in deep searches (e.g., Hjorth et al. 2005b; Fox et al. 2005; Hjorth et al. 2005a; Kann et al. 2011) supports this idea and distinguishes the physical origin of sGRBs from their long-duration counterparts (but see also Fynbo et al. 2006; Della Valle et al. 2006; Gal-Yam et al. 2006).

The classification of GRBs in two groups initially comes from the bimodal distribution of burst duration and spectral hardness in the BATSE sample (Kouveliotou et al. 1993), where the duration  $T_{90} < 2$  s has been regarded as the dividing line between long and short GRBs. Additionally, it has been found for long GRBs (lGRBs) that there is a spectral lag in the arrival-time of photons, with the most energetic ones arriving first. This lag is consistent with zero for sGRBs (Norris & Bonnell 2006). Because both populations have continuous, overlapping distributions in their observables and because telescopes observe in differing bands, it is difficult to impose a single demarcation criterion between the two classes. For this reason, the distinction between long and short GRBs is preferably based on a combination of the high-energy properties (Zhang et al. 2009; Kann et al. 2011; Bromberg et al. 2012, 2013).

The *Swift* satellite (Gehrels et al. 2004) greatly improved the understanding of sGRB progenitors thanks to its quick localization capability. The bulk of these localizations have associated galaxies at relatively low redshifts with a median redshift of  $z \sim 0.5$  (Berger 2014). Unlike lGRBs, sGRB afterglows are faint, making absorption spectroscopy often ineffective. Therefore, most of these measurements come from the associated hosts and is potentially biased towards lower redshifts. Additionally, because the *Swift* sensitivity to sGRB decreases sharply with redshift (Behroozi et al. 2014), the intrinsic redshift distribution of sGRBs is largely unknown at higher redshifts.

The host galaxies of sGRBs are diverse. They are more massive and less actively star-forming on average than lGRB hosts (Fong et al. 2013), while in some cases no host galaxy can be identified above the detection threshold of deep follow-up observations (Berger 2010; Tunnicliffe et al. 2014). Together with their position within their hosts (Fong & Berger 2013), this suggests a progenitor system that can be very long-lived in comparison to lGRBs, with the host stellar mass affecting the sGRB rates more than the star formation rate (SFR) (Berger 2014).

The electromagnetic signals from sGRBs are a promising channel to accurately localize NS mergers (Ghirlanda et al. 2016). This epochal breakthrough occurred recently when the first ever NS–NS GW event was detected by LIGO/Virgo (GW 170817) and associated with the weak sGRB 170817A detected by the *Fermi* and INTEGRAL satellites (Abbott et al. 2017d; Goldstein et al. 2017; Savchenko et al. 2017b). The simultaneous detection of a sGRB and a GW provides new promising ways to constrain the binary inclination angle (Arun et al. 2014; Abbott et al. 2017b) and to measure cosmological distances (Nissanke et al. 2010; Abbott et al. 2017e).

The total lifetime of NS binaries depends on their orbit, mass, spin, initial separations, and subsequent inspiral times. The delay time from formation to explosion impacts the timing and distribution of the enrichment of the ISM with heavy *r*-process elements (van de Voort et al. 2014; Wallner et al. 2015; Ji et al. 2016). Some limits can be calculated using host galaxy star formation history models and spatial distribution of sGRBs within their hosts (Berger 2014). The most distant cosmological bursts, however, offer direct, hard limits on the coalescence timescales.

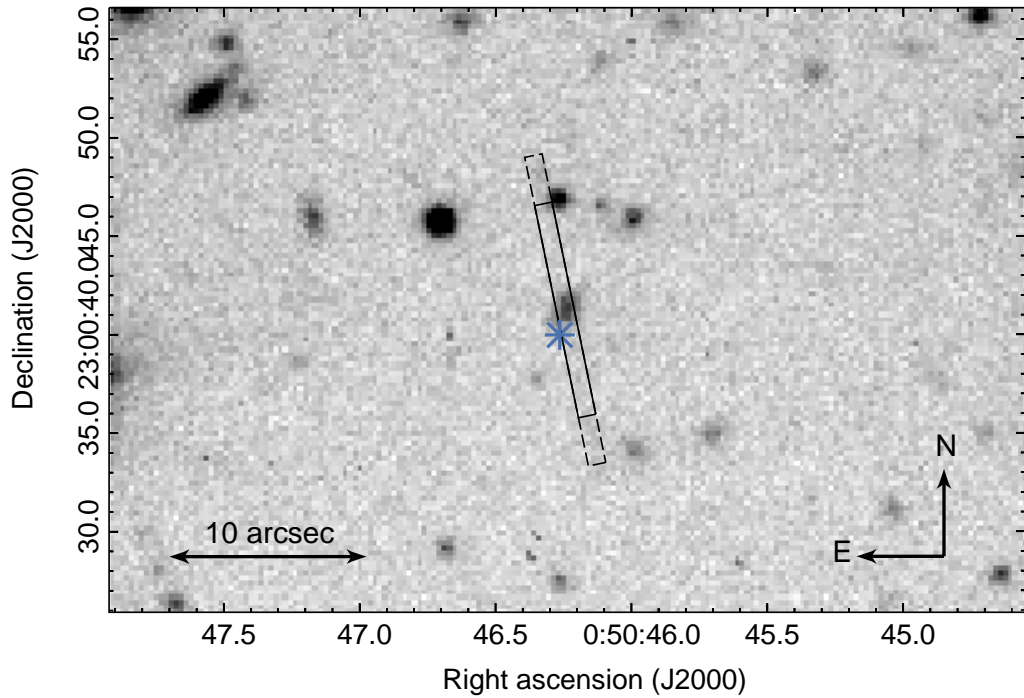


**Figure 3.1:** FORS2  $R$ -band imaging of the field of GRB 111117A with the X-shooter slit overlaid. The slit position represents four epochs of spectroscopic observations taken at similar position angles. The corresponding photometry is shown in Fig. 3.3. The blue asterisk indicates the GRB position (R.A., Dec.) (J2000) = ( $00^{\text{h}} 50^{\text{m}} 46.264^{\text{s}}$ ,  $+23^{\circ} 00' 39.98''$ ) as derived from the *Chandra* observations in [Sakamoto et al. \(2013\)](#).

Here we present a spectrum of the host galaxy of the short GRB 111117A ( $T_{90} = 0.46$  s) and measure its redshift to be  $z = 2.211$ . This value is significantly higher than the previously estimated redshift of  $z \sim 1.3$  based on photometric studies ([Margutti et al. 2012](#); [Sakamoto et al. 2013](#)). We present the GRB’s rest frame properties based on this new distance compared to previous analyses and revisit the host properties derived from the new solution to the spectral energy distribution (SED) fit. While no optical afterglow was detected, the excellent localization from a detection of the X-ray afterglow by the *Chandra* X-ray Observatory allows us to discuss the positioning and environmental properties of this remarkably distant sGRB. We use the  $\Lambda$ CDM cosmology parameters provided by [Planck Collaboration et al. \(2016\)](#) in which the universe is flat with  $H_0 = 67.7 \text{ km s}^{-1} \text{ Mpc}^{-1}$  and  $\Omega_m = 0.307$ . All magnitudes are given in the AB system.

All data, code, and calculations related to the paper along with the paper itself are available [online](#).

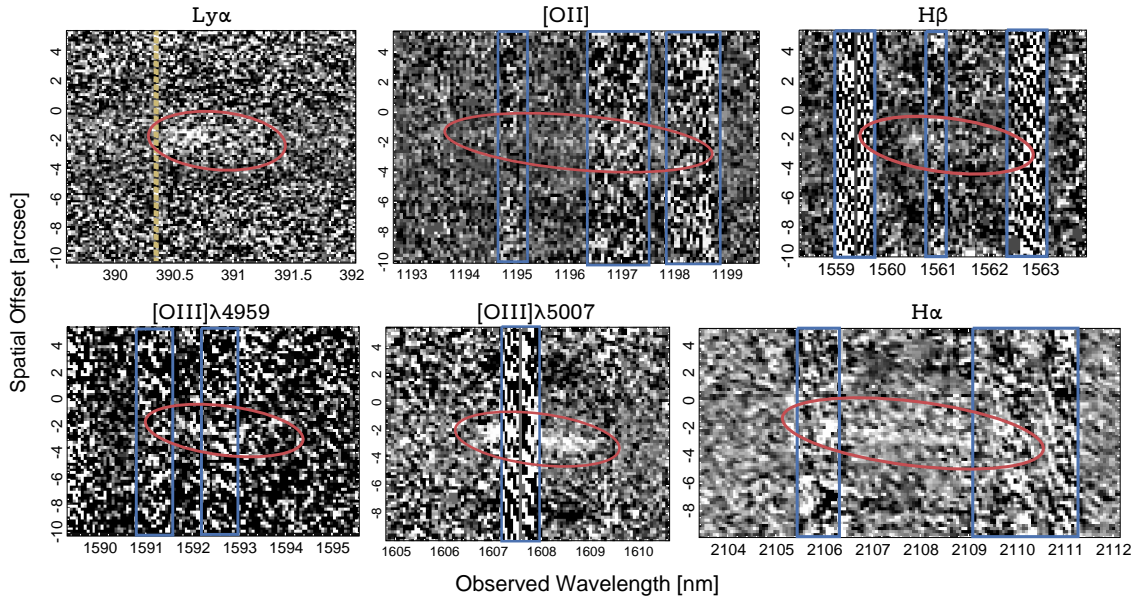


**Figure 3.2:** Two-dimensional images of the emission lines corresponding to Ly $\alpha$ , [O II] $\lambda 3727$ , H $\beta$ , [O III] $\lambda 4959$ , [O III] $\lambda 5007$ , and H $\alpha$ . The location of bright skylines are marked by blue boxes. The locations of the emission lines are indicated with red ellipses. Because the host is observed in nodding mode, negative images of the emission lines appear on both sides in the spatial direction. For the upper left panel containing Ly $\alpha$ , the systemic redshift position of Ly $\alpha$  is marked by a yellow vertical dashed line. The red part of the [O II] $\lambda 3727$ -doublet is affected by atmospheric absorption.

## 3.2 Observations and results

### 3.2.1 Spectroscopic observations and analysis

Spectroscopic observations were carried out using the cross-dispersed echelle spectrograph, VLT/X-shooter (Vernet et al. 2011), at four separate epochs. The burst was observed 38 hours after the Burst Alert Telescope (BAT) trigger under ESO program 088.A-0051 (PI: Fynbo) and again later under ESO program 091.D-0904 (PI: Hjorth). The observations used a simple ABBA nodding pattern, with 5 " nod throws. The X-shooter covers the wavelength range from 3000 Å to 24 800 Å (21 000 Å when the *K*-band blocking filter is used) across three spectroscopic arms. We carried out the bias-correction, flat-fielding, order tracing, wavelength calibration, rectification, and flux calibration using the VLT/X-shooter pipeline version 2.8.4 (Goldoni et al. 2006; Modigliani et al. 2010) run in physical mode. Because the echelle orders are curved across each detector, a rectification algorithm is employed that introduces correlations between neighboring pixels. We selected a pixel scale of 0.2/0.2/0.6 Å/pix for the UVB/VIS/NIR arm to minimize the degree of correlation while conserving the maximum resolution. The observations were combined and

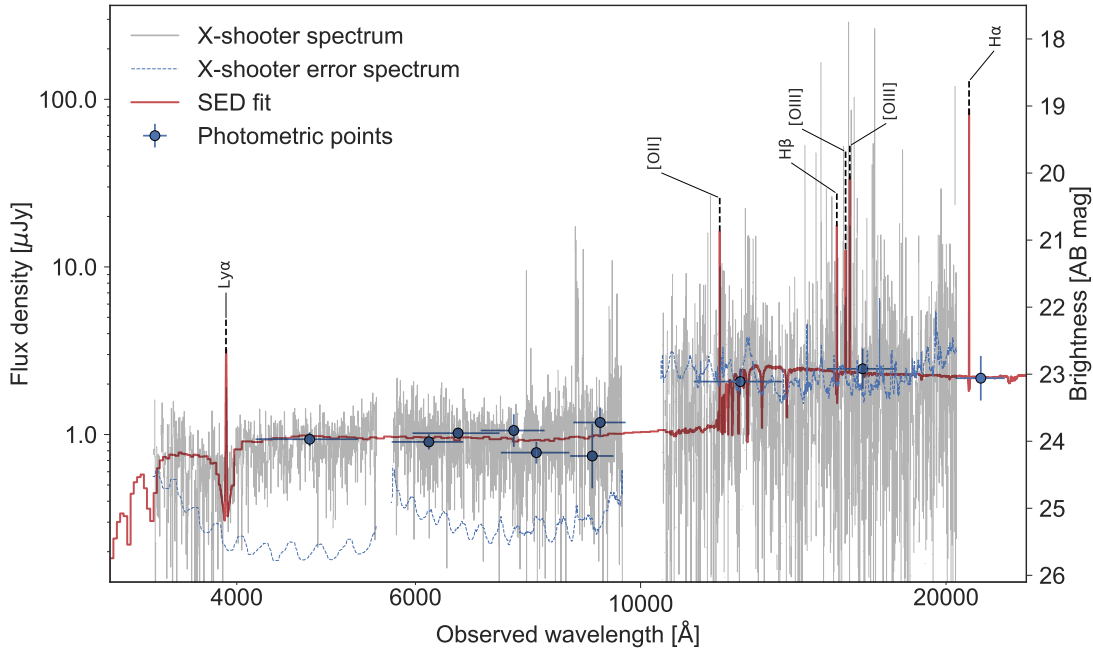


**Figure 3.3:** Best-fit SED to the derived photometry. The detection of Ly $\alpha$  is predicted from the SED fit and confirmed by the spectroscopic observations. Overplotted in gray is the observed spectrum, binned by 6 Å for presentation purposes. Slit losses have been corrected for based on the average seeing of the observations, as confirmed by the comparison with the photometry. The blue dashed curve is the corresponding error spectrum, smoothed for presentation purposes. The spectral gaps at 5500 Å and 10000 Å are due to the merging of the arms.

extracted using the scripts described in Selsing et al. 2017 (in prep.) and available online<sup>2</sup>, where the full spectral point spread function was modeled across each arm and used for the optimal extraction algorithm (Horne 1986). An overview of the spectroscopic observations is given in Table 3.1, and the slit position is shown in Fig. 3.1. Each of the epochs was extracted individually and combined in a weighted fashion where the weight at each pixel was chosen as median variance spectrum of the region surrounding that pixel, thus avoiding basing the weight on the pixel variance. Slit-loss correction was applied on the combined spectrum based on the average seeing of the observations. We show the extracted spectrum in Fig. 3.3.

We determine a redshift of  $z = 2.211 \pm 0.001$  from the simultaneous detection of emission lines belonging to Ly $\alpha$ , [O II] $\lambda 3727$ , H $\beta$ , [O III] $\lambda 4959$ , [O III] $\lambda 5007$ , and H $\alpha$ . The [O II] $\lambda 3727$ , H $\beta$ , and [O III] $\lambda 4959$  lines are detected at low significance ( $\sim 3\sigma$ ). The uncertainty on the redshift is the standard deviation of independent measurements of the redshift based on the individual line centroids (excluding Ly $\alpha$ ). We show cutouts of the 2D spectrum at the position of all the detected lines in Fig. 3.2. The H $\alpha$  line is only visible in the first epoch due to the  $K$ -band blocking filter

<sup>2</sup>[https://github.com/jselsing/XSGRB\\_reduction\\_scripts](https://github.com/jselsing/XSGRB_reduction_scripts)

**Table 3.1:** Overview of the spectroscopic observations. “JH” in the slit width column refers to observations where a  $K$ -band blocking filter has been used. The seeing is determined from the width of the spectral trace of a telluric standard star, observed close in time to the host observation. The spectral resolution,  $R$ , is measured from unresolved telluric absorption lines in the spectrum of the telluric standard star.

Observation epoch		Exposure time (s)			Slit width	Airmass	Seeing	$R$
(UT)		UVB	VIS	NIR	(arcsec)		(arcsec)	VIS/NIR
2011-11-19 01:33		2 × 2400	2 × 2400	8 × 600	1.0/1.0/0.9	1.49	0.75	11600/6700
2013-07-15 09:02		2 × 1200	2 × 1200	8 × 300	1.0/1.0/0.9JH	1.53	0.98	9600/8900
2013-08-03 07:37		2 × 1200	2 × 1200	8 × 300	1.0/1.0/0.9JH	1.55	0.85	11400/11300
2013-08-03 08:34		2 × 1200	2 × 1200	8 × 300	1.0/1.0/0.9JH	1.49	0.85	11400/11300

used for the remaining observations. The nebular lines exhibit a spatial extent of  $\sim 1.^{\prime\prime}5$  and show significant velocity structure along the slit. A drop in the continuum bluewards of the Ly $\alpha$  line further supports the redshift. No spectral evolution is observed across the epochs indicating that there is negligible GRB afterglow contribution to the first epoch spectrum.

Using the luminosity of H $\alpha$ , we can infer the SFR of the host (Kennicutt 1998). At the redshift of the GRB host, H $\alpha$  is observed at around 21 000 Å where the night sky is very bright. In addition, several bright sky-lines are superposed on the line, making it difficult to obtain an accurate estimate of the H $\alpha$  flux. Due to their velocity structure, the lines exhibit clear deviations from a Gaussian and given the low S/N of the spectra we do not attempt any parametric fits. We instead obtain a limit on the SFR by numerically integrating the part of H $\alpha$  free of contamination and obtain  $F_{\text{H},\text{X}\alpha} > 4.1 \times 10^{-17}$  erg s $^{-1}$  cm $^{-2}$ . After converting the Kennicutt (1998) relation to a Chabrier (2003) initial mass function using the conversion factor from Madau & Dickinson (2014), we derive a limit of SFR  $> 7M_{\odot}$  yr $^{-1}$ . We additionally obtain the Ly $\alpha$  line flux by numerically integrating the entire Ly $\alpha$  line complex and obtain  $F_{\text{Ly}\alpha} = (2.0 \pm 0.5) \times 10^{-17}$  erg s $^{-1}$  cm $^{-2}$ , where the error on the flux is found by integrating the associated error spectrum over the same spectral region.

From the SED fit (Sect. 3.2.2) the host is constrained to contain very little or no dust. Consistently, Ly $\alpha$  is detected although its presence does not exclude dust. Therefore, we do not apply a dust-correction to the measured H $\alpha$  flux here. The [O II] line is close to a region of strong telluric absorption, which is why no SFR is inferred from it.

The total extent of the lines in velocity space is  $\sim 450$  km s $^{-1}$ . The line profiles shows an asymmetric “double-horned” profile, indicating that we are seeing a galaxy with a large degree of coherent rotational motion relative to the line of sight. If we assume that we are viewing a spiral galaxy edge-on, this is a measure of the rotational velocity of the gas. If we assume that the spectral resolution and the turbulent width of the lines are negligible compared to the rotational velocity, based on the projected size of the source and the width of the lines we can put

**Table 3.2:** Overview of the photometric observations.

Observation epoch	Exptime	Telescope/instrument	Filter	Airmass	Image quality	Host brightness <sup>a</sup>
(UT)	(ks)				(arcsec)	(AB mag)
2013-08-30 07:43	1.45	VLT/FORS2	<i>g</i>	1.55	0.99	$24.08 \pm 0.09$
2011-11-17 20:07	0.80	GTC/OSIRIS	<i>g</i>	1.15	1.67	$24.13 \pm 0.09$
2011-11-17 20:07	1.20	GTC/OSIRIS	<i>r</i>	1.11	1.50	$23.93 \pm 0.08$
2013-07-17 08:37	1.45	VLT/FORS2	<i>R</i>	1.56	0.74	$23.95 \pm 0.06$
2011-11-28 21:10	3.60	TNG/DOLORES	<i>R</i>	1.01	1.08	$23.96 \pm 0.13$
2011-11-17 20:07	0.36	GTC/OSIRIS	<i>i</i>	1.08	1.50	$23.89 \pm 0.23$
2013-08-03 09:23	1.35	VLT/FORS2	<i>I</i>	1.54	0.93	$24.22 \pm 0.15$
2011-11-28 06:14	1.80	Gemini/GMOS-N	<i>z</i>	1.01	0.84	$24.24 \pm 0.47$
2013-07-13 09:33	1.08	VLT/FORS2	<i>z</i>	1.49	0.63	$23.76 \pm 0.21$
2013-06-24 09:14	1.98	VLT/HAWK-I	<i>J</i>	1.70	0.63	$23.13 \pm 0.18$
2013-06-27 09:21	1.68	VLT/HAWK-I	<i>H</i>	1.63	0.91	$22.94 \pm 0.29$
2013-06-28 09:14	1.92	VLT/HAWK-I	<i>K<sub>s</sub></i>	1.65	0.76	$23.07 \pm 0.32$

<sup>a</sup> All magnitudes are given in the AB system and are not corrected for the expected Galactic foreground extinction corresponding to a reddening of  $E_{B-V} = 0.027$  mag.

a constraint on the dynamical mass of the galaxy (de Blok & Walter 2014). Based on the physical size along the slit and the velocity width of [O III] $\lambda 5007$ , we infer  $M_{\text{dyn}} \gtrsim 10^{10.8} M_{\odot}$ . Because we are viewing the host inclined at an angle relative to edge-on and because the slit is not aligned along the long axis of the host, this value is a lower limit.

### 3.2.2 Imaging observations and SED analysis

In addition to the spectroscopy presented above, we imaged the field of GRB 111117A in multiple broadband filters using the VLT equipped with FORS2 (*gRIz* filters) and HAWK-I (*JHK<sub>s</sub>* filters). These new data are complemented by a re-analysis of some of the imaging used in Margutti et al. (2012) and Sakamoto et al. (2013) that are available to us (GTC *gri*-band, TNG *R*-band, and Gemini *z*-band). A log of the photometric observations and measured brightnesses is given in Table 3.2. Most of the data were taken long after the GRB had faded when no afterglow contribution was present. Given the faintness of the afterglow (see Sect. 3.2.3, and Cucchiara & Cenko 2011; Cenko & Cucchiara 2011), we also expect negligible contribution to the earliest epochs, which is confirmed by the consistency between the two *g*-band measurements.

All data were reduced, analyzed, and fitted in a similar manner, as described in detail in Krühler et al. (2011a) and more recently in Schulze et al. (2018). We use our own Python and IRAF routines to perform a standard reduction that includes bias/flat-field correction, de-fringing (where necessary), sky-subtraction, and stacking of individual images. On the final reduced image products, DAOPHOT (Stetson 1987) was used to derive the reported photometry, where the size of the aperture was chosen to be 2''.0. Because image quality ranges from 0''.6 – 1''.7 and the galaxy

major axis is  $\sim 1''$ , this ensures that, in all cases, the large majority of the flux is collected and low surface brightness light missed in the aperture will not influence the measurement. This method sacrifices some S/N in the best seeing cases for more reliable photometry across differing observing conditions.

Photometric calibration was fixed relative to field stars from the SDSS and 2MASS catalogs in the case of  $griz$  and  $JHK_s$  filters, respectively. For the  $R$ - and  $I$ -band photometry, we used the color transformations of Lupton<sup>3</sup>. We convert all magnitudes into the AB system, and correct for a Galactic foreground of  $E_{B-V} = 0.027$  mag (Schlegel et al. 1998; Schlafly & Finkbeiner 2011).

Noteworthy are the discrepancy of our new VLT/FORS2 photometry and of the re-analysis of the Gemini data compared to the  $z$ -band measurements of Margutti et al. (2012) and Sakamoto et al. (2013). Both of these authors report  $z \sim 23$ , which is brighter than our measurement by  $\sim 1.0$  mag, while data taken in other filters are consistent within the errors. Visual inspection of the Gemini image shows only a marginal detection of the host, which we report here as a  $\sim 2\sigma$  measurement. More conservatively, the  $3\sigma$  upper limit for the Gemini image is  $z > 24.06$ . Objects of magnitude  $z \sim 23$  are clearly seen and are significantly brighter than the GRB host galaxy. The consistency between the deeper FORS2  $z$ -band image and the upper limit derived for the Gemini image lends credence to the inferred magnitudes presented here, see Fig. 3.4.

The multicolor SED is fit using the Bruzual & Charlot (2003) single stellar population models (SSPs) based on Chabrier (2003) with initial mass function in LePhare (Ilbert et al. 2006), where the redshift is fixed to the spectroscopic value of  $z = 2.211$ . For the SED fitting, we create a grid consisting of  $\sim 10^6$  different galaxy templates with four metallicities (0.02, 0.2, 0.4, 1.0  $Z_\odot$ ), different ages, star formation histories, and degrees of extinction. For every model, we calculate the likelihood, and create a probability density function (PDF) for a given parameter by marginalizing over the other parameters. We quote the median of the PDF as the best-fit parameters and the errors are the 16th and 84th percentiles of the PDFs (see, e.g., Schulze et al. 2018, for details on the SED fitting procedure).

The best-fit model is an unreddened galaxy template. The inferred physical parameters are the absolute magnitude ( $M_B = -22.0 \pm 0.1$  mag), the stellar mass ( $\log(M_*/M_\odot) = 9.9 \pm 0.2$ ), the stellar population age ( $\tau = 0.5^{+0.5}_{-0.3}$  Gyr), and the star formation rate ( $\text{SFR}_\text{SED} = 11^{+9}_{-4} M_\odot \text{ yr}^{-1}$ ). We show the SED fit in Fig. 3.3.

Without fixing the redshift to the spectroscopic value, using the revised photometry from Table 3.2, the photometric redshift of the galaxy is  $z_\text{phot} = 2.04^{+0.19}_{-0.21}$ , consistent with the spectroscopic value at the  $1\sigma$  confidence level. The large  $i - z$  color found in previous works was mistakenly interpreted as the 4000 Å break, driving the galaxy photometric redshift to a lower, erroneous value.

---

<sup>3</sup><http://www.sdss3.org/dr8/algorithms/sdssUBVRITransform.php>

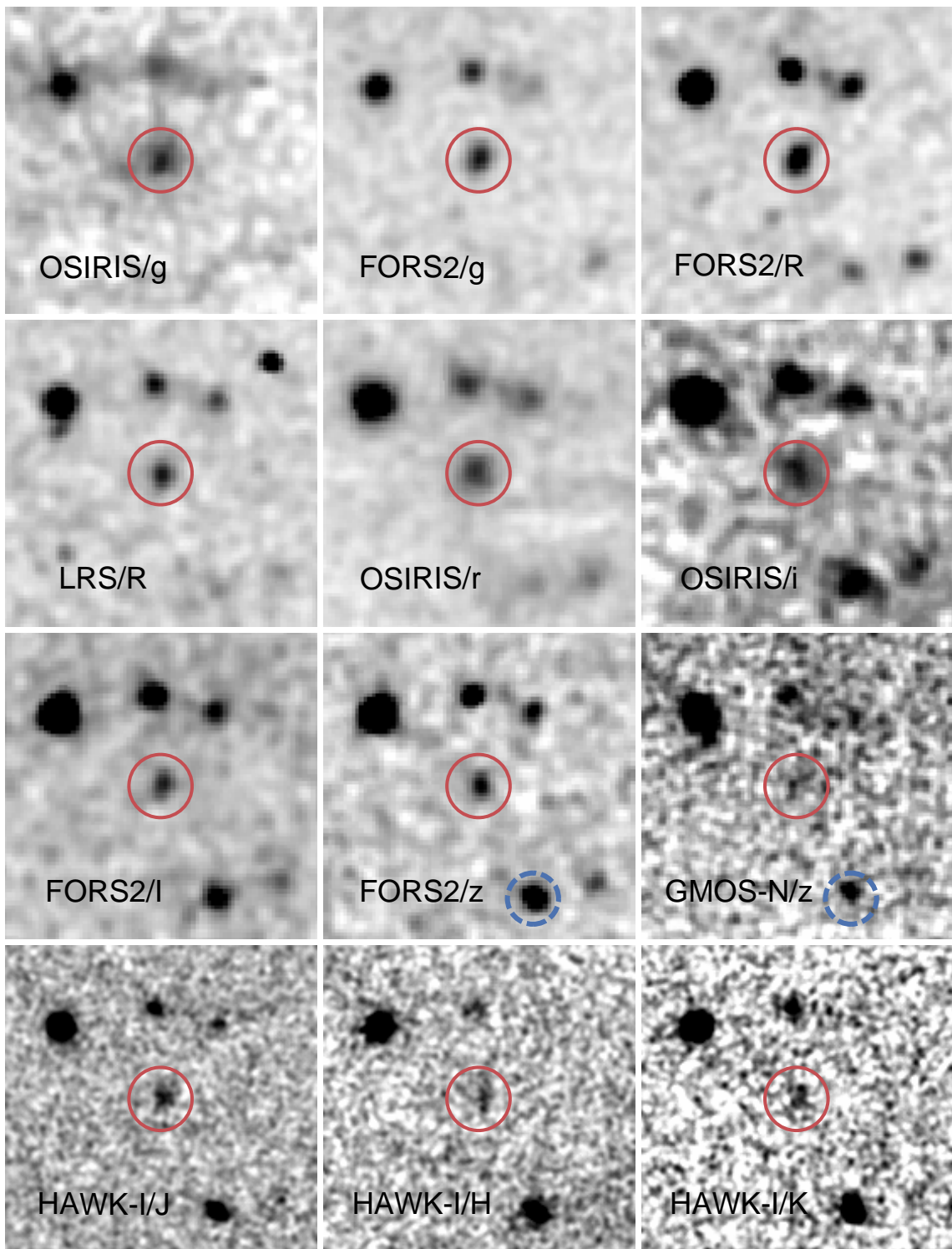


**Figure 3.4:** Mosaic showing all used imaging. The host of GRB 111117A is marked by a red circle with a  $2''.0$  radius. This is the same size as the aperture used to derive the photometry. Each panel is  $20''$  in size, north is up, east is left. Worth noting is the relative depth of the GMOS-N and FORS2  $z$ -band images. For reference, the object located to the southeast of the host and marked with a blue dashed circle has an extinction corrected magnitude of  $23.11 \pm 0.09$  ( $23.10 \pm 0.18$ ) in the FORS2 (GMOS-N)  $z$ -band.

### 3.2.3 X-ray temporal and spectral analysis

We retrieved the automated data products provided by the *Swift*-XRT GRB repository<sup>4</sup> (Evans et al. 2009). The X-ray afterglow light curve can be fit with a single power-law decay with an index  $\alpha = 1.27^{+0.12}_{-0.10}$ . We performed a time-integrated spectral analysis using data obtained in photon counting (PC) mode in the widest time epoch where the 0.3 – 1.5 keV to 1.5 – 10 keV hardness ratio is constant (namely, from  $t - T_0 = 205$  s to  $t - T_0 = 203.5$  ks, for a total of 29.1 ks of data) to prevent spectral changes that can affect the X-ray column density determination (Kopač et al. 2012). The obtained spectrum is described well by an absorbed power-law model and the best-fit spectral parameters are a photon index of  $2.1 \pm 0.4$  and an intrinsic equivalent hydrogen column density  $N_{\text{H},\text{X}}$  of  $2.4^{+2.4}_{-1.6} \times 10^{22} \text{ cm}^{-2}$  ( $z = 2.211$ ), assuming a solar abundance and a Galactic  $N_{\text{H},\text{X}}$  in the burst direction of  $4.1 \times 10^{20} \text{ cm}^{-2}$  (Willingale et al. 2013).

A measure of the optical-to-X-ray flux ratio is parametrized in terms of the darkness-parameter  $\beta_{\text{OX}}$  (Jakobsson et al. 2004). Using the optical afterglow limits ( $r' > 25.5$ , 13.5 hr after the burst; Cucchiara & Cenko 2011; Cenko & Cucchiara 2011), the X-ray light curve can be interpolated and evaluated at the time of the non-detection. We find  $\beta_{\text{OX}} < 0.79$ , consistent with the value that was reported in Sakamoto et al. (2013).

## 3.3 Reinterpretation of the rest-frame properties

Margutti et al. (2012) find a projected offset between the host nucleus and the GRB site of  $1''25 \pm 0''20$  arcsec; Sakamoto et al. (2013) find a similar value of  $1''0 \pm 0''20$  arcsec. These correspond to a projected physical offset at  $z = 2.221$  of  $10.6 \pm 1.7$  kpc and  $8.5 \pm 1.7$  kpc, respectively. Because the angular distance does not change significantly between  $z = 1.3$  and  $z = 2.211$ , all conclusions of Margutti et al. (2012) and Sakamoto et al. (2013) relating to host offset are unaffected.

### 3.3.1 Classification

Based on the BAT light curve,  $T_{90} = 0.46$  s, which is shorter than both the prototypical 2 s (Kouveliotou et al. 1993) and the  $< 0.8$  s suggested to also exclude the shorter tail of the *Swift*-observed IGRB population (Bromberg et al. 2012). Additionally, no signs of extended emission was found by Sakamoto et al. (2013). The spectral lag is  $0.6 \pm 2.4$  ms, consistent with zero. As already pointed out by Margutti et al. (2012) and Sakamoto et al. (2013), this is typical of sGRBs (but see also Bernardini et al. 2015). In conjunction with the duration and the spectral hardness (Sakamoto et al. 2011), GRB 111117A is thus securely classified as a sGRB. Because the observed classification indicators,  $T_{90}$  and hardness ratio, do not depend strongly on redshift (Littlejohns et al. 2013), the updated redshift does not change this designation.

---

<sup>4</sup>[http://www.swift.ac.uk/xrt\\_products/00507901](http://www.swift.ac.uk/xrt_products/00507901)

The intrinsic luminosity is shown in the X-ray light curve (Fig. 3.5) and it is subluminous compared to the majority of lGRBs. The inset in Fig. 3.5 shows the luminosity distribution at 10 ks. The subsamples comprise 402 lGRBs, 31 sGRBs, and GRB 111117A. The sample of lGRBs is from [Evans et al. \(2007, 2009\)](#) and the sample of sGRBs is compiled from [Kann et al. \(2011\)](#); [Berger \(2014\)](#), and [D'Avanzo et al. \(2014\)](#). The mean and the  $1-\sigma$  dispersions of the samples are  $\log(L_{\text{lGRB}}/\text{erg s}^{-1}) = 46.59 \pm 0.87$  and  $\log(L_{\text{sGRB}}/\text{erg s}^{-1}) = 44.96 \pm 0.94$  for the lGRB and sGRB samples, respectively. GRB 111117A had  $\log(L/\text{erg s}^{-1}) = 44.95$  at 10 ks. This is very close to the peak of the sGRB luminosity distribution at 10 ks, but an outlier from the lGRB distribution, further supporting the short classification.

The separation of GRBs in two distinct classes based on their high-energy observables points to an intrinsically different physical origin. Long GRBs are typically interpreted as collapsars ([MacFadyen & Woosley 1999b](#)) in which a single, massive star undergoes gravitational collapse, where the currently preferred model for sGRBs is the merger of two NSs ([Eichler et al. 1989; Nakar 2007](#)). [Bromberg et al. \(2013\)](#) investigated the degree to which high-energy observables of the long and short GRB populations overlap, and quantified the certainty in class membership. According to [Bromberg et al. \(2013\)](#), GRB 111117A has a  $96^{+3}_{-5}\%$  probability of being a sGRB. Compared to two other sGRB candidates at high redshift, GRB 060121 ( $T_{90} = 1.97 \pm 0.06$  s; [de Ugarte Postigo et al. 2006; Levan et al. 2006](#)) at  $1.7 \lesssim z \lesssim 4.5$  ( $17^{+14}_{-15}\%$ ) and GRB 090426 ( $T_{90} = 1.28 \pm 0.09$  s; [Antonelli et al. 2009; Levesque et al. 2010; Thöne et al. 2011](#)) at  $z = 2.609$  ( $10^{+15}_{-10}\%$ ), the certainty in class membership for GRB 111117A is much higher.

Additionally, [Horváth et al. \(2010\)](#) classify both GRB 060121 and GRB 090426 as intermediate-duration bursts because both events have very soft spectra, compared to the hard ones typically seen in sGRBs. Intermediate bursts are very clearly related in their properties to lGRBs ([de Ugarte Postigo et al. 2011a](#)), so they are unlikely to come from compact object mergers. GRB 111117A is also securely classified as a sGRB according to the [Horváth et al. \(2010\)](#) classification scheme.

A number of other GRBs are thought to be short and at relatively high redshift ( $z \gtrsim 0.9$ ). If we consider bursts with a probability of being short  $f_{\text{NC}} > 50\%$ , according to the [Bromberg et al. \(2013\)](#) classification scheme, five sGRB are found: GRB 051210 at  $z \sim 1.3$  ( $f_{\text{NC}} = 82^{+10}_{-61}\%$ ; [Leibler & Berger 2010](#)), GRB 060801 at  $z = 1.131$  ( $f_{\text{NC}} = 95^{+3}_{-5}\%$ ; [Berger et al. 2007](#)), GRB 070714 at  $z = 0.923$  (no  $f_{\text{NC}}$  due to extended emission; [Graham et al. 2009](#)), GRB 090510 at  $z = 0.903$  ( $f_{\text{NC}} = 97^{+1}_{-29}\%$ ; [McBreen et al. 2010](#)), and GRB 100117 at  $z = 0.915$  ( $f_{\text{NC}} = 97^{+1}_{-3}\%$ ; [Fong et al. 2011](#)). Although in individual cases a secure host association (hence redshift determination) is uncertain, there does seem to be a number of sGRBs at  $z \sim 1$ .

This certainly makes GRB 111117A, by far, the highest redshift sGRB detected to date. The redshift and classification of GRB 111117A imply that it occurred when the universe was younger by  $\sim 3$  Gyr compared to any other securely classified sGRB ever detected. If the merger of NSs is

the primary agent for the  $r$ -process element enrichment of the universe (Goriely et al. 2011; Ji et al. 2016; Komiya & Shigeyama 2016; Safarzadeh & Scannapieco 2017), this marks the earliest detection of this process.

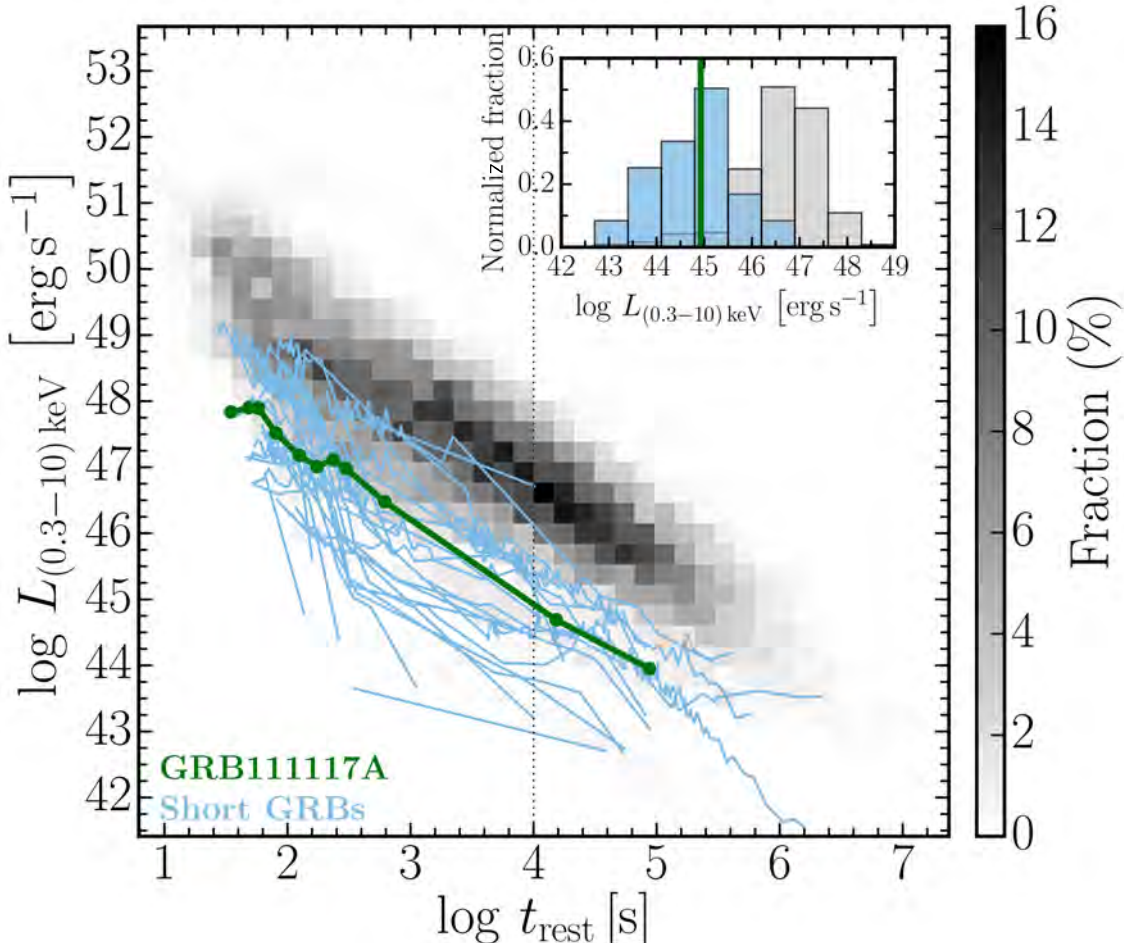


**Figure 3.5:** Rest-frame XRT light curve of GRB 111117A, compared to the general population of XRT light curves of GRBs. The gray shaded region is a compilation of long GRB light curves (Evans et al. 2007, 2009), where the color represents density. The light blue lines are sGRB light curves from bursts with duration of  $T_{90} \lesssim 2$  s and those that were classified as short in Kann et al. (2011); Berger (2014); D’Avanzo et al. (2014). The thick green line is GRB 111117A. Despite the remarkably high redshift, the luminosity is comparable to the bulk of the short burst population, and subluminous compared to the LGRB population. The inset shows the X-ray luminosity distributions of sGRBs and LGRBs at 10 ks, indicated by the vertical dashed line in the main panel.

### 3.3.2 Rest-frame $N_{\mathrm{H},\mathrm{X}}$

We show the recalculated hydrogen equivalent X-ray derived column density,  $N_{\text{H},\text{X}}$ , in Fig. 3.6, where we compare it with the distributions of complete samples of both long and short GRBs. The lGRB sample is from Arcodia et al. (2016) and the sGRB sample is from D’Avanzo et al. (2014).

From the sGRB sample of D'Avanzo et al. (2014) we have excluded GRB 090426, which likely does not belong in a short sample, as highlighted in Sect. 3.3.1. Both comparison samples infer  $N_{\text{H},\text{X}}$  over the largest temporal interval of constant hardness ratio to exclude spectral changes that can affect the X-ray derived column density. The 17 (5) of the 99 (15) long (short) GRBs that do not have measured redshifts have been excluded from our analysis.

GRB 111117A occupies a unique position in Fig. 3.6 with the highest  $N_{\text{H},\text{X}}$  and highest redshift of all sGRBs. The short sample, excluding GRB 111117A, is located at low redshift ( $z < 1$ ) and is found to populate a column density environment similar to that of lGRBs at comparable redshifts (D'Avanzo et al. 2014). The inferred hydrogen column density for GRB 111117A seems to follow the trend with increasing  $N_{\text{H},\text{X}}$  as a function of redshift as found for the lGRB afterglows (Campana et al. 2010; Starling et al. 2013; Arcodia et al. 2016). This is related to what has been found by Kopač et al. (2012) and Margutti et al. (2013) that  $N_{\text{H},\text{X}}$  seems to be comparable for long and short GRBs when compared at similar redshifts.

The redshift evolution of  $N_{\text{H},\text{X}}$  in the hosts of lGRBs is not reproduced by Buchner et al. (2017), who use a different  $N_{\text{H},\text{X}}$  inference methodology. Instead, a correlation between  $N_{\text{H},\text{X}}$  and host stellar mass is suggested. Assuming that the different  $N_{\text{H},\text{X}}$ -fitting methodologies yield comparable results, GRB 111117A has a higher  $N_{\text{H},\text{X}}$  compared to the relation suggested by Buchner et al. (2017) by more than the intrinsic scatter, although some lGRB hosts populate a similar region in the  $N_{\text{H},\text{X}} - M_{\star}$  relation.

The large offset of GRB 111117A relative to the host center derived in Margutti et al. (2012) and Sakamoto et al. (2013) is difficult to reconcile with galaxy-scale gas being the source of the X-ray absorption. Along with the low dust content of the host, the large offset from the host center indicates that the high  $N_{\text{H},\text{X}}$  arises because the density in the GRB surroundings is high (or possibly because the light from the afterglow transverses localized regions of dense gas) (see, e.g., Watson et al. 2013; Krongold & Prochaska 2013). Alternatively, it has been hypothesized that a significant contribution to the observed X-ray  $N_{\text{H},\text{X}}$  could come from the diffuse intergalactic medium and the intervening systems along the line of sight of the GRB (Campana et al. 2012; Arcodia et al. 2016) (but see also Watson et al. 2013; Krongold & Prochaska 2013).

Even assuming a low dust-to-metals ratio, as typically observed in long GRB afterglow sightlines (Galama & Wijers 2001; Schady et al. 2010; Covino et al. 2013), the  $N_{\text{H},\text{X}}$  value derived from the X-ray spectrum corresponds to significant extinction along the afterglow line of sight ( $A_V \gtrsim 1$  mag), which is contrasted with the absence of dust found from the SED fit and supported by the detection of Ly $\alpha$ . This discrepancy between the extinction derived from the GRB afterglow and that obtained using galaxy-wide measures has also been observed occasionally for lGRBs (Perley et al. 2013). For the one sGRB where both parameters were measured (GRB 130603B; de Ugarte Postigo et al. 2014b), they were found to be consistent with  $A_V \sim 1$  mag.

The lack of optical detection is also consistent with a high column along the GRB line of sight, as dust extinction could contribute to the optical faintness. On the contrary, its X-ray afterglow flux lies within the expected distribution given its gamma-ray fluence (D'Avanzo et al. 2014). This is not unexpected, as the X-ray flux is independent of the surrounding medium density (Freedman & Waxman 2001; Berger et al. 2003; Nysewander et al. 2009).

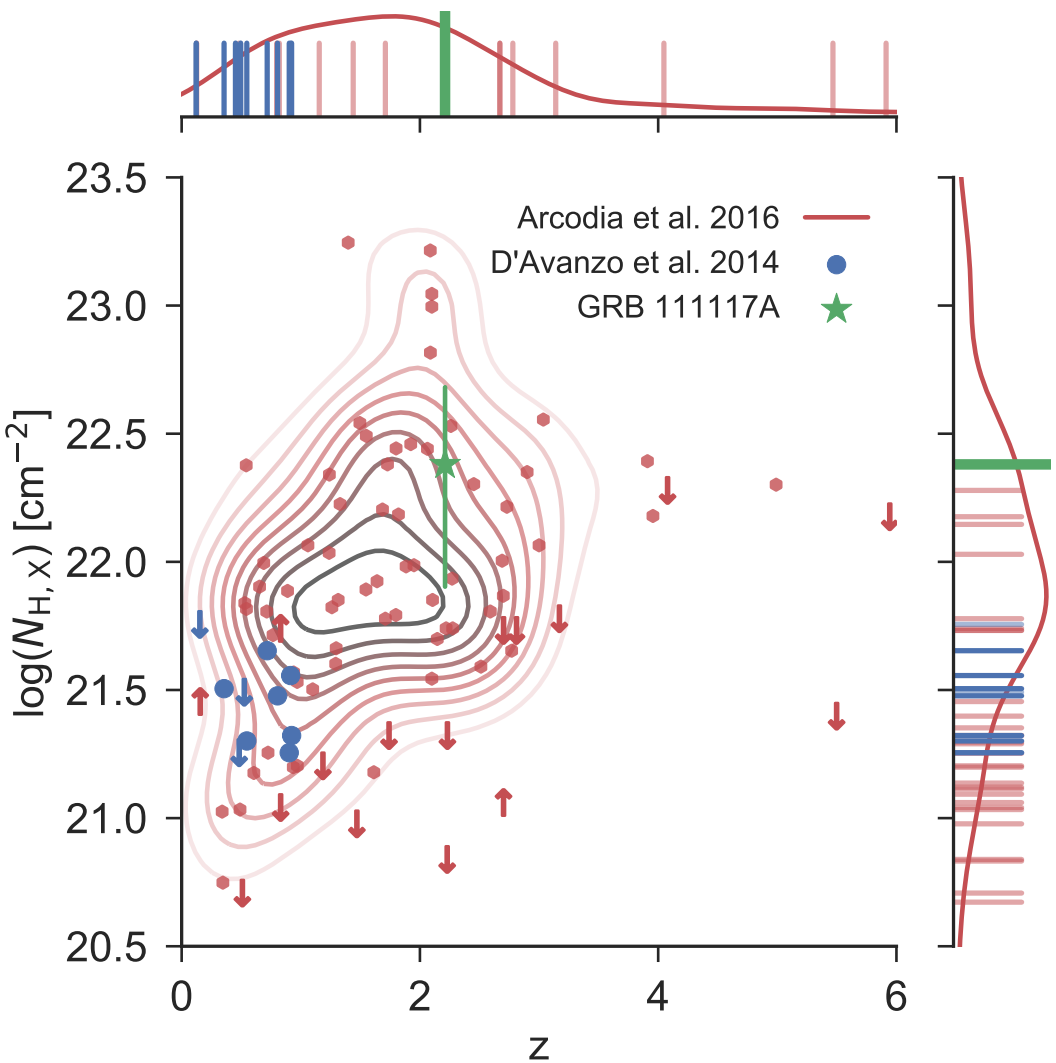


**Figure 3.6:** Rest frame, X-ray derived equivalent hydrogen column density of GRB 111117A compared to complete samples of both long and short populations of GRBs. The sample of lGRBs from Arcodia et al. (2016) is shown in red, where detections are also shown with a kernel density estimate of the points, and the limits on  $N_{\text{H},\text{X}}$  are shown with arrows. The complete sample of sGRB by D'Avanzo et al. (2014) is shown in blue, where again the limits are indicated by arrows. Marginalizations over both axes are shown on the right and at the top of the plot, where the limits are shown as semi-transparent bars and detections as solid ones. The red curves in the marginalization plots are again the kernel density estimates of the Arcodia et al. (2016) sample.

### 3.3.3 Host galaxy

Because of the secure host association, GRB 111117A does not belong to the hostless class of sGRBs (Berger 2010) and because the host exhibits emission lines, this is indicative of a population of relatively young stars. Like the majority of sGRBs (Fong et al. 2013), the host of GRB 111117A is therefore a late-type galaxy and is entirely consistent in terms of stellar mass and stellar age with the general population of sGRB hosts ( $\langle M_* \rangle = 10^{10.1} M_\odot$  and  $\langle \tau_* \rangle = 0.3$  Gyr; Leibler & Berger 2010). Being a late-type host, both the stellar mass and sSFR are entirely within the range expected for the hosts of sGRBs (Behroozi et al. 2014). Our constraint on the dynamical mass is also well accommodated by the expected sGRB host halo mass (Behroozi et al. 2014).

The SFR is  $\sim 1$  order of magnitude higher than the typical SFR for sGRB host galaxies (Berger 2014) and more similar to the SFR found in the hosts of lGRBs at a corresponding redshift (Krühler et al. 2015a). Only two hosts in the sample of short GRBs compiled by Berger (2014) have a more vigorous star formation, placing it at the very upper end of the star formation distribution. The cosmic SFR evolution of the universe likely plays a role due to the proximity of GRB 111117A to the peak of cosmic SFR (Madau & Dickinson 2014). The high SFR is partly a selection effect; a less star-forming galaxy would exhibit weaker emission lines, thus making the redshift harder to determine. Additionally, it is natural to expect some evolution in the hosts of sGRBs with redshift as illustrated for  $N_{\mathrm{H},\mathrm{X}}$  in Sect. 3.3.2.

The simultaneous detection of Ly $\alpha$  and H $\alpha$  allows us to put constraints of the escape fraction of Ly $\alpha$ ,  $f_{\mathrm{esc}}(\mathrm{Ly}\alpha)$ . Using the intrinsic ratio between H $\alpha$  and Ly $\alpha$ , assuming case B recombination (Brocklehurst 1971), and the measured fluxes from the spectrum, we find  $f_{\mathrm{esc}}(\mathrm{Ly}\alpha) < 0.06$ . While the  $f_{\mathrm{esc}}(\mathrm{Ly}\alpha)$  scales with the dust column (Hayes et al. 2011), the resonant scattering of Ly $\alpha$ -photons with neutral hydrogen makes the effective path length of Ly $\alpha$  longer than for H $\alpha$  (Atek et al. 2009). This makes  $f_{\mathrm{esc}}(\mathrm{Ly}\alpha)$  an unreliable proxy for dust column, especially at low dust columns (Atek et al. 2014) where the geometry and dynamics of the H I within the galaxy will affect the Ly $\alpha$  path the most. The  $f_{\mathrm{esc}}(\mathrm{Ly}\alpha)$  inferred for the host is entirely consistent with what is found for field galaxies with similar properties (Oyarzún et al. 2017). The same authors also find that Ly $\alpha$  emitting galaxies mostly have little dust, consistent with what is inferred from the SED fit (see Sect. 3.2.2). The centroid of the Ly $\alpha$  emission is found to be redshifted by  $\sim 240 \pm 90 \text{ km s}^{-1}$  with respect to systemic, which is similar to what is found for long GRB hosts (Milvang-Jensen et al. 2012) and Lyman break galaxies (Shapley et al. 2003) where the outflow is attributed to star formation.

### 3.4 Implications for the redshift distribution of sGRBs

The redshift distribution of GRBs provides valuable information not only on the conditions that drive the formation of these events, but also on the potential influence these cosmic explosions have on the evolution of the universe. Due to the elevated brightness of lGRBs compared to sGRBs (Berger 2014) and their tendency to be associated with the star-forming and therefore dense regions in their hosts (Fruchter et al. 2006; Lyman et al. 2017), the redshifts of lGRBs are easier to measure than those of their sGRB counterparts, where only a single burst has a redshift measurement from the GRB afterglow (Cucchiara et al. 2013; de Ugarte Postigo et al. 2014b). Correspondingly, the redshift distribution of sGRBs is still substantially unconstrained compared to that of lGRBs (see, e.g., Jakobsson et al. 2012b; D’Avanzo 2015; Perley et al. 2016b).

A single sGRB at high redshift does little in terms of constraining the redshift distribution of sGRBs. In particular, other sGRB host redshifts could have been missed because their hosts are intrinsically fainter and thus the high redshift of GRB 111117A is only measured due to the brightness of its host. Berger (2014) compiled a sample of sGRB host luminosities, normalized by the characteristic galaxy luminosity at their respective redshift,  $L_B/L_B^*$ . To convert the SED-inferred  $M_B$  of GRB 111117A to  $L_B/L_B^*$ , we use the characteristic absolute  $B$ -band magnitude of the Schechter function for blue galaxies ( $U - V < 0.25$ ) in the redshift window  $2.0 \leq z \leq 2.5$  from Marchesini et al. (2007) and obtain  $L_B/L_B^* = 1.2$ .

Using the complete, flux-limited selection of *Swift*-detected bursts from D’Avanzo et al. (2014), excluding GRB 111117A and the likely non-sGRB GRB 090426, we have a statistically homogeneous sample from which we can address the implications of the redshift of GRB 111117A. This sample includes sGRBs originating in star-forming galaxies, elliptical galaxies, and apparent hostless sGRBs. Of the 14 hosts in the sample, 10 (71 %) have both measured redshifts and  $L_B/L_B^*$ . Compared to the complete sample, the host of GRB 111117A is brighter than 80 % of the hosts with measured  $L_B/L_B^*$ . Even if we conservatively assume that all the hosts missing  $L_B/L_B^*$  are brighter than the host of GRB 111117A, the host is still brighter than > 60 % of sGRB hosts. The host of GRB 111117A is brighter than 73 % of all 26 hosts with  $L_B/L_B^*$  from Berger (2014).

If we assume that we are able to obtain emission-line redshifts from hosts which are at most 0.5 mag fainter ( $R < 24.5$  mag; Krühler et al. 2012a), and if they were at the redshift of GRB 111117A, we would miss 60 % of the redshifts (6 out of 10 hosts) because the host is too faint. The corresponding number is around 45 % (12 out of 26) of the full sample of Berger (2014), reflecting the lower mean  $L_B/L_B^*$  of the complete sample. Because the average SFR of galaxies hosting lGRBs is higher than for galaxies hosting sGRBs, the fraction of missed burst redshifts is likely higher, although the cosmic SFR evolution could play a role in improving redshift determinability at high  $z$ .

A fraction of the bursts missing redshift are host-less, but appear to be spatially correlated

with galaxies that are likely at moderate redshifts (Tunnicliffe et al. 2014); should some of the remainder be at high redshift, the missed fraction would increase. If we assume that all the bursts that are missing redshifts are at high  $z$  and are missed due to host faintness, 10 out of 14 hosts in the complete sample (71 %) would be missed at  $z = 2.211$ . This serves as an upper limit on the fraction of missed burst redshifts at high  $z$ . Conversely, if all bursts missing redshift were at low redshift and missed for other reasons, 6 out of 14 hosts (43 %) would be missed at  $z = 2.211$ . The two limits indicate that we would miss between 43 % and 71 % of *Swift*-detected sGRB hosts at  $z \sim 2$  due to host faintness.

The theoretical redshift distribution of sGRBs depends on the type of delay-time function used to model the progenitor system. The likelihood preferred lognormal time delay models investigated by Wanderman & Piran (2015) predict a sGRB rate at  $z = 2.211$ , around two orders of magnitude lower than the peak rate at  $z = 0.9$ . According to Wanderman & Piran (2015), this preference depends critically on the absence of sGRBs at  $z \gtrsim 1.2$ . The higher determined redshift of GRB 111117A, and the likely number of additional high- $z$  sGRB could change the preferred time delay models. The redshift of GRB 111117A, on the other hand, is close to the expected peak in sGRB rate calculated using the power-law delay time models (Behroozi et al. 2014; Wanderman & Piran 2015; Ghirlanda et al. 2016), meaning we would be missing a large fraction of sGRB redshifts.

A critical test to assess whether the power-law delay time models can be accommodated by the current observation is to check if the implied sGRB rate at higher redshift does not exceed the number of observed sGRBs without redshifts. Of the 100 sGRBs observed by *Swift*, 20 have secure redshifts, and another 7 have a tentative redshift measurement<sup>5</sup>, meaning that  $> 73\%$  of all sGRBs observed with *Swift* are missing redshifts. More recently, Fong et al. (2017a) (LIGO Scientific Collaboration et al. 2017) compiled a list of 36 (33) sGRBs with redshift measurements and, using this number, the redshift incompleteness of sGRBs decreases to 64 %. In addition to the potential number of high- $z$  events already detected but missing redshifts, Behroozi et al. (2014) parametrized the *Swift* redshift sensitivity and found that the mean detection probability for sGRBs at  $z \sim 2$  was only  $\sim 1\%$  of the mean detection probability at  $z \sim 1$ , assuming that the unknown beaming angle of sGRBs stays constant with time. What this means is that at present, there is almost no limit on the number of sGRBs that could be at redshifts  $z > 2$ .

### 3.5 Constraints on progenitor separation

At  $z = 2.211$ , the age of the universe is 3 Gyr. If the progenitor systems of sGRBs are the merger of two NSs, this sets a hard upper limit to the coalescence timescale for such a system. In the absence

---

<sup>5</sup>This is based on <http://www.astro.caltech.edu/grbox/grbox.php>, selecting all *Swift*-detected sGRBs up to GRB 170428A.

of other mechanisms, the timescale of the orbital decay of the system is set by the energy loss due to GWs, which in turn is set by the mass of the constituent compact objects, the eccentricity of the orbit, and the separation of the two (Postnov & Yungelson 2014). If we assume that the formation timescale of the first galaxies is short compared to the time since the Big Bang (Richard et al. 2011), and that any binary NS formation channel can work sufficiently fast, we can—assuming a mass of each of the NSs in a circular orbit at the time of system formation—place a hard upper limit on the initial separation,  $a_0$ .

In practice, most NS–NS binaries will be eccentric at formation because of the SN natal kicks. For more eccentric orbits, the coalescence timescale decreases, leading to a larger initial separation constraint. As noted by Postnov & Yungelson (2014), it takes eccentricities  $> 0.6$  to significantly shorten the merger time. Due to tidal interactions between the two NSs, the orbits will also tend to circularize with time, lessening the impact of the eccentricity on the constraint.

Additionally, the constraint on initial progenitor separation will change depending on the mass assumed for the constituent NS masses, with higher masses generally resulting in faster inspiral times and weaker constraints of initial separation. We use the NS mass distribution from Kiziltan et al. (2013) to compute a grid of initial progenitor separation constraints, given the range of NS masses allowed. We show the grid in Fig. 3.7. The double NS binary systems have a constituent mass distribution peaked at  $1.33_{-0.12}^{+0.10} M_\odot$  (Kiziltan et al. 2013), which corresponds to  $a_0 < 3.1_{-0.2}^{+0.2} R_\odot$  where the errors are the 68 % posterior predictive intervals.

Using the inferred stellar population age from our SED fit, we obtain a less robust limit on the initial separation of  $a_0 < 2.0_{-0.4}^{+0.4} R_\odot$ . However, this does not account for the possibility that there could be an underlying stellar population of older stars from a previous star formation episode. To investigate the possible impact of the presence of an old stellar population, we followed Papovich et al. (2001) and re-fitted the observed SED with the best-fit template to which an additional stellar population of old stars was added. For each template, this old population was set as the SSP with the same parameters as the best-fit SED except the age, which was set to the age of the Universe at the observed redshift. In principle, this can constrain the maximum contribution of old populations within the photometric error bars (for details, see Papovich et al. 2001). We find a negligible contribution to the stellar mass (i.e., variations much smaller than the statistical uncertainty associated with the best-fit template).

The delay time between formation and explosion is well accommodated by the models of Belczynski et al. (2006) where a range of binary NS systems and their decays are followed in different host potentials; however, some of the longest delay times are excluded. Given the late-type nature of the host, only a small subset of the longest population synthesis models violates the delay time constraint derived here (O’Shaughnessy et al. 2008). The same holds if NS binaries are primarily formed through dynamical interactions in globular clusters (Lee et al. 2010; Church

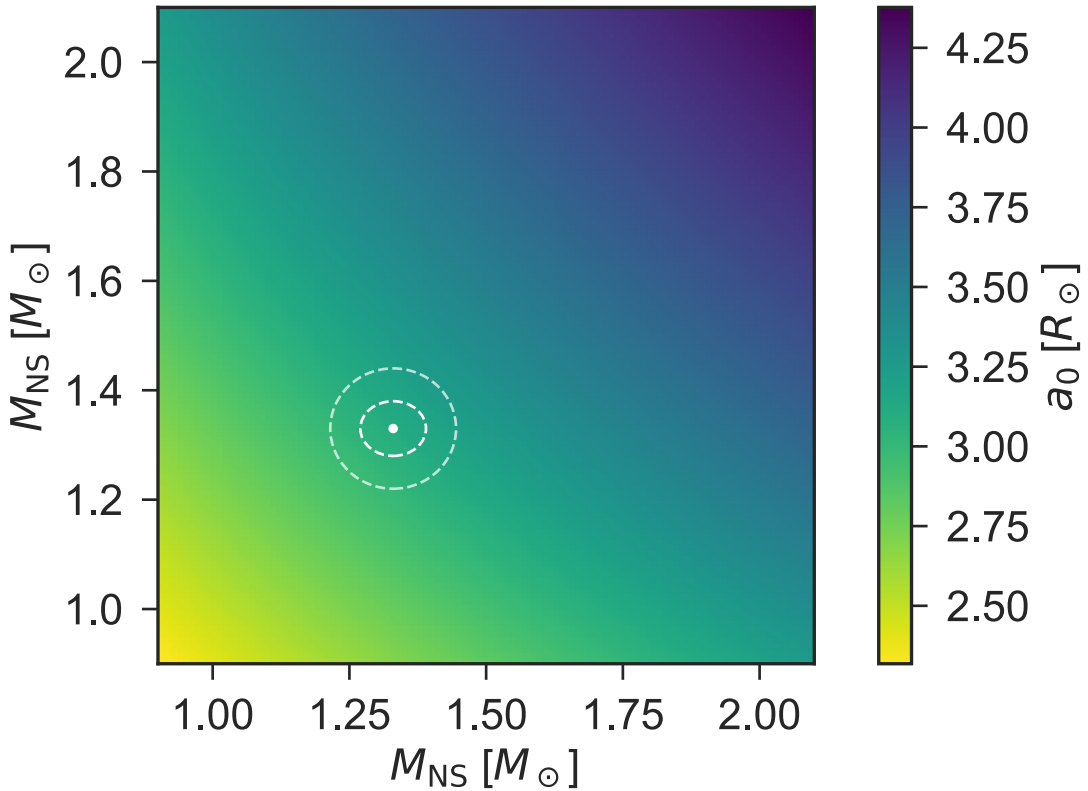


**Figure 3.7:** Constraints on the initial progenitor separation, given binary constituent masses. As can be seen, a heavier system will inspiral faster, leading to a weaker constraint on the initial separation of the binary. The most probable value, the 68 % and 98 % posterior predictive intervals of the NS binary mass distribution from Kiziltan et al. (2013), are shown with the dashed ellipses, which corresponds to a constraint on a maximum initial separation of  $a_0 < 3.1^{+0.2(+0.4)}_{-0.2(-0.4)} R_\odot$ , respectively.

et al. 2011).

### 3.6 Conclusions

We have provided here a revised, spectroscopic redshift measurement for the short GRB 111117A based on host galaxy emission lines, setting it at  $z = 2.211 \pm 0.001$ . This value supersedes the previous photometric redshift estimates of Margutti et al. (2012) and Sakamoto et al. (2013). The erroneous best-fit SED redshift of previous authors is attributed to a discrepancy in the measured  $z$ -band magnitude, and highlights the importance of deep spectroscopic studies of sGRB hosts at medium resolution.

Using the new distance, the X-ray derived  $N_{\text{H},\text{X}}$  towards GRB 111117A is the highest within a complete sample of sGRBs and is consistent with the  $N_{\text{H},\text{X}} - z$  evolution traced by the sight lines of lGRBs. The SFR of the host is in the upper end of the sGRB host SFR distribution and

no significant amount of dust is present. The high  $N_{\text{H},\text{X}}$  is at odds with the large projected host offset and the absence of dust. One possible explanation could be that GRB 111117A is formed through a prompt channel of sGRB formation and originates in an unseen star-forming region located in the outskirts of the host, or a localized region of high H $\alpha$  density along the line of sight.

Although a single burst carries little leverage in terms of constraining the redshift distribution of sGRB, the high redshift of GRB 111117A needs to be accommodated in progenitor models. A lognormal delay time model predicts a very low volumetric density of bursts at  $z \sim 2$ , whereas a power-law delay time model peaks near the GRB 111117A redshift. If more sGRBs are at similarly high redshifts, but are missed because of the faintness of their hosts and afterglows, a lognormal delay time model will be disfavored. Compared to a complete sample of *Swift*-detected sGRB, the host of GRB 111117A is more luminous than 80 % of sGRB hosts with measured luminosities. Assuming a host brightness redshift determination threshold for 43 – 71 % of the sample hosts, we would be unable to determine a redshift if they were at a similar redshift to that of GRB 111117A. This could indicate that, potentially, a significant fraction of *Swift*-detected sGRBs are at high  $z$ , but with redshifts unknown due to host faintness.

Using the age of the universe at the time of explosion allows us to set constraints on the maximum separation between the engine constituents at the time of formation. We find that the maximum separation of two NSs at system formation time is  $a_0 < 3.1 R_\odot$ , which excludes some of the formation channels with the longest timescales.

## Acknowledgements

We thank the anonymous referee for the constructive report. We thank Jens Hjorth and Lise Christensen for useful discussions regarding the interpretation of this event. We thank Mathieu Puech for testing the possible contribution from an older stellar population in the SED. We thank Peter Laursen for fruitful discussions regarding the Ly $\alpha$  escape fraction. TK acknowledges support through the Sofja Kovalevskaja Award to P. Schady. SDV is supported by the French National Research Agency (ANR) under contract ANR-16-CE31-0003 BEaPro. PDA and SCo acknowledge support from ASI grant I/004/11/3. JJ acknowledges support from NOVA and a NWO-FAPESP grant for advanced instrumentation in astronomy. NRT and KW acknowledge support from STFC Consolidated Grant ST/N000757/1. CT acknowledges support from a Spanish National Research Grant of Excellence under project AYA 2014-58381-P and funding associated with a Ram $\tilde{\text{A}}$ n y Caj $\tilde{\text{A}}$ l fellowship under grant number RyC-2012-09984. AdUP acknowledges support from a Ram $\tilde{\text{A}}$ n y Cajal fellowship, a BBVA Foundation Grant for Researchers and Cultural Creators, and the Spanish Ministry of Economy and Competitiveness through project AYA2014-58381-P. ZC acknowledges support from the Spanish research project AYA 2014-58381-P and support from Juan de la Cierva Incorporaci $\tilde{\text{o}}$ n fellowships IJCI-2014-21669. RSR acknowledges AdUP's BBVA

Foundation Grant for Researchers and Cultural Creators and support from the Italian Space Agency (ASI) through Contract n. 2015-046-R.0 and from the European Union Horizon 2020 Programme under the AHEAD project (grant agreement n. 654215). This research made use of Astropy, a community-developed core Python package for Astronomy ([Astropy Collaboration 2013](#)). The analysis and plotting was achieved using the Python-based packages Matplotlib ([Hunter 2007](#)), Numpy, and Scipy ([van der Walt et al. 2011](#)), along with other community-developed packages. This work made use of observations obtained with the Italian 3.6 m Telescopio Nazionale Galileo (TNG) operated on the island of La Palma by the Fundación Galileo Galilei of the INAF (Istituto Nazionale di Astrofisica) at the Spanish Observatorio del Roque de los Muchachos of the Instituto de Astrofísica de Canarias. Based on data from the GTC Archive at CAB (INTA-CSIC) and on observations obtained at the Gemini Observatory, which is operated by the Association of Universities for Research in Astronomy, Inc., under a cooperative agreement with the NSF on behalf of the Gemini partnership: the National Science Foundation (United States), the National Research Council (Canada), CONICYT (Chile), Ministerio de Ciencia, Tecnología e Innovación Productiva (Argentina), and Ministério da Ciência, Tecnologia e Inovação (Brazil).

# 4

## OBSERVATIONS OF A NEUTRON STAR MERGER

This chapter contains the following article:

### **“Spectroscopic identification of r-process nucleosynthesis in a double neutron-star merger”**

Published in *Nature*, vol. 551, issue 7678, pp. 67-70, 2017.

Authors:

E. Pian, P. D’Avanzo, S. Benetti, M. Branchesi, E. Brocato, S. Campana, E. Cappellaro, S. Covino, V. D’Elia, J. P. U. Fynbo, F. Getman, G. Ghirlanda, G. Ghisellini, A. Grado, G. Greco, J. Hjorth, C. Kouveliotou, A. Levan, L. Limatola, D. Malesani, P. A. Mazzali, A. Melandri, P. Møller, L. Nicastro, E. Palazzi, S. Piranomonte, A. Rossi, O. S. Salafia, J. Selsing, G. Stratta, M. Tanaka, N. R. Tanvir, L. Tomasella, D. Watson, S. Yang, L. Amati, L. A. Antonelli, S. Ascenzi, M. G. Bernardini, M. Boër, F. Bufano, A. Bulgarelli, M. Capaccioli, P. G. Casella, A. J. Castro-Tirado, E. Chassande-Mottin, R. Ciolfi, C. M. Copperwheat, M. Dadina, G. De Cesare, A. Di Paola, Y. Z. Fan, B. Gendre, G. Giufrida, A. Giunta, L. K. Hunt, G. Israel, Z.-P. Jin, M. Kasliwal, S. Klose, M. Lisi, F. Longo, E. Maiorano, M. Mapelli, N. Masetti, L. Nava, B. Patricelli, D. Perley, A. Pescalli, T. Piran, A. Possenti, L. Pulone, M. Razzano, R. Salvaterra, P. Schipani, M. Spera, A. Stamerra, L. Stella, G. Tagliaferri, V. Testa, E. Troja, M. Turatto, S. D. Vergani, & D. Vergani

The merger of two neutron stars is predicted to give rise to three major detectable phenomena: a short burst of  $\gamma$ -rays, a gravitational-wave signal, and a transient optical–near-infrared source powered by the synthesis of large amounts of very heavy elements via rapid neutron capture (the r-process) (Lattimer et al. 1977; Eichler et al. 1989; Li & Paczyński 1998). Such transients, named ‘macronovae’ or ‘kilonovae’ (Kulkarni 2005; Tanaka & Hotokezaka 2013; Rosswog et al. 2017; Wollaeger et al. 2017) are believed to be centres of production of rare elements such as gold and platinum (Metzger 2017). The most compelling evidence so far for a kilonova was a very faint near-infrared rebrightening in the afterglow of a short  $\gamma$ -ray burst (Tanvir et al. 2013a; Berger et al. 2013a) at redshift  $z = 0.356$ , although findings indicating bluer events have been reported (Jin et al. 2016). Here we report the spectral identification and describe the physical properties of a bright kilonova associated with the gravitational-wave source (Abbott et al. 2017b) GW170817 and  $\gamma$ -ray burst (Goldstein et al. 2017; Savchenko et al. 2017b) GRB 170817A associated with a galaxy at a distance of 40 megaparsecs from Earth. Using a series of spectra from ground-based observatories covering the wavelength range from the ultraviolet to the near-infrared, we find that the kilonova is characterized by rapidly expanding ejecta with spectral features similar to those predicted by current models (Kasen et al. 2015; Tanaka et al. 2018). The ejecta is optically thick early on, with a velocity of about 0.2 times light speed, and reaches a radius of about 50 astronomical units in only 1.5 days. As the ejecta expands, broad absorption-like lines appear on the spectral continuum, indicating atomic species produced by nucleosynthesis that occurs in the post-merger fast-moving dynamical ejecta and in two slower (0.05 times light speed) wind regions. Comparison with spectral models suggests that the merger ejected 0.03 to 0.05 solar masses of material, including high-opacity lanthanides.

## 4.1 Main

GW170817 was detected on 17 August 2017, 12:41:04 universal time (UT) (Abbott et al. 2017b). A weak, short-duration ( $t \approx 2s$ )  $\gamma$ -ray burst (GRB) in the gravitational-wave error region triggered the Fermi GRB monitor (Fermi-GBM) about two seconds later (Goldstein et al. 2017), and was detected also by INTEGRAL SPI-ACS (spectrometer on the International Gamma-Ray Astrophysics Laboratory (INTEGRAL) anticoincidence system) (Savchenko et al. 2017b). Considerably improved sky localization was obtained from the joint analysis of LIGO and Virgo data of the gravitational-wave event, with a 90 % error region of 33.6 square degrees (Abbott et al. 2017b). This joint gravitational-wave/GRB detection was followed by an extensive worldwide observational campaign using space- and ground-based telescopes to scan the sky region where the events were detected. A new point-like optical source (coordinates right ascension  $\alpha(J2000) = 13^{\text{h}} 09^{\text{m}} 48.09^{\text{s}}$ , declination  $\delta(J2000) = -23^{\circ} 22' 53.3''$ ) was soon reported (Coulter et al. 2017; Valenti et al. 2017), located at 10 arcsec from the centre of the S0 galaxy NGC 4993 ( $z = 0.00968$ ; Jones et al. 2009) in

the ESO 508-G018 group and at a distance of 40 Mpc from Earth, consistent with the luminosity distance of the gravitational-wave signal. It was first named ‘SSS17a’ and ‘DLT17ck’, but here we use the official IAU designation, AT 2017gfo.

We carried out targeted and wide-field optical/near-infrared imaging observations of several bright galaxies within the reconstructed sky localization of the gravitational-wave signal with the Rapid Eye Mount (REM) telescope and with the European Southern Observatory (ESO) Very Large Telescope (VLT) Survey Telescope (ESO-VST). This led to the detection of AT 2017gfo in the REM images of the field of NGC 4993, which were obtained 12.8 h after the gravitational-wave/GRB event. Following the detection of this source, we started an imaging and spectroscopic follow-up campaign at optical and near-infrared wavelengths. Imaging was carried out with the REM telescope, the ESO-VST and the ESO-VLT. A series of spectra was obtained with the VLT/X-shooter in the wavelength range 3200–24800 Å, with VLT/FORS2 (Focal Reducer/low-dispersion Spectrograph) in 3500–9000 Å and with Gemini-S/GMOS in 5500–9000 Å (see [Kasliwal et al. \(2017\)](#) for GMOS reduction and analysis details). Overall, we observed the source with an almost daily cadence during the period 17 August 2017 to 3 September 2017 (about 0.5–17.5 days after the gravitational-wave/GRB trigger; details are provided in Methods). We present here the results of the observations carried out in August 2017.

As described in the following, the analysis and modelling of the spectral characteristics of our dataset, together with their evolution with time, result in a good match with the expectations for kilonovae, providing the first compelling observational evidence for the existence of such elusive transient sources. Details of the observations are provided in Methods.

We adopted a foreground Milky Way extinction of  $E(B - V) \approx 0.1$  mag and the extinction curve of [Cardelli et al. \(1989\)](#) and used them to correct both magnitudes and spectra (see Methods). The extinction within the host galaxy is negligible according to the absence of substantial detection of characteristic narrow absorption features associated with its interstellar medium. The optical light curve resulting from our data is shown in Fig. 4.1 and the sequence of X-shooter, FORS2 and GMOS spectra is shown in Fig. 4.2. Apart from Milky Way foreground lines, the spectrum is otherwise devoid of narrow features that could indicate association with NGC 4993. In the slit, which was displaced from the position of the transient by  $3''$ – $10''$  (0.6–2.0 kpc in projection), we detected narrow emission lines exhibiting noticeable structure, both spatially and in velocity space (receding at  $100 - 250$  km s $^{-1}$  with respect to the systemic velocity), which were probably caused by the slit crossing a spiral structure of the galaxy (see Methods).

The first X-shooter spectrum of the transient shows a bright, blue continuum across the entire wavelength coverage – with a maximum at about 6000 Å and total luminosity of  $3.2 \times 10^{41}$  erg s $^{-1}$  – that can be fitted with the spectrum of a blackbody of temperature  $5000 \pm 200$  K and a spherical equivalent radius of approximately  $8 \times 10^{41}$  cm. At a phase of 1.5 days after the gravitational-

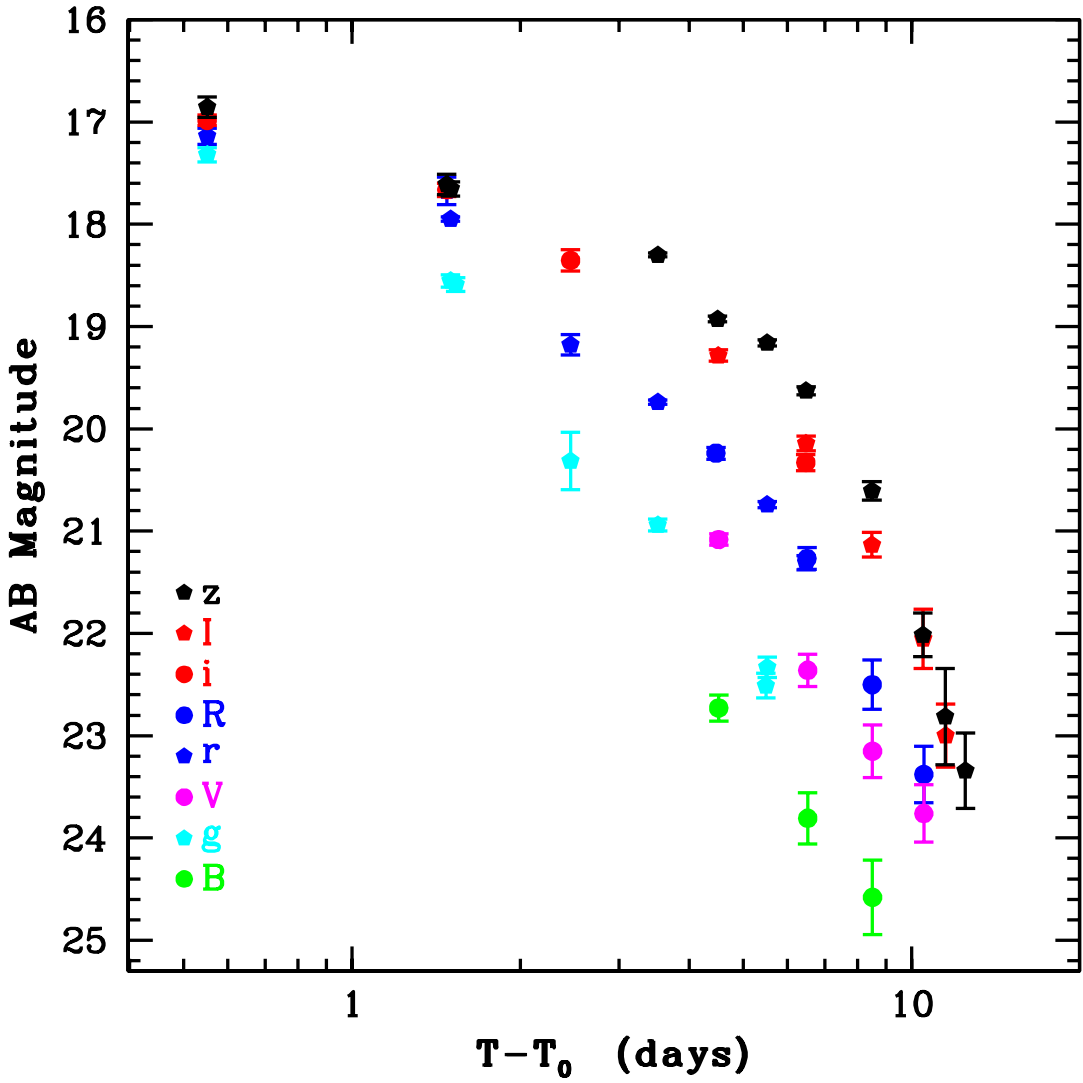


**Figure 4.1:** The data shown for each filter (see legend) are listed in Fig. 4.4. Details of data acquisition and analysis are reported in Methods. The x axis indicates the difference in days between the time at which the observation was carried out T and the time of the gravitational-wave event T0. The error bars show the  $1\sigma$  confidence level. The data have not been corrected for Galactic reddening.

wave/GRB trigger, this indicates an expansion velocity of the ejected material of about  $0.2c$ . The temperature is considerably lower than that inferred from photometric observations about  $20\text{ \AA Lh}$  earlier (about 8000 K; Malesani 2017), suggesting rapid cooling. On top of this overall blackbody spectral shape are undulations that may represent very broad absorption features similar to those predicted by merger ejecta simulations (Tanaka et al. 2018). We refrain from connecting these to the expansion velocity because they may be combinations of many lines with poorly known properties.

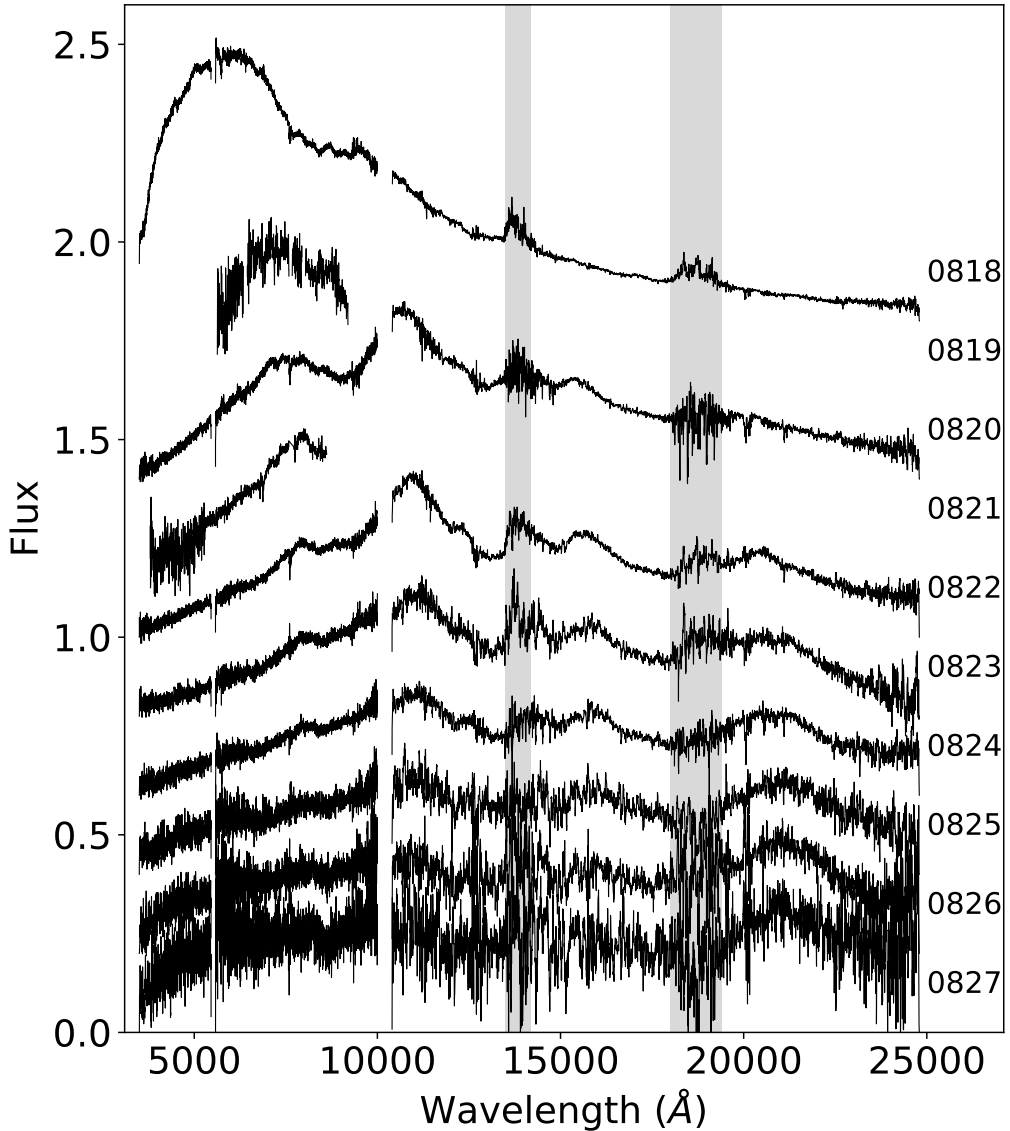


**Figure 4.2:** VLT/X-shooter, VLT/FORS2 and Gemini/GMOS spectra of AT 2017gfo. Details of data acquisition and analysis are reported in Methods. For each spectrum, the observation epoch is reported on the left (phases with respect to the gravitation-wave trigger time are reported in Fig. 4.5; the flux normalization is arbitrary). Spikes and spurious features were removed and a filter median of 21 pixels was applied. The shaded areas mark the wavelength ranges with very low atmospheric transmission. The data have not been corrected for Galactic reddening.

At the second epoch, one day later, when the spectrum covered only the optical range, the maximum moved to longer wavelengths, indicating rapid cooling. At the third epoch, when

near-infrared wavelength information was again available, the peak shifted further to 11000 Å and the overall spectral shape changed. This indicated that the photosphere was receding, the ejecta was becoming increasingly transparent and more absorption lines became visible. The near-infrared part of the spectrum evolved in flux and shape much less rapidly than the optical part and spectrally broad absorption features ( $\Delta\lambda/\lambda \sim 0.1 - 0.2$ ) were observed. These rapid changes are not consistent with supernova time evolution and are attributed to a kilonova (see Methods and Figure 4.7).

Unlike supernova absorption lines, the identification of kilonova atomic species is not secure. The neutron-rich environment of the progenitors suggests that *r*-process nucleosynthesis is the mechanism responsible for the elemental composition of the ejecta. Lacking line identification, we included various plausible nuclear reaction networks in radiation-transfer models of kilonova spectrum formation. A fraction of the synthesized atoms are radioactive; while decaying they heat the ejecta, which then radiates thermally. All the atomic species present in the ejecta have various degrees of excitation and ionization and thus absorb from the continuum and cause the formation of lines. The models that aim at reproducing these lines assume a total explosion energy, a density profile and an abundance distribution of the ejecta. In kilonovae, it is often envisaged that nucleosynthesis takes place in different regions with different neutron excesses and ejecta velocities; typically, a post-merger dynamical ejecta region and a disk-wind region.

Various models predict different emission components and different synthesized masses. Three models with different electron (or proton) fractions  $Y_e$  (see Methods) are presented in [Tanaka et al. \(2018\)](#). We compare our spectra with a scenario in which the following three components contribute to the observed spectra (Fig. 4.3): a lanthanide-rich dynamical ejecta region with a proton fraction in the range  $Y_e = 0.1 - 0.4$  and a velocity of  $0.2c$  (orange in Fig. 4.3), and two slow ( $0.05c$ ) wind regions, one with  $Y_e = 0.25$  and mixed (lanthanide-free and lanthanide-rich) composition (green) and one with  $Y_e = 0.30$  that is lanthanide-free (blue). Each of these spectra falls short of the observed luminosity by a factor of about 2, while other predictions ([Tanaka & Hotokezaka 2013](#); [Kasen et al. 2015](#)) have a discrepancy of an order of magnitude. To investigate the applicability of the model to the present, more luminous spectra than predicted previously, we have assumed that the ejecta mass involved is larger. By decreasing the high- $Y_e$  (0.3) wind component to 30 % of the value used in the original model and increasing both the intermediate- $Y_e$  (0.25) wind component and the contribution of the dynamical ejecta nucleosynthesis by a factor of 2, we obtain a satisfactory representation of the first spectrum (Fig. 4.3).

Although direct rescaling of these models is not in principle correct (for larger masses, we expect that the spectrum of each ejecta could change), we can estimate that the ejected mass was about  $0.03 - 0.05 M_\odot$  and that the high- $Y_e$ -wind ejecta (blue line) is considerably suppressed, possibly because of the viewing angle pointing away from the GRB, a narrow jet angle or both.

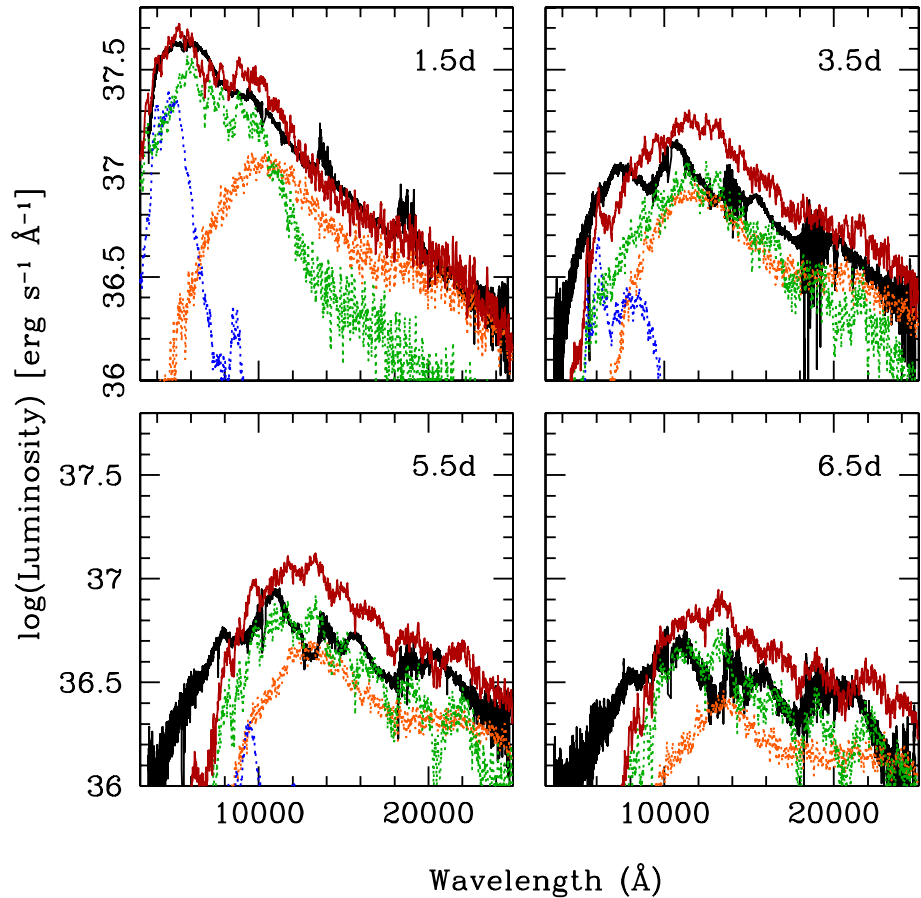


**Figure 4.3:** X-shooter spectra (black line) at the first four epochs and kilonova models: dynamical ejecta ( $Y_e = 0.1$ , orange), wind region with proton fraction  $Y_e = 0.3$  (blue) and  $Y_e = 0.25$  (green). The red curve represents the sum of the three model components.

This also suggests that the ejecta has a wide range of  $Y_e$  values, which may vary as a function of latitude.

At each successive epoch, the same components represent the observed spectral features in a less satisfactory way. This indicates that the set of adopted opacities is not completely adequate, as the cooling of the gas is not accompanied by lines of different ionization states, and that the radioactive input may also not be accurately known.

Because a short GRB was detected in association with a gravitational-wave trigger, we evaluated the expected contribution of the GRB afterglow at the epochs of our observations. Nine days after the GW170817 trigger, an X-ray source was discovered by the Chandra X-ray observatory at a position consistent with the kilonova and with a flux of about  $4.5 \times 10^{-15}$  erg cm $^{-2}$  s $^{-1}$  (0.3–8 keV). This source could be delayed X-ray afterglow emission from GRB170817A produced by an off-beam jet (Troja et al. 2017c), which may account for the otherwise small probability of having an aligned short-GRB jet within such a small volume (Patricelli et al. 2016). This X-ray emission is consistent with different scenarios: a structured jet with an energy per solid angle decreasing with the angular distance from the axis, viewed at large angles (see, for example, Salafia et al. 2015), a cocoon accelerated quasi-isotropically at mildly relativistic velocities by the jet (Lazzati et al. 2017; Nakar & Piran 2016) or a simple uniform jet observed at large angles. All these situations produce an optical afterglow much fainter than that of the kilonova (see Methods). On the other hand, if we assume that the early (0.45 days after the gravitational-wave event) optical flux that we measured is afterglow emission, we estimate an X-ray flux of more than  $10^{-12}$  erg cm $^{-2}$  s $^{-1}$  and a 6-GHz radio flux density of approximately 10 mJy at the same epoch. These estimates are not consistent with the absence of X-ray and radio detections at the corresponding epochs (Bannister 2017; Evans et al. 2017).

Our long and intensive monitoring and wide range of wavelength coverage allowed the unambiguous detection of time-dependent kilonova emission and full sampling of its time evolution. Our observations not only confirmed the association of the transient with the gravitational wave, but, combined with the short-GRB detection, also proved beyond doubt that at least some short-duration GRBs are indeed associated with compact star mergers. Furthermore, this first detection provides important insights into the environment of merging neutron stars. The location of the gravitational-wave counterpart is only about 2 kpc (projected distance) away from the centre of an early-type galaxy. This offset is typical for short GRBs (see, for example, Fong et al. 2010) and is consistent with predictions from theoretical models of merging neutron stars (see, for example, Belczynski et al. 2006). Moreover, the location of the counterpart does not appear to coincide with any globular cluster, which suggests a field origin for this neutron-star binary or a relatively low-velocity ejection from a globular cluster. The nearest possible globular clusters are more than 2.5'' (corresponding to 500 pc) away from the source position (Levan et al. 2017). The formation

channel of this event could be explored with future modelling and simulations. Finally, since this GRB was rather under-energetic (isotropic  $\gamma$ -ray output of about  $10^{46}$  erg) and probably off-axis with respect to the line of sight, we conclude that there may be a large number of similar nearby off-axis short bursts at frequencies lower than those of  $\gamma$ -rays that are also gravitational-wave emitter candidates but were not followed up. The present event has demonstrated how the search of the randomly oriented parent population of short GRBs can be made effective by coordinated gravitational interferometry and multi-wavelength observations.

## Acknowledgments

This work is based on observations made with the ESO telescopes at the Paranal Observatory under programmes ID 099.D-0382 (Principal Investigator (PI): E. Pian), 099.D-0622 (PI: P.D'Avanzo), 099.D-0191 (PI: A. Grado) and with the REM telescope at the ESO La Silla Observatory under programme ID 35020 (PI: S. Campana). Gemini observatory data were obtained under programme GS-2017B-DD-1 (PI: L. P. Singer). We thank the Gemini Observatory for performing these observations, the ESO Director General for allocating discretionary time and the ESO operation staff for support. We thank D. Fugazza for technical support with operating the REM telescope remotely and REM telescope director E. Molinari. We acknowledge INAF for supporting the project "Gravitational Wave Astronomy with the first detections of adLIGO and adVirgo experiments" (PI: E.B.) and support from ASI grant I/004/11/3. J.H. was supported by a VILLUM FONDEN Investigator grant (project number 16599). M.M.K. acknowledges support from the GROWTH (Global Relay of Observatories Watching Transients Happen) project funded by the National Science Foundation under PIRE grant number 1545949.

## Author contribution

E. Pian and P. D'Avanzo are PIs of the two active ESO VLT programs and coordinated the work. J. Selsing reduced all the X-shooter spectra presented in Figure 2 and wrote the relevant sections. M. Tanaka developed the kilonova spectral models. E. Cappellaro assisted with the spectral analysis. P. Mazzali provided the liaison between spectral observations and kilonova theory: he coordinated the theoretical interpretation, developed the match between the synthetic and observed spectra (Figure 3), and wrote the part on their description and discussion. S. Campana coordinated the REM observations. S. Covino, A. Grado and A. Melandri reduced and analysed the optical photometry (Figure 1). M. Kasliwal provided the Gemini spectrum. D. Malesani assisted with early observation planning. G. Ghirlanda, G. Ghisellini and O. S. Salafia wrote the section on the off-beam jet with contributions from L. Amati, Y.Z. Fan, Z.P. Jin and T. Piran. D. Watson assisted with the analysis of spectra in light of thermal models and assisted with

paper writing. E. Brocato was the Principal Investigator of the GRAvitational Wave Inaf TeAm (GRAWITA) for GW electromagnetic follow-up. M. Branchesi liaised GRAWITA with LIGO-VIRGO collaborations activities. A. Grado coordinated the ESO-VST observations. L. Limatola and F. Getman developed the pipeline to reduce the VST data. N. Tanvir and A. Levan assisted with NIR data calibration issues. J. P. U. Fynbo, J. Hjorth and C. Kouveliotou assisted with paper writing and short GRB expertise. L. Nicastro supervised the data flow and handling. S. Piranomonte and V. D'Elia contributed to the data reduction and analysis of the X-shooter spectra. E. Palazzi, A. Rossi, G. Stratta and G. Greco participated in the organization of the observations and image analysis and provided specific input for photometry calibration. L. Tomasella, S. Yang, and S. Benetti contributed to the data analysis, with particular reference to ISM spectral features. P. Møller assisted with issues related to ESO policies and observation planning. This effort was led by GRAWITA, that includes most co-authors, and is based on GW electromagnetic follow-up programs at ESO and at many telescopes both in Italy and at the Canary Islands. All GRAWITA members contributed to the work development at many phases from preparation of proposals, coordination with the LIGO-VIRGO collaborations, activation of approved programs at many facilities, data acquisition, reduction, analysis, interpretation and presentation.

## Author Information

Reprints and permissions information are available at [www.nature.com/reprints](http://www.nature.com/reprints)

The authors declare that they have no competing financial interests.

Correspondence and requests for materials should be addressed to E. Pian (e-mail: [pian@iasfbo.inaf.it](mailto:pian@iasfbo.inaf.it)).

## 4.2 Methods

### 4.2.1 Optical/NIR imaging

Our first observations of the field of AT 2017gfo were carried out with the 60-cm robotic telescope REM ([Chincarini et al. 2003](#)), which is located at the ESO La Silla Observatory (Chile), in the *g*, *r*, *i*, *z* and *H* bands from 18 August 2017 01:29:28 UT (12.8 h after the gravitational-wave/GRB event). The field was included in targeted observations of catalogued galaxies in the LigoâšVirgo Collaboration skymap that were aimed at searching for an optical/near-infrared counterpart of the gravitational-wave event and started on 17 August 2017 at 23:11:29 UT (10.5 h after the gravitational-wave/GRB event) ([Melandri 2017a,b](#)). Following this first detection, we began an extensive follow-up campaign of optical/near-infrared imaging carried out almost daily for 0.5–17.5 days after the time of the gravitational-wave/GRB trigger. These observations were performed using the ESO VLT, equipped with the X-shooter acquisition camera and the FORS2 instrument, and

with the ESO VST, which is equipped with the OmegaCAM instrument (Pian 2017; D’Avanzo 2017; Grado 2017a,b). The complete record of our photometric observations in August 2017 is presented in Fig. 4.4. The optical/near-infrared light curves are shown in Fig. 4.1. For REM and FORS2 images, data reduction was carried out following the standard procedures: subtraction of an averaged bias frame and division by a normalized flat frame. The astrometric solution was computed using the USNO-B1.0 catalogue (<http://www.nofs.navy.mil/data/fchpix/>). Aperture photometry was performed using SExtractor (Bertin & Arnouts 1996) and the PHOTOM package of the Starlink software (<http://starlink.eao.hawaii.edu/starlink>). The photometric calibration was achieved by observing the Landolt standard field and using the Pan-STARRS catalogue (<https://panstarrs.stsci.edu>). To minimize any systematic effect, we performed differential photometry with respect to a selection of local isolated and non-saturated reference stars. As shown in Extended Data Fig. 1, the transient is embedded in the host galaxy light, so that the background around its position is highly inhomogeneous, making accurate photometry measurements arduous. To minimize the effect of flux contamination from the host light, we fitted the transient with an analytical profile. The result obtained from the fit was then subtracted from an image acquired in the neighbourhood of the transient. This procedure was repeated for each frame. After this subtraction, the background around the transient position was much more uniform, enabling accurate photometric measurements. A dedicated procedure was applied for the reduction and analysis of the wide-field images obtained with the VST (Capaccioli & Schipani 2011). The telescope is equipped with OmegaCAM (Kuijken 2011), a camera with a field of view of one square degree and 0.21-arcsec pixels. The data were processed with a dedicated pipeline for the VST-OmegaCAM observations (dubbed VST-tube43). The pipeline searches for new data in the ESO Data archive and, if available, automatically downloads and processes them by performing the following main steps: pre-reduction, astrometric and photometric calibration and mosaic production. The optical transient magnitude in the AB system is the point-spread-function fitting magnitude measured on the image after subtracting a model of the galaxy obtained fitting the isophotes with the IRAF/STSDAS task ELLIPSE (Tody & Hanisch 1993). The reference catalogue APASS DR9 was used for the absolute photometric calibration.

#### 4.2.2 FORS2 spectroscopic observations

FORS2 spectra were acquired with the 600B and 600RI grisms, covering the 3500–8600 Å wavelength range fully. In all measurements, we used a 1'' slit to obtain an effective resolution of  $R \approx 800 - 1000$ . Spectral extraction was performed with the IRAF software package (IRAF is the Image Reduction and Analysis Facility made available to the astronomical community by the National Optical Astronomy Observatories, which are operated by AURA, Inc. under contract

with the US National Science Foundation; <http://iraf.noao.edu>). Wavelength and flux calibration of the spectra were performed using helium–argon lamps and spectrophotometric stars. A check for slit losses was carried out by matching the flux-calibrated spectra to our simultaneous photometry data (see Fig. 4.4 and 4.5) and showed that the derived spectral shape is robust.

#### 4.2.3 X-shooter spectroscopic observations

The cross-dispersed echelle spectrograph, X-shooter ([Vernet et al. 2011](#)), which is mounted on the VLT, was used to observe the optical/near-infrared counterpart of GW170818. The observing campaign started on the night following the discovery of GW170817 and continued until the source had faded below the detection limit (see Fig. 4.5) of X-shooter. The observations were carried out using a standard ABBA nodding pattern. Similar position angles of the slit were used for all observations. The position of the slit on the source is shown in Fig. 4.6.

The spectroscopic data obtained with X-shooter were managed with the Reflex interface ([Freudling et al. 2013](#)) and reduced using version 2.9.3 of the X-shooter pipeline ([Modigliani et al. 2010](#)). The reduction cascade consists of bias subtraction, order tracing, flat fielding, wavelength calibration, flux calibration using the spectrophotometric standard EG274 ([Moehler et al. 2014](#)), background subtraction and order rectification – all carried out using calibration files obtained nightly. The wavelength solution was refined by cross-correlating the observed sky spectra with a synthetic sky spectrum ([Noll et al. 2012; Jones et al. 2013](#)), leading to a wavelength solution more accurate than  $1 \text{ km s}^{-1}$ . Because X-shooter is a cross-dispersed echelle spectrograph, the individual echelle orders are curved across each detector, and a rectification algorithm that correlates neighbouring pixels must be employed. A sampling of  $0.2 \text{ \AA}$ ,  $0.2 \text{ \AA}$  or  $0.6 \text{ \AA}$  per pixel (in the ultraviolet  $B$ , visible and near-infrared arms, respectively) in the rectified image was chosen to minimize this correlation while conserving the maximal resolving power. The effective resolving power of each observation was obtained from fits to unsaturated telluric absorption lines and yielded mean values of 4290, 8150 and 5750 in the ultraviolet  $B$ , visible and near-infrared arms, respectively. These resolving powers are better than the nominal values of the instrument (4290, 7410 and 5410; see <https://www.eso.org/sci/facilities/paranal/instruments/xshooter/inst.html>) because the seeing point-spread function was narrower than the slit width. Each night, immediately following the observations of the scientific standard, telluric standard stars were also observed, at an airmass comparable to the target airmass. Using the observations of these standard stars, the atmospheric transmission spectrum was obtained using Molecfit ([Smette et al. 2015; Kausch et al. 2015](#)). Host continuum contamination was visible as a faint background gradient along the slit. To minimize this contamination, we used the background regions closest to the target. The images were combined in nightly sets using a weighting scheme with a moving background variance

measure wide enough to avoid the variance measure being pixel-based and, therefore, unsuitable for Poisson-noise-dominated images. For a subset of the observations, the signal-to-noise ratio in the spectral trace was large enough to build a model of the spectral line-spread function and to employ an optimal extraction algorithm (Horne 1986), but for most of the data, an aperture covering the entire trace was used. To establish an accurate flux calibration, slit loss corrections were calculated using the average seeing full-width at half-maximum of the nightly observations along with the theoretical wavelength dependence of seeing (Fried 1966). The slit losses were obtained by integrating a synthetic two-dimensional point-spread function over the width of the slits and corrections were made accordingly.

#### 4.2.4 Foreground dust extinction

We estimated the intervening dust extinction towards the source by using the Na I D line doublet at 5896 Å. On the basis of the strength of the line in our Galaxy, we derive  $E(B - V) = 0.09$  mag using component D1,  $E(B - V) = 0.05$  mag using component D2, and  $E(B - V) = 0.06$  mag using the sum (Poznanski et al. 2012). The galactic extinction is thus limited to  $E(B - V) < 0.1$  mag. Similar upper limits of  $E(B - V)$  are obtained from the upper limits of the equivalent widths of the undetected KI 7699 Å absorption line (Munari & Zwitter 1997) ( $EW < 0.04$  Å) and of the undetected 8620 Å diffuse interstellar band (Munari et al. 2008) ( $EW < 0.04$  Å). These estimates and limits are marginally consistent with the value of  $E(B - V) = 0.11$  mag obtained from COBE/DIRBE maps covering that sky region (Schlafly & Finkbeiner 2011).

#### 4.2.5 Spectrum analysis and interpretation

The first-epoch X-shooter spectrum was fitted with the spectrum of a blackbody with temperature of  $5000 \pm 200$  K (Fig. 4.7). The main deviations from this fit are two absorption-like lines at 8100 Å and 12300 Å that evolve with time and become more pronounced in the second spectrum. At the first epoch, all deviations from the blackbody spectrum are below about 10 % in the range 3500 Å to 20000 Å, indicating that the fit is very satisfactory. Moreover, the expansion speed of  $0.2c$  that we derive from the blackbody radius at this epoch (1.5 days) is consistent with the width of the absorption lines that we observe in the second spectrum ( $\Delta\lambda/\lambda \sim 0.1 - 0.2$ ), confirming that the blackbody emission in the first spectrum is highly effective.

The first four X-shooter spectra were compared with calculations by kilonova models (Tanaka et al. 2018). The models use atomic structure calculations for Se ( $Z = 34$ ), Ru ( $Z = 44$ ), Te ( $Z = 52$ ), Ba ( $Z = 56$ ), Nd ( $Z = 6$ ) and Er ( $Z = 68$ ) to construct atomic data for a wide range of  $r$ -process elements. By using two different atomic codes, the atomic structure calculations returned opacities that differed from those of the observed spectra by a factor of up to about 2. Multiwavelength radiative-transfer simulations were then used to predict possible variations of

kilonova emission. For each model, the abundance in the ejecta was assumed to be homogeneous. However, a high- $Y_e$  component should dominate near the polar region and a low- $Y_e$ /dynamical component should develop in the equatorial region. For each model, the energy release followed a power law ( $t^{-1.3}$ ), where  $t$  is the time, owing to the collective effect of the radioactive decay of various nuclei with different lifetimes. The efficiency of the energy deposition was also taken into account, and the energy deposition rate was somewhat steeper than  $t^{-1.3}$  because  $\gamma$ -rays can escape without depositing energy.

We emphasize that we have not attempted a real fit of this model to our X-shooter spectra, but have rather looked into an interpretation that is in reasonable agreement with our data. The match is satisfactory for the first X-shooter spectrum, but not for the following three. For this reason, we refrained from deriving a light curve model. In principle, one may fold the synthetic spectral model with the sensitivity curve of any given broad-band filter and integrate the flux in the corresponding band and compare it with the observed one. However, the result may be misleading, regardless of how persuasive it is at face value. Such a spectral comparison allows one to determine the wavelength ranges in which the model is effective and those in which it fails. Integration of the model over a broad wavelength interval cancels the spectral ‘memory’ and prevents a critical assessment of the result. In other words, since the spectral model is not completely satisfactory, the comparison of synthetic and observed photometry is not meaningful, although it may seem a good match.

#### 4.2.6 Description of the spectral evolution

The first X-shooter spectrum, obtained at  $t = 1.5$  d after the gravitational-wave/GRB trigger, shows an almost featureless, moderately blue continuum. The overall spectral energy distribution is similar to that of early, broad-line core-collapse supernovae. Although at this relatively low temperature (about 5000 K), supernovae typically show strong broad features, a good match is obtained with the early spectra of the type-Ib supernova SN 2008D/XRF 080109 (Mazzali et al. 2008) by using the supernova spectral classification tool GELATO(Harutyunyan et al. 2008). As shown in Fig. 4.7, the X-shooter extended spectral range displays the presence of some large-scale differences from the blackbody fit (dotted line) that are indicative of multi-component contributions, which also suggest a kilonova event.

In the next two days, the spectrum shows a very rapid evolution. The continuum temperature rapidly drops to about 3300 K, and broad features emerge with peaks at 10700 Å and 16000 Å. These broad features point to very high expansion velocity and rapid evolution to a low ejected mass. The combination of the spectral properties and their evolution are unlike those of any known supernova types and are very similar to the predicted outcomes of kilonova models.

In the following week, the temperature derived from the optical continuum seems to remain

roughly constant while the peak at 10700 Å drifts to longer wavelengths (11200 Å at day 6) and decreases in intensity. Ten days after discovery, the dominant feature in the spectrum is a broad emission centred at about 21000 Å.

#### 4.2.7 Host emission analysis

Extending 3''–10'' (0.6–2.0 kpc in projection) from the position of the gravitational-wave counterpart are emission lines formed in the host galaxy. The lines are identified as [O II] $\lambda\lambda$ 3726 Å and 3726 Å H $\beta$ , [O III] $\lambda\lambda$ 4959 Å and 5007 Å H $\alpha$ , [N II] $\lambda\lambda$ 6549 Å and 6583 Å and [S II] $\lambda\lambda$ 6717 Å and 6731 Å and they exhibit both spatial and velocity structure along the extent of the slit, as shown in Fig. 4.8.

From the brightest blob of emission, centred at 6'' (1.2 kpc in projection) from the source, we measured a receding velocity of  $247 \pm 15 \text{ km s}^{-1}$  relative to the host nucleus (adopting a systemic velocity of NGC 4993 of  $2916 \pm 15 \text{ km s}^{-1}$ ). Along the spatial direction of the slit, closer to the source, the emission line centroids become more blue-shifted, approaching a recession velocity of  $100 \text{ km s}^{-1}$  relative to the NGC 4993 systemic velocity. The velocity range ( $150 \text{ km s}^{-1}$ ) of the line emission along the slit indicates coherent motion of the gas along the slit. This is further supported by the dust lanes superposed on the host nucleus (Coulter et al. 2017; Pan et al. 2017). The presence of spiral arms was also noted in Levan et al. (2017). A strong [N II] $\lambda$ 6583 Å line relative to H $\alpha$ , combined with a weak H $\beta$  relative to [O III] $\lambda$ 5007 Å indicates a radiation field dominated by active galactic nucleus activity, as reported previously (Kasliwal et al. 2017; Hallinan et al. 2017) and supported by the presence of a central radio source (Alexander et al. 2017). Using the Balmer decrement, the calculated extinction at the position of the line emission is  $E(B - V) = 0.21 \pm 0.21$ .

#### 4.2.8 Off-beam jet scenario

GRB170817A had a fluence of  $2.2 \times 10^{-7} \text{ erg cm}^{-2}$  in the 10–1000 keV energy range, as observed by the Fermi-GBM. At a distance of 40 Mpc, this fluence corresponds to a  $\gamma$ -ray isotropic equivalent energy  $E_{\text{iso}} \sim 4.3 \times 10^{46} \text{ erg}$ . The peak energy is  $E_{\text{peak}} = 128 \pm 48 \text{ keV}$  (Savchenko et al. 2017b; Goldstein et al. 2017). The observed  $E_{\text{iso}}$  is three to four orders of magnitude smaller than the average energy of short GRBs with known redshift (D’Avanzo et al. 2014; Berger 2014).

For illustration, let us consider a very simple model of a uniform conical jet with semi-aperture angle  $\theta_{\text{jet}}$  observed off-beam, that is, at a viewing angle  $\theta_{\text{view}} > \theta_{\text{jet}}$ . In this case, larger bulk Lorentz factors  $\Gamma$  correspond to larger debeaming factors  $b = E_{\text{iso}}(0^\circ)/E_{\text{iso}}(\theta_{\text{view}})$  for a fixed  $\theta_{\text{view}}$  (Ghisellini et al. 2006; Salafia et al. 2016). Given the small distance of 40 Mpc and that the luminosity function probably decreases with increasing luminosity (see, for example, Wanderman & Piran 2015; Ghirlanda et al. 2016), we can assume that the on-axis luminosity of this burst

belongs to the low-luminosity tail of the luminosity function of the short GRB. For this reason, we assume  $E_{\text{iso}}(0^\circ) = 10^{50}$  erg, which gives  $b = 2500$ . The probability of a jet oriented at an angle smaller than  $< \theta_{\text{view}}$  is  $P(< \theta_{\text{view}}) = 1 - \cos \theta_{\text{view}}$ . A probability  $P > 10\%$  indicates  $\theta_{\text{view}} > 26^\circ$ . An off-axis viewing angle larger than about  $30^\circ$  is also suggested by the expected rate of the joint gravitational-wave and Fermi-GBM detection (Patricelli et al. 2016) rescaled to the actual observations. By combining equations (2) and (3) from Ghisellini et al. (2006), it is possible to estimate the observed energy  $E_{\text{iso}}$  and peak energy  $E_{\text{peak}}$  as a function of  $\theta_{\text{view}}$  and  $\Gamma$  for a given  $\theta_{\text{jet}}$ . With  $\theta_{\text{view}} = 30^\circ$ ,  $b = 2500$  ( $E_{\text{iso}}(0^\circ) = 10^{50}$  erg) requires  $\Gamma = 10$  for  $\theta_{\text{jet}} = 10^\circ$ . The latter is consistent with the few existing estimates of short-GRB opening angles (Fong et al. 2016b) and  $\Gamma \approx 10$  is within the dispersion limits of the  $\Gamma - E_{\text{iso}}$  relation (Ghirlanda et al. 2012; Liang et al. 2013) for  $E_{\text{iso}}(0^\circ) \sim 10^{50}$  erg. With these values,  $E_{\text{peak}}(0^\circ)$  turns out to be approximately 2 MeV and the corresponding comoving frame peak energy is about 100 keV. If photons with much larger energies were absorbed by pair production, we would expect (as observed at  $30^\circ$ ) a spectral cutoff at about 650 keV, which is larger than the peak energy observed by the Fermi-GBM. Although these values of  $E_{\text{peak}}(0^\circ)$  and  $E_{\text{iso}}(0^\circ)$  are consistent with those observed in short GRBs, they locate this burst relatively far from the possible spectral energy correlations of short GRBs.

Figure 4.9 shows the predicted afterglow light curves at 6 GHz, the  $R$ -band and 1 keV. The filled circle shows the X-ray flux at 15 days after the gravitational-wave/GRB trigger (Troja et al. 2017c; Piro & Kollmeier 2017; van Eerten 2018; Haggard et al. 2017). The arrows show two representative radio upper limits: at 8.65 days (obtained (Moldon & Beswick 2017) by adding together six e-MERLIN observations at 5 GHz) and at 20 days (obtained (Mooley 2017) with MeerKAT at 1.5 GHz). To obtain the model curves, we assumed the parameters  $\theta_{\text{jet}} = 10^\circ$ ,  $\theta_{\text{view}} = 30^\circ$ , isotropic-equivalent kinetic energy  $E_{\text{k,iso}} = 10^{50}$  erg,  $\Gamma = 10$ , an interstellar medium with uniform density  $n = 2 \times 10^{-3} \text{ cm}^{-3}$  and standard micro-physical parameters at the shock, that is,  $\epsilon_e = 0.1$ ,  $\epsilon_B = 0.01$  (where  $\epsilon_e$  and  $\epsilon_B$  are the fraction of shock energy carried by the electrons and by the magnetic field, respectively) and electron energy injection power-law index  $p = 2.1$ . We used standard afterglow dynamics and radiation codes (van Eerten et al. 2010). As can be seen, the  $R$  flux is always below  $2 \times 10^{-5}$  mJy, corresponding to  $R > 28$ , and therefore orders of magnitude lower than kilonova emission.

MJD <sup>a</sup>	Phase <sup>b</sup> (days)	Telescope	Instrument	Exposure (seconds)	Filter	Mag <sup>c</sup>
57987.02	4.5	VLT	FORS2	480	B	22.729 ± 0.128
57989.02	6.5	VLT	FORS2	600	B	23.807 ± 0.251
57991.01	8.5	VLT	FORS2	600	B	24.581 ± 0.363
57983.05	0.55	REM	ROS2	720	g	17.320 ± 0.070
57984.00	1.5	VLT	XS	90	g	18.553 ± 0.060
57984.03	1.5	REM	ROS2	720	g	18.591 ± 0.068
57984.96	2.5	REM	ROS2	720	g	20.314 ± 0.282
57986.02	3.5	VLT	XS	90	g	20.940 ± 0.060
57987.99	5.5	VST	OmegaCam	200	g	22.507 ± 0.122
57988.02	5.5	VLT		90	g	22.332 ± 0.100
57987.02	4.5	VLT	FORS2	240	V	21.082 ± 0.054
57989.02	6.5	VLT	FORS2	600	V	22.361 ± 0.158
57991.01	8.5	VLT	FORS2	600	V	23.152 ± 0.256
57993.01	10.5	VLT	FORS2	840	V	23.761 ± 0.280
57983.05	0.5	REM	ROS2	720	r	17.140 ± 0.080
57983.98	1.5	REM	ROS2	720	r	17.675 ± 0.134
57984.00	1.5	VLT	XS	90	r	17.951 ± 0.020
57984.96	2.5	REM	ROS2	720	r	19.178 ± 0.100
57986.02	3.5	VLT	XS	90	r	19.740 ± 0.020
57986.97	4.5	VLT	FORS2	240	R	20.238 ± 0.058
57988.02	5.5	VLT	XS	90	r	20.740 ± 0.030
57988.98	6.5	VST	OmegaCam	200	r	21.310 ± 0.075
57989.00	6.5	VLT		240	R	21.268 ± 0.106
57991.00	8.5	VLT	FORS2	240	R	22.501 ± 0.240
57993.01	10.5	VLT	FORS2	360	R	23.379 ± 0.277
57983.05	0.55	REM	ROS2	720	i	16.984 ± 0.050
57983.98	1.5	REM	ROS2	720	i	17.664 ± 0.064
57984.96	2.5	REM	ROS2	720	i	18.354 ± 0.105
57987.01	4.5	VLT	FORS2	300	I	19.284 ± 0.055
57988.97	6.5	VST	OmegaCam	200	i	20.329 ± 0.089
57988.98	6.5	VLT	FORS2	300	I	20.142 ± 0.072
57990.99	8.5	VLT	FORS2	300	I	21.133 ± 0.119
57992.99	10.5	VLT	FORS2	300	I	22.052 ± 0.289
57994.00	11.5	VLT	FORS2	630	I	23.000 ± 0.309
57983.05	0.55	REM	ROS2	720	z	16.854 ± 0.100
57983.98	1.5	REM	ROS2	720	z	17.611 ± 0.098
57984.00	1.5	VLT	XS	90	z	17.654 ± 0.070
57986.02	3.5	VLT	XS	90	z	18.300 ± 0.020
57987.00	4.5	VLT	FORS2	300	z	18.927 ± 0.027
57988.02	5.5	VLT	XS	90	z	19.160 ± 0.030
57988.98	6.5	VLT	FORS2	300	z	19.627 ± 0.039
57990.99	8.5	VLT	FORS2	300	z	20.606 ± 0.092
57992.98	10.5	VLT	FORS2	600	z	22.014 ± 0.214
57993.98	11.5	VLT	FORS2	720	z	22.815 ± 0.471
57994.98	12.5	VLT	FORS2	1350	z	23.342 ± 0.368

**Figure 4.4:** Log of photometric observations. <sup>a</sup>JD - 2,400,000.5; <sup>b</sup>After GW trigger time; <sup>c</sup>AB magnitudes, not corrected for Galactic extinction ( $E_{B-V}=0.11$ ).

UT <sup>a</sup>	MJD <sup>b</sup>	Phase <sup>c</sup> (days)	Instrument	Slit/Grism (arcsec)	Exp.Time (s)	Airmass (min/max)	Seeing (arcsec)	F <sup>d</sup> <sub>Vis</sub>	F <sup>d</sup> <sub>NIR</sub>
18.97	57983.97	1.5	VLT/X-shooter	1.0/0.9/0.9	2400	1.45/1.72	0.61	166	40
19.95	57984.95	2.5	Gemini-S/GMOS	–	600	2.5/2.7	–	53	–
20.98	57985.98	3.5	VLT/X-shooter	1.0/0.9/0.9	3600	1.52/2.12	0.9	27.8	36.5
21.98	57986.98	4.5	VLT/FORS2	600RI	1800	1.58/1.86	0.88	18	–
22.03	57987.03	4.5	VLT/FORS2	600B	700	2.60/2.91	0.59	18	–
22.98	57987.98	5.5	VLT/X-shooter	1.0/0.9/0.9	3600	1.58/2.25	0.71	10.8	23.9
23.98	57988.98	6.5	VLT/X-shooter	1.0/0.9/0.9	3600	1.74/2.33	0.87	7.0	15.4
24.98	57989.98	7.5	VLT/X-shooter	1.0/0.9/0.9	3600	1.66/2.44	0.53	6.3	12
25.98	57990.98	8.5	VLT/X-shooter	1.0/0.9/0.9	2400	1.74/1.98	0.65	6.1	8.2
26.97	57991.97	9.5	VLT/X-shooter	1.0/0.9/0.9	3600	1.69/2.50	0.78	5.1	6.0
27.97	57992.97	10.5	VLT/X-shooter	1.0/0.9/0.9	3600	1.70/2.53	0.67	4.7	4.5

**Figure 4.5:** Log of spectroscopic observations. <sup>a</sup> UT days of Aug 2017. <sup>b</sup> JD - 2,400,000.5. <sup>c</sup> After GW trigger time. <sup>d</sup> Fluxes at 6000 and 15000 Å in  $10^{-18}$  erg s<sup>-1</sup> cm<sup>-2</sup> Å<sup>-1</sup>, not corrected for reddening; uncertainties are  $\sim 10\%$ .

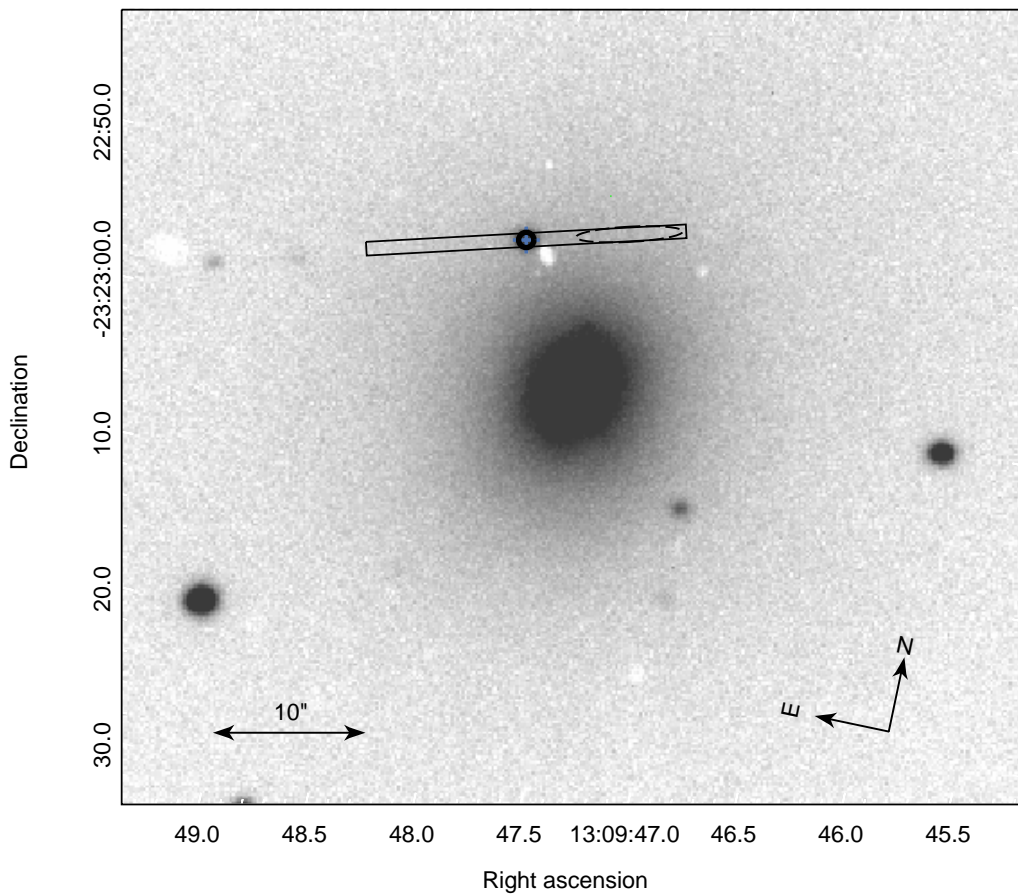


**Figure 4.6:** The image was obtained with the X-shooter acquisition camera (*z* filter). The X-shooter slit is overlaid as a rectangle. The position of the optical transient is marked by a blue circle. The position of the line emission in the slit is marked by an ellipse. The dust lanes that are visible in the host intersect the slit at the position of the line emission.

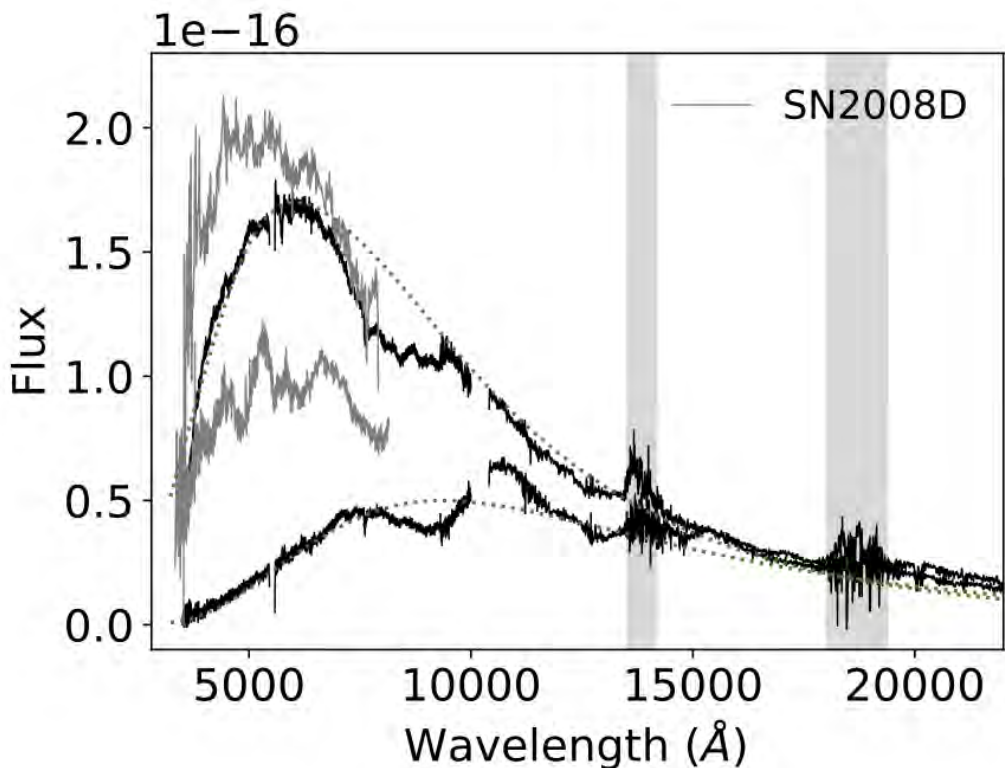


**Figure 4.7:** The two early X-shooter spectra of GW170817, obtained 1.5 and 3.5 days after discovery, are compared with the spectra of the type-Ib supernova SN 2008D (Mazzali et al. 2008), obtained 2-5 days after the explosion (light grey, arbitrarily scaled in flux,  $\times 10^{-17}$ ). The shaded areas represent wavelength intervals with low atmospheric transmission. The dotted green lines show the black-body fits of the optical continuum of GW170817 with temperature 5000 K and 3200 K.

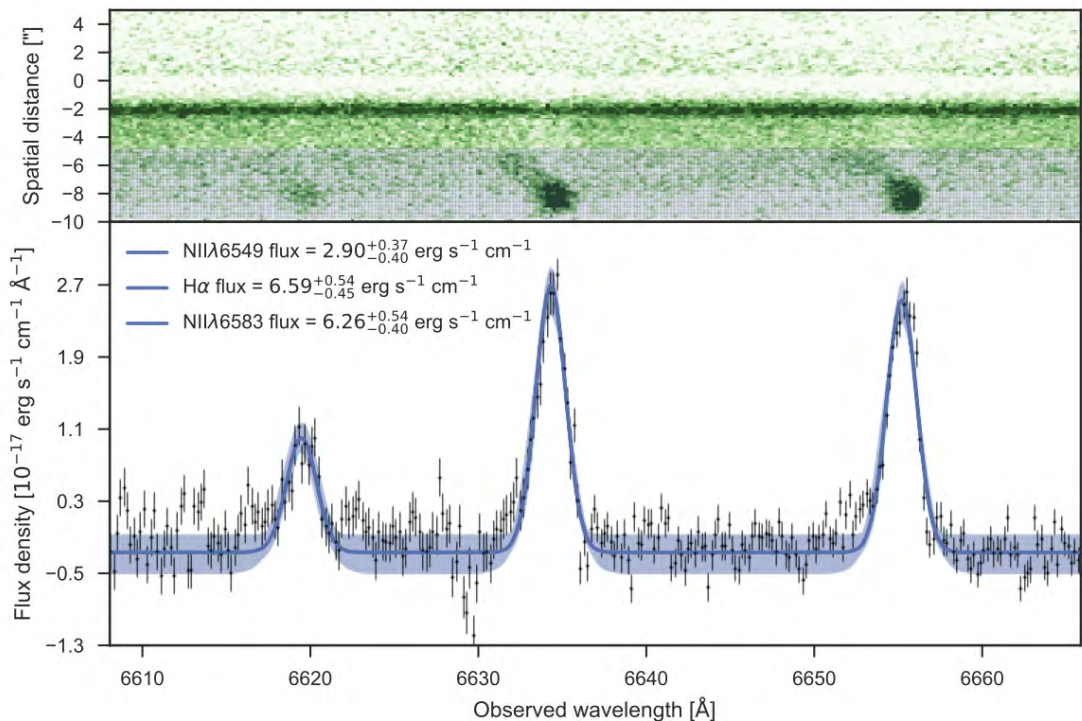


**Figure 4.8:** Top, the rectified, X-shooter two-dimensional image. The dark line visible across the entire spectral window is the bright continuum of the optical transient and the offset. The dark green blobs indicate the position of the line emission from  $\text{N II}\lambda 6549 \text{\AA}$ ,  $\text{H}\alpha$ , and  $\text{N II}\lambda 6583 \text{\AA}$ . Bottom, the line emission and the line fits. The integrated line fluxes are given, normalized by a factor of  $10^{-17}$  for clarity. The error bars on the black points represent the individual  $1\sigma$  spectral uncertainties. The blue shaded area represents  $1\sigma$  uncertainty.

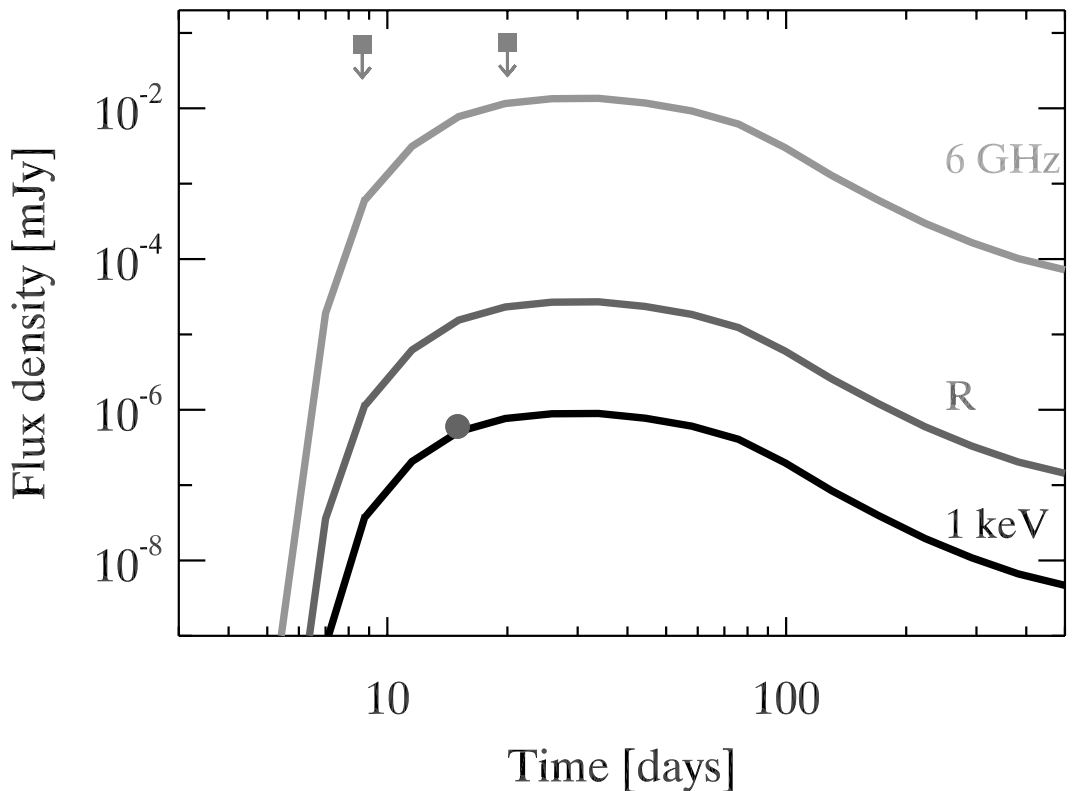


**Figure 4.9:** Off-axis GRB afterglow modeling. Synthetic X-ray (black curve), optical (dark grey curve) and radio (light grey curve) light curves of the GRB afterglow, as predicted by an off-axis jet model, derived using standard afterglow dynamics and radiation codes (van Eerten et al. 2010). The filled dot symbol shows the X-ray detection (Troja et al. 2017c; Piro & Kollmeier 2017; van Eerten 2018) and the arrows two representative radio upper limits (Moldon & Beswick 2017; Mooley 2017).

# 5

## **FINDING THE ORIGIN OF R-PROCESS ELEMENTS IN THE UNIVERSE**

This chapter contains the following article:

**“Discovery of neutron-capture elements in a neutron star merger”**

In preparation for *Nature*, 2018.

Authors:

D. Watson, C J. Hansen, J Selsing, A Koch, D Malesani, A C. Andersen, J P. U. Fynbo, A Arcones, A Bauswein, S Covino, A Grado, K E. Heintz, L. Hunt, C. Kouveliotou, G. Leloudas, A. Levan, P. Mazzali & E. Pian

The rapid (*r*) neutron capture process that creates half of all the elements heavier than iron was first theorised six decades ago. (Burbidge et al. 1957b) But where this *r*-process creates the heavy elements is still unknown. Circumstantial evidence (Ji et al. 2016) implicates neutron star mergers, (Lattimer et al. 1977; Eichler et al. 1989; Freiburghaus et al. 1999) with their associated optical/infrared kilonovae proposed to be powered by the radioactive decay of freshly-synthesised neutron-capture elements. (Metzger et al. 2010; Barnes & Kasen 2013; Tanvir et al. 2013a) The kilonova, AT2017gfo, emerging from the gravitational-wave-discovered neutron star merger, GW170817, (Abbott et al. 2017b) was the first kilonova with detailed spectroscopy and was argued to have properties broadly consonant with this proposal. (Coulter et al. 2017; Pian et al. 2017; Smartt et al. 2017) However, no robust spectroscopic identification of neutron-capture elements was made. We report here the identification of the neutron-capture element strontium in the spectra of AT2017gfo. Our identification of a neutron-capture element associated with the collision of two extreme-density stars establishes an origin for *r*-process elements. It also demonstrates that neutron stars almost certainly contain neutron-rich matter, as hypothesised more than eighty years ago (Baade & Zwicky 1934).

## 5.1 Main

The most detailed information available for a kilonova comes from a series of spectra of AT2017gfo taken over several weeks with the medium resolution, ultraviolet (320 nm) to near-infrared (2480 nm) spectrograph, X-shooter, mounted at the Very Large Telescope at the European Southern Observatory. These spectra were first presented in refs. (Pian et al. 2017) and (Smartt et al. 2017), and allow us to track the evolution of the kilonova’s primary electromagnetic output from 1.5 days until 10 days after the event. Detailed modelling of these spectra has yet to be done owing to the limited understanding of the phenomenon and the expectation that a very large number of moderate to weak lanthanide lines with unknown oscillator strengths would dominate the spectra (Kasen et al. 2017). Despite the expected complexity, we sought to identify individual elements in the early spectra because the first few epochs of X-shooter spectra are well-reproduced by relatively simple models (Pian et al. 2017) with later epochs becoming apparently more emission-line dominated in the infrared.

The first epoch spectrum can be reproduced over the entire observed spectral range with a single-temperature blackbody spectrum with the major deviations short of 1  $\mu\text{m}$  from a pure blackbody captured by two very broad ( $\sim 0.2c$ ) absorption components. These components are observed centred at about 350 nm and 810 nm (Fig. 5.1). The shape of the ultraviolet absorption component is not well constrained because it lies close to the edge of our sensitivity limit and may simply be cut off below about 350 nm. The presence of the absorption feature at 810 nm at this epoch has been noted in earlier publications (Smartt et al. 2017; Pian et al. 2017). The observed

temperature with this fit is  $\sim 4800$  K.

The fact that the spectrum is very well reproduced by a single temperature blackbody in the first epoch suggests a population of states close to local thermal equilibrium (LTE). We therefore use the LTE line analysis and spectrum synthesis code MOOG (Sneden 1973; Sneden et al. 2012) and our own LTE spectral synthesis code (see Methods). We adopt a fiducial temperature of 3700 K, which is our final model’s best-fit temperature corrected by the Doppler factor ( $-0.23$ ) of the absorption features we determine below; changing the temperature of our LTE model in the range 3700–5100 K does not significantly affect our results.

To identify the absorption features, we seek lines with wavelengths blueshifted by 0.1–0.3c, corresponding approximately to 390–500 nm and 900–1160 nm in the rest frame (see Methods). The lines will also be broadened with an observed width dependent on the velocity and geometry. For spherically expanding ejecta, the broadening of the line will be similar to the expansion velocity of the gas. We do not attempt a detailed geometric model here because it depends on assumptions about the geometry of the gas and the wavelength-dependent opacity, with significant relativistic and time-delay corrections.

We adopt an initially agnostic view on the expected abundances. We use solar *r*-process abundance ratios (total solar abundances of heavy elements (Lodders et al. 2009) with *s*-process elements subtracted (Bisterzo et al. 2014)), and abundances from two metal-poor stars, old enough to be dominated by the *r*-process in their neutron-capture abundances (Honda et al. 2007; Sneden et al. 2000). These three sets span a wide range in the ratio of light to heavy *r*-process abundances (Fig. 5.2). We also produce absorption spectra for each element individually (Extended Data Figs. 5.6 and 5.7).

Our LTE models with abundances from a solar-scaled *r*-process and metal-poor star abundances all show that Sr produce a strong feature observed centred at  $\sim 800$  nm, as well as features shortward of  $\sim 400$  nm, for our adopted blueshift (Fig. 5.3, see also Extended Data Fig. 5.7). The restframe wavelengths of the longer wavelength features are 1000–1100 nm. Of all the *r*-process elements only Sr, and Eu display strong absorption features in this longer wavelength region of the spectrum (Extended Data Fig. 5.7). Eu, however, produces far stronger absorption features in the optical region at about 650 nm and below, and we do not observe these. Furthermore, other lanthanides are co-produced with Eu ( $Z=63$ ) with similar abundances (e.g. La, Nd, Dy), and would produce spectral features that we do not observe. In our models, Eu does not appear strongly in any case because it is one to two orders of magnitude less abundant than Sr both in metal-poor stars and in the Sun. The spectral features we observe can therefore only be Sr.

The 810 nm feature was previously proposed (Smartt et al. 2017) to originate in absorption from Cs I and Te I. This identification can be ruled out because neither Cs I nor Te I produce strong lines in a plasma at this temperature (Extended Data Fig. 5.7). Much stronger lines would

be expected from ions of other elements co-produced with Cs ( $Z=55$ , e.g. from La II, see Methods). Lines from Cs I and Te I are almost never detected in stellar spectra for this reason (Sneden et al. 2010).

The most abundant  $r$ -process elements are the first-peak elements, with  $A \sim 80$ , and of these, it is Sr, Y, and Zr ( $Z=40$ ) that are easily detected in a low density,  $\sim 4000$  K thermal plasma, because these elements have low excitation potentials for their singly-charged ions (see ref. (Sneden et al. 2010) and Methods). Seen in this context, the detection of Sr in AT2017gfo is not surprising, in spite of prior expectations that the spectra would be dominated by heavier elements (Kasen et al. 2017). Ba and the lanthanide series contribute significantly to the total opacity of  $r$ -process material in the optical region of the spectrum (Fig. 5.3). We do not detect strong optical features. However, we cannot easily exclude the presence of  $A \gtrsim 140$  elements on this basis. The atomic levels in Sr that give the absorption lines observed at 810 nm are metastable. Photo-excitation can increase the population in these states, strengthening the 810 nm feature significantly (Jeffery & Branch 1990) compared to resonance ultraviolet absorption lines (Fig. 5.3, *inset*). This pumping of the levels producing the infrared lines means that these lines are enhanced compared to every LTE level in the same region of the spectrum, so that even with a substantial lanthanide absorption, these Sr metastable lines would still dominate. Even if we could exclude the presence of heavier elements in the outer layers of the thermal expanding cloud, there is no way from these early spectra to exclude that such elements could exist at lower depths or in an obscured component (Perego et al. 2014; Martin et al. 2015).

Since a simple  $r$ -process abundance LTE model can account well for the first epoch spectrum, we expand it to the subsequent three epochs while the kilonova is still at least partially blackbody-like. With a freely expanding explosion we expect to begin observing P Cygni lines once the outer absorbing ‘atmosphere’ begins to become partially optically thin and attain a significant physical radius with respect to the photospheric radius. We fit the first four epochs as a blackbody with P Cygni lines from Sr. We fit only the strongest lines to reduce our computational time to a manageable level. However, these lines provide most of the opacity at these wavelengths. These fits are shown in Fig. 5.4 and offer a compelling reproduction of the spectra at all three epochs. The P Cygni model has free parameters for the velocities of the photosphere and atmosphere, which change the shape of the profile. The fit is remarkable given its simplicity and our lack of knowledge of the system geometry. We note that P Cygni emission components are always centred close to the rest wavelength of the spectral lines, so the observed wavelength of the emission line is not a free parameter. The most prominent emission component observed throughout the spectral series is centred close to 1050 nm, and the weighted restframe centre of the infrared lines from Sr is also 1050 nm. This adds to our confidence in the line identification based on the simple thermal  $r$ -process absorption model.

We further confirm our results using a moving plasma radiative transfer code, TARDIS [Kerzendorf & Sim \(2014\)](#), extending the code’s atomic database to include elements up to  $_{92}\text{U}$  with the latest [Kurucz linelists Kurucz \(2017\)](#) with its 2.31 million lines. Our TARDIS models produce results very similar to our static-code models, reproducing the spectra well (Fig. 5.13). In particular, the P Cygni emission/absorption structure is well-reproduced as expected, confirming our LTE and MOOG modelling, and showing Sr dominating the features around 1  $\mu\text{m}$ .

Extreme-density stars composed of neutrons were proposed shortly after the discovery of the neutron ([Baade & Zwicky 1934](#)), and identified with pulsars three decades later ([Hewish et al. 1968](#)). However, no spectroscopic confirmation of the composition of neutron stars has ever been made. The identification here of Sr associated with the explosive collision of two such stars, elements that could only be synthesised so quickly under an extreme neutron flux, provides spectroscopic evidence for neutron-rich matter directly associated with neutron stars.

The identification of Sr also gives us the first spectroscopically-identified site for the rapid neutron-capture process. This discovery demonstrates specifically that the weak *r*-process takes place in neutron star mergers. It is thus clearly important to consider lighter *r*-process elements in addition to the lanthanide elements ([Barnes & Kasen 2013](#)) in shaping the kilonova emission spectrum. While we are so far unable to identify or exclude the presence of such heavier elements in AT2017gfo, observations of abundances in stars in dwarf galaxies ([Ji et al. 2016](#)) suggest that large amounts of Sr are produced together with Ba ( $Z=56$ ) in infrequent events, implying the existence of a site that produces both weak and main *r*-process elements together in quantity, as found in some models ([Wanajo et al. 2014; Just et al. 2015](#)). This is consistent with our analysis of AT2017gfo and we find it plausible that main *r*-process elements were also present in AT2017gfo, as suggested based on analysis of its lightcurve ([Drout et al. 2017; Tanvir et al. 2017b](#)). The production of both main and weak *r*-process elements in a single site and the observed difference in their relative abundances in various stellar spectra (e.g. Fig. 5.2 and ref. ([Hansen et al. 2014](#))), suggest that the relative efficiencies of the main and weak *r*-processes could vary from merger to merger.

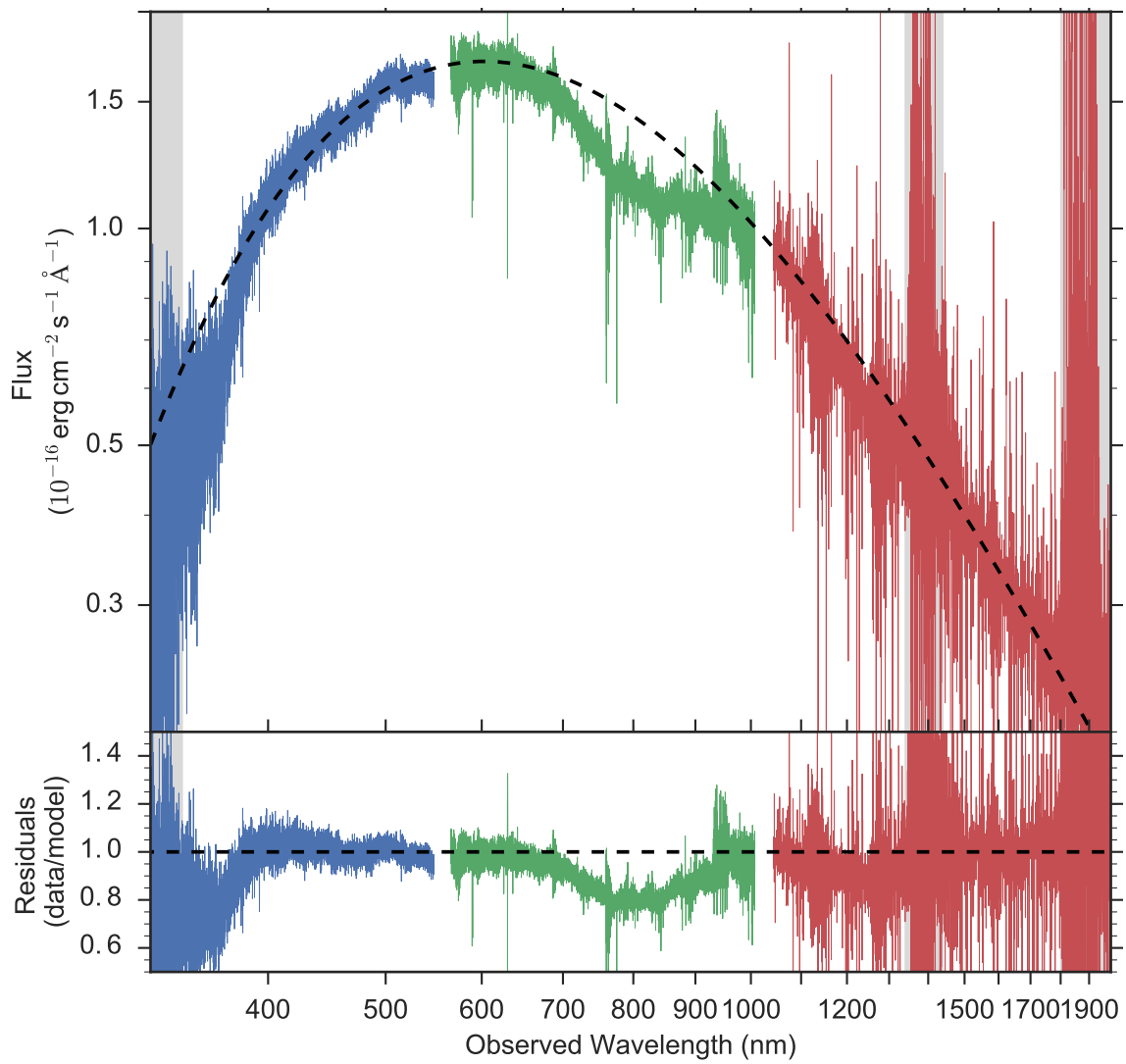


**Figure 5.1:** Spectrum of AT2017gfo at 1.5 days after the merger, fit with a blackbody with three broad absorption features. The three arms of the spectrograph are shown in blue, green, and red colours. The dashed line is the blackbody alone from the best fit blackbody with Gaussian absorption components. The residuals of data divided by the blackbody only are shown in the lower panel. The data in the sections plotted in grey are affected by telluric features or are poorly-calibrated regions and are not included in the fit.

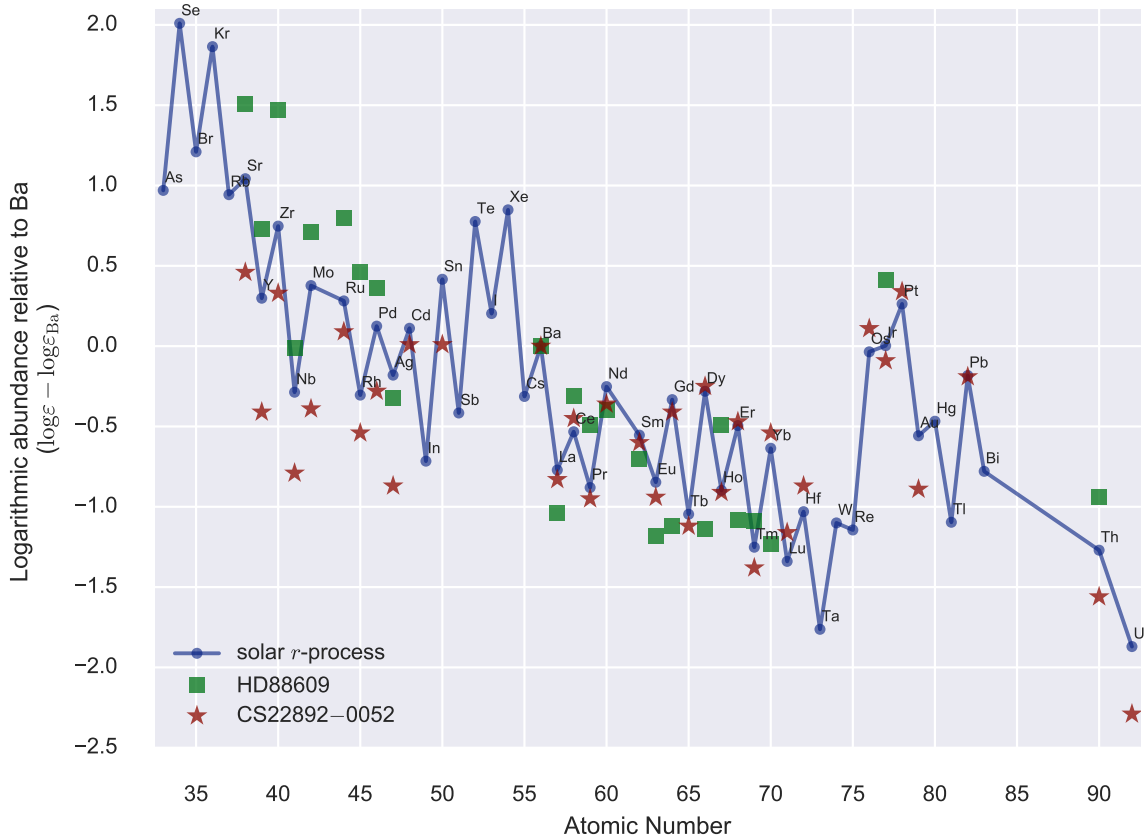


**Figure 5.2:** The abundances of elements produced by the *r*-process. Relative *r*-process abundances normalized to the Ba abundance are shown for the sun and two metal-poor stars, one rich in heavy *r*-process elements, CS 22892–052 ([Sneden et al. 2003, 2009](#)), and the other rich in light *r*-process elements, HD 88609 ([Honda et al. 2007](#)). These are the abundances of the elements used in Fig. 5.3, *inset*.

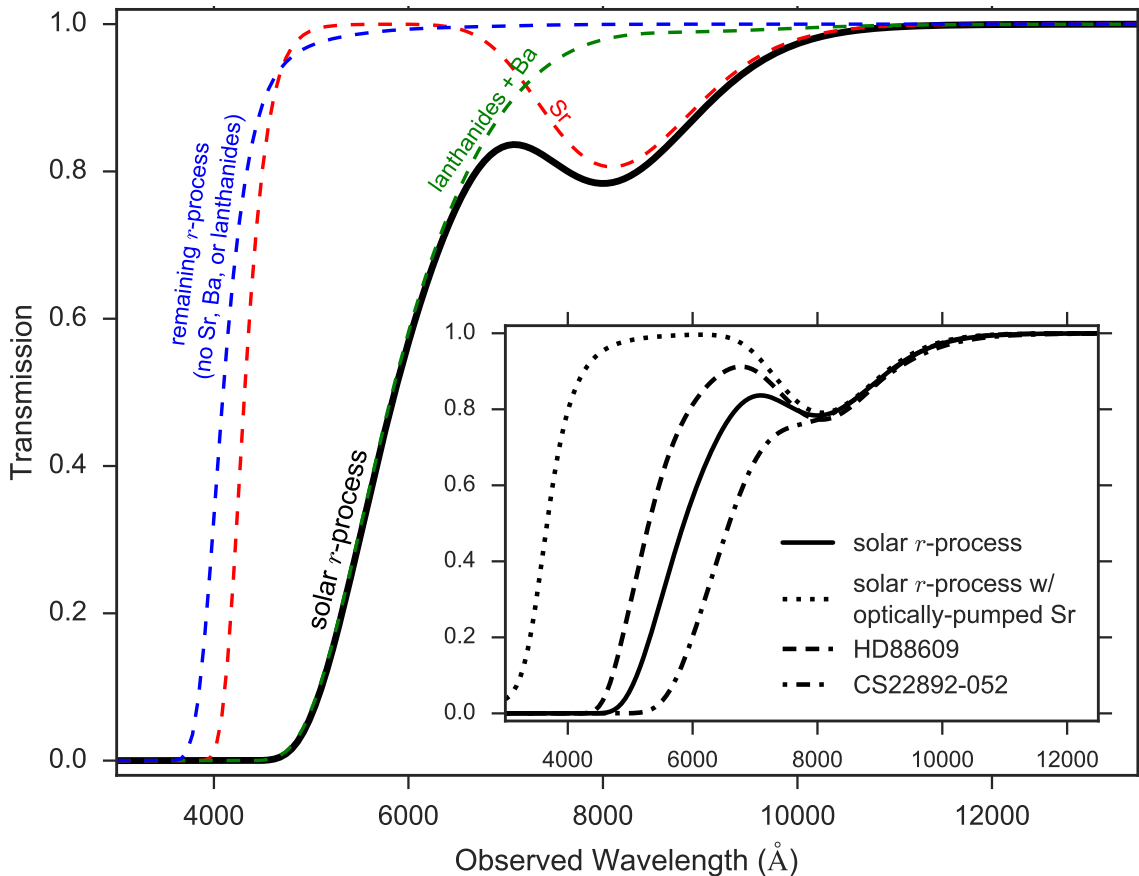


**Figure 5.3:** Thermal  $r$ -process transmission spectrum. The spectra are based on the lines formed in a gas in local thermal equilibrium with a temperature of 3700 K and an electron density of  $10^7 \text{ cm}^{-3}$ , broadened by  $0.2c$  and Doppler blueshifted by  $0.23c$ . The spectra are all normalized to have the same absorption at 810 nm. The spectrum produced by the solar  $r$ -process abundance ratio mix is plotted as a solid line. The contributions to this spectrum by only Sr (red dashed), by Ba and the lanthanide elements (green dashed), and by the remaining  $r$ -process elements (blue dashed) are shown. Sr are plotted alone to demonstrate that of all the  $r$ -process elements, only these two elements contribute to the feature observed at 810 nm. In the *inset*, spectra are shown resulting from a solar  $r$ -process abundance ratio (solid line, as main panel), the same solar  $r$ -process abundances with a strongly enhanced population in the Sr  $4p^64d\ ^2D$  level (dotted line), and from the  $r$ -process abundance ratios of the metal-poor stars HD 88609 (Honda et al. 2007) (dashed line) and CS 22892–052 (Sneden et al. 2003, 2009) (dash-dotted line).

## Acknowledgments

We thanks Jens Hjorth and Nanda Rea for useful discussions. Work in this paper was based on observations made with ESO Telescopes at the Paranal Observatory under programmes 099.D-0382 (PI: E. Pian), 099.D-0622 (PI: P. D'Avanzo), 099.D-0376 (PI: S. J. Smartt), and 099.D-0191 (PI: A. Grado). We thank the ESO Director General for allocating Discretionary Time to this programme and the ESO operation staff for excellent support. DW and DM are supported in part by Independent Research Fund Denmark grant DFF - 7014-00017. AA is supported by the European Research Council through ERC Starting Grant No. 677912 EUROPIUM. AB acknowledges support by the Klaus Tschira Foundation. SC acknowledges partial funding from Agenzia Spaziale Italiana-Istituto Nazionale di Astrofisica grant I/004/11/3. GL is supported by a research grant (19054) from Villum Fonden. AJL acknowledges funding from the European Research Council under grant agreement No. 725246, and from STFC via grant number ST/P000495/1. EP acknowledges funding from ASI INAF grant I/088/06/0, and from INAF project: ‘Gravitational Wave Astronomy with the first detections of aLIGO and aVIRGO experiments’

## Author Information

The authors declare that they have no competing financial interests.

Correspondence should be addressed to D. Watson (e-mail: darach@nbi.ku.dk).

## Author contribution

DW, CJH, and JS were the primary drivers of the project; AK, DM, JPUF, and ACA were involved in important discussions developing the understanding of the physical processes. All authors contributed to discussions and editing the paper. DW did the initial blackbody with absorber fits to the first epoch spectrum and created Figs. 5.1 and 5.3, and Extended Data Fig. 5.7, made the initial line identification, and recognised the P Cygni profiles in the later epochs, wrote the LTE code, and was the primary author of the main text. CJH computed the initial models and synthetic spectra with MOOG, and generated the MOOG spectra for HD 88609 and CS 22892–052. CJH and AK produced the MOOG spectra from 3000–20 000 Å for the kilonova template photosphere for all heavy elements. CJH wrote related sections on MOOG spectrum synthesis and significant parts of the text on nucleosynthesis. AK provided the line lists. JS reduced and processed all the X-shooter data, produced the P Cygni fitting codes and fit the P Cygni profiles to all epochs, generated the TARDIS synthetic spectra, produced Fig. 5.4 and Extended Data Figs. 5.5, 5.6, 5.9, 5.10, 5.11, and 5.12, 5.13, wrote the related methods sections and a significant part of the main text.

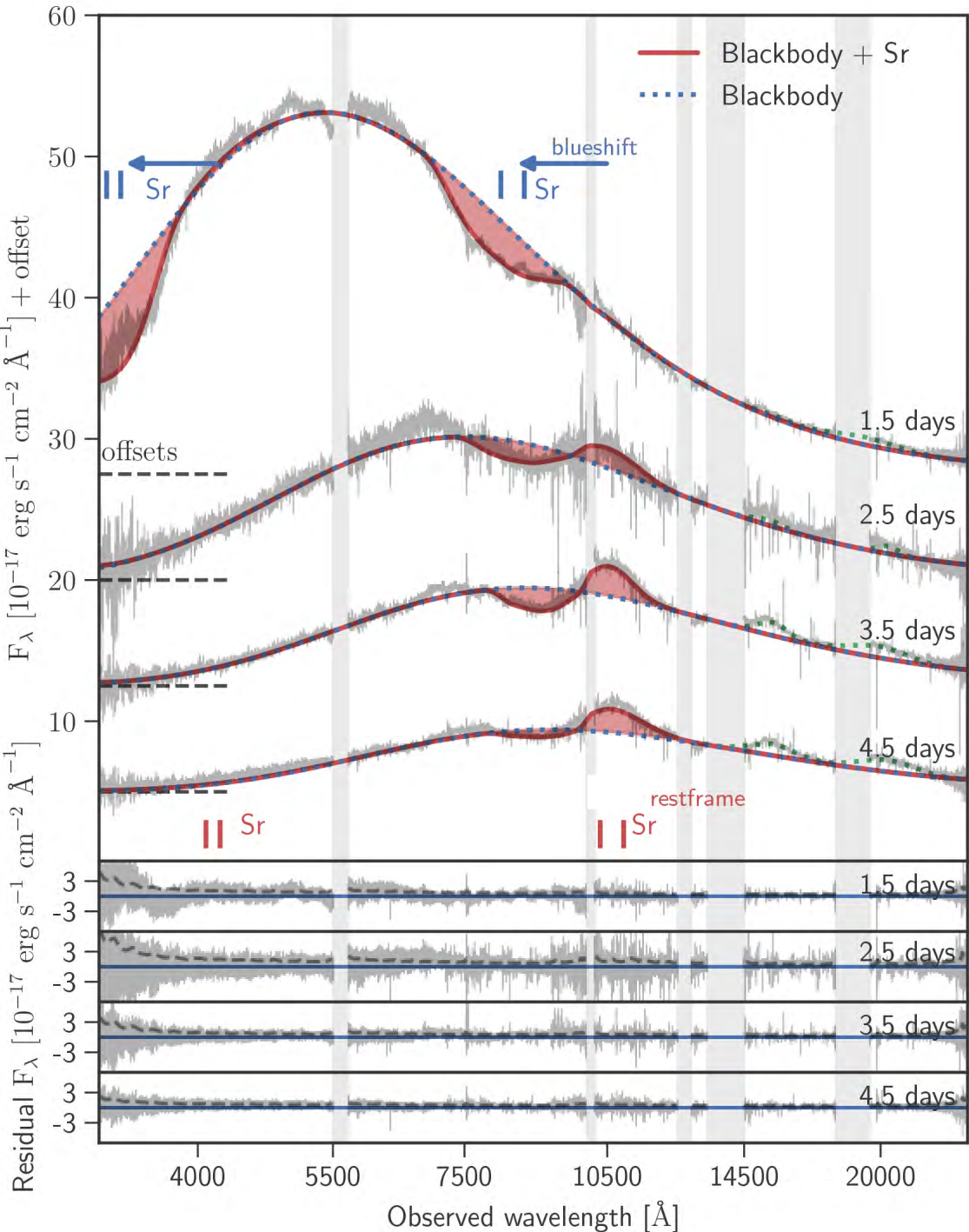


**Figure 5.4:** Spectral series of AT2017gfo from days 1.5, 2.5, 3.5, and 4.5 after the merger. In all panels, the data from VLT/X-shooter are shown in grey and have been smoothed by a 10-pixel median filter for presentation. A vertical offset has been applied to each epoch for clarity of presentation, with the zero of the flux indicated by the dashed black horizontal line segment. The model fits, a blackbody with P Cygni profiles for the strongest Sr lines (indicated), are shown as solid red lines. The blue, dotted line shows the underlying blackbody without the P Cygni components, and the partially transparent red fill shows the P Cygni contribution. The green dotted line indicates Gaussian emission profiles added to the overall fit in the infrared to ensure the continuum fit is not biased. The four bottom panels show the residuals between the model and the observed spectra for days 1.5, 2.5, 3.5, 4.5 after the NS merger, respectively. The lines from Sr included in the P Cygni model are shown at rest (red) and with a blueshift ( $-0.23c$ , blue) indicated by the length of the blue arrow.

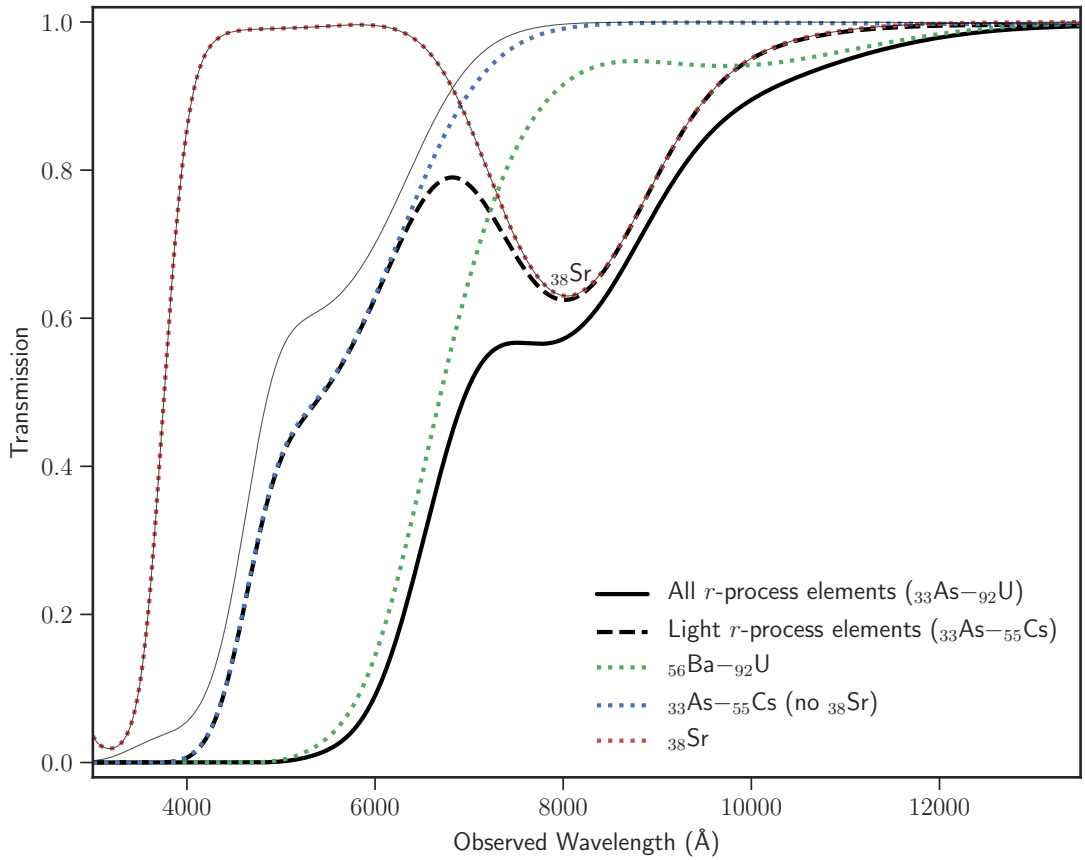


**Figure 5.5: Extended Data:** Synthetic  $r$ -process transmission spectra generated using MOOG, where the relative abundances are solar  $r$ -process spectra. The spectra are blueshifted, broadened and normalized as in Fig. 5.3. The solid, black line is the total transmission spectrum for an atmosphere containing all the  $r$ -process elements ( $^{33}\text{As}$ – $^{92}\text{U}$ ). The dashed, black line is the same spectrum, only including the light  $r$ -process elements ( $^{33}\text{As}$ – $^{55}\text{Cs}$ ). The contributions from different subsets of species are also shown. The green, dotted line shows the heavy  $r$ -process elements ( $^{56}\text{Ba}$ – $^{92}\text{U}$ ), the blue, dotted lines shows the light  $r$ -process elements ( $^{33}\text{As}$ – $^{55}\text{Cs}$  excluding Sr), which are both shown individually as thin, black lines and summed in the red, dotted line. This plot shows how Sr stand out in absorption, regardless of the composition of the material. The normalization is arbitrary and different to the LTE equivalent in Fig. 5.3 for display reasons.

## 5.2 Methods

### 5.2.1 Spectral synthesis

Two different codes were used to compute synthetic absorption spectra. We used MOOG (Sneden et al. 2012) and our own single temperature and density LTE code.

MOOG is a synthetic spectrum code normally used to generate synthetic absorption spectra of photospheres in cool stars under the assumption of local thermodynamic equilibrium. It requires

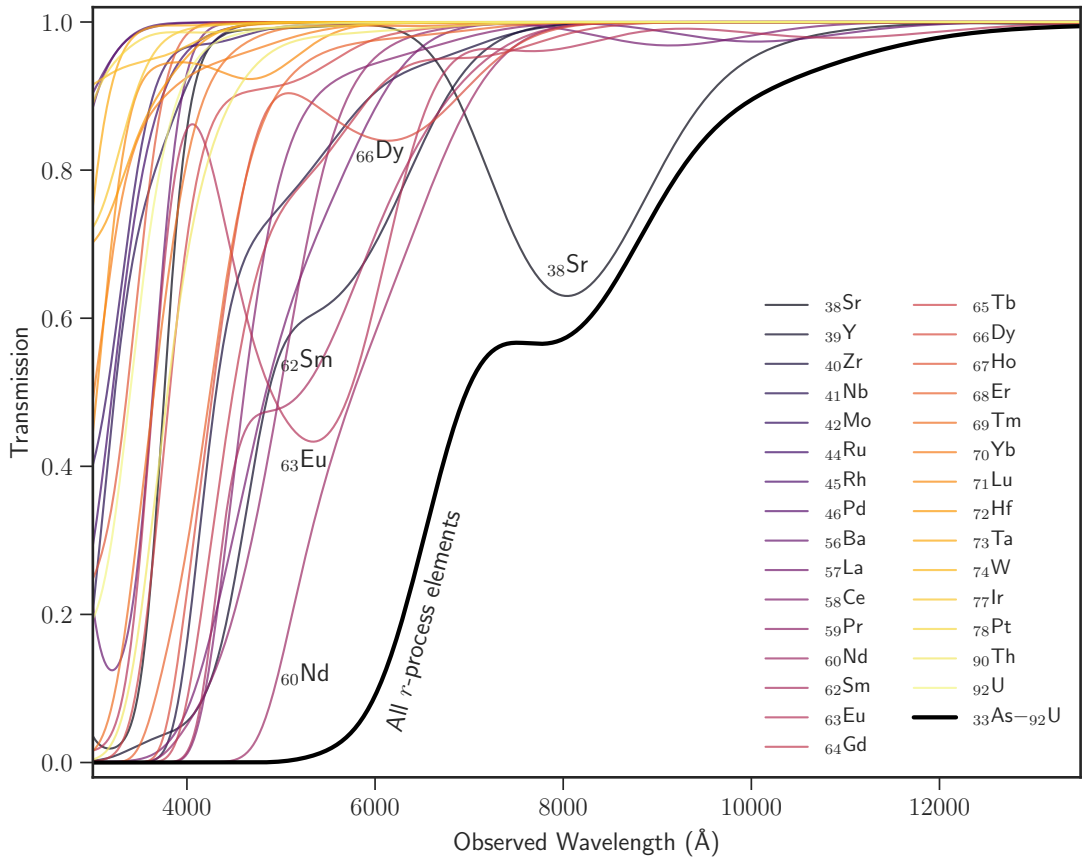


**Figure 5.6: Extended Data:** Synthetic  $r$ -process transmission spectra generated using MOOG, similar to what is shown in Extended Data Fig. 5.5, except that all element contributions are shown individually. The elements contributing most at the reddest wavelengths are noted in the plot.

a model atmosphere that dictates how temperature, gas pressure, and electron density behave in different layers of the surface gas. The second requirement is a line list containing the rest wavelength of the absorption transition, the element or ion in which the transition takes place, the excitation potential of the lower level, and the oscillator strength. The atomic data are based on refs. (Biémont & Quinet 2003; Den Hartog et al. 2003; Lawler et al. 2001b,c,a, 2006; Sneden et al. 2009) with updates from NIST. The strength of the absorption features are calculated solving radiative transfer equations, assuming that the velocity distribution is Maxwellian, and that excitations and ionisations are described by the Boltzmann and Saha equations, respectively. The line/wing damping follows a scaled Unsöld approximation.

Our own code assumes only a gas in LTE, and that the Boltzmann and Saha equations can be used to get the ionisation and excitation state of each element individually. We then use the line lists above and level information from NIST to determine the relative strengths of the lines.

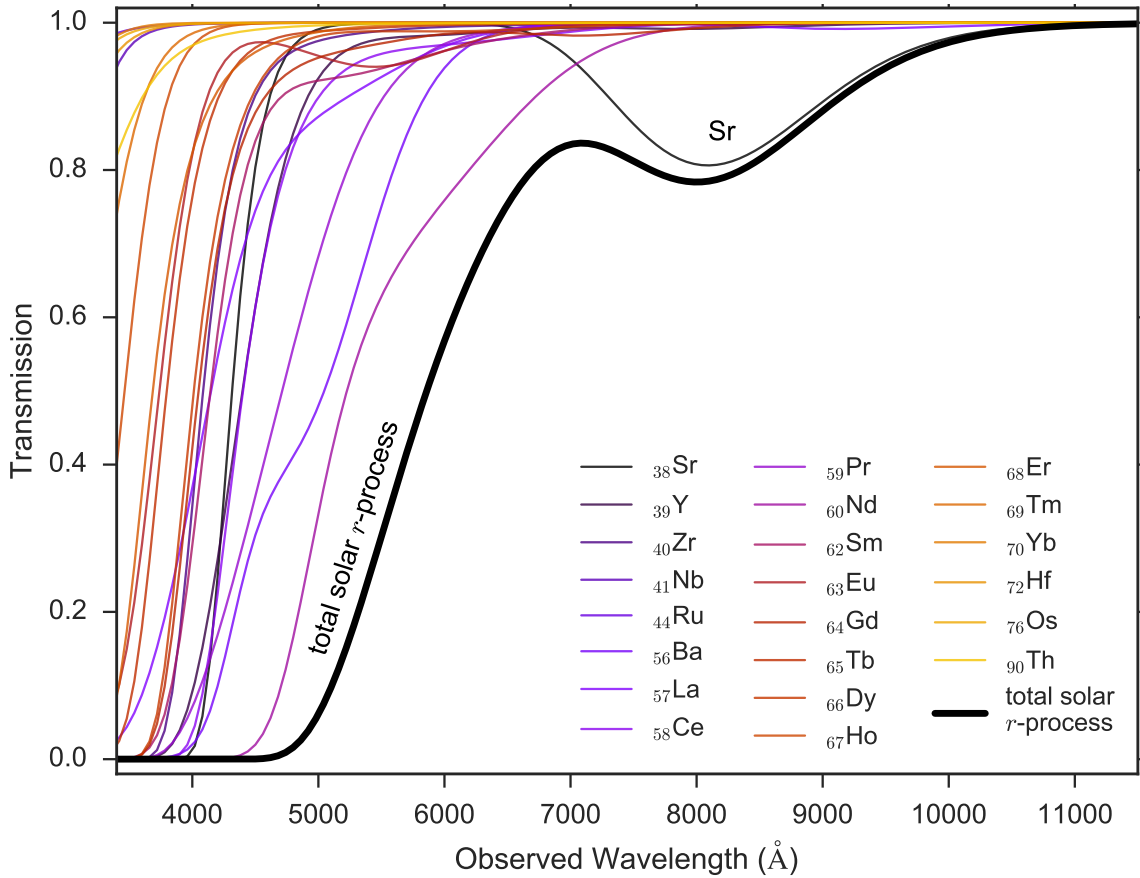


**Figure 5.7: Extended Data:** LTE transmission spectra for  $r$ -process elements plotted individually. The abundances of elements are scaled to the solar  $r$ -process and the spectra are velocity broadened, blueshifted and normalised as in Fig. 5.3. The total solar  $r$ -process spectrum is plotted as a thick black line. The contributions from Sr clearly dominate at  $\sim 8000\text{ \AA}$ , with no significant contribution from any other element.

We adopted a fiducial electron density of  $\log n_e = 7.8$ , based on the mean density of  $0.04 M_\odot$  of singly-ionized material in a sphere with the area of the best-fit blackbody. The density of the atmosphere is almost certainly not higher than this.

To make sure the MOOG models and our LTE calculations are reasonably comparable, for the MOOG models, an effective temperature at the surface of the photosphere of  $T_{\text{eff}} \sim 5500\text{ K}$  and a surface gravity of  $\log g=0$  following temperature and density profiles in Kurucz model atmospheres, gives rise to a temperature of  $3800\text{ K}$  and an electron density of  $n_e = 10^7\text{ cm}^{-3}$  within the photosphere. Absorption lines from lanthanide ions are believed to be an important source of opacity due to transitions with unknown oscillator strengths. For an LTE plasma, it is likely that such lines are important and could create a complex continuum (Kasen et al. 2013, 2017). However, the lanthanide opacity is extremely high in the ultraviolet and blue regions of the spectrum. The fact that we detect blue emission in the spectrum of AT2017gfo is already a strong

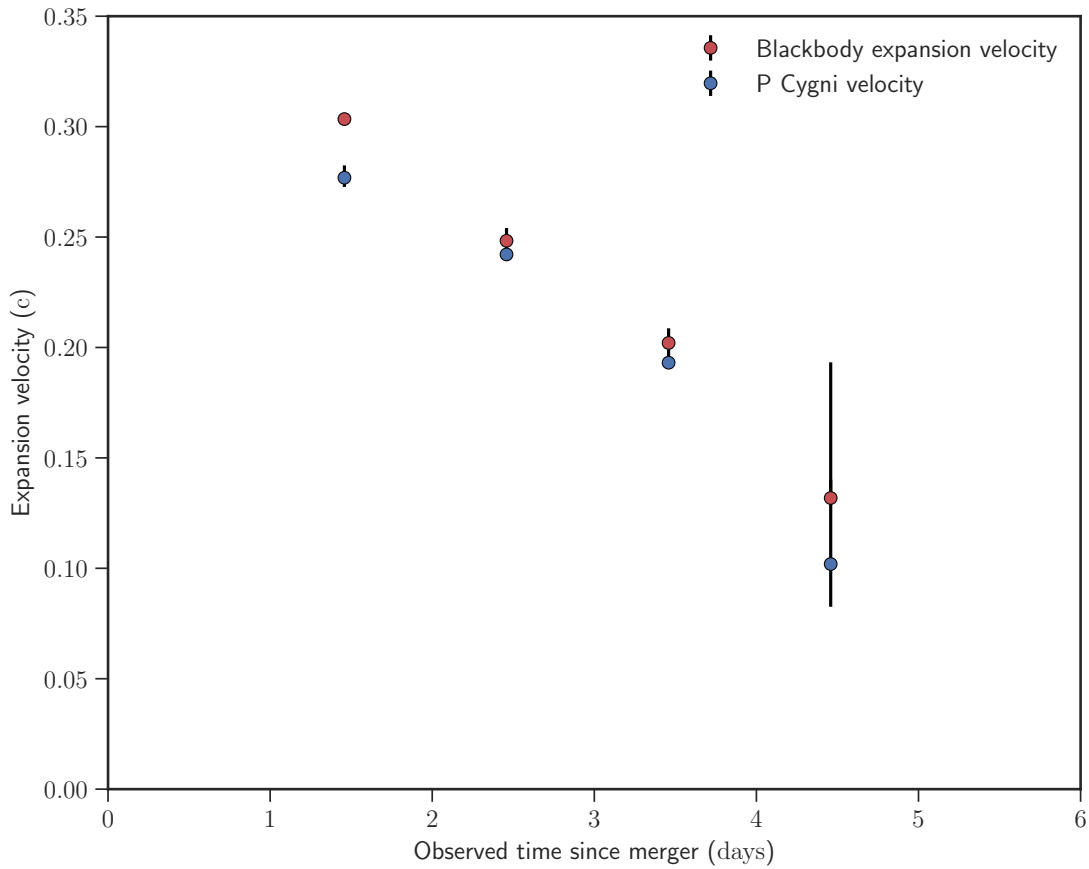


**Figure 5.8: Extended Data:** Evolution of the ejecta expansion velocity as determined from the absorption line widths (blue points) and the blackbody radius (red points). The correspondence between the two independent estimates is striking.

indication that lanthanide elements do not dominate the continuum spectrum, as suggested by other authors (McCully et al. 2017). Furthermore, if, as indicated by the similar relative strength of the infrared lines compared to the ultraviolet lines, the infrared feature arises from levels that are strongly overpopulated due to optical pumping, this feature will dominate over every other possible feature at these wavelengths if we assume a solar-like *r*-process abundance pattern.

Synthetic spectra are generated using both codes based on line lists containing *r*-process elements, and which are capable of producing strong features in an LTE plasma at these temperatures. We include all elements from  $^{33}\text{As}$  up to  $^{83}\text{Bi}$  as well as  $^{90}\text{Th}$  and  $^{92}\text{U}$ . We do not include the elements  $^{35}\text{Se}$ ,  $^{36}\text{Br}$ ,  $^{37}\text{Kr}$ ,  $^{53}\text{I}$ , or  $^{54}\text{Xe}$  as they produce no strong or moderate lines at these temperatures and are rarely detected in stellar spectra (Sneden et al. 2010). These elements have first excitation energies above 5.97 eV for their neutral and singly charged ions, giving a fractional population  $< 10^{-8}$  at our fiducial temperature. Neither do we include elements with no stable isotopes ( $^{43}\text{Tc}$  and  $^{61}\text{Pm}$ ), nor any molecules.

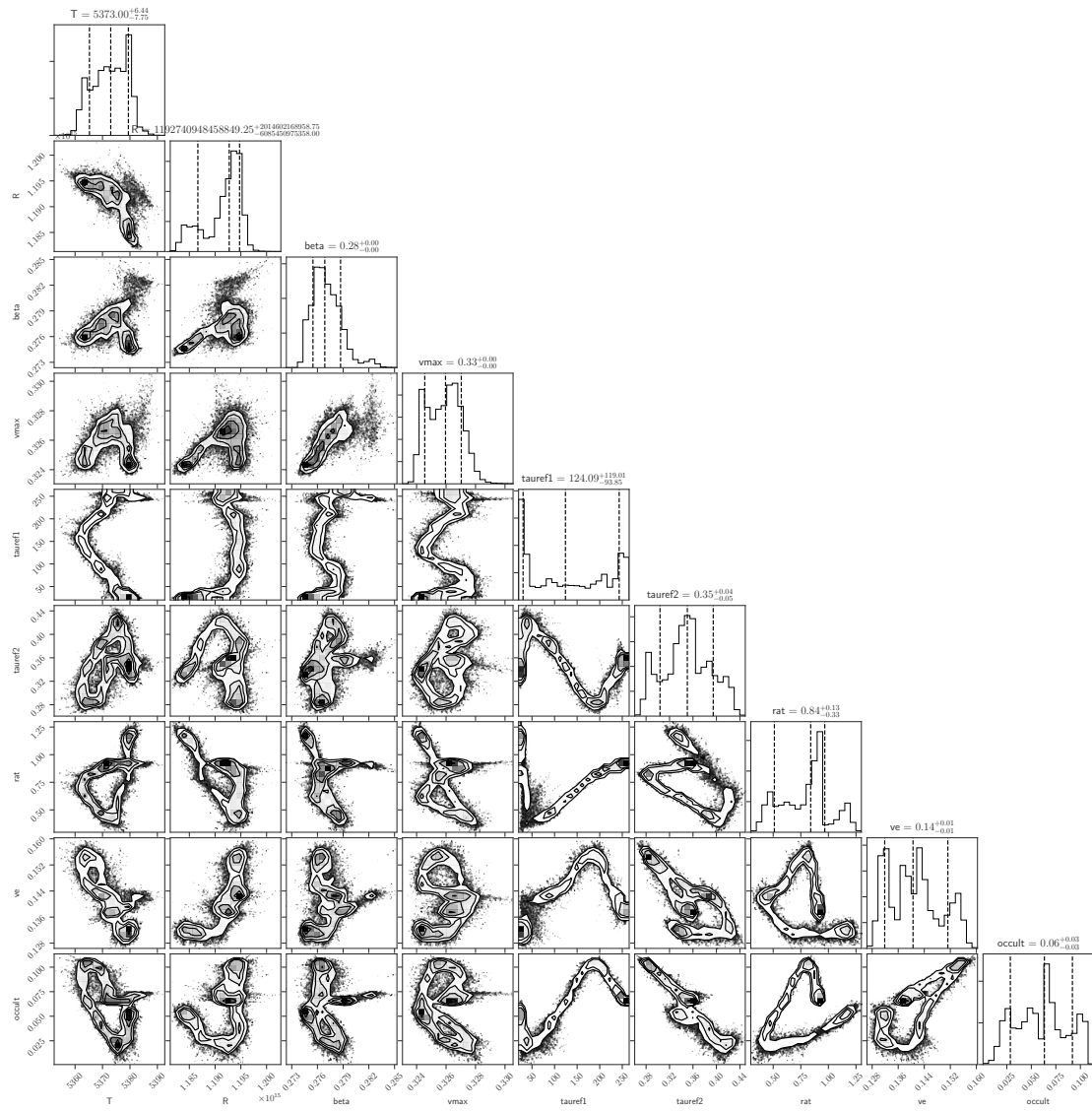


**Figure 5.9: Extended Data:** Posterior probability distributions from the MCMC runs for the parameters of the final model for the first epoch spectrum.

Our line lists contain the strongest lines for LTE spectra at these temperatures. Since we are interested in finding strong, isolated lines, this procedure should effectively capture all lines that could realistically be candidates.

### 5.2.2 Spectral modelling

What appears as two separate emission components are identified in the spectra. First, a nearly blackbody spectrum modified by absorption features, that appears to cool over time. Second, an emission component at redder wavelengths that increases in strength relative to the first component with time. These two components do not necessarily arise due to discrete ejection

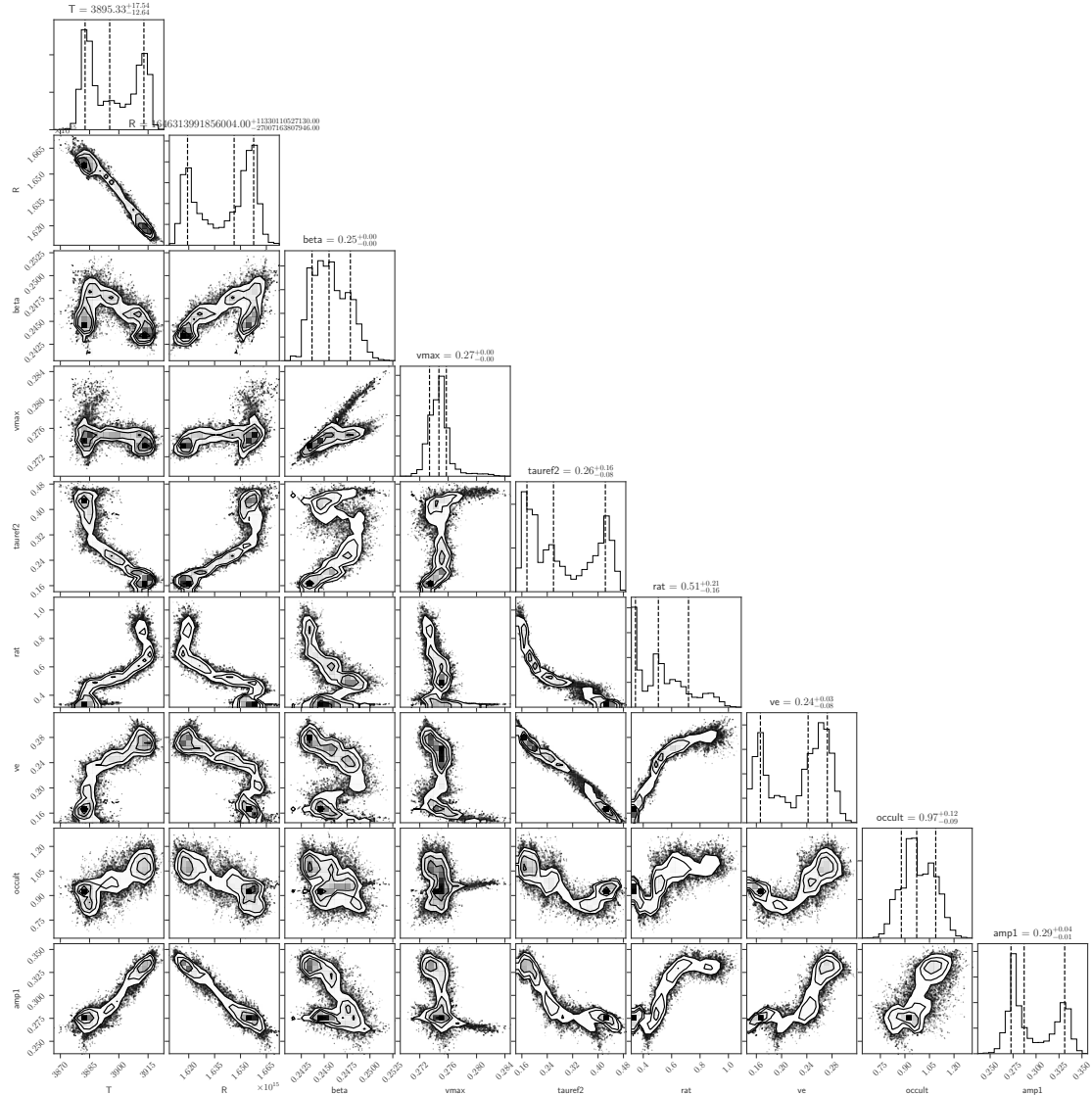


**Figure 5.10: Extended Data:** Same as Extended Data Fig. 5.9 except for the second epoch spectrum.

mechanisms, but may reflect that different parts of the spectrum probe different physical depths and thus physical conditions, through the wavelength-dependent expansion opacity (Karp et al. 1977; Barnes & Kasen 2013). Here we focus only on the thermal component in the blue part of the spectrum and model it as a blackbody with an extended envelope. We model the second component with Gaussian emission lines in order not to bias the overall continuum fit at shorter wavelengths, but do not interpret them. However, these features clearly provide important information on the composition of the plasma and must be addressed in future studies.

The expansion velocity of the gas can be inferred from the expansion of the blackbody from the time of the explosion. Due to the optical thickness of a blackbody, we would only be presented

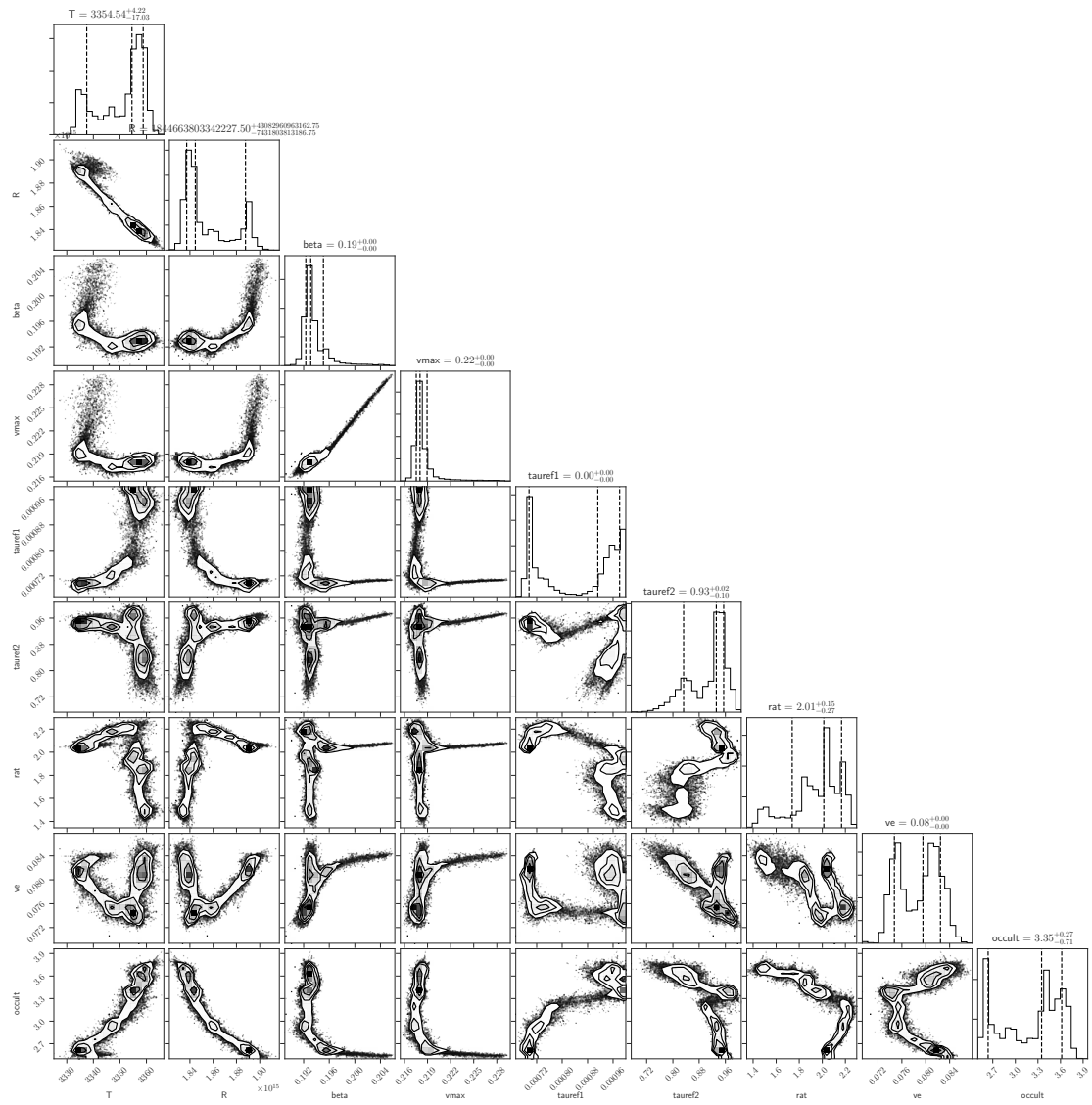


**Figure 5.11: Extended Data:** Same as Extended Data Fig. 5.9 except for the third epoch spectrum.

with the front face of the explosion. Consequently, pure absorption features in the spectrum should be blueshifted by the mean Doppler shift induced by the expansion speed of the gas. Conservatively, we allow 0.1–0.3c as the range of the blueshift (Pian et al. 2017; Shappee et al. 2017; Waxman et al. 2017), which depends on the details of the geometry of the system and thus restrict our search for lines in the first epoch to rest wavelengths of 350 nm and 810 nm × 1.1–1.3.

At the densities of the ejecta, the dominant source of opacity is expansion opacity (Kasen et al. 2013, 2017). This effect is able to establish an apparent thermalisation through photo-equilibration of the states (Pinto & Eastman 2000). With wavelength-dependent opacity, the physical depth traced at each wavelength varies. Because the large majority of lines are in the blue end of the

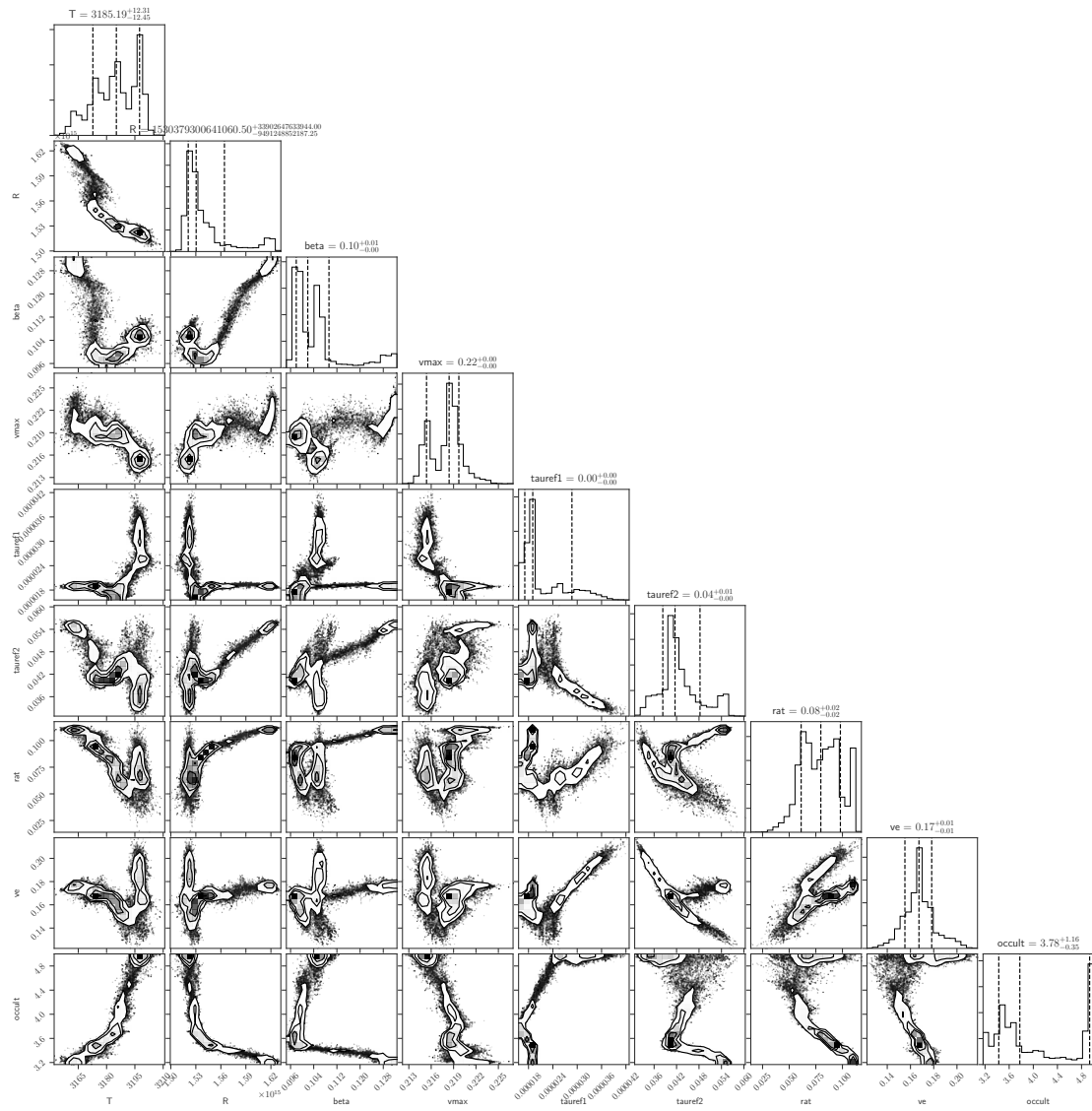


**Figure 5.12: Extended Data:** Same as Extended Data Fig. 5.9 except for the fourth epoch spectrum.

spectrum, the expansion opacity there will be higher and, conversely, the physical depth shallower. This causes the relative strength of UV/near-infrared lines to change compared to the pure LTE transmission values, with bluer absorption lines less prominent relative to near-infrared ones. Additionally, because the population of states is photo-equilibrated, metastable states will be enhanced relative to non-metastable, as compared to LTE values (Jeffery & Branch 1990). For this reason, we cannot easily use the relative LTE strengths of the lines, and instead use independent optical depth parameters ( $\tau$ ) for the two absorption feature fits.

### 5.2.3 P Cygni modelling

The expansion velocity of the photosphere is very high (0.2–0.3c). At the measured temperature of the photosphere, the thermal widths of individual lines are very narrow compared to the gross velocity structure. This means that the resonance region is very small and the Sobolev approximation can be used in the Elementary Supernova (ES) model as a prescription for the absorption structure near isolated lines (Jeffery & Branch 1990). We use the implementation of the P Cygni profile in the ES from <https://github.com/unoebauer/public-astro-tools>, where the profile is parametrized in terms of the rest wavelength,  $\lambda_0$ , the optical depth of the line,  $\tau$ , two scaling velocities for the radial dependence of  $\tau$ , the photospheric velocity, and the maximal velocity of the ejecta. The latter two parameters specify the velocity stratification. The expansion velocity of the photosphere is simultaneously used for the relativistic Doppler correction to the blackbody temperature. Additionally, because the implementation of the P Cygni profile we are using does not include the relative population of the states in the transition, we have included a parameter for enhancement/suppression of the P Cygni emission component.

For practical reasons, we cannot fit all lines simultaneously. However, fortunately, a handful of lines provide most of the opacity. Because the relative opacity dictates the apparent strengths of the lines, we divide the spectrum into ultraviolet/blue and red/infrared regions to find the lines that will be strongest in their respective spectral region. We do this because the opacity changes so severely from the infrared to the optical (Fig. 5.3). We make the division at 600 nm where the opacity increases sharply, however choosing 550 nm or 700 nm makes no difference. We then include the strongest lines in each region (all lines with a minimum strength of 20% of the strongest line). The resultant lines are the strong resonance lines from the ground state of Sr II at 407.771 and 421.552 nm, and the lines from the Sr II 4p<sup>6</sup>4d metastable states at 1032.731, 1091.489, and 1003.665 nm. These lines are all modelled using the same P Cygni profile prescription, where the relative strengths of each of the lines in the two absorption complexes are set by the LTE relations, and in spite of the relative simplicity of the analysis, provides a surprisingly good fit to the data.

The final model we use to fit the spectrum is a relativistically-corrected blackbody photosphere absorbed by an expanding atmosphere, containing the four above-mentioned Sr II transitions, described by independent optical depths for each of the three sets: infrared and ultraviolet Sr lines. The ratios of the lines internally in each set are defined by their LTE strengths. In the fitting model we also use two additional Gaussian emission lines at long wavelengths from the second emission component in order not to bias the long wavelength continuum fit. The best fit parameters and their associated errors are found by sampling the posterior probability distributions of the parameters, assuming flat priors on all parameters. The fitting framework used is LMFIT (Newville et al. 2016) and the sampling is done using emcee (Foreman-Mackey et al.

2013). We initiate 100 samplers, each sampling for 1000 steps. We discard the first 100 steps as a burn-in phase of the MCMC chains. We use the median of the marginalized posterior probability distribution as the best-fit values, and the 16th and 84th percentiles as the uncertainties. The best-fit models are shown in Fig. 5.4. The objective function, being highly non-linear, causes the posterior probability distributions to be highly complex (see Extended Data Figs. 5.9, 5.10, 5.11, and 5.12) and thus the best-fit values difficult to optimize. However, the peak of the distributions are well centered, meaning the best-fit values are well constrained, regardless of the posterior probability distribution complexity.

#### 5.2.4 Expansion velocity evolution

The fits constrain two independent parameters that can be used to infer the velocity of the ejected material. The photospheric expansion velocity used to determine the width of the P Cygni line profile and the blackbody radius, which scales with the square root of the observed luminosity and can be converted to an expansion velocity based on the time of observation. These two parameters are uncorrelated, as supported by the MCMC posterior probability function samples, and therefore constitute two independent measurements of the same physical quantity. We show a plot of the evolution of these two parameters in Extended Data Fig. 5.8. The correspondence between the two estimates of the expansion velocity is striking, especially given that the ratio of the estimates is geometry-dependent. Only the first epoch showing a slightly discrepant value, and there we expect a P Cygni model not to be entirely applicable. This close correspondence between the two independent measures and the reasonable values inferred further supports the validity of the line identification and the overall model.

#### 5.2.5 TARDIS modelling

To generate the TARDIS synthetic spectra, we set up the physical models using the inferred photospheric expansion velocities at the chosen epochs. For homologously expanding ejecta, the velocity of the atmosphere layers are at all times specified by the outer edge expansion and the photospheric expansion. We adopt a power-law density structure of the ejecta, parametrized in terms of velocity and epoch:  $\rho(v, t) = \rho_0(t_0)^3(v/v_0)^{-n}$ , and we find that the line shapes depends on the assumed slope. For steeper slopes, a larger fraction of the line absorption is closer to the line center. At each epoch, the temperature of the photosphere is chosen so that an atmosphere with no lines returns a blackbody-like spectrum similar to best-fit blackbody, as found in simple P Cygni model fits. Both the excitation and ionization structure of the elements in the atmosphere is assumed to be set by LTE where we assume for similitude a constant temperature throughout the atmosphere. This approach does not capture the likely optical pumping of the meta-stable lines and the non-LTE effects that will populate the upper levels relative to the lower ones for

metastable transitions. We adopt the solar *r*-process abundance ratio as shown in Fig. 5.2, starting from  $_{31}\text{Ga}$ . We consecutively run the simulation in three steps, including heavier elements. For the first set of simulations, we include only the elements from  $_{31}\text{Ga}$  to  $_{37}\text{Rb}$  and, as can be seen in Fig. 5.2, no lines cause a significant deviation from a blackbody. Next we include  $_{38}\text{Sr}$  to  $_{41}\text{Zr}$  which forms the strong feature observed centred at 810 nm in the first epoch, primarily due to the SrII lines at  $\sim 1\mu\text{m}$ . We set the density,  $\rho_0$  and the density slope,  $n$ , so that the synthetic spectrum matches the observed spectrum best. Last we run the same simulation, including all elements from  $_{31}\text{Ga}$  to  $_{92}\text{U}$ . The feature at 810 nm is unaffected. The TARDIS models do not demonstrate that the feature at 810 nm must be formed by Sr, but no other known lines form this feature.

### 5.2.6 Exclusion of the Cs I and Te I identification

The Cs I 6s–6p resonance transitions (Smartt et al. 2017) require Cs I to be present in the gas. But because Cs has the lowest first ionisation potential of any element, the singly-charged ions of other elements inevitably synthesised with Cs (Burbidge et al. 1957b), such as La II, Eu II, and Gd II, are millions of times more abundant than Cs I in an LTE plasma at close to the observed blackbody temperatures, and far more at temperatures that produce significant strong lines from Te I. These other elements will cause absorption lines that are at least two orders of magnitude stronger in the same wavelength region as the proposed Cs and Te lines, e.g. the 706.62 nm, 742.66 nm, or 929.05 nm lines of La II, Eu II, and Gd II respectively, to name one of each. The same argument holds for the excited state transition of Te I which has a very high excitation energy of 5.49 eV; the relative population of the Te I excited state is extremely low, less than  $10^{-7}$ . Thus, no realistic scenario exists in which either of these lines can be detected without orders of magnitude stronger lines from other elements dominating.

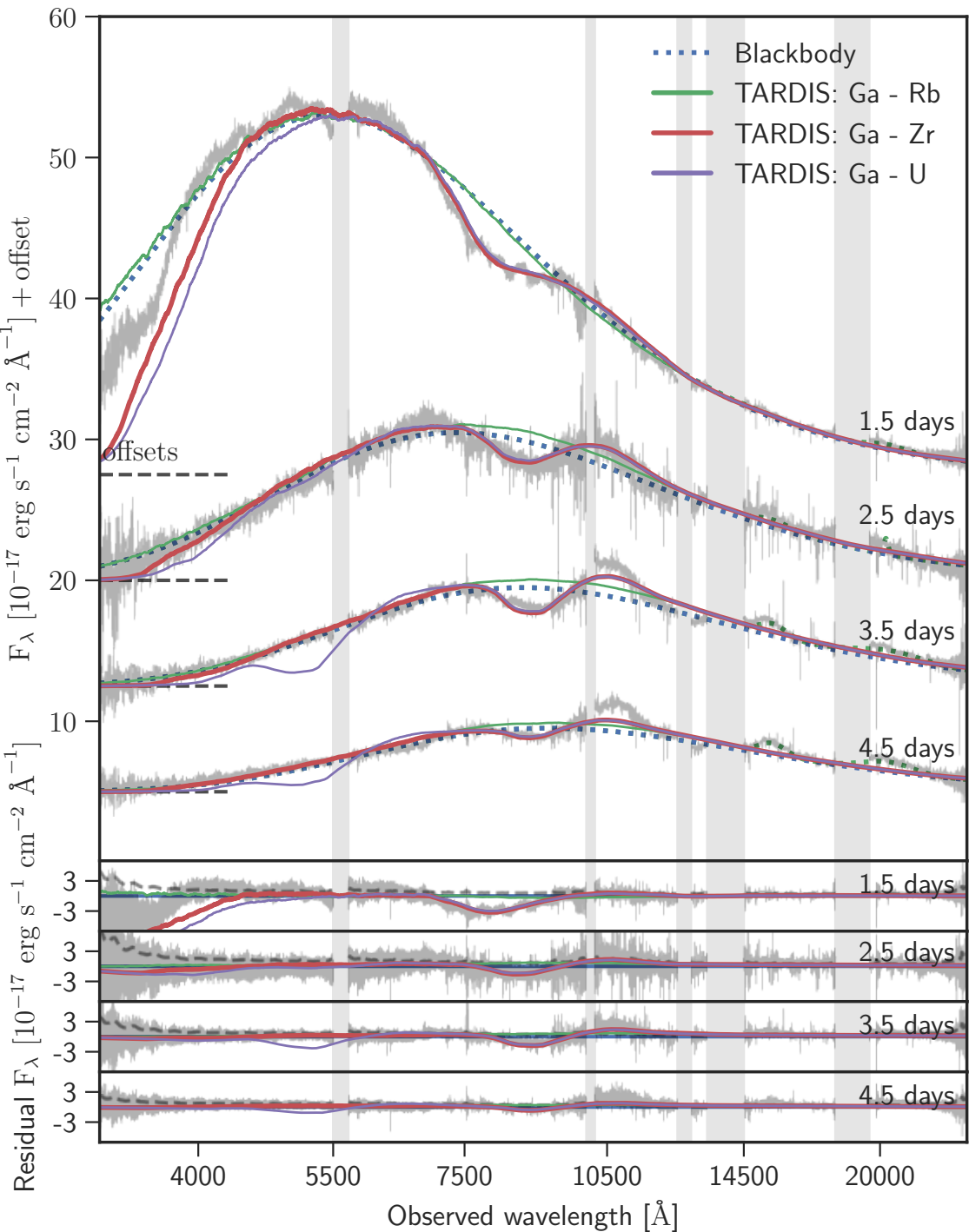


**Figure 5.13: Extended Data:** TARDIS models generated to match the data from the first four epochs, similar to Fig. 5.4. The green line is the synthetic TARDIS spectrum using the r-process abundances and including from  $_{31}\text{Ga}$  up to  $_{37}\text{Rb}$ . The red line is additionally including  $_{38}\text{Sr}$ ,  $_{39}\text{Y}$ , and  $_{30}\text{Zr}$ . The purple line is including all elements from  $_{31}\text{Ga}$  to  $_{92}\text{U}$ , their respective abundances set by the solar r-process abundances, as shown in Fig. 5.2. This shows that the 810 nm absorption features can adequately be explained as due to Sr II, Y II and Zr II.

## CONCLUSIONS AND OUTLOOK

---

I will here sum up the conclusions that are drawn from the work presented here. In Chapter 2, I present the XSGRB legacy sample of GRB afterglows and I show that it is not significantly different from the underlying, parent *Swift* sample and thus representative for the general population of GRB afterglows. I describe the data-reduction process in detail and make a public release of this data to use in the astronomical community. I have constrained the fraction of dark bursts in the XSGRB legacy sample to be similar to what is found in other complete samples. I measure the column density of neutral hydrogen,  $N_{\text{HI}}$ , in all the GRB afterglows where it is possible, thereby expanding the number of GRB afterglow  $N_{\text{HI}}$  measurements by  $\sim 30$  per cent. This sample has already been the subject of a series of papers (See Sect. 5.2.6), and will continue to form the basis for forthcoming papers, examining the details of the sample. This sample will be the benchmark for GRB afterglow sample studies in the future, as it will literally take more than eight years of continuous effort to collect a new sample of similar size. However, because GRBs are observable at such extreme distances, they continue to be a invaluable tool for the study of the early universe (Tanvir et al. 2009; Cucchiara et al. 2011; Tanvir et al. 2017a). The endeavor of continuing the follow-up of GRB afterglows has now been taken over by the stargate collaboration. This collaboration encompasses most of the European researchers that use ESO facilities to study GRBs and their associated SNe. Stargate has already borne fruit with the successful follow-up of the nearby GRB/SN, GRB 171205A/SN 2017iuk (Izzo et al. in prep) and the potential detection of the shock breakout in GRB 180205 (Bolmer et al. in prep). As the primary person responsible for the data-reduction of X-shooter data obtained under the stargate umbrella, I will continue to play a significant role in GRBs research.

In Chapter 3, I presented the revised redshift of GRB 111117A, the properties of its host, and the implications for short GRB progenitor formation channels. This GRB had previously been the subject of two publications that, as I have shown, derived wrong photometric redshifts based on a photometric measurement error. With the new revised redshift, GRB 111117A is the high-confidence short GRB with the highest measured redshift. The redshift of GRB 111117A makes it an important benchmark for short GRB detectability, as models of the intrinsic redshift distribution of short GRBs depend sensitively on high-redshift GRBs. That GRB 111117A is at

$z = 2.211$  provides evidence against a lognormal delay time distribution between progenitor formation and binary neutron star merger. Additionally, because the universe is only 3 Gyrs old at  $z = 2.211$ , the binary neutron star system that gave rise to GRB 111117A had to be separated by  $< 3.1 R_\odot$  at formation, if the orbital decay is due to the emission of gravitational waves. The discovery of more high-redshift short GRBs is a crucial piece of work that need to be continued, if we are to accurately determine the redshift distribution of GRBs - a distribution that is essential for the expected rate of gravitational wave counterparts in upcoming runs of the LIGO/Virgo gravitational wave detectors (Lamb et al. 2017; Fong et al. 2017b).

In Chapter 4, I present part of the discovery that was named the [Science breakthrough of the year 2017](#). We here show spectral and photometric evolution of this completely new phenomena and showcase how the data compare with synthetic models. We show that there is a gross similarity between the data and the models, indicating that the merger of two neutron stars produce a kilonova, powered by radioactive decay of freshly synthesized *r*-process elements. Through the comparison with models, we additionally constrain the mass in the ejecta. My contribution to the work was primarily ensuring the highest possible quality of the reduction of the spectroscopic data and the analysis of the host, but I also significantly contributed to the main text. The work presented in Chapter 4 is only a small part of the combined international effort of follow-up and understanding of this new a fantastic phenomenon (Smartt et al. 2017; Kasen et al. 2017; Abbott et al. 2017d). The work presented in Chapter 4 is only the tip of the iceberg that is kilonova research, as I also showcase in Chapter 5, where we identify the spectral features caused by the presence of Sr and Y in the ejecta. This identification is at odds with previous identifications of the same features by different elements (Smartt et al. 2017). The identification we provide in Chapter 5 is a very concrete evidence that a neutron star merger produces at least the light *r*-process elements. This is additionally the first unequivocal identification of the site of *r*-process element formation and potentially one of the strongest evidences that neutron stars are made primarily of neutrons.

Understanding and interpreting the wealth of data that was obtained of AT 2017gfo is still a task that is far from complete, and the number of components and their nature required to explain the light-curve and the spectral evolution is still very much a matter of debate (Kasen et al. 2017; Villar et al. 2017; Waxman et al. 2017; Arcavi 2018). And while the ejecta mass and composition of AT2017gfo appear to be adequate to explain the *r*-process abundances, there are still open questions regarding the required duty-cycle between formation and coalescence (Hotokezaka et al. 2018). Because the ejecta composition and dynamics are expected to depend sensitively on the details of the progenitor system (e.g. chirp mass, spin, etc.), kilonovae are expected to exhibit large variation in their spectral characteristics (Metzger 2017) and therefore it is essential to figure out what degree of variation kilonovae will exhibit in their observed characteristics.

While AT 2017gfo is the first electromagnetic counterpart to a gravitational wave signal, it is unlikely to be the last. Since the discovery of AT2017gfo, the gravitational wave detectors LIGO/Virgo have been offline for upgrades. Projected to come online again in November 2018, the gravitational wave detectors will make use of their upgrades. With a sensitivity that should be close to doubled, the volume probed for gravitational waves is eight times as large and it is estimated that we could expect up to  $\sim 1$  binary neutron star merger **every month**. And this is just the beginning. KAGRA, the Japanese laser interferometer is expected to be in operation around 2020 with additionally, LIGO India projected to begin operations in 2024. So we are really at the dawn of the gravitational wave era.

To prepare for the era of multi-messenger astronomy, the users of ESO facilities for the follow-up to the counterparts to gravitational waves have decided to join together in the ENGRAVE collaboration. This collaboration is designed to apply for a wide range of ESO follow-up capabilities and it will be the umbrella under which the gravitational wave follow-up will lead. As an expert of X-shooter, I will hopefully contribute to the continued exploration of these new, wondrous phenomena which promise a golden age of discoveries.

## LIST OF PUBLICATIONS

---

### Publications by topic (ADS) (16-03-2018)

submitted: 22 – first author: 3 – citations: 468

#### Gravitational wave counterparts

1. Watson et al., *Discovery of neutron-capture elements in a neutron star merger*, Submitted to **Nature**, 2018
2. Pian et al., *Spectroscopic identification of r-process nucleosynthesis in a double neutron-star merger*, **Nature**, 2017 ([arXiv:1710.05858](#))
3. Abbot et al., *Multi-messenger Observations of a Binary Neutron Star Merger*, **ApJ**, 848, L12, 2017 ([arXiv:1710.05833](#))

#### Gamma-ray bursts

4. Heintz et al., *Chemical evolution of high redshift GRB host galaxies*, submitted to **A&A**
5. Zafar et al., *X-shooting GRBs at high redshift: probing dust production history*, submitted to **MNRAS**
6. Tanvir et al., *The escape fraction of ionizing radiation from massive stars*, submitted to **MNRAS**
7. Zafar et al., *X-shoted GRBs: A slightly steeper extinction curve for star-forming regions*, submitted to **MNRAS**
8. Heintz et al., *Highly-ionized metals as probes of the circumburst gas in the natal regions of gamma-ray bursts*, submitted to **MNRAS**
9. Selsing et al., *The X-shooter GRB afterglow legacy sample (XS-GRB)*, submitted to **A&A**([arXiv:1802.07727](#))

10. Heintz et al., *The luminous, massive and solar metallicity galaxy hosting the Swift  $\gamma$ -ray burst GRB 160804A at  $z = 0.737$* , MNRAS, 474, 2, 2018, ([arXiv:1711.02706](#))
11. **Selsing** et al., *The host galaxy of the short GRB111117A at  $z=2.211$ : impact on the short GRB redshift distribution and progenitor channels*, accepted for publication in A&A([arXiv:1707.01452](#))
12. Christensen et al., *Solving the conundrum of intervening strong MgII absorbers towards GRBs and quasars*, A&A, 608A, 84C, 2017, ([arXiv:1709.01084](#))
13. Heintz et al., *Steep extinction towards GRB 140506A reconciled from host galaxy observations: Evidence that steep reddening laws are local*, A&A, 601, A83, 2017, ([arXiv:1703.07109](#))
14. Krühler et al., *GRB hosts through cosmic time. VLT/X-Shooter emission-line spectroscopy of 96  $\gamma$ -ray-burst-selected galaxies at  $0.1 < z < 3.6$* , A&A, 581, A125, 2017, ([arXiv:1505.06743](#))
15. Japelj et al., *Spectrophotometric analysis of gamma-ray burst afterglow extinction curves with X-Shooter*, A&A, 579, A74, 2017, ([arXiv:1503.03623](#))

## Supernovae

16. Cano et al., *A spectroscopic look at the gravitationally lensed type Ia SN 2016geu at  $z=0.409$* , MNRAS, 473, 3, 2018, ([arXiv:1708.05534](#))
17. Rodney et al., *Two Peculiar Fast Transients in a Strongly Lensed Host Galaxy*, Accepted for publication in **Nature Astronomy**([arXiv:1707.02434](#))
18. Kelly et al., *An individual star at redshift 1.5 extremely magnified by a galaxy-cluster lens*, Accepted for publication in **Nature Astronomy**([arXiv:1706.10279](#))
19. Kelly et al., *SN Refsdal: Classification as a Luminous and Blue SN 1987A-like Type II Supernova*, ApJ, 831, 205, 2016, ([arXiv:1512.09093](#))
20. Rodney et al., *SN Refsdal: Photometry and Time Delay Measurements of the First Einstein Cross Supernova*, ApJ, 820 50, 2016, ([arXiv:1512.05734](#))
21. Kelly et al., *Deja Vu All Over Again: The Reappearance of Supernova Refsdal*, ApJ, 819 L8, 2016, ([arXiv:1512.04654](#))

## Quasars

22. **Selsing** et al., *An X-Shooter composite of bright  $1 < z < 2$  quasars from UV to infrared*, A&A, 585, A87, 2016, ([arXiv:1510.08058](#))

## RESUMÉ PÅ DANSK

---

Langt størstedelen af vores univers henligger i mørke, dets enorme udbredelse kun gennemtrængt at et tyndt spindelvæv af materie. Inde i dette spindelvæv har tyngdekraften arbejdet med at danne øer af lys, lavet af gigantiske samlinger af stjerner. Disse sammensmelninger af stof, som vi sidenhen er kommet til at kende som galakser, bærer historien om det liv, de har levet i form af deres kemiske sammensætning. På ethvert tidspunkt er denne sammensætning styret af den gas, der har formet stjernerne, samt den uundgåelige kemiske berigelse, som bliver drevet af stjernernes umættelige appetit for at gøre lette grundstoffer tungere. De eksplosioner, der enten markerer enden på nogle stjerners liv eller er resultatet af sammensmelningen af stjernernes askeprodukter, spreder kimen til en ny generation af stjerner, der er mere rige og komplekse i deres sammensætning. Som et led i vores erkendelse af vores plads i universet, kan vi undersøge den kosmiske historie, de grundstoffer, vi består af, fortæller. Denne afhandling undersøger de kraftigste eksplosioner i universet, gammaglimt. Den fokuserer på, hvordan de kan bruges til at undersøge det mørke univers, når deres lys kortvarigt gennemtrænger universet, samt hvilke konsekvenser disse begivenheder har for det univers, der huser dem. Jeg præsenterer her et homogent udvalgt datasæt af gammaglimt, der er resultatet af otte års sammenhængende indsats. Spektrene, som udgør datasættet, er rige på information om gassen, støvet, metallerne og molekylerne omkring eksplosionerne. De dækker en lang række rødforskydninger, og på den måde giver det unikke indsigter i både stjernedannelseshistorien og den kemiske udviklingshistorie for universet. Denne skattekiste har gjort det muligt for mig et opdage særligt betydningsfulde begivenheder, hvilket inkluderer at bestemme GRB 111117A til at være det fjernehvide korte gammaglimt, der nogenside er fundet. Studiet af dette enkelte glimt gjorde, at jeg kunne begrænse den mulige intrinsiske rødforskydningsfordeling for korte gammaglimt og de fysiske betingelserne i de systemer, der giver anledning til korte gammaglimt. Her præsenterer jeg også observationerne af det elektromagnetiske modstykke til et sammenfaldende kort gammaglimt og et tyngdebølggesignal, hvilket blev lavet ved sammenstødet mellem to neutronstjerner. Disse data indeholder hemmeligheden om, hvilke fysiske mekanismer der ligger bag dette utrolige fænomen, vi kalder en kilonova. I de spektroskopiske data af kilonovaen identificerer vi de spektrale signaturer fra lette *r*-proces grundstoffer, hvilket er den første overbevisende indikation på, hvor disse elementer bliver dannet.

## BIBLIOGRAPHY

---

- Abadie J., et al., 2012, *Phys. Rev. D - Part. Fields, Gravit. Cosmol.*, 85, 082002
- Abbott B. P., et al., 2016a, *Phys. Rev. X*, 6
- Abbott B. P., et al., 2016b, *Phys. Rev. Lett.*, 116
- Abbott B. P., et al., 2016c, *ApJS*, 227, 14
- Abbott B. P., et al., 2016d, *Astrophys. J. Lett. Vol. 826, Issue 1, Artic. id. L13, 8 pp. (2016)*, 826
- Abbott B. P., et al., 2017a, *Phys. Rev. Lett.*, 118, 221101
- Abbott B. P., et al., 2017b, *Phys. Rev. Lett.*, 119
- Abbott B. P., et al., 2017c, *Phys. Rev. Lett.*, 119, 161101
- Abbott B. P., et al., 2017d, *Astrophys. J. Lett.*, 848, L12
- Abbott B. P., et al., 2017e, *ApJ*, 848, L13
- Abbott B. P., et al., 2017f, *ApJ*, 851, L35
- Abrarov S. M., Quine B. M., 2015a, *J. Math. Res.*, 7, 44
- Abrarov S. M., Quine B. M., 2015b, *J. Math. Res.*, 7, 163
- Ackermann M., et al., 2014, *Sci*, 343, 42
- Alexander K. D., et al., 2017, *Astrophys. J.*, 848
- Amati L., Guidorzi C., Frontera F., Della Valle M., Finelli F., Landi R., Montanari E., 2008, *MNRAS*, 391, 577
- Andreoni I., et al., 2017, *PASA*, 34
- Antonelli L. A., et al., 2009, *A&A*, 507, L45

- Antonelli L. A., et al., 2010, GRB Coordinates Network, Circular Service, No. 10620, #1 (2010),  
**10620**
- Aptekar R. L., et al., 1995, [SSRv](#), 71, 265
- Arabsalmani M., et al., 2018, [MNRAS](#), 473, 3312
- Arcavi I., 2018
- Arcavi I., et al., 2017, [Nature](#), 551, 64
- Arcodia R., Campana S., Salvaterra R., 2016, [A&A](#), 590, A82
- Argast D., Samland M., Thielemann F.-K., Qian Y.-Z., 2004, [A&A](#), 416, 997
- Arun K. G., Tagoshi H., Pai A., Mishra C. K., 2014, [Phys. Rev. D](#), 90, 024060
- Ashall C., et al., 2017, eprint arXiv:1702.04339, pp 1–18
- Astropy Collaboration 2013, [A&A](#), 558, A33
- Atek H., Kunth D., Schaerer D., Hayes M., Deharveng J. M., Östlin G., Mas-Hesse J. M., 2009, [A&A](#), 506, L1
- Atek H., Kunth D., Schaerer D., Miguel Mas-Hesse J., Hayes M., Östlin G., Kneib J.-P., 2014, [A&A](#), 561, A89
- Atwood W. B., et al., 2009, [ApJ](#), 697, 1071
- Axelsson M., et al., 2012, [Astrophys. J. Lett.](#), 757, L31
- Baade W., Zwicky F., 1934, [Proceedings of the National Academy of Science](#), 20, 259
- Bañados E., et al., 2017, [Nature](#), 553, 473
- Band D. L., 2006, [ApJ](#), 644, 378
- Band D., et al., 1993, [ApJ](#), 413, 281
- Bannister K., 2017, Gcn Circ., 21559
- Barnacka A., Loeb A., 2014, [Astrophys. J. Lett.](#), 794, L8
- Barnes J., Kasen D., 2013, [ApJ](#), 775, 18
- Barthelmy S. D., 2000, in AIP Conf. Proc.. AIP, pp 731–735, doi:10.1063/1.1361631, <http://aip.scitation.org/doi/abs/10.1063/1.1361631>

- Barthelmy S. D., et al., 2005, [SSRv](#), 120, 143
- Baumgartner W. H., Tueller J., Markwardt C. B., Skinner G. K., Barthelmy S., Mushotzky R. F., Evans P. A., Gehrels N., 2013, [Astrophys. Journal, Suppl. Ser.](#), 207, 19
- Bauswein A., Goriely S., Janka H. T., 2013, [ApJ](#), 773, 78
- Behroozi P. S., Ramirez-Ruiz E., Fryer C. L., 2014, [ApJ](#), 792, 123
- Belczynski K., Perna R., Bulik T., Kalogera V., Ivanova N., Lamb D. Q., 2006, [ApJ](#), 648, 1110
- Belczynski K., Holz D. E., Bulik T., O'Shaughnessy R., 2016, [Nature](#), 534, 512
- Belczynski K., et al., 2017, eprint arXiv:1712.00632
- Benner D. C., Rinsland C. P., Devi V. M., Smith M. A. H., Atkins D., 1995, [JQSRT](#), 53, 705
- Berger E., 2007, [ApJ](#), 670, 1254
- Berger E., 2009, [ApJ](#), 690, 231
- Berger E., 2010, [ApJ](#), 722, 1946
- Berger E., 2011a, [NewAR](#), 55, 1
- Berger E., 2011b, GRB Coordinates Network, Circular Service, No. 12193, #1 (2011), [12193](#)
- Berger E., 2014, [ARA&A](#), 52, 43
- Berger E., Kulkarni S., Frail D., 2003, [ApJ](#), 590, 379
- Berger E., et al., 2005, [Nature](#), 438, 988
- Berger E., et al., 2007, [ApJ](#), 664, 1000
- Berger E., et al., 2011, [ApJ](#), 743
- Berger E., Fong W., Chornock R., 2013b, [ApJ](#), 774, L23
- Berger E., Fong W., Chornock R., 2013a, [Astrophys. J. Lett.](#), 774, L23
- Bernardini M. G., et al., 2015, [MNRAS](#), 446, 1129
- Bertin E., Arnouts S., 1996, [A&AS](#), 117, 393
- Bethe H. A., 1990, [RvMP](#), 62, 801
- Bethe H. A., Wilson J. R., 1985, [ApJ](#), 295, 14

- Biémont E., Quinet P., 2003, *Physica Scripta Volume T*, 105, 38
- Bisterzo S., Travaglio C., Gallino R., Wiescher M., Käppeler F., 2014, *ApJ*, 787, 10
- Blandford R. D., Znajek R. L., 1977, *MNRAS*, 179, 433
- Bloom J. S., Kulkarni S. R., Djorgovski S. G., 2002, *AJ*, 123, 1111
- Bloom J. S., et al., 2006, *ApJ*, 638, 354
- Boella G., Butler R. C., Perola G. C., Piro L., Scarsi L., Bleeker J. A., 1997, *A&AS*, 122, 299
- Bouwens R. J., et al., 2015, *ApJ*, 803, 1
- Briggs M. S., et al., 1996, *ApJ*, 459, 40
- Brocklehurst M., 1971, *MNRAS*, 153, 471
- Bromberg O., Nakar E., Piran T., Sari R., 2012, *ApJ*, 749, 110
- Bromberg O., Nakar E., Piran T., Sari R., 2013, *ApJ*, 764, 179
- Bromberg O., Granot J., Lyubarsky Y., Piran T., 2014, *MNRAS*, 443, 1532
- Bruzual G., Charlot S., 2003, *MNRAS*, 344, 1000
- Bucciantini N., Thompson T. A., Arons J., Quataert E., Del Zanna L., 2006, *MNRAS*, 368, 1717
- Buchner J., Schulze S., Bauer F. E., 2017, *MNRAS*, 464, 4545
- Bufano F., et al., 2010, GRB Coordinates Network, Circular Service, No. 10543, #1 (2010), [10543](#)
- Bufano F., et al., 2012, *ApJ*, 753, 67
- Burbidge E. M., Burbidge G. R., Fowler W. A., Hoyle F., 1957a, *Reviews of Modern Physics*, 29, 547
- Burbidge E. M., Burbidge G. R., Fowler W. A., Hoyle F., 1957b, in [Burbidge et al. \(1957a\)](#), p. 547
- Burrows D. N., et al., 2005, *SSRv*, 120, 165
- Burrows D. N., et al., 2007, in Siegmund O. H. W., ed., Vol. 6686, SPIE Conf. Ser.. International Society for Optics and Photonics, p. 668607 ([arXiv:0803.1844](#)), doi:[10.1117/12.735130](#), <http://proceedings.spiedigitallibrary.org/proceeding.aspx?doi=10.1117/12.735130>
- Campana S., Thöne C. C., de Ugarte Postigo A., Tagliaferri G., Moretti A., Covino S., 2010, *MNRAS*, 402, 2429

- Campana S., et al., 2012, [MNRAS](#), 421, 1697
- Cano Z., et al., 2011, [ApJ](#), 740
- Cano Z., et al., 2014, [Astron. Astrophys. Vol. 568, id.A19, 16 pp.](#), 568
- Cano Z., et al., 2017a, [A&A](#), 605, A107
- Cano Z., Wang S. Q., Dai Z. G., Wu X. F., 2017b, [Adv. Astron.](#), 2017, 1
- Cantiello M., et al., 2018, [ApJ](#), 854, L31
- Cao Y., et al., 2013, [Astrophys. J. Lett.](#), 775, L7
- Capaccioli M., Schipani P., 2011, [The Messenger](#), 146, 2
- Cardelli J. A., Clayton G. C., Mathis J. S., 1989, [ApJ](#), 345, 245
- Castor J. I., Abbott D. C., Klein R. I., 1975, [ApJ](#), 195, 157
- Castro Cerón J. M., Michałowski M. J., Hjorth J., Watson D., Fynbo J. P. U., Gorosabel J., 2006, [ApJ](#), 653, L85
- Castro-Tirado A. J., et al., 2005, [A&A](#), 439, L15
- Castro-Tirado A. J., et al., 2010, [A&A](#), 517, A61
- Cavallo G., Rees M. J., 1978, [MNRAS](#), 183, 359
- Cenko S. B., Cucchiara A., 2011, GRB Coord. Network, Circ. Serv. No. 12577, 12577
- Chabrier G., 2003, [PASP](#), 115, 763
- Chen T.-W., Klose S., Guelbenzu A. N., Bolmer J., Krühler T., Greiner J., 2016, GRB Coordinates Network, Circular Service, No. 19975, #1 (2016), [19975](#)
- Chincarini G., et al., 2003, [The Messenger](#), 113, 40
- Chornock R., Berger E., 2011, GRB Coordinates Network, Circular Service, No. 11518, #1 (2011), [11518](#)
- Chornock R., et al., 2017, [Astrophys. J. Lett. Vol. 848, Issue 2, Artic. id. L19, 7 pp. \(2017\)](#), 848
- Christensen L., Hjorth J., Gorosabel J., 2004, [A&A](#), 425, 913
- Christensen L., Fynbo J. P. U., Prochaska J. X., Thöne C. C., de Ugarte Postigo A., Jakobsson P., 2011, [ApJ](#), 727, 73

- Christensen L., et al., 2017, [A&A](#), 608, A84
- Church R. P., Levan A. J., Davies M. B., Tanvir N., 2011, [MNRAS](#), 413, 2004
- Cobb B. E., Bloom J. S., Perley D. A., Morgan A. N., Cenko S. B., Filippenko A. V., 2010, [ApJ](#), 718, L150
- Colgate S. A., White R. H., 1966, [ApJ](#), 143, 626
- Corsi A., et al., 2016, [ApJ](#), 830, 42
- Costa E., et al., 1997, [Nature](#), 387, 783
- Coulter D. A., et al., 2017, [Sci](#), 358, 1556
- Covino S., et al., 2013, [MNRAS](#), 432, 1231
- Covino S., et al., 2017, [Nat. Astron.](#), 1, 791
- Coward D. M., Howell E. J., Branchesi M., Stratta G., Guetta D., Gendre B., Macpherson D., 2013, [MNRAS](#), 432, 2141
- Cowperthwaite P. S., et al., 2017, [Astrophys. J. Lett. Vol. 848, Issue 2, Artic. id. L17, 10 pp. \(2017\)](#), 848
- Cucchiara A., Cenko S. B., 2011, GRB Coord. Network, Circ. Serv. No. 12567,, 12567
- Cucchiara A., et al., 2011, [ApJ](#), 736, 7
- Cucchiara A., et al., 2013, [ApJ](#), 777, 94
- Cucchiara A., Fumagalli M., Rafelski M., Kocevski D., Prochaska J. X., Cooke R. J., Becker G. D., 2015, [ApJ](#), 804, 51
- D'Avanzo P., 2015, [JHEAp](#), 7, 73
- D'Avanzo P., 2017, Gcn Circ., 21653
- D'Avanzo P., et al., 2011a, GRB Coordinates Network, Circular Service, No. 12284, #1 (2011), [12284](#)
- D'Avanzo P., Vergani S. D., Flores H., Malesani D., Watson D., Levan A. J., Fynbo J. P. U., 2011b, GRB Coordinates Network, Circular Service, No. 12542, #1 (2011), [12542](#)
- D'Avanzo P., et al., 2014, [MNRAS](#), 442, 2342
- D'Avanzo P., et al., 2018

- D'Elia V., 2015, [Proc. Int. Astron. Union](#), 11, 251
- D'Elia V., Stratta G., 2011, [A&A](#), 532, A48
- D'Elia V., et al., 2009, [ApJ](#), 694, 332
- D'Elia V., et al., 2010, [A&A](#), 523, A36
- D'Elia V., Goldoni P., Malesani D., Tanvir N. R., Fynbo J. P. U., Melandri A., 2012a, GRB Coordinates Network, Circular Service, No. 13227, #1 (2012), [13227](#)
- D'Elia V., Goldoni P., Xu D., Krühler T., Fynbo J. P. U., Malesani D., Hartoog O. E., Tanvir N. R., 2012b, GRB Coordinates Network, Circular Service, No. 13494, #1 (2012), [13494](#)
- D'Elia V., Xu D., de Ugarte Postigo A., Malesani D., Fynbo J. P. U., Goldoni P., Tanvir N. R., Krühler T., 2012c, GRB Coordinates Network, Circular Service, No. 13507, #1 (2012), [13507](#)
- D'Elia V., et al., 2014, [A&A](#), 564, A38
- D'Elia V., et al., 2015a, GRB Coordinates Network, Circular Service, No. 18187, #1 (2015), [18187](#)
- D'Elia V., Krühler T., Xu D., Jakobsson P., Tanvir N. R., de Ugarte Postigo A., 2015b, GRB Coordinates Network, Circular Service, No. 18318, #1 (2015), [18318](#)
- D'Elia V., Xu D., Malesani D., Fynbo J. P. U., Flores H., Wiersema K., Watson D., 2016, GRB Coordinates Network, Circular Service, No. 19192, #1 (2016), [19192](#)
- De Mink S. E., Langer N., Izzard R. G., Sana H., De Koter A., 2013, [ApJ](#), 764, 166
- De Pasquale M., et al., 2003, [ApJ](#), 592, 1018
- Della Valle M., et al., 2006, [Nature](#), 444, 1050
- Den Hartog E. A., Lawler J. E., Sneden C., Cowan J. J., 2003, [ApJS](#), 148, 543
- Dessauges-Zavadsky M., Chen H.-W., Prochaska J. X., Bloom J. S., Barth A. J., 2006, [ApJ](#), 648, L89
- Di Matteo T., Perna R., Narayan R., 2002, [ApJ](#), 579, 706
- Díaz M. C., et al., 2017, [Astrophys. J. Lett. Vol. 848, Issue 2, Artic. id. L29, 5 pp. \(2017\)](#), 848
- Djorgovski S. G., Frail D. A., Kulkarni S. R., Bloom J. S., Odewahn S. C., Diercks A., 2001, [ApJ](#), 562, 654
- Dong Y. M., Qin Y. P., 2005, [MNRAS](#), 358, 1267
- Drouet M. R., et al., 2017, [Sci](#), 358, 1570

- Duncan R. C., Thompson C., 1992, [ApJ](#), 392, L9
- Dyk S. D. V., Li W., Filippenko A. V., 2003, [PASP](#), 115, 1289
- Eichler D., Livio M., Piran T., Schramm D. N., 1989, [Nature](#), 340, 126
- Elliott J., et al., 2013a, [A&A](#), 556, A23
- Elliott J., Schmidl S., Greiner J., Kann D. A., Ciceri S., Mancini L., 2013b, GRB Coordinates Network, Circular Service, No. 14898, #1 (2013), [14898](#)
- Esposito L. W., Harrison E. R., 1975, [ApJ](#), 196, L1
- Evans P. A., et al., 2007, [A&A](#), 469, 379
- Evans P. A., et al., 2009, [MNRAS](#), 397, 1177
- Evans P. A., et al., 2017, [Sci](#), 358, 1565
- Fenimore E. E., Madras C., Nayakshin S., 1996, [ApJ](#), 20, 30
- Fernández R., Metzger B. D., 2016, [Annu. Rev. Nucl. Part. Sci.](#), 66, 23
- Filippenko A. V., 1982, [PASP](#), 94, 715
- Fiore F., et al., 2005, [ApJ](#), 624, 853
- Flores H., et al., 2010, GRB Coordinates Network, Circular Service, No. 11317, #1 (2010), [11317](#)
- Flores H., et al., 2013a, GRB Coordinates Network, Circular Service, No. 14491, #1 (2013), [14491](#)
- Flores H., Covino S., de Ugarte Postigo A., Fynbo J., Krühler T., Xu D., Tanvir N., 2013b, GRB Coordinates Network, Circular Service, No. 14493, #1 (2013), [14493](#)
- Fong W., Berger E., 2013, [ApJ](#), 776, 18
- Fong W., Berger E., Fox D. B., 2010, [ApJ](#), 708, 9
- Fong W.-f., et al., 2011, [ApJ](#), 730, 26
- Fong W., et al., 2013, [ApJ](#), 769, 56
- Fong W., et al., 2016a, [ApJ](#), 833, 151
- Fong W., et al., 2016b, [ApJ](#), 833, 151
- Fong W., et al., 2017a, [Astrophys. J. Lett.](#), 848, L23

- Fong W., et al., 2017b, [ApJ](#), 848, L23
- Foreman-Mackey D., Hogg D. W., Lang D., Goodman J., 2013, [PASP](#), 125, 306
- Foucart F., et al., 2017, [Class. Quantum Gravity](#), 34
- Fox D. B., et al., 2005, [Nature](#), 437, 845
- Frail D. A., Kulkarni S. R., Nicastro L., Feroci M., Taylor G. B., 1997, [Nature](#), 389, 261
- Freedman D. L., Waxman E., 2001, [ApJ](#), 547, 922
- Freiburghaus C., Rosswog S., Thielemann F.-K., 1999, [ApJ](#), 525, L121
- Freudling W., Romaniello M., Bramich D. M., Ballester P., Forchi V., García-Dabló C. E., Moehler S., Neeser M. J., 2013, [A&A](#), 559, A96
- Fried D. L., 1966, [J. Opt. Soc. Am.](#), 56, 1380
- Friis M., et al., 2015, [MNRAS](#), 451, 167
- Fruchter A. S., et al., 1999, [ApJ](#), 519, L13
- Fruchter A. S., et al., 2006, [Nature](#), 441, 463
- Fryer C. L., Heger A., 2005, [ApJ](#), 623, 302
- Fynbo J. U., et al., 2001, [A&A](#), 369, 373
- Fynbo J. P. U., et al., 2006, [Nature](#), 444, 1047
- Fynbo J. P. U., et al., 2009, [ApJS](#), 185, 175
- Fynbo J. P. U., de Ugarte Postigo A., D'Elia V., Xu D., Malesani D., 2012a, GRB Coordinates Network, Circular Service, No. 13477, #1 (2012), [13477](#)
- Fynbo J. P. U., et al., 2012b, GRB Coordinates Network, Circular Service, No. 14120, #1 (2012), [14120](#)
- Fynbo J. P. U., Xu D., Malesani D., Krühler T., Perley D. A., D'Elia V., 2013, GRB Coordinates Network, Circular Service, No. 14286, #1 (2013), [14286](#)
- Fynbo J. P. U., et al., 2014a, [A&A](#), 512, 1
- Fynbo J. P. U., Tanvir N. R., Jakobsson P., Xu D., Malesani D., Milvang-Jensen B., 2014b, GRB Coordinates Network, Circular Service, No. 16217, #1 (2014), [16217](#)

- Gal-Yam A., et al., 2006, [Nature](#), 444, 1053
- Galama T. J., Wijers R. A. M. J., 2001, [ApJ](#), 549, L209
- Galama T. J., et al., 1998, [Nature](#), 395, 670
- Gammie C. F., McKinney J. C., Toth G., 2003, [ApJ](#), 589, 444
- Gehrels N., et al., 2004, [ApJ](#), 611, 1005
- Gehrels N., et al., 2005, [Nature](#), 437, 851
- Gehrels N., et al., 2006, [Nature](#), 444, 1044
- Gehrels N., Ramirez-Ruiz E., Fox D., 2009, [ARA&A](#), 47, 567
- Ghirlanda G., 2007, [R. Soc. London Philos. Trans. Ser. A](#), 365, 1385
- Ghirlanda G., Nava L., Ghisellini G., Celotti A., Firmani C., 2009, [Astron. Astrophys. Vol. 496, Issue 3, 2009, pp.585-595](#), 496, 585
- Ghirlanda G., Nava L., Ghisellini G., Celotti A., Burlon D., Covino S., Melandri A., 2012, [MNRAS](#), 420, 483
- Ghirlanda G., et al., 2016, [A&A](#), 594, A84
- Ghisellini G., Lazzati D., 1999, [MNRAS](#), 11, 5
- Ghisellini G., Ghirlanda G., Mereghetti S., Bosnjak Z., Tavecchio F., Firmani C., 2006, [MNRAS](#), 372, 1699
- Ginsburg A., et al., 2016, Astroquery V0.3.1, doi:10.5281/ZENODO.44961, <https://github.com/astropy/astroquery>
- Goldoni P., Royer F., François P., Horrobin M., Blanc G., Vernet J., Modigliani A., Larsen J., 2006, [Ground-based Airborne Instrum. Astron. Ed. by McLean](#), 6269, 80
- Goldoni P., Flores H., Malesani D., Levan A. J., Tanvir N. R., Fynbo J. P. U., 2010, GRB Coordinates Network, Circular Service, No. 10684, #1 (2010), [10684](#)
- Goldoni P., de Ugarte Postigo A., Fynbo J. P. U., 2013, GRB Coordinates Network, Circular Service, No. 15571, #1 (2013), [15571](#)
- Goldstein A., Connaughton V., Briggs M. S., Burns E., 2015, [Astrophys. Journal, Vol. 818, Issue 1, Artic. id. 18, 12 pp. \(2016\)](#), 818

- Goldstein A., et al., 2017, [Astrophys. J. Lett.](#), 848, L14
- Goriely S., Bauswein A., Janka H.-T., 2011, [ApJ](#), 738, L32
- Gorosabel J., et al., 2005, [A&A](#), 444, 711
- Grado A., 2017a, Gcn Circ., 21598
- Grado A., 2017b, Gcn Circ., 21703
- Graff P. B., Lien A. Y., Baker J. G., Sakamoto T., 2016, [ApJ](#), 818, 55
- Graham J. F., Fruchter A. S., 2013, [ApJ](#), 774, 119
- Graham J. F., Fruchter A. S., 2017, [ApJ](#), 834, 170
- Graham J. F., et al., 2009, [ApJ](#), 698, 1620
- Greiner J., et al., 2008, [PASP](#), 120, 405
- Greiner J., et al., 2011, [A&A](#), 526, A30
- Greiner J., et al., 2014, [A&A](#), 568, A75
- Greiner J., et al., 2015, [Nature](#), 523, 189
- Greiner J., et al., 2018, eprint arXiv:1802.01882
- Groot P. J., et al., 1998, [ApJ](#), 493, L27
- Groot P., et al., 2010, GRB Coordinates Network, Circular Service, No. 10441, #1 (2010), [10441](#)
- Grossman D., Korobkin O., Rosswog S., Piran T., 2014, [MNRAS](#), 439, 757
- Haggard D., Nynka M., Ruan J. J., Kalogera V., Cenko S. B., Evans P., Kennea J. A., 2017, [Astrophys. J.](#), 848
- Hallinan G., et al., 2017, [Sci](#), 358, 1579
- Hammer F., Flores H., Schaefer D., Dessauges-Zavadsky M., Le Floc'h E., Puech M., 2006, [arXiv.org](#), astro-ph, 103
- Hamuy M., Suntzeff N. B., Heathcote S. R., Walker A. R., Gigoux P., Phillips M. M., 1994, [PASP](#), 106, 566
- Hansen C. J., Montes F., Arcones A., 2014, [ApJ](#), 797, 123

- Hartoog O. E., Malesani D., Wiersema K., Krühler T., Schulze S., de Ugarte Postigo A., D'Elia V., Fynbo J. P. U., 2012, GRB Coordinates Network, Circular Service, No. 13730, #1 (2012), [13730](#)
- Hartoog O. E., et al., 2013a, [MNRAS](#), 430, 2739
- Hartoog O. E., Xu D., Malesani D., Tanvir N. R., Fynbo J. P. U., Kaper L., D'Elia V., 2013b, GRB Coordinates Network, Circular Service, No. 15494, #1 (2013), [15494](#)
- Hartoog O. E., Malesani D., Sanchez-Ramirez R., de Ugarte Postigo A., Levan A. J., Fynbo J. P. U., Vreeswijk P. M., Kaper L., 2014, GRB Coordinates Network, Circular Service, No. 16437, #1 (2014), [16437](#)
- Hartoog O. E., et al., 2015, [A&A](#), 580, A139
- Harutyunyan A. H., et al., 2008, [A&A](#), 488, 383
- Hayes M., Schaefer D., Östlin G., Mas-Hesse J. M., Atek H., Kunth D., 2011, [ApJ](#), 730, 8
- Heintz K. E., Malesani D., de Ugarte Postigo A., Pursimo T., Kruehler T., Telting J., Fynbo J. P. U., 2016, GRB Coordinates Network, Circular Service, No. 20020, #1 (2016), [20020](#)
- Heintz K. E., et al., 2017, [A&A](#), 601, A83
- Heintz K. E., et al., 2018, [MNRAS](#), 474, 2738
- Hewish A., Bell S. J., Pilkington J. D. H., Scott P. F., Collins R. A., 1968, [Nature](#), 217, 709
- Hjorth J., Bloom J. S., 2011, in Kouveliotou C., Wijers R. A. M. J., Woosley S., eds, No. 1973, Gamma-Ray Bursts. Cambridge University Press, Cambridge, pp 169–190 ([arXiv:1104.2274](#)), doi:10.1017/CBO9780511980336.010, <http://ebooks.cambridge.org/ref/id/CBO9780511980336A094>
- Hjorth J., et al., 2003, [Nature](#), 423, 847
- Hjorth J., et al., 2005a, [Nature](#), 437, 859
- Hjorth J., et al., 2005b, [ApJ](#), 630, L117
- Hjorth J., et al., 2012, [ApJ](#), 756, 187
- Hjorth J., Melandri A., Malesani D., Krühler T., Xu D., 2013, GRB Coordinates Network, Circular Service, No. 14365, #1 (2013), [14365](#)
- Hjorth J., et al., 2017, [Astrophys. J. Lett.](#) Vol. 848, Issue 2, Artic. id. L31, 6 pp. (2017)., 848
- Hogg D. W., Fruchter A. S., 1999, [ApJ](#), 520, 54

- Honda S., Aoki W., Ishimaru Y., Wanajo S., 2007, [ApJ](#), 666, 1189
- Horne K., 1986, [PASP](#), 98, 609
- Horváth I., Bagoly Z., Balázs L. G., de Ugarte Postigo A., Veres P., Mészáros A., 2010, [ApJ](#), 713, 552
- Hotokezaka K., Beniamini P., Piran T., 2018
- Hu L., et al., 2017, [Sci. Bull.](#), 62, 1433
- Hulse R. A., Taylor H. J., 1974, [Bull. Am. Astron. Soc.](#), 6, 453
- Hunter J. D., 2007, [CSE](#), 9, 90
- Ilbert O., et al., 2006, [A&A](#), 457, 841
- Im M., et al., 2017, [Astrophys. J. Lett.](#) Vol. 849, Issue 1, Artic. id. L16, 7 pp. (2017), 849
- Ivanova N., Heinke C. O., Rasio F. A., Belczynski K., Fregeau J. M., 2008, [MNRAS](#), 386, 553
- Izzo L., et al., 2017, [MNRAS](#), 472, 4480
- Jakobsson P., Hjorth J., Fynbo J. P. U., Watson D., Pedersen K., Björnsson G., Gorosabel J., 2004, [ApJ](#), 617, L21
- Jakobsson P., et al., 2005, [ApJ](#), 629, 45
- Jakobsson P., et al., 2006, [A&A](#), 447, 897
- Jakobsson P., et al., 2012a, [ApJ](#), 752, 62
- Jakobsson P., et al., 2012b, [ApJ](#), 752, 62
- Janka H. T., 2012, [Annu. Rev. Nucl. Part. Sci.](#), 62, 407
- Janka H. T., Langanke K., Marek A., Martínez-Pinedo G., Müller B., 2007, [Phys. Rep.](#), 442, 38
- Japelj J., et al., 2015, [A&A](#), 579, A74
- Jeffery D. J., Branch D., 1990, in Wheeler J. C., Piran T., Weinberg S., eds, Supernovae, Jerusalem Winter School for Theoretical Physics. p. 149
- Ji A. P., Frebel A., Chiti A., Simon J. D., 2016, [Nature](#), 531, 610
- Jin Z. P., Li X., Cano Z., Covino S., Fan Y. Z., Wei D. M., 2015, [Astrophys. J. Lett.](#), 811, L22
- Jin Z.-P., et al., 2016, [Nat. Commun.](#), 7, 12898

- Jones E., Oliphant T., Peterson P., 2001, SciPy: Open source scientific tools for Python, <http://www.scipy.org/>
- Jones D. H., et al., 2009, *MNRAS*, 399, 683
- Jones A., Noll S., Kausch W., Szyszka C., Kimeswenger S., 2013, *A&A*, 560, A91
- Just O., Bauswein A., Pulpillo R. A., Goriely S., Janka H.-T., 2015, *MNRAS*, 448, 541
- Kann D. A., et al., 2011, *ApJ*, 734, 96
- Kann D. A., et al., 2017, eprint arXiv:1706.00601
- Karp A. H., Lasher G., Chan K. L., Salpeter E. E., 1977, *ApJ*, 214, 161
- Kasen D., Badnell N. R., Barnes J., 2013, *ApJ*, 774, 25
- Kasen D., Fernández R., Metzger B. D., 2015, *MNRAS*, 450, 1777
- Kasen D., Metzger B., Barnes J., Quataert E., Ramirez-Ruiz E., 2017, *Nature*, 551, 80
- Kasliwal M. M., et al., 2017, *Sci*, 358, 1559
- Kastaun W., Ciolfi R., Endrizzi A., Giacomazzo B., 2017, *Phys. Rev. D*, 96
- Katz J. I., 1994, *ApJ*, 432, L107
- Kausch W., et al., 2015, *A&A*, 576, A78
- Kennicutt R. C., 1998, *ARA&A*, 36, 189
- Kerzendorf W. E., Sim S. A., 2014, *MNRAS*, 440, 387
- Kewley L. J., Brown W. R., Geller M. J., Kenyon S. J., Kurtz M. J., 2007, *AJ*, 133, 882
- Kistler M. D., Yüksel H., Beacom J. F., Hopkins A. M., Wyithe J. S. B., 2009, *ApJ*, 705, L104
- Kiziltan B., Kottas A., De Yoreo M., Thorsett S. E., 2013, *ApJ*, 778, 66
- Klebesadel R. W., Strong I. B., Olson R. A., 1973, *ApJ*, 182, L85
- Knust F., Kann D. A., Krühler T., Greiner J., 2015, GRB Coordinates Network, Circular Service, No. 17767, #1 (2015), [17767](#)
- Kocevski D., et al., 2009, *ApJ*, 702, 377
- Komissarov S. S., Barkov M. V., 2009, *MNRAS*, 397, 1153

- Komiya Y., Shigeyama T., 2016, [ApJ](#), 830, 76
- Kopač D., et al., 2012, [MNRAS](#), 424, 2392
- Kouveliotou C., Meegan C. A., Fishman G. J., Bhat N. P., Briggs M. S., Koshut T. M., Paciesas W. S., Pendleton G. N., 1993, [ApJ](#), 413, L101
- Krongold Y., Prochaska J. X., 2013, [ApJ](#), 774, 115
- Kröhler T., et al., 2011a, [A&A](#), 526, A153
- Kröhler T., et al., 2011b, [A&A](#), 534, A108
- Kröhler T., et al., 2012a, [ApJ](#), 758, 46
- Kröhler T., Fynbo J. P. U., Milvang-Jensen B., Tanvir N., Jakobsson P., 2012b, GRB Coordinates Network, Circular Service, No. 13134, #1 (2012), [13134](#)
- Kröhler T., et al., 2012c, GRB Coordinates Network, Circular Service, No. 13930, #1 (2012), [13930](#)
- Kröhler T., et al., 2013a, [A&A](#), 557, A18
- Kröhler T., Malesani D., Xu D., Fynbo J. P. U., Levan A. J., Tanvir N. R., D'Elia V., Perley D., 2013b, GRB Coordinates Network, Circular Service, No. 14264, #1 (2013), [14264](#)
- Kröhler T., Xu D., Sanchez-Ramirez R., Malesani D., Fynbo J., Flores H., 2013c, GRB Coordinates Network, Circular Service, No. 14390, #1 (2013), [14390](#)
- Kröhler T., Tanvir N. R., Malesani D., Xu D., Fynbo J. P. U., 2014a, GRB Coordinates Network, Circular Service, No. 15900, #1 (2014), [15900](#)
- Kröhler T., Malesani D., de Ugarte Postigo A., Melandri A., Fynbo J. P. U., 2014b, GRB Coordinates Network, Circular Service, No. 16194, #1 (2014), [16194](#)
- Kröhler T., Vreeswijk P. M., Fynbo J. P. U., 2014c, GRB Coordinates Network, Circular Service, No. 16401, #1 (2014), [16401](#)
- Kröhler T., et al., 2015a, [A&A](#), 581, A125
- Kröhler T., Xu D., Fynbo J. P. U., Malesani D., Cano Z., de Ugarte Postigo A., 2015b, GRB Coordinates Network, Circular Service, No. 17420, #1 (2015), [17420](#)
- Kröhler T., et al., 2016a, GRB Coordinates Network, Circular Service, No. 19186, #1 (2016), [19186](#)
- Kröhler T., Xu D., Bolmer J., Wiersema K., Malesani D., Sanchez-Ramirez R., Fynbo J. P. U., 2016b, GRB Coordinates Network, Circular Service, No. 19971, #1 (2016), [19971](#)

- Kröhler T., Kuncarayakti H., Schady P., Anderson J. P., Galbany L., Gensior J., 2017, *A&A*, 602, A85
- Kuijken K., 2011, *The Messenger*, 146, 8
- Kulkarni S. R., 2005
- Kulkarni S. R., et al., 1999a, *Nature*, 398, 389
- Kulkarni S. R., et al., 1999b, *ApJ*, 522, L97
- Kumar P., Zhang B., 2015, *Phys. Rep.*, 561, 1
- Kurucz R. L., 2017, *Canadian Journal of Physics*, 95, 825
- Kyutoku K., Ioka K., Okawa H., Shibata M., Taniguchi K., 2015, *Phys. Rev. D - Part. Fields, Gravit. Cosmol.*, 92
- LIGO Scientific Collaboration Virgo Collaboration Monitor F. G.-R. B., INTEGRAL 2017, *ApJ*, 848, L13
- Lamb D. Q., Reichart D. E., 2000, *ApJ*, 536, 1
- Lamb G. P., Tanaka M., Kobayashi S., 2017, *MNRAS*, p. 472
- Lattimer J. M., Mackie F., Ravenhall D. G., Schramm D. N., 1977, *ApJ*, 213, 225
- Lawler J. E., Wickliffe M. E., Cowley C. R., Sneden C., 2001a, *ApJS*, 137, 341
- Lawler J. E., Bonvallet G., Sneden C., 2001b, *ApJ*, 556, 452
- Lawler J. E., Wickliffe M. E., den Hartog E. A., Sneden C., 2001c, *ApJ*, 563, 1075
- Lawler J. E., Den Hartog E. A., Sneden C., Cowan J. J., 2006, *ApJS*, 162, 227
- Lazzati D., López-Cámara D., Cantiello M., Morsony B. J., Perna R., Workman J. C., 2017, *ApJ*, 848, L6
- Le Floc'h E., et al., 2003, *A&A*, 400, 499
- Lee W. H., Ramirez-Ruiz E., van de Ven G., 2010, *ApJ*, 720, 953
- Leibler C. N., Berger E., 2010, *ApJ*, 725, 1202
- Letchworth K. L., Benner D. C., 2007, *JQSRT*, 107, 173
- Levan A. J., et al., 2006, *ApJ*, 648, L9

- Levan A. J., et al., 2013, [ApJ](#), 781, 13
- Levan A. J., et al., 2017, [ApJ](#), 848, L28
- Levesque E. M., et al., 2010, [MNRAS](#), 401, 963
- Levinson A., Globus N., 2013, [ApJ](#), 770, 159
- Li L.-X., Paczyński B., 1998, [Astrophys. Journal](#), Vol. 507, Issue 1, pp. L59-L62., 507, L59
- Liang E.-W., et al., 2013, [ApJ](#), 774, 13
- Lien A., Sakamoto T., Gehrels N., Palmer D. M., Barthelmy S. D., Graziani C., Cannizzo J. K., 2014, [ApJ](#), 783, 24
- Lien A., et al., 2016, [ApJ](#), 829, 7
- Lipunov V. M., et al., 2017, [Astrophys. J. Lett.](#), 850, L1
- Littlejohns O. M., Tanvir N. R., Willingale R., Evans P. A., O'Brien P. T., Levan A. J., 2013, [MNRAS](#), 436, 3640
- Lloyd N. M., Petrosian V., 2000, [ApJ](#), 543, 722
- Lodders K., Palme H., Gail H.-P., 2009, [Landolt Börnstein](#),
- López S., et al., 2016, [A&A](#), 594, A91
- Lucy L. B., Solomon P. M., 1970, [ApJ](#), 159, 879
- Lyman J. D., et al., 2017, [MNRAS](#), 1817, stx220
- Lyman J. D., et al., 2018, eprint arXiv:1801.02669
- MacFadyen A. I., Woosley S. E., 1999a, [ApJ](#), 524, 262
- MacFadyen A. I., Woosley S. E., 1999b, [ApJ](#), 524, 262
- MacFadyen A. I., Woosley S. E., Heger A., 2001, [ApJ](#), 550, 410
- Madau P., Dickinson M., 2014, [ARA&A](#), 52, 415
- Maeder A., Meynet G., 2012, [RvMP](#), 84, 25
- Malesani D., 2017, [Gcn Circ.](#), 21577
- Malesani D., Palazzi E., 2010, GRB Coordinates Network, Circular Service, No. 10631, #1 (2010), [10631](#)

- Malesani D., et al., 2004, [ApJ](#), 609, L5
- Malesani D., Fynbo J. P. U., Christensen L., de Ugarte Postigo A., Milvang-Jensen B., Covino S., 2009a, GRB Coordinates Network, [9761](#)
- Malesani D., et al., 2009b, GRB Coordinates Network, [9942](#)
- Malesani D., Schulze S., de Ugarte Postigo A., Xu D., D'Elia V., Fynbo J. P. U., Tanvir N. R., 2012, GRB Coordinates Network, Circular Service, No. 13649, #1 (2012), [13649](#)
- Malesani D., Krühler T., Perley D., Fynbo J. P. U., Xu D., Milvang-Jensen B., Goldoni P., Schulze S., 2013a, GRB Coordinates Network, Circular Service, No. 14225, #1 (2013), [14225](#)
- Malesani D., Xu D., Fynbo J. P. U., Krühler T., Perley D. A., Vergani S. D., Goldoni P., 2013b, GRB Coordinates Network, Circular Service, No. 14291, #1 (2013), [14291](#)
- Malesani D., et al., 2015a, GRB Coordinates Network, Circular Service, No. 17755, #1 (2015), [17755](#)
- Malesani D., Tanvir N. R., Krühler T., de Ugarte Postigo A., Flores H., Xu D., Fynbo J. P. U., 2015b, GRB Coordinates Network, Circular Service, No. 18540, #1 (2015), [18540](#)
- Malesani D., Krühler T., Heintz K. E., Fynbo J. P. U., 2016, GRB Coordinates Network, Circular Service, No. 20180, #1 (2016), [20180](#)
- Marchesini D., et al., 2007, [ApJ](#), 656, 42
- Margutti R., et al., 2012, [ApJ](#), 756, 63
- Margutti R., et al., 2013, [MNRAS](#), 428, 729
- Margutti R., et al., 2018, eprint arXiv:1801.03531
- Markwardt C. B., et al., 2016, GRB Coordinates Network, Circular Service, No. 19974, #1 (2016), [19974](#)
- Martin D., Perego A., Arcones A., Thielemann F.-K., Korobkin O., Rosswog S., 2015, [ApJ](#), 813, 2
- Maselli A., et al., 2014, [Sci](#), 343, 48
- Matsuoka M., et al., 2009, [PASJ](#), 61, 999
- Maund J. R., Smartt S. J., Kudritzki R. P., Podsiadlowski P., Gilmore G. F., 2004, [Nature](#), 427, 129
- Mazzali P. A., Valenti S., Della Valle M., 2008, [Sci. Vol. 321, Issue 5893, pp. 1185- \(2008\)](#), 321, 1185
- McBreen S., et al., 2010, [A&A](#), 516, A71

- McCully C., et al., 2017, [ApJ](#), 848, L32
- McKinney J. C., Blandford R. D., 2009, [Mon. Not. R. Astron. Soc. Lett.](#), 394, L126
- Mckinney J. C., Tchekhovskoy A., Blandford R. D., 2012, [MNRAS](#), 423, 3083
- Meegan C. A., Fishman G. J., Wilson R. B., Horack J. M., Brock M. N., Paciesas W. S., Pendleton G. N., Kouveliotou C., 1992, [Nature](#), 355, 143
- Melandri A., 2017a, Gcn Circ., 21532
- Melandri A., 2017b, Gcn Circ., 21556
- Melandri A., et al., 2012, [MNRAS](#), 421, 1265
- Melandri A., et al., 2015, [A&A](#), 581, A86
- Meng Y.-Z., et al., 2018
- Mészáros P., Rees M. J., 1993, [ApJ](#), 405, 278
- Meszaros P., Rees M. J., 1996, [ApJ](#), 476, 232
- Metzger B. D., 2017, [LRR](#), 20, 3
- Metzger B. D., Berger E., 2012a, [ApJ](#), 746
- Metzger B. D., Berger E., 2012b, [ApJ](#), 746, 48
- Metzger M. R., Djorgovski S. G., Kulkarni S. R., Steidel C. C., Adelberger K. L., Frail D. A., Costa E., Frontera F., 1997, [Nature](#), 387, 878
- Metzger B. D., Thompson T. a., Quataert E., 2007, [ApJ](#), 659, 561
- Metzger B. D., et al., 2010, [MNRAS](#), 406, 2650
- Metzger B. D., Giannios D., Thompson T. A., Bucciantini N., Quataert E., 2011, [MNRAS](#), 413, 2031
- Michałowski M. J., et al., 2016, eprint arXiv:1610.06928
- Micol A., Arnaboldi M., Delmotte N. A. R., Mascetti L., Retzlaff J., 2016, in Peck A. B., Seaman R. L., Benn C. R., eds, Vol. 9910, Obs. Oper. Strateg. Process. Syst. VI. International Society for Optics and Photonics, p. 991030, doi:10.1117/12.2232655, <http://proceedings.spiedigitallibrary.org/proceeding.aspx?doi=10.1117/12.2232655>
- Milvang-Jensen B., et al., 2010, GRB Coordinates Network, Circular Service, No. 10876, #1 (2010), 10876

- Milvang-Jensen B., Fynbo J. P. U., Malesani D., Hjorth J., Jakobsson P., Møller P., 2012, [ApJ](#), 756, 25
- Modigliani A., et al., 2010, [SPIE Astron. Telesc. + Instrum.](#), 7737, 773728
- Modjaz M., 2011, [AN](#), 332, 434
- Modjaz M., et al., 2006, [ApJ](#), 645, L21
- Modjaz M., Liu Y. Q., Bianco F. B., Graur O., 2015, [ApJ](#), 832, 108
- Moehler S., et al., 2014, [A&A](#), 568, A9
- Moffat A. F. J., 1969, [A&A](#), 3, 455
- Moldon J., Beswick R., 2017, Gcn Circ., 21804
- Molinari E., et al., 2007, [A&A](#), 469, L13
- Mooley K., 2017, Gcn Circ., 21891
- Morgan A. N., et al., 2014, [MNRAS](#), 440, 1810
- Müller B., 2017, [Proc. Int. Astron. Union](#), 12, 17
- Munari U., Zwitter T., 1997, [A&A](#), 318, 269
- Munari U., et al., 2008, [A&A](#), 973, 969
- Mundell C. G., et al., 2013, [Nature](#), 504, 119
- Nagataki S., 2009, [ApJ](#), 704, 937
- Nagataki S., 2018, [Reports Prog. Phys.](#), 81, 026901
- Nakar E., 2007, [Phys. Rep.](#), 442, 166
- Nakar E., Piran T., 2003, [ApJ](#), 598, 400
- Nakar E., Piran T., 2016, [Astrophys. J.](#), 834, 28
- Narayan R., Paczynski B., Piran T., 1992, [ApJ](#), 395, L83
- Nava L., Nakar E., Piran T., 2016, [MNRAS](#), 455, 1594
- Newville M., Stensitzki T., Allen D. B., Rawlik M., Ingargiola A., Nelson A., 2016, Lmfit: Non-Linear Least-Square Minimization and Curve-Fitting for Python, Astrophysics Source Code Library (ascl:1606.014)

- Nicholl M., et al., 2017, *Astrophys. J. Lett.* Vol. 848, Issue 2, Artic. id. L18, 8 pp. (2017)., 848
- Nissanke S., Holz D. E., Hughes S. A., Dalal N., Sievers J. L., 2010, *ApJ*, 725, 496
- Noll S., Kausch W., Barden M., Jones A. M., Szyszka C., Kimeswenger S., Vinther J., 2012, *A&A*, 543, A92
- Norris J. P., Bonnell J. T., 2006, *ApJ*, 643, 266
- Norris J. P., Nemiroff R. J., Bonnell J. T., Scargle J. D., Kouveliotou C., Paciesas W. S., Meegan C. A., Fishman G. J., 1996, *Astrophys. J.* v.459, 459, 393
- Noterdaeme P., et al., 2012, *A&A*, 547, L1
- Nysewander M., Fruchter A. S., Pe'er A., 2009, *ApJ*, 701, 824
- O'Shaughnessy R., Belczynski K., Kalogera V., 2008, *ApJ*, 675, 566
- Oechslin R., Janka H. T., Marek a., 2006, *A&A*, 409, 20
- Oesch P. A., et al., 2016, *ApJ*, 819, 129
- Olivares E. F., et al., 2012, *A&A*, 539, A76
- Olivares E. F., et al., 2015, *A&A*, 577, A44
- Osborne J. P., Beardmore A. P., Evans P. A., Goad M. R., 2016, GRB Coordinates Network, Circular Service, No. 19969, #1 (2016), [19969](#)
- Oyarzún G. A., Blanc G. A., González V., Mateo M., Bailey J. I., 2017, *ApJ*, 843, 133
- Paczynski B., 1986, *ApJ*, 308, L43
- Pagnini G., Mainardi F., 2010, *JCoAM*, 233, 1590
- Palmerio J., Krühler T., Malesani D., Fynbo J. P. U., 2017, GRB Coordinates Network, Circular Service, No. 20589, #1 (2017), [20589](#)
- Pan Y. C., et al., 2017, *Astrophys. J.*, 848
- Papovich C., Dickinson M., Ferguson H. C., 2001, *ApJ*, 559, 620
- Patricelli B., Razzano M., Celli G., Fidecaro F., Pian E., Branchesi M., Stamerra A., 2016, *J. Cosmol. Astropart. Phys.*, 2016, 056
- Pe'er A., 2008, *ApJ*, 682, 463

- Pe'er A., 2015, [Adv. Astron.](#), 2015, 1
- Pe'er A., Zhang B.-B., Ryde F., McGlynn S., Zhang B., Preece R. D., Kouveliotou C., 2012, [MNRAS](#), 420, 468
- Pe'er A., Long K., Casella P., 2017, [ApJ](#), 846, 54
- Perego A., Rosswog S., Cabezón R. M., Korobkin O., Käppeli R., Arcones A., Liebendörfer M., 2014, [MNRAS](#), 443, 3134
- Perley D. A., et al., 2009, [AJ](#), 138, 1690
- Perley D. A., Bloom J. S., Cenko S. B., Cobb B. E., Morgan A. N., Miller A. A., Klein C. R., 2010, GRB Coordinates Network, Circular Service, No. 10399, #1 (2010), [10399](#)
- Perley D. A., et al., 2011, [AJ](#), 141, 36
- Perley D. A., et al., 2013, [ApJ](#), 778, 128
- Perley D. A., et al., 2014, [ApJ](#), 781, 37
- Perley D. A., et al., 2015, [ApJ](#), 801, 102
- Perley D. A., et al., 2016a, [ApJ](#), 817, 7
- Perley D. A., et al., 2016b, [ApJ](#), 817, 8
- Perley D. A., et al., 2017, [Mon. Not. R. Astron. Soc. Lett.](#), 465, L89
- Pescalli A., et al., 2016, [A&A](#), 587, A40
- Pian E., 2017, Gcn Circ., 21592
- Pian E., et al., 2006, [Nature](#), 442, 1011
- Pian E., et al., 2017, [Nature](#), 551, 67
- Pinto P. A., Eastman R. G., 2000, [ApJ](#), 530, 757
- Piran T., 1999, [Phys. Rep.](#), 314, 575
- Piran T., 2004, [RvMP](#), 76, 1143
- Piran T., 2005, [RvMP](#), 76, 1143
- Piran T., Nakar E., Rosswog S., 2013, [MNRAS](#), 430, 2121

- Piranomonte S., Vergani S. D., Malesani D., Fynbo J. P. U., Wiersema K., Kaper L., 2011, GRB Coordinates Network, Circular Service, No. 12164, #1 (2011), [12164](#)
- Piro A. L., Kollmeier J. A., 2017, [ApJ](#), 855, 103
- Planck Collaboration et al., 2016, [A&A](#), 594, A13
- Popham R., Woosley S. E., Fryer C., 1999, [Astrophys. J.](#), 518, 356
- Postnov K. A., Yungelson L. R., 2014, [LRR](#), 17, 3
- Pozanenko A., Mazaeva E., Sergeev A., Reva I., Volnova A., Klunko E., Korobtsev I., 2015, GRB Coordinates Network, Circular Service, No. 17903, #1 (2015), [17903](#)
- Pozanenko A., et al., 2017, [Astrophys. J. Lett.](#) Vol. 852, Issue 2, Artic. id. L30, 18 pp. (2018)., 852
- Poznanski D., Prochaska J. X., Bloom J. S., 2012, [MNRAS](#), 426, 1465
- Preece R. D., Briggs M. S., Mallozzi R. S., Pendleton G. N., Paciesas W. S., Band D. L., 1999, [ApJS](#), 126, 19
- Prochaska J. X., et al., 2004, [ApJ](#), 611, 200
- Prochaska J. X., et al., 2007, [ApJS](#), 168, 231
- Prochaska J. X., et al., 2009, [ApJ](#), 691, L27
- Pugliese V., Xu D., Tanvir N. R., Wiersema K., Fynbo J. P. U., Milvang-Jensen B., D'Elia V., 2015, GRB Coordinates Network, Circular Service, No. 17672, #1 (2015), [17672](#)
- Pugliese G., Covino S., Krühler T., Xu D., Tanvir N. R., 2016, GRB Coordinates Network, Circular Service, No. 18982, #1 (2016), [18982](#)
- Qian Y.-Z., 2000, [ApJ](#), 534, L67
- Rau A., Krühler T., Greiner J., 2013, GRB Coordinates Network, Circular Service, No. 15330, #1 (2013), [15330](#)
- Rees M. J., Meszaros P., 1992, [MNRAS](#), 258, 41P
- Rezzolla L., Giacomazzo B., Baiotti L., Granot J., Kouveliotou C., Aloy M. A., 2011, [Astrophys. J. Lett.](#), 732, L6
- Richard J., Kneib J.-P., Ebeling H., Stark D. P., Egami E., Fiedler A. K., 2011, [Mon. Not. R. Astron. Soc. Lett.](#), 414, L31

- Ricker G. R., Team H. S., 2004, Am. Astron. Soc. HEAD Meet. #8, id.18.06; Bull. Am. Astron. Soc. Vol. 36, p.942, 36, 942
- Robertson B. E., Ellis R. S., 2012, [ApJ](#), 744, 95
- Rodriguez C. L., Zevin M., Pankow C., Kalogera V., Rasio F. A., 2016, [ApJ](#), 832, L2
- Rol E., Wijers R. A. M. J., Kouveliotou C., Kaper L., Kaneko Y., 2005, [ApJ](#), 624, 868
- Roming P. W., et al., 2005, [SSRv](#), 120, 95
- Rossi E. M., Lazzati D., Salmonson J. D., Ghisellini G., 2004, [MNRAS](#), 354, 86
- Rossi A., et al., 2012, [A&A](#), 545, A77
- Rossi A., Piranomonte S., Savaglio S., Palazzi E., Michałowski M. J., Klose S., Hunt L. K., Amati L., 2014, [A&A](#), 47, 1
- Rosswog S., 2005, [ApJ](#), 634, 1202
- Rosswog S., Liebendoerfer M., Thielemann F. K., Davies M. B., Benz W., Piran T., 1998, [A&A](#), 341, 499
- Rosswog S., Feindt U., Korobkin O., Wu M.-R., Sollerman J., Goobar A., Martinez-Pinedo G., 2017, [Class. Quantum Gravity](#), 34, 104001
- Rowlinson A., Patruno A., O'Brien P. T., 2017, [MNRAS](#), 472, 1152
- Ruffert, M.; Janka, H.-T.; Schaefer G., 1996, [A&A](#), v.311, p.532
- Safarzadeh M., Scannapieco E., 2017, [MNRAS](#), 471, 2088
- Sakamoto T., et al., 2011, [ApJS](#), 195, 2
- Sakamoto T., et al., 2013, [ApJ](#), 766, 41
- Sakamoto T., et al., 2016, GRB Coordinates Network, Circular Service, No. 19276, #1 (2016), [19276](#)
- Salafia O. S., Ghisellini G., Pescalli A., Ghirlanda G., Nappo F., 2015, [MNRAS](#), 450, 3549
- Salafia O. S., Ghisellini G., Pescalli A., Ghirlanda G., Nappo F., 2016, [MNRAS](#), 461, 3607
- Salvaterra R., et al., 2009, [Nature](#), 461, 1258
- Salvaterra R., et al., 2012, [ApJ](#), 749, 68
- Samsing J., Macleod M., Ramirez-Ruiz E., 2014, [ApJ](#), 784, 71

- Sana H., Gosset E., Nazé Y., Rauw G., Linder N., 2008, [MNRAS](#), 386, 447
- Sana H., Gosset E., Evans C. J., 2009, [MNRAS](#), 400, 1479
- Sanchez-Ramirez R., et al., 2012, GRB Coordinates Network, Circular Service, No. 14035, #1 (2012), [14035](#)
- Sánchez-Ramírez R., et al., 2017, [MNRAS](#), 464, 4624
- Sari R., Esin A. A., 2001, [ApJ](#), 548, 787
- Sari R., Piran T., Halpern J., 1999, [ApJ](#), 519, L17
- Savaglio S., 2006, [NJPh](#), 8, 195
- Savaglio S., Glazebrook K., Le Borgne D., 2009, [ApJ](#), 691, 182
- Savchenko V., et al., 2017a, [Astrophys. J. Lett.](#) Vol. 848, Issue 2, Artic. id. L15, 8 pp. (2017), 848
- Savchenko V., et al., 2017b, [Astrophys. J. Lett.](#), 848, L15
- Schady P., et al., 2010, [MNRAS](#), 401, 2773
- Schady P., et al., 2015, [A&A](#), 579, A126
- Schlafly E. F., Finkbeiner D. P., 2011, [ApJ](#), 737, 103
- Schlegel D. J., Finkbeiner D. P., Davis M., 1998, [ApJ](#), 500, 525
- Schulze S., Covino S., Flores H., Fynbo J. P. U., Milvang-Jensen B., Sollerman J., Xu D., 2011, GRB Coordinates Network, Circular Service, No. 12770, #1 (2011), [12770](#)
- Schulze S., et al., 2012, GRB Coordinates Network, Circular Service, No. 13257, #1 (2012), [13257](#)
- Schulze S., Malesani D., Cucchiara A., Tanvir N. R., Krühler T., Postigo A. D. U., Leloudas G., 2014a, [A&A](#), 102, 1
- Schulze S., Wiersema K., Xu D., Fynbo J. P. U., 2014b, GRB Coordinates Network, Circular Service, No. 15831, #1 (2014), [15831](#)
- Schulze S., et al., 2015, [ApJ](#), 808, 73
- Schulze S., et al., 2018, [MNRAS](#), 473, 1258
- Sekiguchi Y., Kiuchi K., Kyutoku K., Shibata M., Taniguchi K., 2016, [Phys. Rev. D](#), 93, 124046
- Selsing J., Fynbo J. P. U., Christensen L., Krogager J.-K., 2015, [A&A](#), 87, 14

- Selsing J., et al., 2016a, GRB Coordinates Network, Circular Service, No. 19274, #1 (2016), [19274](#)
- Selsing J., Heintz K. E., Malesani D., Xu D., de Ugarte Postigo A., Tanvir N. R., Wiersema K., Fynbo J. P. U., 2016b, GRB Coordinates Network, Circular Service, No. 20061, #1 (2016), [20061](#)
- Selsing J., et al., 2018b, eprint arXiv:1707.01452, pp 1–8
- Selsing J., et al., 2018a, pp 1–43
- Shakura N. I., Sunyaev R. A., 1973, *X- Gamma-Ray Astron.*, 500, 155
- Shapley A. E., Steidel C. C., Pettini M., Adelberger K. L., 2003, *ApJ*, 588, 65
- Shappee B. J., et al., 2017, *Sci*, 358, 1574
- Sheffer Y., Prochaska J. X., Draine B. T., Perley D. A., Bloom J. S., 2009, *ApJ*, 701, L63
- Shibata M., Taniguchi K., 2006, *Phys. Rev. D - Part. Fields, Gravit. Cosmol.*, 73
- Siegel D. M., Metzger B. D., 2017, *Phys. Rev. Lett.*, 119, 231102
- Siegel D. M., Ciolfi R., Harte A. I., Rezzolla L., 2013, *Phys. Rev. D - Part. Fields, Gravit. Cosmol.*, 87
- Smartt S. J., 2009, *ARA&A*, 47, 63
- Smartt S. J., Vreeswijk P. M., Ramirez-Ruiz E., Gilmore G. F., Meikle W. P. S., Ferguson A. M. N., Knapen J. H., 2002, *ApJ*, 572, L147
- Smartt S. J., Maund J. R., Hendry M. A., Tout C. A., Gilmore G. F., Mattila S., Benn C. R., 2004, *Sci*, 303, 499
- Smartt S. J., et al., 2017, *Nature*, 551, 75
- Smette A., et al., 2015, *A&A*, 576, A77
- Sneden C. A., 1973, PhD thesis, THE UNIVERSITY OF TEXAS AT AUSTIN.
- Sneden C., Cowan J. J., Ivans I. I., Fuller G. M., Burles S., Beers T. C., Lawler J. E., 2000, *ApJ*, 533, L139
- Sneden C., et al., 2003, *ApJ*, 591, 936
- Sneden C., Lawler J. E., Cowan J. J., Ivans I. I., Den Hartog E. A., 2009, *ApJS*, 182, 80
- Sneden C., Cowan J. J., Gallino R., 2010, in Cunha K., Spite M., Barbuy B., eds, IAU Symposium Vol. 265, Chemical Abundances in the Universe: Connecting First Stars to Planets. pp 46–53, doi:10.1017/S1743921310000141

- Sneden C., Bean J., Ivans I., Lucatello S., Sobeck J., 2012, MOOG: LTE line analysis and spectrum synthesis, Astrophysics Source Code Library (ascl:1202.009)
- Soares-Santos M., et al., 2017, *Astrophys. J. Lett.* Vol. 848, Issue 2, Artic. id. L16, 7 pp. (2017), 848
- Soderberg A. M., Ramirez-Ruiz E., 2003, *MNRAS*, 345, 854
- Soderberg A. M., et al., 2006, *ApJ*, 650, 261
- Soderberg A. M., et al., 2010, *Nature*, 463, 513
- Sparre M., et al., 2011a, *ApJ*, 735, L24
- Sparre M., et al., 2011b, GRB Coordinates Network, Circular Service, No. 11607, #1 (2011), [11607](#)
- Sparre M., et al., 2014, *ApJ*, 785, 150
- Spruit H. C., 2002, *A&A*, 381, 923
- Stanek K. Z., et al., 2003, *ApJ*, 591, L17
- Stanek K. Z., et al., 2007, *ApJ*, 654, L21
- Starling R. L. C., et al., 2011, *MNRAS*, 411, 2792
- Starling R. L. C., Willingale R., Tanvir N. R., Scott A. E., Wiersema K., O'Brien P. T., Levan A. J., Stewart G. C., 2013, *MNRAS*, 431, 3159
- Stetson P. B., 1987, *PASP*, 99, 191
- Sudilovsky V., Kann D. A., Schady P., Klose S., Greiner J., Krühler T., 2013, GRB Coordinates Network, Circular Service, No. 15250, #1 (2013), [15250](#)
- Svensson K. M., Levan A. J., Tanvir N. R., Fruchter A. S., Strolger L.-G., 2010, *MNRAS*, 405, 57
- Tanaka M., 2016, *Adv. Astron.*, 2016, 1
- Tanaka M., Hotokezaka K., 2013, *ApJ*, 775
- Tanaka M., et al., 2018, *ApJ*, 852, 109
- Tanvir N. R., et al., 2009, *Nature*, 461, 1254
- Tanvir N. R., et al., 2010, GRB Coordinates Network, Circular Service, No. 11123, #1 (2010), [11123](#)
- Tanvir N. R., et al., 2012a, *ApJ*, 754, 46

- Tanvir N. R., Fynbo J. P. U., Melandri A., Levan A. J., Xu D., D'Elia V., 2012b, GRB Coordinates Network, Circular Service, No. 13890, #1 (2012), [13890](#)
- Tanvir N. R., Levan A. J., Fruchter A. S., Hjorth J., Hounsell R. A., Wiersema K., Tunnicliffe R. L., 2013a, *Nature*, 500, 547
- Tanvir N. R., Levan A. J., Fruchter A. S., Hjorth J., Hounsell R. A., Wiersema K., Tunnicliffe R. L., 2013b, *Nature*, 500, 547
- Tanvir N. R., Wiersema K., Xu D., Fynbo J. P. U., 2013c, GRB Coordinates Network, Circular Service, No. 14882, #1 (2013), [14882](#)
- Tanvir N. R., Xu D., Zafar T., Covino S., Schulze S., 2015a, GRB Coordinates Network, Circular Service, No. 18080, #1 (2015), [18080](#)
- Tanvir N. R., Krühler T., Malesani D., Xu D., de Ugarte Postigo A., Pugliese G., 2015b, GRB Coordinates Network, Circular Service, No. 18524, #1 (2015), [18524](#)
- Tanvir N. R., Xu D., Krühler T., Malesani D., Fynbo J. P. U., Pugliese G., Levan A. J., Cano Z., 2016a, GRB Coordinates Network, Circular Service, No. 19350, #1 (2016), [19350](#)
- Tanvir N. R., Krühler T., De Cia A., Wiersema K., Xu D., Malesani D., 2016b, GRB Coordinates Network, Circular Service, No. 20104, #1 (2016), [20104](#)
- Tanvir N. R., Krühler T., Wiersema K., Xu D., Malesani D., Milvang-Jensen B., Fynbo J. P. U., 2016c, GRB Coordinates Network, Circular Service, No. 20321, #1 (2016), [20321](#)
- Tanvir N. R., et al., 2017a, eprint arXiv:1703.09052
- Tanvir N. R., et al., 2017b, *ApJ*, 848, L27
- Tauris T. M., et al., 2017, *ApJ*, 846, 170
- Tavani M., et al., 2009, *A&A*, 502, 995
- Taylor G. B., Frail D. A., Berger E., Kulkarni S. R., 2004, *ApJ*, 609, L1
- Tchekhovskoy A., McKinney J. C., Narayan R., 2008, *MNRAS*, 388, 551
- Tepper García T., 2006, *MNRAS*, 369, 2025
- Thompson T. A., Chang P., Quataert E., 2004, *ApJ*, 611, 380
- Thöne C. C., Greiner J., Savaglio S., Jehin E., 2007, *ApJ*, 671, 628
- Thöne C. C., et al., 2009, GRB Coordinates Network, Circular Service, No. 10233, #1 (2009), [10233](#)

- Thöne C. C., de Ugarte Postigo A., Vreeswijk P., D'Avanzo P., Covino S., Fynbo J. P. U., Tanvir N., 2010, GRB Coordinates Network, Circular Service, No. 10971, #1 (2010), [10971](#)
- Thöne C. C., et al., 2011, [MNRAS](#), 414, 479
- Thöne C. C., et al., 2013, [MNRAS](#), 428, 3590
- Tody D., Hanisch R. J., 1993, IRAF in the Nineties. Vol. 52
- Troja E., et al., 2017a, [Nature](#), 547, 425
- Troja E., et al., 2017b, [Nature](#), 547, 425
- Troja E., et al., 2017c, [Nature](#), 551, 71
- Trujillo I., Aguerri J. A. L., Cepa J., Gutiérrez C. M., 2001, [MNRAS](#), 328, 977
- Tunnicliffe R. L., et al., 2014, [MNRAS](#), 437, 1495
- Ukwatta T. N., Wózniak P. R., 2016, [MNRAS](#), 455, 703
- Ukwatta T. N., et al., 2016, GRB Coordinates Network, Circular Service, No. 19148, #1 (2016), [19148](#)
- Usov V. V., 1992, [Nature](#), 357, 472
- Uzdensky D. A., MacFadyen A. I., 2006, [ApJ](#), 647, 1192
- Valenti S., et al., 2017, [ApJ](#), 848, L24
- Van Dyk S. D., et al., 2018, ] arXiv:1803.01050v1
- Vergani S. D., Petitjean P., Ledoux C., Vreeswijk P., Smette A., Meurs E. J. A., 2009, [A&A](#), 503, 771
- Vergani S. D., et al., 2010a, GRB Coordinates Network, Circular Service, No. 10495, #1 (2010), [10495](#)
- Vergani S. D., D'Avanzo P., Levan A. J., Covino S., Malesani D., Hjorth J., Antonelli L. A., 2010b, GRB Coordinates Network, Circular Service, No. 10512, #1 (2010), [10512](#)
- Vergani S. D., Levan A. J., D'Avanzo P., Covino S., Malesani D., Hjorth J., Tanvir N. R., Antonelli L. A., 2010c, GRB Coordinates Network, Circular Service, No. 10513, #1 (2010), [10513](#)
- Vergani S. D., et al., 2011a, [A&A](#), 535, A127
- Vergani S. D., et al., 2011b, GRB Coordinates Network, Circular Service, No. 12677, #1 (2011), [12677](#)

- Vergani S. D., et al., 2015, [A&A](#), 581, A102
- Vernet J., et al., 2009, [Proc. Int. Astron. Union](#), 5, 535
- Vernet J., et al., 2011, [A&A](#), 536, A105
- Verrecchia F., et al., 2017, [Astrophys. J. Lett.](#) Vol. 850, Issue 2, Artic. id. L27, 9 pp. (2017)., 850
- Villar V. A., et al., 2017, [ApJ](#), 851, L21
- Vink J. S., de Koter A., 2005, [A&A](#), 442, 587
- Vink J. S., Gräfener G., Harries T. J., 2011, [A&A](#), 536, L10
- Virgili F. J., et al., 2013, [ApJ](#), 778
- Voss R., Tauris T. M., 2003, [MNRAS](#), 342, 1169
- Vreeswijk P. M., et al., 2007, [A&A](#), 468, 83
- Vreeswijk P. M., Kaufer A., Spyromilio J., Schmutzler R., Ledoux C., Smette A., De Cia A., 2010, The VLT Rapid-Response Mode: implementation and scientific results, doi:10.1111/j.1365-2958.2010.01727.x,  
<https://www.eso.org/sci/libraries/SPIE2010/7737-22.pdf>
- Vreeswijk P., Fynbo J., Melandri A., 2011, GRB Coordinates Network, Circular Service, No. 12648, #1 (2011), [12648](#)
- Vreeswijk P. M., et al., 2013, [A&A](#), 549, A22
- Wallner A., et al., 2015, [Nat. Commun.](#), 6, 5956
- Wanajo S., 2013, [Astrophys. J. Lett.](#), 770, L22
- Wanajo S., Sekiguchi Y., Nishimura N., Kiuchi K., Kyutoku K., Shibata M., 2014, [ApJ](#), 789, L39
- Wanderman D., Piran T., 2015, [MNRAS](#), 448, 3026
- Watson D., Jakobsson P., 2012, [ApJ](#), 754, 89
- Watson D., et al., 2013, [ApJ](#), 768, 23
- Waxman E., Ofek E., Kushnir D., Gal-Yam A., 2017
- Wheeler J. C., Yi I., Hoflich P., Wang L., 2000, [ApJ](#), 537, 810
- Wiersema K., et al., 2011, GRB Coordinates Network, Circular Service, No. 12431, #1 (2011), [12431](#)
- Wiersema K., et al., 2012a, [MNRAS](#), 426, 2

- Wiersema K., et al., 2012b, GRB Coordinates Network, Circular Service, No. 12991, #1 (2012), [12991](#)
- Wiersema K., et al., 2014, *Nature*, 509, 201
- Wijers R. A. M. J., Bloom J. S., Bagla J. S., Natarajan P., 1998, *MNRAS*, 294, L13
- Willingale R., Starling R. L. C., Beardmore A. P., Tanvir N. R., O'Brien P. T., 2013, *MNRAS*, 431, 394
- Winkler C., et al., 2003, *A&A*, 411, L1
- Wollaeger R. T., et al., 2017
- Woosley S. E., 1993, *ApJ*, 405, 273
- Woosley S. E., Heger A., 2006, *ApJ*, 637, 914
- Woosley S. E., Eastman R. G., Schmidt B. P., 1999, *ApJ*, 516, 788
- Wu M. R., Tamborra I., Just O., Janka H. T., 2017, *Phys. Rev. D*, 96
- Xu D., Fynbo J. P. U., D'Elia V., Tanvir N. R., 2012, GRB Coordinates Network, Circular Service, No. 13460, #1 (2012), [13460](#)
- Xu D., et al., 2013a, *ApJ*, 776
- Xu D., et al., 2013b, GRB Coordinates Network, Circular Service, No. 14273, #1 (2013), [14273](#)
- Xu D., et al., 2013c, GRB Coordinates Network, Circular Service, No. 14757, #1 (2013), [14757](#)
- Xu D., et al., 2013d, GRB Coordinates Network, Circular Service, No. 14816, #1 (2013), [14816](#)
- Xu D., et al., 2013e, GRB Coordinates Network, Circular Service, No. 14956, #1 (2013), [14956](#)
- Xu D., Malesani D., Tanvir N., Krühler T., Fynbo J., 2013f, GRB Coordinates Network, Circular Service, No. 15450, #1 (2013), [15450](#)
- Xu D., et al., 2013g, GRB Coordinates Network, Circular Service, No. 15451, #1 (2013), [15451](#)
- Xu D., Malesani D., Tanvir N. R., D'Elia V., de Ugarte Postigo A., Krühler T., Fynbo J. P. U., 2014a, GRB Coordinates Network, Circular Service, No. 15645, #1 (2014), [15645](#)
- Xu D., Levan A. J., Fynbo J. P. U., Tanvir N. R., D'Elia V., Malesani D., 2014b, GRB Coordinates Network, Circular Service, No. 16983, #1 (2014), [16983](#)
- Xu D., Vreeswijk P. M., Fynbo J. P. U., D'Elia V., Wiersema K., Tanvir N. R., de Ugarte Postigo A., Covino S., 2014c, GRB Coordinates Network, Circular Service, No. 17040, #1 (2014), [17040](#)

- Xu D., Levan A. J., de Ugarte Postigo A., Tanvir N. R., Malesani D., Fynbo J. P. U., 2015a, GRB Coordinates Network, Circular Service, No. 17832, #1 (2015), [17832](#)
- Xu D., Tanvir N. R., Malesani D., Fynbo J. P. U., 2015b, GRB Coordinates Network, Circular Service, No. 18506, #1 (2015), [18506](#)
- Xu D., Malesani D., Fynbo J. P. U., Tanvir N. R., Levan A. J., Perley D. A., 2016a, GRB Coordinates Network, Circular Service, No. 19600, #1 (2016), [19600](#)
- Xu D., Heintz K. E., Malesani D., Wiersema K., Fynbo J. P. U., 2016b, GRB Coordinates Network, Circular Service, No. 19773, #1 (2016), [19773](#)
- Xu D., Heintz K. E., Malesani D., Fynbo J. P. U., 2017, GRB Coordinates Network, Circular Service, No. 20458, #1 (2017), [20458](#)
- Xu S., Yang Y.-P., Zhang B., 2018, *ApJ*, 853, 43
- Yang B., et al., 2015a, *Nat. Commun.*, 6, 7323
- Yang B., et al., 2015b, *Nat. Commun.*, 6, 7323
- Yoon S.-C., Langer N., 2005, *A&A*, 443, 643
- Yoon S.-C., Langer N., Norman C., 2006, *A&A*, 460, 199
- Zhang B., et al., 2009, *ApJ*, 703, 1696
- Zheng W., Filippenko A. V., Yuk H., Zhu Y., Perley D. A., 2015, GRB Coordinates Network, Circular Service, No. 18273, #1 (2015), [18273](#)
- Zitrin A., et al., 2015, *Astrophys. J. Lett.*, 810, L12
- de Blok W. J. G., Walter F., 2014, *AJ*, 147, 96
- de Mink S. E., Mandel I., 2016, *MNRAS*, 460, 3545
- de Ugarte Postigo A., et al., 2006, *ApJ*, 648, L83
- de Ugarte Postigo A., et al., 2009a, GRB Coordinates Network, [9015](#)
- de Ugarte Postigo A., et al., 2009b, GRB Coordinates Network, Circular Service, No. 1042, #1 (2009), [10042](#)
- de Ugarte Postigo A., et al., 2010, *A&A*, 513, A42
- de Ugarte Postigo A., et al., 2011a, *A&A*, 525, A109

- de Ugarte Postigo A., et al., 2011b, GRB Coordinates Network, Circular Service, No. 11579, #1 (2011), [11579](#)
- de Ugarte Postigo A., et al., 2011c, GRB Coordinates Network, Circular Service, No. 12258, #1 (2011), [12258](#)
- de Ugarte Postigo A., et al., 2014a, [A&A](#), 563, A62
- de Ugarte Postigo A., et al., 2014b, [A&A](#), 563, A62
- de Ugarte Postigo A., Krühler T., Flores H., Fynbo J. P. U., 2015a, GRB Coordinates Network, Circular Service, No. 17523, #1 (2015), [17523](#)
- de Ugarte Postigo A., Xu D., Malesani D., Tanvir N. R., 2015b, GRB Coordinates Network, Circular Service, No. 17822, #1 (2015), [17822](#)
- de Ugarte Postigo A., Thöne C., Lombardi G., Perez A., 2015c, GRB Coordinates Network, Circular Service, No. 18274, #1 (2015), [18274](#)
- de Ugarte Postigo A., Pugliese G., Xu D., Malesani D., 2016a, GRB Coordinates Network, Circular Service, No. 18886, #1 (2016), [18886](#)
- de Ugarte Postigo A., Malesani D., Krühler T., Xu D., Schulze S., Hjorth J., Tanvir N. R., 2016b, GRB Coordinates Network, Circular Service, No. 19154, #1 (2016), [19154](#)
- de Ugarte Postigo A., Kann D. A., Izzo L., Thöne C. C., Castro-Rodriguez N., Velarde G. G., 2016c, GRB Coordinates Network, Circular Service, No. 20014, #1 (2016), [20014](#)
- de Ugarte Postigo A., et al., 2016d, GRB Coordinates Network, Circular Service, No. 20342, #1 (2016), [20342](#)
- van Dokkum P. G., 2001, [PASP](#), 113, 1420
- van Eerten H., 2018
- van Eerten H. J., Leventis K., Meliani Z., Wijers R. A. M. J., Keppens R., 2010, [MNRAS](#), 403, 300
- van Paradijs J., et al., 1997, [Nature](#), 386, 686
- van Paradijs J., Kouveliotou C., Wijers R. A. M. J., 2000, [ARA&A](#), 38, 379
- van de Voort F., Quataert E., Hopkins P. F., Kere D., Faucher-Giguere C.-A., 2014, [MNRAS](#), 447, 140
- van der Horst A. J., Kouveliotou C., Gehrels N., Rol E., Wijers R. A. M. J., Cannizzo J. K., Racusin J., Burrows D. N., 2009, [ApJ](#), 699, 1087
- van der Walt S., Colbert S. C., Varoquaux G., 2011, [CSE](#), 13, 22